Many-body effects in nanoscale fluid transport

Nikita Kavokine

PSL
UNIVERSITÉ PARIS

THÈSE DE DOCTORAT
DE L'UNIVERSITÉ PSL

Préparée à l'École Normale Supérieure

Effets à *N* corps dans le transport de fluides aux nanoéchelles

Soutenue par
Nikita KAVOKINE
Le 30 juin 2021

Ecole doctorale n° 564
Physique en Île de France

Spécialité
Physique de la matière molle et nanosciences

Composition du jury :

Carlo SIRTORI Professeur, ENS	*Président*
Elisabeth CHARLAIX Professeur, Univ. Grenoble-Alpes	*Rapporteur*
David ANDELMAN Professeur, Univ. Tel Aviv	*Rapporteur*
Benoît DOUCOT Professeur, Sorbonne Université	*Invité*
Thierry GIAMARCHI Professeur, Univ. Genève	*Examinateur*
Francois PEETERS Professeur, Univ. Antwerp	*Examinateur*
Bo PERSSON Professeur, Univ. Jülich	*Examinateur*
Lydéric BOCQUET Professeur, ENS	*Directeur de thèse*

ENS | PSL

Thèse de doctorat de
l'Université de recherche Paris Sciences et Lettres

préparée à l'École Normale Supérieure

Many-body effects in nanoscale fluid transport

---

présentée par

Nikita Kavokine

afin d'obtenir le grade de
Docteur de l'Université de recherche Paris Sciences et Lettres

dirigée par
Prof. Lydéric Bocquet

Soutenue publiquement le 30 juin 2021 devant le Jury composé de

Prof. Carlo Sirtorti	Président
Prof. Élisabeth Charlaix	Rapporteur
Prof. David Andelman	Rapporteur
Prof. Benoît Douçot	Invité
Prof. Thierry Giamarchi	Examinateur
Prof. Francois Peeters	Examinateur
Prof. Bo Persson	Examinateur
Prof. Lydéric Bocquet	Directeur de thèse

Quand on ne sait pas où l'on va, il faut y aller. Et le plus vite possible![1]
– Jacques Rouxel, *Les Shadoks*.

[1]When you don't know where you're going, you must go there. And fast!

Remerciements

I would like to open these acknowledgements by expressing my sincere gratitude to all the members the Jury. I am particularly grateful to Elisabeth Charlaix and David Andelman for taking the time to write very thorough reports on this thesis, and to Carlo Sirtori for taking on the function of president. And I would like thank Benoît Douçot, Thierry Giamarchi, Francois Peeters and Bo Persson, together with the aforementioned Jury members for their detailed reading of this manuscript and their in-depth questions during the defence. I was sincerely impressed by the interest that the Jury expressed towards this work.

Cette thèse a été réalisée au sein de l'équipe Micromégas, au département de physique de l'École Normale Supérieure, sous la direction de Lydéric Bocquet.

Je continue donc en français afin de remercier Lydéric pour l'environnement exceptionnel dans lequel j'ai pu pas passer mes quatre années de thèse. Merci pour l'énorme confiance que tu m'as accordée, et pour m'avoir appris ce que c'est que de faire de la recherche. En particulier – et c'est un apprentissage difficile mais essentiel – la recherche, c'est savoir se débrouiller tout seul avec ses problèmes. Mais c'est aussi la conscience qu'aucun problème n'est insurmontable : si le problème en vaut le peine, peu importent les outils nécessaires pour le résoudre. Je comprends maintenant la phrase d'Anne Sylvestre en épigraphe de ta page web : *Là où j'ai peur, j'irai.* C'est pour cela qu'une version un peu moins chevaleresque de cette devise figure en épigraphe de ma thèse. J'espère emporter dans ma future vie scientifique un peu de cette intuition qui te pointe toujours vers les bonnes questions à se poser.

Merci à Alessandro Siria et Antoine Niguès, qui font vivre dans l'équipe un environnement expérimental très riche dont j'ai beaucoup profité en tant que (semi) théoricien. Merci à Giulio Biroli et à Jérôme Tignon, qui ont accepté de constituer mon comité de suivi de thèse.

Je voudrais maintenant remercier les collègues avec qui j'ai eu l'occasion de travailler pendant cette thèse. Avant tout, Paul Robin : merci Paul d'avoir mené le travail sur les memristors, et merci pour toutes les discussions, toujours fructueuses parce qu'on réfléchit de la même façon. Merci à Anton Robert pour les magnifiques simulations et les discussions sur la friction quantique, et à Sophie Marbach pour les discussions initiales sur le Coulomb blockade. Merci à Antoine Niguès, pour son enthousiasme sur les bizarreries des "colloïdes chinois", et merci à Baptiste Coquinot, pour la confiance accordée en montant dans le bateau de la friction quantique. Merci à Adrien Delahais et Romain Blattner pour leur travail effectué en stage.

Je remercie chaleureusement les différentes personnes avec qui j'ai eu l'occasion d'avoir des échanges scientifiques pendant cette thèse : Benoit Douçot – dont les éclairages sur les questions de matière condensée ont été précieux ; Giulio Biroli – pour les conseils avisés

en termes de poursuite de carrière ; David Dean, Rodolphe Vuilleumier, Marie-Laure Bocquet, et enfin Roland Netz, pour son formidable accueil à Berlin[2].

Merci à Dounia Benzouak pour sa disponibilité et son enthousiasme, merci également à Nora Sadaoui, Annie Ribaudeau, Benoit Paulet et Zaire Dissi, qui assurent tous les jours le bon fonctionnement du laboratoire.

Je remercie maintenant tous les collègues de l'équipe Micromégas avec qui j'ai passé de très bons moments durant ces quatre années. Je ne parviendrai sans doute pas à citer tout le monde sans omission, et encore moins à trouver les bons mots pour dire tout ce que je dois à chacun, mais je tente une revue par ordre chronologique. Jean et Antoine – votre grande maîtrise des manips m'a toujours inspiré le respect ; Anthony – respect aussi, de ta rigueur de théoricien et de ta descente de bière ; Laetitia – quand j'ai besoin d'énergie, je repense à comment tu montais les escaliers ; Luca – grâce à toi, je sais où trouver la meilleure mozzarella de Paris ; Timothée – les soirées sushi me manquent ! Sara – toujours la tête connue en conf ; Amin – père du lab cleaning, et Edimbourg, c'était trop bien ; Yuki et Christie – vous avez fait l'ambiance de l'IPGG ; Vasu et Javier – merci pour bien des fous rires ; Nicolas – qui connait toujours l'humeur du patron de Golosino ; Lucie, Marc, Soufiane, et enfin, Alice, Théo et Paul, sans qui les -1 n'aurait jamais été le même. Merci pour tous les déjeuners, les restos, les bières clandestines, le micromégasale, les discussions philosophiques de 22h30 devant l'Axopatch, et tous les autres bons moments passés ensemble.

Merci à mes parents, qui m'ont donné un tellement bon exemple que je l'ai suivi malgré moi. Mais non, je ne ferai jamais des polaritons !

Merci enfin à Roxane, pour son soutien inconditionnel même dans les moments les plus difficiles de la préparation de cette thèse.

[2]Thank you Roland for hosting me in your group !

Foreword

This thesis concerns the study of liquids confined to the nanometre scale, or *nanofluidics*. Why should anyone care about liquids in tiny pipes? A basic answer is: because there is a difference with liquids in larger pipes. Indeed, as physicists, we have a rather complete understanding of how water flows, say, through a garden hose. But as we make the garden hose smaller and smaller, at which point are we going to find something that we do not understand?

The answer to this question is far from obvious. What we know for sure, is that scale reduction does eventually bring about new physics. Indeed, the smallest pipes one can imagine are biological ion channels, and those are known to be qualitatively very different from garden hoses: take, for instance, the hugely permeable aquaporin [1], the potassium-ion specific KCsA channel [2], or the mechano-sensitive Piezo channel [3]. Yet, there is a gray area between the garden hose and the aquaporin, in which it is not entirely clear what aspects of macroscopic fluid dynamics break down and when.

This gray area – which is, more precisely, between the micrometer and the molecular scale – is the realm of nanofluidics. It is not only an interesting place to look for new physics: it also turns out to be particularly relevant in terms of applications [4]. Indeed, water desalination, or, more generally, ultrafiltration, involves water passing through channels of sizes comparable with ion diameters. Similarly, the generation of so-called *blue energy* – energy extracted from salinity gradients – involves water flows in nanometre scale channels [5]. In a context where balancing energy demand and supply becomes critical [6], membrane-based separation processes are particularly promising. As an example, separation processes in general represent one half of the United States' industrial energy consumption. Most of these are based on distillation and require heating, while membrane-based alternatives would use up to 90% less energy [7].

From a basic science point of view, a lot of inspiration for designing "smarter" nanoscale transport processes comes from the aforementioned biological channels. Nanofluidics follows in general a bottom-up approach: instead of investigating complex biological systems directly, researchers attempt to identify their elementary physical ingredients by studying well-controlled artificial channels [8, 9]. The fundamental properties that are identified in this way may then either lead to upscaling in membrane technology [10], or to engineering bio-inspired advanced functionalities at smaller scales: this is the nascent field of iontronics [11]. Therefore, given the biological inspiration and the nature of potential applications, nanofluidics in general – and this thesis in particular – are mostly concerned with water as the fluid. Now, especially in physiological conditions, water contains ions, so that water and ion transport are two indissociable aspects of nanofluidics.

As opposed to experiments in nanoscale fluid transport, the corresponding theoretical investigations mostly rely on a top-down approach [9]. Specifically, equations that

are derived for fluids at the mesoscopic scale are extended almost down to molecular-scale confinements. Such an apparently crude procedure has been surprisingly successful: for example, the Navier-Stokes equation is found to be valid down to about 1 nm confinement [12]. Yet, as smaller and smaller scales are reached in artificial nanofluidic devices [9], evidence accumulates for exotic phenomena that are beyond the reach of continuum theory: stochastic ion transport through narrow carbon nanotubes [13, 14], unusual ion and water dynamics in two-dimensional capillaries [15–18], and anomalous water slippage on carbon-based materials [19–25], to name only a few. These unexplained phenomena have recently been compiled in a review by the CENT collaboration on nanofluidics [26], which identifies the "critical knowledge gaps in mass transport through single-digit nanopores" – nanopores with sub-10 nm dimensions, scale at which most of the unexplained phenomena come into play.

The main goal of this thesis has been to develop new theoretical tools for nanofluidics, beyond the reach of the usual continuum and mean field equations. In particular, I show that a range of unexpected phenomena arise in nanoscale fluid transport due to **many-body effects**. These many-body effects are a consequence of what I call *interaction confinement*: the presence of a wall affects not only the particles' translational degrees of freedom, but also their interactions. I first show that Coulomb interactions become stronger in confinement, leading to enhanced ionic correlations and many-ion effects relevant to iontronic applications. Then, I explore the correlations between the dynamics of interfacial water and of the confining wall electrons, which result in a quantum contribution to hydrodynamic friction, shedding some light on the anomalous behaviour of the water-carbon interface. Finally, I present the development of an experimental setup for the direct optical measurement of water slippage in two-dimensional confinement. This thesis is organised into four parts.

- Part I is an introduction to nanofluidics and to the problems tackled in this thesis. Chapter 1 gives a brief account of the experimental sate of the art [i], and describes the well-established continuum and mean-field framework for fluids at the nanoscale. Chapter 2 introduces the notion of interaction confinement, and explores the consequences for ionic interactions in one- and two-dimensional channels.

- Part II concerns the many-ion effects that are predicted as a consequence of interaction confinement. Chapter 3 presents a theory of ionic Coulomb blockade [ii], that arises in 1D channels gated by a surface charge; Chapter 4 describes an ionic memristor effect that leads to neuromorphic behaviour in 2D channels [iii].

- Part III presents a new theoretical description for the solid-liquid interface, that takes into account the coupled dynamics of the fluid and solid electrons in a field theory framework [iv]. The only chapter (Chapter 5) predicts a quantum contribution to hydrodynamic friction, which provides an explanation for the radius-dependence of water slippage in carbon nanotubes [23].

- Part IV accounts for the experimental work performed during my PhD. Chapter 6 presents a direct measurement of the water slip length in two-dimensional carbon nanochannels, via confocal fluorescence imaging: this work is still ongoing at the time of writing of this manuscript. Chapter 7 concerns the experimental investigation of a photomechanical transduction phenomenon observed in a colloidal

suspension [v]. Although it is not exactly a nanoscale phenomenon, I found it to be a consequence of a many-body effect in the colloidal dynamics.

This thesis is based on the following publications:

i. N. Kavokine, R. R. Netz and L. Bocquet. "Fluids at the Nanoscale: from Continuum to Subcontinuum transport". *Annu. Rev. Fluid. Mech.* **53**, 377 – 410 (2021)

ii. N. Kavokine, S. Marbach, A. Siria and L. Bocquet. "Ionic Coulomb blockade as a fractional Wien effect". *Nat. Nanotech.* **14**, 573 – 578 (2019)

iii. P. Robin, N. Kavokine and L. Bocquet. "Modelling of emergent memory and voltage spiking in ionic transport through angström-scale slits". *Science* (2021)

iv. N. Kavokine, A. Robert, M.-L. Bocquet and L. Bocquet. "Fluctuation-induced quantum friction in nanoscale water flows". arXiv:2105.03413, *under review.* (2021)

v. N. Kavokine, S. Zou, R. Liu, A. Niguès, B. Zou and L. Bocquet. "Ultrafast photomechanical transduction through thermophoretic implosion". *Nat. Commun.* **11**, 1 – 7 (2020).

Contents

Part I

Nanofluidics and interaction confinement

Chapter 1

Introduction to fluids at the nanoscale

Contents

This chapter is based on the following publication: N. Kavokine, R. R. Netz and L. Bocquet. "Fluids at the Nanoscale: from Continuum to Subcontinuum transport". *Annu. Rev. Fluid. Mech.* **53**, 377 – 410 (2021).

1.1 Introduction

Fluid flows at the nanometre scale have been studied indirectly in various disciplines for the last fifty years [27]. However, it is only fifteen years ago that nanofluidics has emerged as a field on its own, first as a natural extension of microfluidics towards smaller scales. Back then, it was an issue in itself to establish that nanofluidics deserves its own name, meaning that there are specific effects at the nano-scale that are not present at the micro-scale.

Indeed, the "ultimate scale" for observing specific effects is set by the molecular size of the fluid ; more precisely, a critical confinement $\ell_c = 1$ nm has been generally accepted as the limit of validity for the Navier-Stokes equation [12, 28]. Moreover, it is at the molecular scale that the fluidic functions of biological systems emerge: from the giant permeability and perfect selectivity of the aquaporin [1], to the ion specificity of KcsA channels [2], to the mechano-sensitivity of Piezo channels [3], to name a few. However,

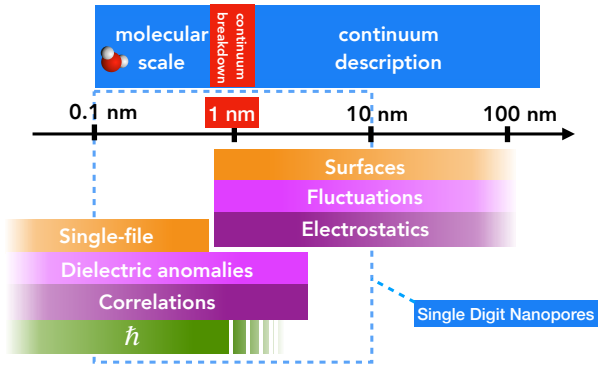

Figure 1.1

An overview of nanofluidic lengthscales: the main ingredients of the physics above and below the continuum limit.

ten years ago, the exploration of this ultimate scale was hindered by technical challenges, as molecular scale channels could not be fabricated artificially.

A decade later, nanofluidics has firmly established itself as a field [8]. Indeed, lengthscales associated with the electrostatics and the fluctuations of surfaces may reach up to several tens of nanometres, and their effects may be probed specifically in systems without molecular scale confinement [12, 28, 29] (figure. 1.1). These lengthscales govern the key nanofluidic phenomena that have been demonstrated over the last ten years, such as, for instance, fast flows in carbon nanotubes [20], diffusio-osmotic energy conversion [10] or diode-type effects [30].

However, the progress in fabrication technology has now allowed to overcome the challenges that have hindered the development of nanofluidics at the ultimate scales, and artificial devices with confinement down to about one water molecule size (3 Å) have been achieved, in 0D, 1D or 2D geometry [17, 24, 31]. It is therefore an exciting time for nanofluidics, since it now has the potential to reverse-engineer biological functions: minimal artificial systems that mimic biological processes may be designed and studied. Furthermore, nanofluidics is known for its short path from fundamental science to applications and innovation, and developments in single channel fabrication are likely to have direct implications for filtration and membrane science [8].

In the quest for scale reduction, theory has been lagging behind experiment. Indeed, having been developed in the wake of microfluidics, theoretical approaches to nanofluidics have largely been based on continuum and mean field equations [12]. While these approaches have been surprisingly successful down to few-nanometre lengthscales, they do eventually break down, as ionic correlations, dielectric anomalies and other subcontinuum effects come into play (Fig 1.1): this thesis is concerned with the study of some of these effects. The first chapter starts with a brief overview of the latest experimental developments in nanofluidics, which set the application ground for theory. Then, the basic continuum equations for nanofluidics are presented, with an emphasis on their extension to the smallest scales. Chapter 2 then focuses on the limits of these equations, which are set in particular by the phenomenon of *interaction confinement*.

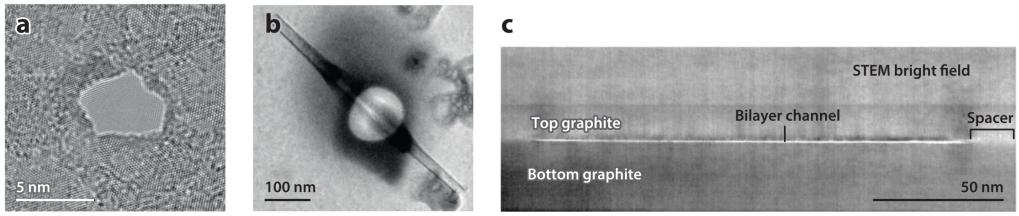

Figure 1.2

State-of-the-art nanofluidic systems of various dimensions. **a.** TEM-drilled nanopore in single layer MoS_2 [31]. **b.** Boron nitride nanotube inserted into a SiN membrane [10]. **c.** TEM image of the nanoslit device fabricated by Radha *et al.* [15].

1.2 The toolbox of experimental systems

Nanofluidics generally follows a bottom-up approach. Elementary phenomena are understood at the well-controlled scale of the individual channel, before eventually being applied to more complex systems. Hence, the design of these well-controlled systems is paramount to the development of the field. We start this chapter by going through the systems that have so far been achieved, in order of dimensionality.

1.2.1 Nanopores

Nanopores are channels whose length L and diameter d are both in the nanometre range (figure 1.2a). Initial studies focused on solid-state nanopores drilled through membranes made out of ceramics such as SiN of SiC [32,33]. More recently the advent of 2D materials, such as graphene, hexagonal boron nitride (hBN) or MoS_2, allowed for the exploration of nanopores in atomically thin membranes [34,35]. Essentially three types of fabrication pathways have been reported for well-controlled nanopores in 2D materials.

- Drilling with an electron or a focused ion beam (FIB). A single 5 nm pore drilled in monolayer graphene was first reported by Garaj *et al.* [34]. FIB drilling of arrays of nanopores in bilayer graphene, ranging from 7.6 nm to 1 μm in diameter, was reported in [36].

- Electrochemical etching. Feng *et al.* [37] reported the opening of pores in monolayer MoS_2 when placed in a salt solution in between two electrodes. Applying a potential above the oxydation potential of MoS_2 resulted in the gradual removal of single MoS_2 units, thus creating an opening of controlled size. Nanopores down to 0.6 nm in diameter have been reported [38].

- The use of intrinsic defects in 2D materials. Large area membranes made of graphene or hBN are known to exhibit defects in the form of pores, ranging in size from a few angstroms to 15 nm depending on conditions [39, 40], or such defects may be generated on purpose in smaller membranes using ultraviolet-induced oxidative etching [41]. The chemical vapour deposition (CVD) graphene membranes described in [42] exhibited pores in the sub-2 nm range spaced by 70 to 100 nm.

Placing the membrane on top of a 30-40 nm pore of a SiN membrane allowed to statistically isolate and study a single pore.

1.2.2 Nanotubes

Nanotubes are cylindrical channels of diameter d in the nanometre range, and length $L \gg d$ (figure 1.2b). They are typically made out of carbon, or the isoelectronic boron nitride. The nanotubes themselves, as a product of self-assembly, are readily available, but interfacing a nanotube to a fluidic system and avoiding leakage is still an experimental challenge. Three distinct strategies for addressing this challenge have been reported.

- Building a microfluidic system on top of CVD-grown single-walled carbon nanotubes. The systems may comprise one or several carbon nanotubes, typically of diameter 1 to 2 nm. The tubes generally have very high aspect ratio with lengths up to 0.5 mm [14, 43, 44], although similarly built systems with 20 μm long nanotubes have also been reported [45].

- Insertion of a multiwalled nanotube into a solid state membrane. Siria *et al.* [10] reported the fabrication of nanofluidic devices comprising a single boron nitride nanotube, inserted into a hole milled in a SiN membrane by direct nanomanipulation under SEM. The hole could be sealed *in situ* by cracking of naphtalene induced by the electron beam. The method was later extended to carbon nanotubes [23], of 30 to 100 nm inner diameter and about 1 μm in length, and recently to smaller, 2 nm inner diameter, multiwall carbon nanotubes [46].

- Insertion of nanotubes into a lipid membrane. Very short (5 to 10 nm) and very narrow (0.8 to 2 nm in diameter) nanotubes may be incerted into a supported lipid membrane [47]. Nanotubes were brought in contact with the lipid bilayer thanks to a microinjection probe. Recently, Noy and colleagues [24] reported the self-assembly of similar nanotubes, which they term carbon nanotube porins, into phospholipid vesicles. A single patch of membrane could also be isolated in order to study a single porin.

1.2.3 Nanoslits down to angström confinements

Slit-like channels with one dimension below tens of nanometers were first made using micro- and nano- fabrication techniques. But recently, Radha *et al.* [15] reported the manufacturing of two-dimensional channels by van der Waals assembly of 2D materials (figure 1.2c). A few layers of graphene were used as spacers between two crystals of graphite, hBN or MoS_2, allowing for atomically smooth channels of a few μm in length, 100 nm in width and down to 7 Å in height, that is the thickness of two graphene layers. Very recently, water transport through one-graphene-layer thick (3.4 Å) channels was reported [17].

This brief overview highlights that nanofluidics at the molecular scale is now a reality. Not only molecular scale confinement is possible, but the geometry of the confinement and the nature of the confining materials can also be tuned.

1.3 Liquid transport

1.3.1 Navier-Stokes equation

The two-centuries-old Navier-Stokes equation is remarkably robust at describing fluid flow down to the smallest scale, typically $\ell_c = 1$ nm for water in normal pressure and temperature conditions [12]. This length scale is essentially a lower bound for defining a fluid viscosity η. Indeed, in macroscopic fluid mechanics, the kinematic viscosity $\nu = \eta/\rho$, where ρ is the mass density, plays the role of a diffusion coefficient for the fluid momentum. For such a diffusion coefficient to be defined, the time required for momentum to diffuse across the system, ℓ_c^2/ν, must be larger than the timescale of molecular motion, which is the microscopic origin of diffusion. A water molecule at a thermal agitation speed of 300 $\mathrm{m \cdot s^{-1}}$ moves by its own size in $\tau_c = 10^{-12}$ s, which defines a molecular time scale. Therefore, viscosity may be defined down to a system size

$$\ell_c \sim \sqrt{\nu \tau_c} \sim 1 \text{ nm}. \tag{1.1}$$

Below this length scale, water structuring due to surfaces, memory effects and other sub-continuum phenomena come into play. For water flow at 10 nm length scales, the Reynolds number remains smaller than 0.1 up to fluid velocities of 10 $\mathrm{m \cdot s^{-1}}$. Hence, in nanofluidic systems, inertial effects may be safely neglected, and the fluid flow is described by the Stokes equation:

$$\eta \Delta v + f = \nabla p, \tag{1.2}$$

where p is the pressure and f a body force, which may be due, for example, to the application of an electric field, as discusses in section 1.4.

1.3.2 Boundary conditions

Stokes flow is often solved with no-slip boundary conditions: the velocity of the liquid is assumed to vanish at a solid-liquid interface. This is, however, a limiting case of the more general Navier partial slip boundary condition, which enforces that the viscous stress at the interface should be balancing the solid liquid friction force. Within linear response theory, the friction force is proportional to the liquid velocity. For a fluid flowing in the direction x along a surface of normal z, the force balance per unit area writes $\sigma_{xz} = \lambda v_x$, with $[\sigma]$ the stress tensor and λ the friction coefficient per unit area (expressed in $\mathrm{N \cdot s \cdot m^{-3}}$). For a Newtonian fluid, $\sigma_{xz} = \eta \partial_z v_x$, which allows one to rewrite the Navier boundary condition as

$$v_x = b \frac{\partial v_x}{\partial z}\bigg|_{\text{wall}}, \tag{1.3}$$

introducing the slip length $b = \eta/\lambda$. The slip length can be geometrically interpreted as the depth inside the solid where the linearly extrapolated fluid velocity profile vanishes. Accordingly, the no-slip boundary condition corresponds to $\lambda \to \infty$ or $b \to 0$. The effect of the partial slip condition is to simply shift the no-slip velocity profile by the slip velocity, which is not negligible roughly within a slip length from the wall (figure 1.3). Since slip lengths up to tens of nanometers have been measured on atomically smooth (and hydrophobic) surfaces [15, 21, 23, 48], slippage is expected to play a crucial role in nanofluidics, and Part III of this thesis is devoted to the study of its microscopic origin.

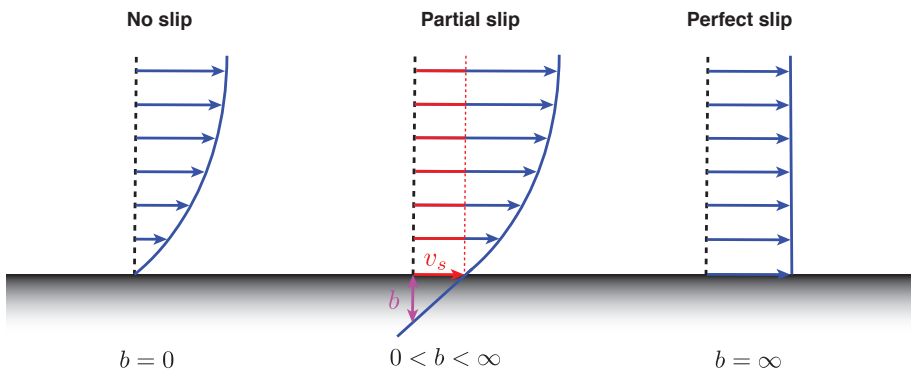

Figure 1.3

Geometric interpretation of the Navier partial slip boundary condition, and definition of the slip length b.

In the smallest channels, of size $R \ll b$, a perfect slip boundary condition may even be appropriate: the flow is then controlled by entrance effects.

1.3.3 Geometry and entrance effects

Experimentally, the flow profile inside a nanofluidic channel can hardly be resolved, and one typically measures the total flow rate Q. Under a pressure drop ΔP and no-slip boundary conditions, the flow rate through a cylindrical channel of radius R is given by the Hagen-Poiseuille formula:

$$Q_c = \frac{\pi R^4}{8\eta L}\Delta P. \tag{1.4}$$

This formula assumes a channel length $L \gg R$, and thereby neglects the effect of channel mouths on the flow rate. But the transition from a macroscopic reservoir to a nanoscale channel is a source of viscous dissipation, as the streamlines need to be bent in order for the fluid to enter the channel. These entrance effects may be examined by considering the flow through an infinitely thin nanopore, which is of interest in itself, given the geometry of certain nanofluidic devices (see section 1.2). This problem was addressed by Sampson [49]. For a nanopore of radius R (and vanishing length) under pressure drop ΔP, Sampson obtained the expression of the flow rate as

$$Q_p = \frac{R^3}{3\eta}\Delta P. \tag{1.5}$$

The scaling in Sampson's formula naturally emerges from a Stokes equation where the only lengthscale is R: $\eta\Delta v = \nabla p \Rightarrow \eta v/R^2 \sim \Delta P/R$, and the typical fluid velocity is $v \sim Q/R^2$. In order to estimate the flow rate through a channel taking into account entrance effects, one may simply add the hydrodynamic resistances of the pore ($\mathcal{R}_p$) and the channel ($\mathcal{R}_c$). If one writes $Q_c = (\Delta P)_c/\mathcal{R}_c$ and $Q_p = (\Delta P)_p/\mathcal{R}_p$, then the entrance-corrected flow rate Q_{pc} is obtained by imposing $Q_p = Q_c = Q_{pc}$ and $\Delta P =$

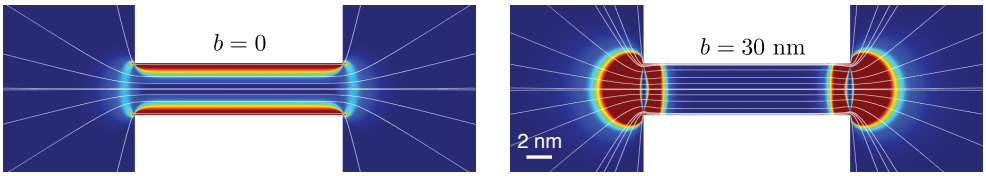

Figure 1.4

Viscous dissipation rate, and streamlines, for the pressure-driven flow of water across a nanopore, as obtained from a finite-element solution of the Stokes equation (COMSOL) for two values of the slip length b. The color scale, from blue to red, encodes the viscous dissipation. In the presence of slippage, the dissipation is mostly at the channel entrances.

$(\Delta P)_c + (\Delta P)_p$, so that

$$Q_{pc} = \frac{\Delta P}{\mathcal{R}_h + \mathcal{R}_p} = \frac{\pi R^4}{8\eta L} \frac{\Delta P}{1 + \frac{3\pi}{8}\frac{R}{L}}. \tag{1.6}$$

An exact computation [50] shows that the error made by this a priori crude approximation is less than 1%. Equation 1.6 makes a continuous transition between the nanopore and nanochannel regimes, and shows that entrance effects are apparently negligible for channel lengths that exceed a few channel radii.

However, the above discussion has crucially not taken into account slippage, which, as we have highlighted in the previous section, is a strong effect at the nanoscale. Introducing a non-zero slip length b, the flow rate though a channel becomes

$$Q_c = \frac{\pi R^4}{8\eta L}\left(1 + \frac{4b}{R}\right)\Delta P, \tag{1.7}$$

while the flow rate through a pore is not significantly affected [51], since the source of dissipation in that case is mostly geometric. A full expression can be obtained by gathering previous results, but in the limit where $b \gg R$, the entrance-corrected flow rate becomes

$$Q_{pc} = \frac{R^3}{3\eta} \frac{\Delta P}{1 + \frac{2L}{3\pi b}}. \tag{1.8}$$

Thus, the hydrodynamic resistance is actually dominated by entrance effects as long as the channel is shorter than the slip length, rather than the channel radius (see figure 1.4). In the presence of significant slippage, one should check whether the low Reynolds number assumption still holds. The average velocity through a channel of radius $R = 5$ nm and length $L = 1$ μm, with slip length $b = 30$ nm, under a pressure drop $\Delta P = 1$ bar is $v = 8$ mm $\cdot$ s^{-1}, which is 25 times faster than the no-slip result, but still well below the 1 m $\cdot$ s^{-1} threshold established above.

1.4 Ion transport

The behaviour of ions in nanofluidic systems is of great practical interest with applications ranging from biological ion channels [2] to ionic liquids inside nanoporous electrodes [52, 53]. Ion transport also provides an indirect way of probing fluid transport, which is often

useful, since electric currents are much easier to measure than fluid flow. However, due to their long range Coulomb interactions and diffusive dynamics, ions in nanochannels give rise to physics of great complexity. In this section, we only sketch the main results with particular emphasis on how well-known equations apply to the smallest channels, and we refer the reader to other reviews on the subject [12, 28, 29] for more details.

1.4.1 Basic equations

Consider an aqueous solution of monovalent salt. Let ρ_+, ρ_- be the densities of positive and negative ions, respectively; D the diffusion coefficient, here assumed to be the same for ions of either sign, and ϕ the electrostatic potential. In a mean-field treatment, the convective-diffusive dynamics of ions are described by a Smoluchowski equation:

$$\frac{\partial \rho_\pm}{\partial t} = \nabla \cdot \left(D\nabla\rho_\pm \mp \frac{eD}{k_B T}(\nabla\phi)\rho_\pm + v\rho_\pm \right), \tag{1.9}$$

where e is the unit charge, ϕ the electrostatic potential and v is the fluid velocity field. The mean-field assumption implies in particular that correlations between the ions can be neglected: the potential importance of such correlations in nanofluidics will be discussed in the next chapter. Until then, we proceed by specifying the electrostatic potential through Poisson's equation,

$$\Delta\phi = -e\frac{\rho_+ - \rho_-}{\epsilon}, \tag{1.10}$$

where ϵ is the dielectric permittivity of water. For now we assume it to be isotropic, though this assumption may break down for nano-confined water, as we discuss in chapter 2. Lastly, we specify the flow velocity through the Stokes equation, which now includes an electrostatic term:

$$\eta\Delta v - e(\rho_+ - \rho_-)\nabla\phi = \nabla p. \tag{1.11}$$

We now apply these three coupled equations to a specific geometry, though the discussion that follows could be generalised to channels of any shape. For simplicity, we consider a slit-like channel of height h, width w and length L, with $w, L \gg h$, connecting two reservoirs of salt solution at concentration ρ_s, extending along the direction x, between $z = 0$ and $z = h$. When considering ion transport, it is important to note that most surfaces are charged in water, due either to the dissociation of surface groups or to the adsorption of ions [54–56]. We hence assume the channel wall carries a surface charge density $-\Sigma e$ (Σ is expressed in elementary charges per unit area, and we assume here the surface charge to be negative).

1.4.2 Ionic conductance

We first neglect the coupling of ion transport to water transport, and consider the electrophoretic (EP) contribution to the ionic current under an applied electric field E: this means that we start by setting the fluid velocity $v = 0$. In the steady state, the Smoluchowski equation (1.9) reduces to the so-called Nernst-Planck equations for the constant ionic fluxes (along the x direction):

$$j_\pm = D\nabla_x\rho_\pm \mp \frac{eD}{k_B T}(\nabla_x\phi)\rho_\pm. \tag{1.12}$$

Together with the Poisson equation (1.10), these constitute the widely used Poisson-Nernst-Planck (PNP) framework. In our geometry, the condition $L \gg h$ ensures that in the middle of the channel $\nabla_x \rho_\pm = 0$; moreover to first order in E, $\nabla_x \phi = -E$ and the densities reduce to their equilibrium values. Hence, the EP contribution to the ionic current writes

$$I_{\text{ep}} = w \int_0^h \mathrm{d}z (j_+ - j_-) = w \frac{e^2 D}{k_B T} \int_0^h \mathrm{d}z (\rho_+ + \rho_-) E. \tag{1.13}$$

In order to compute I_{ep}, one needs to find the equilibrium solution of the coupled PNP equations for ρ_+ and ρ_-. At equilibrium $j_\pm = 0$ and the Nernst-Planck equations (1.12) can be integrated, imposing that in the reservoirs $\phi = 0$ and $\rho_\pm = \rho_s$. This yields a Boltzmann distribution for the ions in the electrostatic potential

$$\rho_\pm = \rho_s \exp\left(\mp \frac{e\phi}{k_B T}\right) \equiv \rho_s e^{\mp \psi}, \tag{1.14}$$

introducing a dimensionless potential ψ. Combining this with the Poisson equation (1.10) yields the Poisson-Boltzmann (PB) equation:

$$\Delta \psi - \lambda_D^{-2} \sinh(\psi) = 0, \tag{1.15}$$

which introduces the Debye length $\lambda_D = (8\pi \rho_s \ell_B)^{-1/2}$, with $\ell_B = e^2/(4\pi\epsilon k_B T)$ the Bjerrum length. In our geometry, the PB equation has an implicit solution in terms of an elliptic integral [57, 58]. We will not exploit it here, however, and we will instead recover the relevant limiting behaviours from qualitative considerations.

It is well known that, roughly speaking, the Debye length sets the extension of the diffuse layer of counterions next to a charged surface [59]. Hence, if the channel height $h \gg \lambda_D$, its two opposing walls do not 'see' each other. We expect the conductance to be the sum of a bulk term, and a surface term originating in the two Debye layers:

$$I_{\text{ep}} = 2w \frac{e^2 D}{k_B T} E(\rho_s h + \Sigma). \tag{1.16}$$

where $\rho_s h$ and Σ account for the number of charge carriers in the bulk and at surfaces, respectively. In the opposite limit where $h \ll \lambda_D$, there is no more distinction between surface and bulk. All the quantities may be considered uniform across the channel: this is called the Debye overlap regime. However, one may not assume that the channel contains only counterions, and one should go back to the thermodynamic equilibrium with the reservoirs, which in this case bears the name of Donnan equilibrium [12]. One has $\rho_\pm = \rho_s e^{\mp\psi}$, which implies a chemical equilibrium $\rho_+ \rho_- = \rho_s^2$ in the channel. Going further, in the limit of long channel length, there should be local electroneutrality: $h(\rho_+ - \rho_-) = 2\Sigma$. This yields

$$\rho_\pm = \sqrt{\rho_s^2 + (\Sigma/h)^2} \pm \Sigma/h, \tag{1.17}$$

and the current-voltage relation in the Debye overlap is

$$I_{\text{ep}} = 2w \frac{e^2 D}{k_B T} E \sqrt{(\rho_s h)^2 + \Sigma^2}. \tag{1.18}$$

Equation 1.18 displays the first peculiarity of small channels: one may not simply add the surface and bulk contributions. Table 1.1 lists the values of Debye length for different

ρ_s (M)	λ_D (nm)
10^0	0.3
10^{-1}	1.0
10^{-2}	3.1
10^{-3}	9.6

Debye length: $\lambda_D = (8\pi\rho_s\ell_B)^{-1/2}$. Thickness of the diffuse layer of counterions next to a charged surface.
Bjerrum length: $\ell_B = e^2/(4\pi\epsilon_0 k_B T)$. Distance between two unit charges at which their interaction energy is $k_B T$.
Dukhin length: $\ell_{Du} = \Sigma/\rho_s$. Channel width below which surface conductance dominates over bulk conductance.
Gouy-Chapman length: $\ell_{GC} = (2\pi\Sigma\ell_B)^{-1}$. Distance a unit charge must travel from a charged surface so that its electrostatic energy is reduced by $k_B T$.

Material	Σ (C · m^{-2})	Σ (e · nm^{-2})	ℓ_{GC} (nm)	ℓ_{Du} at 0.1 M (nm)
Graphene oxide [56]	0.01	0.06	4	1
Silica [60]	0.05	0.3	0.8	5
Carbon nanotube [61]	0.16	1	0.2	17
BN nanotube [10]	1.4	9	0.03	150

Table 1.1

Electrostatic lengthscales. Values of Debye length, Gouy-Chapman length and Dukhin length in a range of conditions.

electrolyte concentrations, showing that the Debye overlap regime is indeed relevant for experimentally accessible nanofluidic systems (see section 1.2). Qualitatively, eqs. (1.16) and (1.18) both predict saturation of the conductance at low salt concentrations at a value determined by the surface charge. The saturation occurs when $\rho_s \sim \Sigma/h$, which can be recast in the form $h \sim \rho_s/\Sigma \equiv \ell_{Du}$. ℓ_{Du} is called the Dukhin length and quantifies the competition between bulk and surface contributions to the conductance. For a channel narrower than ℓ_{Du}, surface contributions dominate, and vice versa. The Dukhin length is going to be important in our upcoming discussion of entrance effects.

At this point, a remark should be made concerning the range of validity of equations (1.16) and (1.18). Indeed, they have been derived from qualitative considerations, without reference to the exact solution of the PB equation. Now, from eqs. (1.13) and (1.14), one obtains more generally

$$I_{\mathrm{ep}} = 2w\frac{e^2 D}{k_B T}\left(\rho_s h\cosh(\psi(h/2)) + \frac{\mathcal{E}}{2k_B T}\right), \tag{1.19}$$

where $\mathcal{E} = (\epsilon/2)\int_0^h (\partial_z\phi)^2 \mathrm{d}z$ is the electrostatic energy per unit area. The electric double layer can be pictured as a capacitor with charge Σ, hence one would expect its electrostatic energy to scale as Σ^2; moreover, this is the prediction of the linearised PB equation, i.e. eq. (1.15) with the approximation $\sinh\psi \approx \psi$. This is in contrast to, eq. (1.16), which predicts a linear scaling of the conductance with Σ: this scaling must therefore come from the non-linearities of the PB equation. The PB equation may be linearised if the potential varies by less than $k_B T$ across the Debye layer (or across the channel if there is Debye overlap). This is the case in the high concentration/low surface charge limit and specifically when the Debye length is smaller than the so-called Gouy-Chapman length: $\ell_{GC} = (2\pi\Sigma\ell_B)^{-1}$. On the other hand, eq. (1.18), valid for the Debye overlap regime, is safe from a condition on ℓ_{GC}, as it predicts both quadratic and linear scalings depending on the value of Σ, as long as there is Debye overlap.

1.4.3 Entrance effects

Similarly to what we have discussed for liquid and gas transport, we may now ask, for ion transport, what is the additional electrical resistance due to the channel - reservoir interface. Equivalently, we may want to estimate the ionic conductance of a nanopore of small aspect ratio, say of radius R and length $L \sim R$. The problem has first been considered in the context of biological channels by Hille [62] and Hall [63]. Hall solved the electrostatic problem with an electrode at infinity and an equipotential disk accounting for the entrance of the pore. Translating the solution into scaling arguments, the current through the pore entrance is $I \sim \pi R^2 \kappa_b \Delta V_{\text{out}}/R$, where ΔV_{out} is the voltage drop at the entrance of the pore, which is expected to occur over a distance R, and not over the macroscopic distance between the electrodes. This defines an electrical access resistance as the ratio $\Delta V_{\text{out}}/I$. We now specialise to the thin Debye layer regime $\lambda_D \ll R$. If one simply sums the access resistance and the channel resistance as given by eq. (1.16) (adapted to cylindrical geometry), the current-voltage relation becomes

$$I_{\text{ep}} = \kappa_b \left(\frac{L}{\pi R^2} \frac{1}{1 + \ell_{Du}/R} + \frac{1}{\alpha R} \right)^{-1} \Delta V, \tag{1.20}$$

with α a geometric factor which is 2 in Hall's computation, and introducing the bulk conductivity $\kappa_b = 2e^2 D \rho_s/(k_B T)$. The above equation predicts vanishing conductance as $\rho_s \to 0$, since the access resistance becomes infinite in this limit; however, this is not what is observed experimentally in short nanopores [31, 64]. This inconsistency arises because, for a surface-charged pore, the access current has a surface contribution, in addition to the bulk contribution. This surface contribution may be evaluated starting from charge conservation at the surface, which imposes a relation between the axial and radial components of the electric field, as pointed out by Khair and Squires [65]:

$$\kappa_b E_r = \partial_x [\kappa_s \theta(x) E_x], \tag{1.21}$$

with κ_s the surface conductance and θ the Heaviside function, accounting for the discontinuity of surface charge at the pore boundary, which leads to subtle consequences. Indeed, it reveals that the Dukhin length, $\ell_{Du} = \Sigma/\rho_s \sim \kappa_s/\kappa_b$, is the relevant lengthscale for the surface contribution to the electric field outside the pore, instead of the channel radius or Debye length. The Dukhin length appears here as an electrostatic healing length: feeding the surface conduction at the nanopore mouth disturbs the electric field lines in the bulk over a length ℓ_{Du}. This interpretation is supported by the numerical results of ref. [64] as shown in figure 1.5a. The bending of the electric field lines can be estimated by a perturbative approach [64] that leads to an analytical expression for the corrected current-voltage relation:

$$I_{\text{ep}} = \kappa_b \left(\frac{L}{\pi R^2} \frac{1}{1 + \ell_{Du}/R} + \frac{1}{\alpha R + \beta \ell_{Du}} \right)^{-1} \Delta V. \tag{1.22}$$

The surface-charged pore therefore appears, from the perspective of entrance effects, as an uncharged pore of effective size $R + \ell_{Du}$, since the geometrical prefactor $\beta \approx 2$. In the limit of vanishing salt concentration, $\rho_s \to 0$, the conductance indeed saturates, and, as expected, the entrance correction disappears in the limit of large aspect ratio pores. Lee *et al.* [64] successfully compared the prediction of eq. (1.22) to experimental measurements in SiN nanopores in the range $100 - 500$ nm. More recently, it has been used to describe conductance measurements in MoS_2 nanopores down to 2 nm in diameter [31].

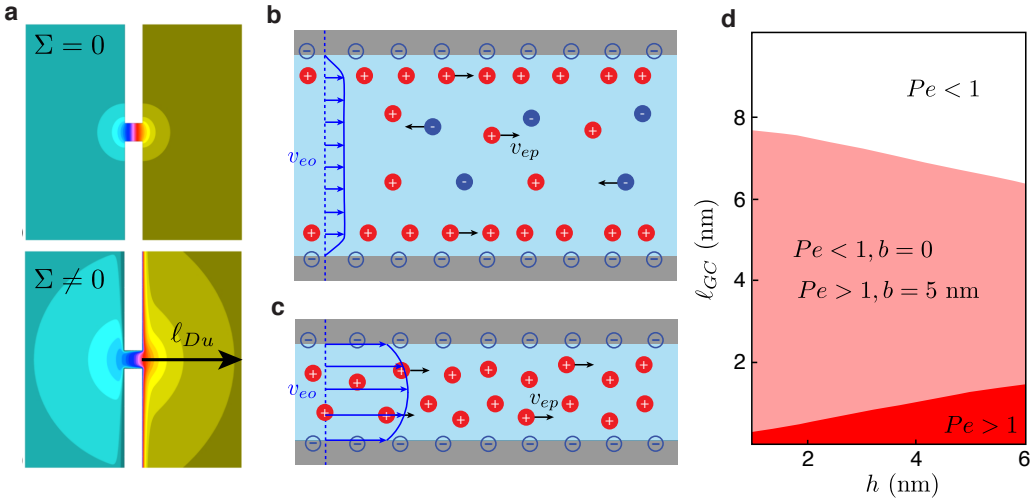

Figure 1.5

a. Colour plot of the electrostatic potential around a nanopore immersed in a salt solution and subject to a voltage drop, in the charged and in the uncharged case. Around a charged pore, the lengthscale for variation of the potential is set by the Dukhin length. Adapted from [64]. **b.** and **c.** Schematic representation of coupled ion and fluid transport in a nanochannel under electric field driving: in the thin Debye layer limit (**b.**) and in Debye overlap in the presence of slippage (**c.**). The electro-osmotic contribution dominates in the latter case. **d.** Peclet number (defined in the text), as a function of channel width and Gouy-Chapman length. The region in parameter space where $Pe > 1$ is coloured in dark red in the no-slip case, and in light red when slippage is present.

1.4.4 Coupling with fluid flow

So far, we have neglected any coupling of ion transport to fluid transport. However, in the presence of charged surfaces, an external electric field exerts a net force on the charged Debye layer, which sets the fluid in motion. This interfacially-driven flow is termed electro-osmotic (EO) flow. The EO flow in turn drags along the ions in the Debye layer, which makes a supplementary contribution to the ionic current, that we denote I_{eo}. This contribution has a convenient exact expression in the slit-like geometry considered in section 1.4.1. In analogy to eq. (1.13),

$$I_{\text{eo}} = 2w \int_0^{h/2} e(\rho_+ - \rho_-)v(z)\mathrm{d}z. \tag{1.23}$$

From the Poisson equation (1.10), we may replace $e(\rho_+ - \rho_-) = -\epsilon\partial_z^2\phi$. Then, integrating by parts,

$$I_{\text{eo}} = 2w\epsilon \left[\int_0^{h/2} \partial_z\phi\partial_z v \,\mathrm{d}z + v(0)\partial_z\phi|_0 \right]. \tag{1.24}$$

Now, we may use the partial slip boundary condition $v(0) = b\partial_z v|_0$, as well as the electrostatic boundary condition $\partial_z\phi|_0 = e\Sigma/\epsilon$. This stems from the Gauss theorem applied to the surface, and the assumption that the medium outside the channel has

much lower dielectric permittivity than water [58]. Moreover, an integration of the Stokes equation (1.11) allows the replacement $\partial_z v = -(\epsilon E/\eta)\partial_z \phi$. Altogether, we obtain

$$I_{\rm eo} = w\left[\frac{2\epsilon}{\eta}\mathcal{E} + \frac{2be^2\Sigma^2}{\eta}\right]E, \tag{1.25}$$

where $\mathcal{E} = (\epsilon/2)\int_0^h (\partial_z\phi)^2 {\rm d}z$ is the electrostatic energy per unit surface introduced in the previous section. It appears here that slippage has an additive contribution to the EO current, which strikingly does not depend on any electrolyte properties.

We now consider the result in two limiting cases. First, in the thin Debye layer limit, by comparing with eq. (1.19), one may identify

$$I_{\rm eo} = \frac{k_B T}{2\pi\ell_B\eta D} I_{\rm ep}^{\rm surf} + 2w\frac{be^2\Sigma^2}{\eta}E, \tag{1.26}$$

where $I_{\rm ep}^{\rm surf}$ is the surface contribution to the electrophoretic current. To quantify the importance of the EO contribution, one may compute the analogue of a Peclet number:

$$Pe = \frac{I_{\rm eo}}{I_{\rm ep}^{\rm surf}} = \frac{3}{2}\frac{d_i}{\ell_B}\left(1 + \frac{b}{\ell_{GC}}\right). \tag{1.27}$$

We have introduced here the ion diameter d_i by using the Einstein relation $D = k_B T/(3\pi\eta d_i)$ and we recall that $\ell_{GC} = (2\pi\Sigma\ell_B)^{-1}$. In water at room temperature, $d_i \sim \ell_B \sim 0.7$ nm, therefore, in the absence of slippage, the EO contribution is of the same order as the surface EP contribution, $Pe \sim 1$. Table 1.1 lists, for reference, values of the Gouy-Chapman length for typical surface charge values. As these are generally in the nanometre range, even in the case of moderate slippage ($b \sim 10$ nm), there is a strong enhancement of the EO contribution. The threshold confinement below which the resulting surface contribution dominates over the bulk contribution is given by a rescaled Dukhin length: $\ell_{Du}^* = (b/\ell_{GC})\ell_{Du}$.

Second, in the Debye overlap regime, the EO current is readily determined from eq. (1.23), since the ion densities may then be considered uniform across the channel and are given by eq. (1.17). Uniform ionic densities also imply that the flow has no longer a surface, but rather a volume driving. It is simply a Poiseuille flow, with the pressure gradient $\Delta P/L$ replaced by the electric driving force $e(\rho_+ - \rho_-)E$. Altogether one obtains

$$I_{\rm eo} \simeq \frac{wh}{3\eta}e^2\Sigma^2\left(1 + \frac{6b}{h}\right)E. \tag{1.28}$$

Since in Debye overlap it makes no more sense to distinguish a surface and a bulk contribution, we define the Peclet number as the ratio of the EO current to the total EP current:

$$Pe = \frac{I_{\rm eo}}{I_{\rm ep}} = \frac{d_i}{\ell_B}\frac{h}{4\ell_{GC}}\frac{1 + 6b/h}{\sqrt{1 + (h/\ell_{Du})^2}}. \tag{1.29}$$

Figure 1.5d illustrates the dependence of this Peclet number on h and ℓ_{GC}, with $\rho_s = 10^{-2}$ M so that there is Debye overlap. In the absence of slippage, the EO contribution dominates only for high surface charges. However, if a small slip length $b = 5$ nm is introduced, the Peclet number exceeds 1 for all reasonable surface charges. Indeed, the

Peclet number is then essentially determined by the ratio b/ℓ_{GC}. This highlights that in the Debye overlap regime, ionic conduction should be mostly driven by electro-osmosis.

If strong EO flows are expected, then the reciprocal effect, streaming current, is expected to be large as well. The streaming current results from the application of a pressure gradient $\Delta P/L$: in Debye overlap, the charge density $2\Sigma/h$ is simply dragged along by the Poiseuille flow. The current reads

$$I_{\rm str} \simeq hw\frac{eh\Sigma}{6\eta}\left(1+\frac{6b}{h}\right)\frac{\Delta P}{L} \equiv hw\frac{-\epsilon\zeta}{\eta}\frac{\Delta P}{L}, \tag{1.30}$$

where we have phenomenologically defined the zeta potential (ζ) via the streaming mobility. Independent measurements of the surface charge through the voltage-driven current and of the zeta potential from the pressure-driven current may allow in principle to estimate the slip length b. Such an estimate does not replace a direct measurement, however, in particular because the slip length may directly depend on surface charge [66], and surface charges may be mobile [67, 68].

1.5 The big picture

In this Chapter, we gave an overview of the basic theoretical framework for fluids at the nanoscale. The main points are:

- Nanofluidic devices with molecular-scale confinement are today within reach. In general, nanofluidic systems are probed by liquid or ion transport measurements under a pressure or a voltage drop.
- Liquid transport is well-described by the Stokes equation, with the addition of wall slippage. The value of the slip length is crucial in determining a channel's permeability.
- Ion transport is understood in terms of the mean-field PNP framework, where the crucial ingredients are the channel surface charge, and the coupling between ion and liquid transport through electro-osmosis and streaming. These couplings are strongly affected by flow slippage at the channel walls.

Chapter 2

Interaction confinement

Contents

2.1 Introduction

As the scale of a nanofluidic system is reduced, some of the assumptions that are at the root of the continuum and mean-field equations exposed in the previous Chapter necessarily break down. A general overview of the corresponding *sub-continuum* effects is given in [9]. Notably, as channels reach the molecular scale, fluid structuring and thermal fluctuations play an overwhelming role. In this Chapter, we will focus on one particular sub-continuum effect, which leads to the breakdown of mean-field theory, and yet does not rely on fluid structuring. I call this effect *interaction confinement*, and it is at the basis of most of the phenomena discussed in the remainder of this thesis.

Interaction confinement means that the presence of a confining wall not only affects a particle's translational degrees of freedom, but also its interactions. Typically, we will consider Coulomb interactions of fluid particles, which are affected by the confining wall's electromagnetic response. As the simplest example of interaction confinement, consider a point-like ion in a narrow channel. Let us imagine that the channel is filled with water, with high dielectric permittivity (typically, $\epsilon_w = 80$) and embedded in a dielectric membrane with low permittivity $\epsilon_m = 2$. Then, due to the dielectric contrast, the electric field lines produces by the ion are forced to remain parallel to the channel walls (figure 2.1), so that inside the channel the Coulomb potential resembles a 1D Coulomb potential.

The idea of electric field shaping by dielectric discontinuities is far from being new. As early as 1969, Parsegian [69] realised that ions faced an energy barrier upon translocation through a biological channel embedded in a lipid membrane. For a channel of length L on the order of its radius R, and an ion of charge e, an approximate expression for this so-called self-energy barrier is

$$\mathcal{E}_s = \frac{e^2}{4\pi\epsilon_0\epsilon_w}\frac{L}{R^2}. \tag{2.1}$$

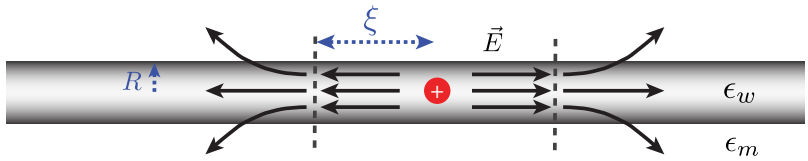

Figure 2.1

Sketch of interaction confinement for an ion inside a nanoscale channel: the dielectric contrast forces the electric field to remain parallel to the channel wall over a length ξ.

This is precisely the electromagnetic energy associated with the 1D-like electric field depicted in figure 2.1, whose magnitude is, according to Gauss' law, $E = e/(2\pi R^2 \epsilon_0 \epsilon_w)$. In a channel of length $L \gg R$, the 1D electric field actually leaks from the channel walls over a typical length ξ (which is on the order of a few channel radii, as detailed in the following), so that the self-energy barrier is

$$\mathcal{E}_s = \frac{e^2}{4\pi\epsilon_0\epsilon_w}\frac{\xi}{R^2}. \tag{2.2}$$

Several authors have proposed solutions of Poisson's equation for ions confined by dielectric walls [70–72]. Yet, the consequences of modified ionic interactions on the ion dynamics have remained largely unexplored. It may seem at first sight that dielectric discontinuities are fully taken into account in the PNP framework, as it involves solving Poisson's equation. However, PNP equations are intrinsically mean-field, and they cannot capture ionic correlations that result from confined interactions. We shall see that such correlations are the main consequence of interaction confinement, as ionic interactions in narrow channels become stronger than in the bulk. Nanofluidic systems with interaction confinement therefore require new theoretical tools, some of which we propose in Part II of this thesis.

This Chapter is organised as follows. We first establish analytical expressions for the Coulomb interaction under dielectric confinement, in the two experimentally relevant (1D and 2D) geometries. This allows us to determine the approximate dimensions of nanofluidic systems where interaction confinement will be important. While the 1D derivation has analogues in the literature [70, 72], for the 2D case we introduce an original approach based on surface response functions. Then, taking advantage of the surface response approach, we discuss the effect of dielectric anisotropy and electronic properties of the wall material on confined interactions. Finally, we sketch the consequences of interaction confinement beyond ionic correlations.

2.2 Ions in nanotubes

We consider a point charge $+e$ placed in the middle of a cylindrical channel of radius R and infinite length. The channel is filled with water, with dielectric permittivity ϵ_w, and is embedded in a local dielectric medium with permittivity ϵ_m. We will use, unless stated otherwise $\epsilon_w = 80$ and $\epsilon_m = 2$. We define cylindrical coordinates (r, z) with the z axis along the channel length and the charge placed at the origin. The electrostatic potential

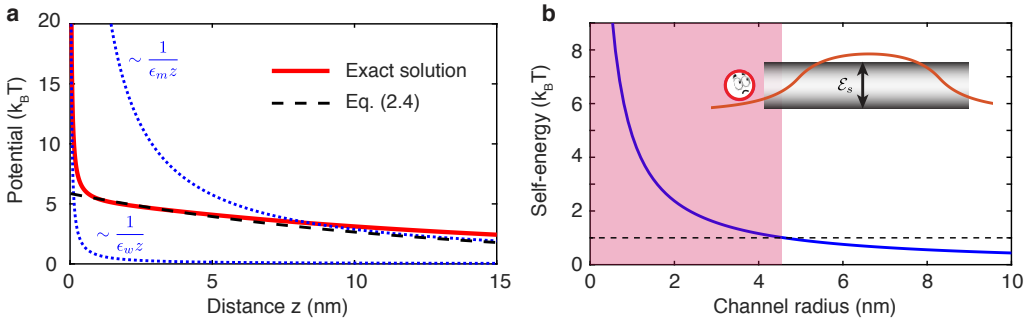

Figure 2.2

Interaction confinement in a 1D (nanotube) geometry. **a.** Potential along the channel axis, for a channel radius $R = 2$ nm. **b.** Self-energy barrier as a function of channel radius. The shaded region corresponds to channel radii for which the self-energy barrier is greater than $k_{\mathrm{B}}T$.

then satisfies the Poisson equation:

$$\partial_r^2\phi + \frac{1}{r}\partial_r\phi + \partial_z^2\phi = -\frac{e}{\epsilon_0\epsilon}\frac{\delta(r)\delta(z)}{2\pi r}, \tag{2.3}$$

with $\epsilon = \epsilon_w, \epsilon_m$. eq. (2.3) is solved by Fourier transforming along the z direction, and enforcing continuity of the displacement field and of the potential at the channel boundary; in the general, the inverse Fourier transform has then to be carried out numerically. Details of the computation are given in Appendix A.1, and figure 2.2 shows the result obtained for the potential $\phi(0, z)$ with $R = 2$ nm.

Here we discuss qualitatively the result. At short distances (much smaller than the channel radius), only the dielectric response of the water is visible and the potential is $\phi(z) \sim 1/(\epsilon_w z)$. At long distances (much larger than the channel radius), it is the dielectric response of the confining medium that matters and $\phi(z) \sim 1/(\epsilon_m z)$. At intermediate distances, the electric field lines are essentially parallel to the channel due to the dielectric contrast $\epsilon_w \gg \epsilon_s$, and the potential, which is well described by an exponential function, resembles a 1D Coulomb potential:

$$\phi(x) \approx \frac{e\xi}{2\pi\epsilon_0\epsilon_w R^2} e^{-z/\xi}. \tag{2.4}$$

ξ is the typical length over which the 1D electric field escapes through the channel boundaries (figure 2.1), that depends on the ratio ϵ_w/ϵ_m and channel radius; $\xi = 6.3R$ for $\epsilon_w/\epsilon_m = 40$ [70]. It is notable that so far no assumption on the channel radius was made, so that formally this 1D regime exists for a channel of any size. However, it is only relevant if it leads to ion-ion interactions stronger than k_BT, that is if $e\phi(R) > k_BT$, for a monovalent ion. This defines a limiting channel radius, below which ionic interactions are affected by the confining medium: $R_c \sim 7.5$ nm. Another criterion for the importance of interaction confinement effects is the value of the self-energy barrier (figure 2.2): we find that it is greater than $k_{\mathrm{B}}T$ for $R \lesssim 4$ nm.

2.3 Ions in nano-slits

We now consider a point charge $+e$ placed in the middle of a slit-like channel of height h and infinite length and width. As before, the channel is filled with water, with dielectric permittivity ϵ_w, and is embedded in a local dielectric medium with permittivity ϵ_m. We define cylindrical coordinates $(\boldsymbol{\rho}, z)$, with the z axis perpendicular to the channel, and place the charge at the origin. At this point, we could, as in the 1D case, solve the Poisson equation with the appropriate boundary conditions. But instead, we will introduce a more powerful approach based on *surface response functions*, which will ultimately allow us to discuss media with non-local dielectric response.

The surface response function $g(q,\omega)$ may be defined as a reflection coefficient for evanescent plane waves. If an external potential $\phi_{\text{ext}}(\boldsymbol{\rho}, z, t) = \phi_0 e^{i(\mathbf{q}\boldsymbol{\rho}-\omega t)} e^{q(z+h/2)}$ acts, say, on the confining wall at $z < -h/2$, then the potential induced by the confining wall in the half-space $z > -h/2$ is $\phi_{\text{ind}}(\boldsymbol{\rho}, z, t) = -\phi_0 g(q,\omega) e^{i(\mathbf{q}\boldsymbol{\rho}-\omega t)} e^{-q(z+h/2)}$. In this Chapter we will only be concerned with static potentials, hence we will use $g(q) \equiv g(q, \omega = 0)$. Surface response functions are discussed in detail in Appendix B, where it is shown how they can be evaluated starting from materials' electronic properties. For the local dielectric medium of permittivity ϵ_m, the surface response function is

$$g_m(q) = \frac{\epsilon_m - \epsilon_w}{\epsilon_m + \epsilon_w}, \tag{2.5}$$

taking into account that outside the medium m is water of permittivity ϵ_w.

With these definitions, we may readily determine the Coulomb potential inside the two-dimensional channel. It is the sum of the "external" potential produced by the test charge $+e$, and of the "induced" potential produced by the polarisation charges in the confining walls. The external potential is simply the 3D Coulomb potential $\phi_{\text{ext}}(\mathbf{r}) = e/(4\pi\epsilon_0\epsilon_w|\mathbf{r}|)$, which supports the following Fourier decomposition:

$$\phi_{\text{ext}}(\rho, z) = \frac{e}{4\pi\epsilon_0\epsilon_w} \int \frac{\mathrm{d}\mathbf{q}}{(2\pi)^2} \frac{2\pi}{q} e^{-q|z|} e^{i\mathbf{q}\boldsymbol{\rho}}. \tag{2.6}$$

The induced potential may be determined separately for every wavevector q. Let $\phi^m_{\text{ext}}(q)$ be the external potential acting on the wall at $z = -h/2$. It is the sum of the potential produced by the test charge, and of the induced potential created by the polarisation charges in the medium at $z > h/2$, both screened by the water dielectric constant. By symmetry, the external potential is the same in the upper and lower dielectric medium. This yields the following self-consistent equation:

$$\phi^m_{\text{ext}}(q) = \frac{e}{4\pi\epsilon_0\epsilon_w} \frac{2\pi}{q} e^{-qh/2} - g_m(q)\phi^m_{\text{ext}}(q) e^{-qh}. \tag{2.7}$$

We are interested in the total potential in the plane $z = 0$, which is

$$\phi_{\text{tot}}(q, z = 0) = \phi_{\text{ext}}(q, z = 0) - 2g_m(q)\phi^m_{\text{ext}}(q) e^{-qh/2}. \tag{2.8}$$

Making use of eq. (2.7), we obtain

$$\phi_{\text{tot}}(q, 0) = \frac{e}{4\pi\epsilon_0\epsilon_w} \frac{2\pi}{q} \left(1 - \frac{2g_m(q)e^{-qh}}{1 + g_m(q)e^{-qh}}\right). \tag{2.9}$$

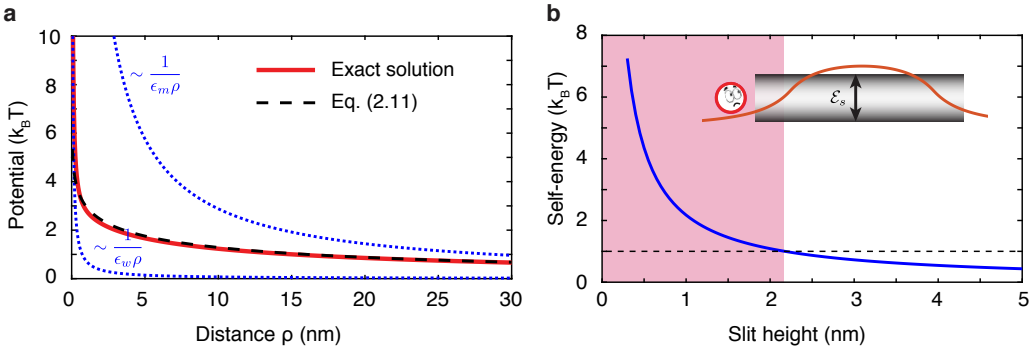

Figure 2.3

Interaction confinement in a 2D (nano-slit) geometry. **a.** Potential along the channel axis, for a channel height $h = 2$ nm. **b.** Self-energy barrier as a function of channel height. The shaded region corresponds to channel radii for which the self-energy barrier is greater than $k_\mathrm{B}T$.

The potential in real space is then obtained by inverse Fourier transformation, which thanks to the rotational symmetry reduces to

$$\phi_\mathrm{tot}(\rho, 0) \equiv \phi(\rho) = \int_0^{+\infty} \frac{\mathrm{d}q}{2\pi}\, q J_0(q\rho)\phi_\mathrm{tot}(q, 0), \tag{2.10}$$

with J_0 the Bessel function of the first kind.

Analytical expressions for the real space potential may be provided in terms of series expansions: these are reported in Appendix A.2. Here, we focus on the qualitative interpretation of the results. For illustration, the real-space Coulomb potential obtained in a slit of height $h = 2$ nm is shown in figure 2.3. Similarly to the 1D case, at distances $\rho \ll h$, the test charge only "sees" the dielectric response of water, and $\phi(\rho) \sim 1/\epsilon_w\rho$. Conversely, at large distances $\rho \gg h$, the potential is mostly screened by the walls, and $\phi(\rho) \sim 1/\epsilon_m\rho$. At intermediate distances, there is, as in 1D, a regime where the electric field lines remain parallel to the channel walls, but in the present 2D geometry this corresponds to a logarithmic potential, as opposed to linear in the 1D case. In this logarithmic region, the potential supports the following analytical approximation, in the limit of strong dielectric contrast (see Appendix A.2):

$$\phi(\rho) = \frac{e\mathcal{K}}{2\pi\epsilon_0\epsilon_w h} \log\left(\frac{\rho + \xi}{\rho}\right), \tag{2.11}$$

where $\mathcal{K} \approx 1.1$, and "leakage" of the electric field over a distance $\xi = \epsilon_w h/(2\epsilon_m)$ is taken into account. This analytical expression is plotted in figure 2.3a and is found to be in excellent agreement with the exact solution. Figure 2.3b shows the self-energy barrier (discussed in section 1) as a function of channel height h, determined according to $\mathcal{E}_s = e\phi_\mathrm{ind}(0, 0)/2$. It is found to be greater than $k_\mathrm{B}T$ for $h \lesssim 2$ nm, which roughly establishes a threshold for the importance of interaction confinement effects in 2D geometry.

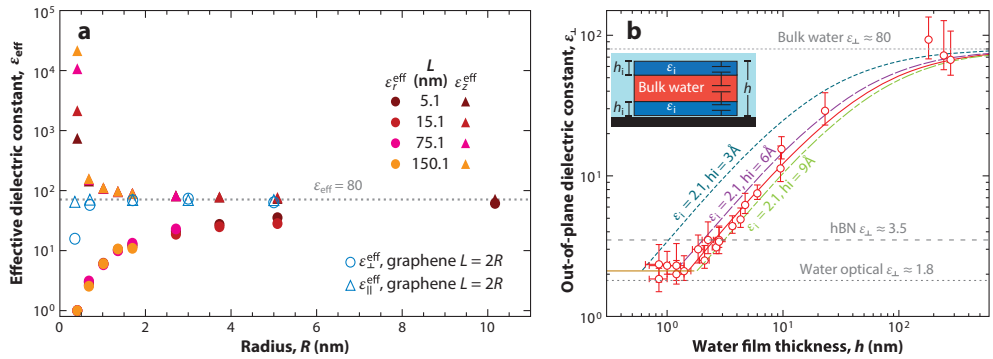

Figure 2.4

Dielectric anomalies in confined water. **a**. Components of the dielectric permittivity tensor of water in a carbon nanotube, as a function of nanotube radius, as determined from MD simulations. Adapted with permission from [72]. **b**. Experimental results for the transverse dielectric constant of water in planar confinement, as a function of confinement width. Adapted with permission from [73].

2.4 Dielectric anisotropy

We have so far assumed that the screening properties of water are described by a uniform dielectric constant ϵ_w. While this is a good approximation in the bulk up to molecular lengthscales, it is no longer so under confinement. Precisely, the total electric field $\mathbf{E}$ in water is the sum of the polarisation field of the water molecules and of the externally applied field $\mathbf{D}/\epsilon_0$, where $\mathbf{D}$ is the electric displacement, and so far we have assumed the simple relation $\mathbf{D} = \epsilon_w \epsilon_0 \mathbf{E}$. However, the most general (static) linear response may be anisotropic, space-dependent and non-local:

$$D_\alpha(\mathbf{r}) = \epsilon_0 \sum_\beta \int \mathrm{d}\mathbf{r}' \epsilon_{\alpha\beta}(\mathbf{r}, \mathbf{r}') E_\beta(\mathbf{r}'). \tag{2.12}$$

The relative permittivity is then a tensor with components $\epsilon_{\alpha\beta}(\mathbf{r}, \mathbf{r}')$, $\alpha, \beta \in \{x, y, z\}$. While MD simulations show that the dielectric response in water may be considered local ($\epsilon_{\alpha\beta}(\mathbf{r}, \mathbf{r}') = \epsilon_{\alpha\beta}(\mathbf{r})\delta(\mathbf{r}-\mathbf{r}')$), it becomes anisotropic and space-dependent in the vicinity of interfaces, as a consequence of water layering [74,75]. Qualitatively, the orientations of the water dipoles are anti-correlated in the direction perpendicular to the interface, resulting in a reduced permittivity in that direction, while the permittivity is largely unaffected parallel to the interface. In planar confinement, this behaviour could be captured by an effective medium model, in which the water is described by a space-independent, but anisotropic permittivity $(\epsilon_\parallel, \epsilon_\perp)$ (the parallel direction is not confined). While $\epsilon_\parallel$ essentially retains its bulk value, $\epsilon_\perp$ is reduced by up to an order of magnitude for confinements below 1 nm [76,77]. Such a reduction of the perpendicular dielectric response was recently observed experimentally for water confined between a graphite and a boron nitride crystal [73]. A deviation from the bulk value was measured up to nearly 100 nm confinement (figure 2.4). The results were well described by assuming each interface carried a 7 Å thick layer of very low permittivity ($\epsilon_w = 2.1$) "electrically dead water".

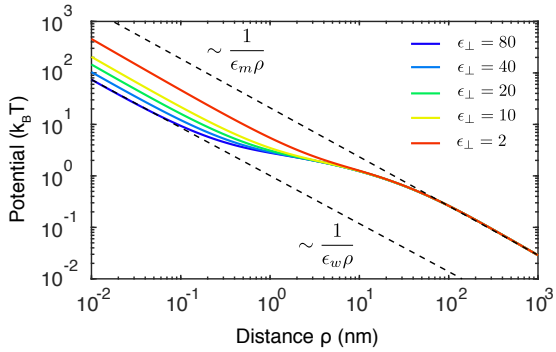

Figure 2.5

Coulomb potential created by an ion of charge e inside a nano-slit of height $h = 2$ nm, filled with water with anisotropic dielectric permittivity. The permittivity along the slit direction is fixed at $\epsilon_\parallel = 80$, while the permittivity in the perpendicular direction is varied.

An effective medium model based on MD simulations was developed by Loche *et al.* [72] for cylindrical confinement of water in carbon nanotubes. Similarly to the case planar case, the radial permittivity is found to be reduced by up to an order of magnitude for tube radii smaller than 3 nm (figure 2.4). However, for the smallest tubes (below 1 nm radius), the longitudinal permittivity is found to increase with respect to its bulk value, and it skyrockets 1 to 3 orders of magnitude in a 0.4 nm radius tube, where water is in a single file arrangement.

The dielectric anisotropy of water clearly has an influence on the Coulomb interactions under confinement. In general, this influence may be assessed by solving Poisson's equation, which now takes the form

$$\nabla \left(\bar{\bar{\epsilon}} \cdot \nabla \phi \right) = -\frac{e}{\epsilon_0} \delta(\mathbf{r}), \tag{2.13}$$

with $\bar{\bar{\epsilon}}$ the dielectric tensor. In the nanotube geometry, the computation is reported in Appendix A.1. In the nano-slit geometry, the anisotropy may be taken into account within the formalism of surface response functions. In an infinite medium with dielectric tensor components $(\epsilon_\parallel, \epsilon_\perp)$, the potential created by a point charge e placed at the origin is

$$\phi_{\text{ext}}(\rho, z) = \frac{e}{4\pi\epsilon_0 \sqrt{\epsilon_\parallel \epsilon_\perp} \sqrt{\rho^2 + \frac{\epsilon_\parallel}{\epsilon_\perp} z^2}}, \tag{2.14}$$

which becomes, after Fourier transformation,

$$\phi_{\text{ext}}(q, z) = \frac{e}{4\pi\epsilon_0 \sqrt{\epsilon_\parallel \epsilon_\perp}} \frac{2\pi}{q} e^{-aq|z|}, \tag{2.15}$$

with $a = \sqrt{\epsilon_\parallel / \epsilon_\perp}$. Hence, taking into account the dielectric anisotropy amounts to replacing $\epsilon_w \mapsto \sqrt{\epsilon_\parallel \epsilon_\perp}$, and introducing factors a in all the exponentials of the type e^{-qz}. In particular, the confining wall's surface response function becomes

$$g_m(q) = \frac{\epsilon_m - \sqrt{\epsilon_\parallel \epsilon_\perp}}{\epsilon_m + \sqrt{\epsilon_\parallel \epsilon_\perp}}, \tag{2.16}$$

and the Fourier-transformed potential at the channel midplane is

$$\phi_{\mathrm{tot}}(q,0) = \frac{e}{4\pi\epsilon_0\sqrt{\epsilon_\parallel\epsilon_\perp}}\frac{2\pi}{q}\left(1 - \frac{2g_m(q)e^{-aqh}}{1+g_m(q)e^{-aqh}}\right). \tag{2.17}$$

The analytical expression in eq. (2.11) for the logarithmic region of the potential still holds, with $\epsilon_w \mapsto \sqrt{\epsilon_\parallel\epsilon_\perp}$ and $\xi = \epsilon_\parallel h/(2\epsilon_m)$.

The qualitative consequence of these modified expressions is illustrated in figure 2.5, which shows the Coulomb potential produced by an ion inside a slit of height $h = 2$ nm. The parallel dielectric constant of water is fixed at $\epsilon_\parallel = 80$, while different values are taken for $\epsilon_\perp$. The dielectric anisotropy mainly affects the potential at short distances $\rho \ll h$, where the scaling becomes $\phi(\rho) \sim 1/\sqrt{\epsilon_\parallel\epsilon_\perp}\rho$. Since the effective dielectric constant seen by the potential at short distances is reduced, it becomes larger than in the isotropic case: this effectively shifts the logarithmic region to larger distances. In a nanotube geometry, the consequences of dielectric anisotropy on ionic interactions have been studied extensively in [72]. The effect is qualitatively the same as in 2D, except that, somewhat counterintuitively, the short-distance scaling of the potential along the axial direction involves the radial dielectric constant: $\phi(z) \sim 1/\epsilon_r z$. In general, one may conclude that ionic interactions are underestimated if nano-confined water is assumed to have the bulk dielectric properties.

2.5 Metallicity of the confining walls

We have discussed up till now ionic interactions in nanoscale channels with perfectly insulating walls. Such an assumption has traditionally been made for biological channels embedded in lipid membranes, and it is relevant for a range of artificial channel materials such as silica or hexagonal boron nitride. But many artificial channels are now being made out of graphite and related materials [15, 23], in which conduction electrons are present; pores with carbon-based walls also occur in nanoporous carbon electrodes [52,53]. These carbon-based materials may be electrically conducting: it is therefore of interest to explore the influence of conduction electrons on ionic interactions in confinement. Existing computations of confined Coulomb potentials that do not make the approximation of a perfect insulator make instead the approximation of a perfectly metallic wall [72, 78–80]. But in order to tackle realistic systems, one would like an approach that could deal with confining wall electronic properties in between these two extremes.

The surface response function framework is perfectly suited for such a purpose. Indeed, within the so-called *specular reflection* approximation (see [81] and Appendix B.4), the surface response function of a material can be computed given any form of its non-local bulk dielectric function $\epsilon(q,q_z)$:

$$g_m(q,\omega) = \frac{1-\sqrt{\epsilon_\parallel\epsilon_\perp}q\ell_q}{1+\sqrt{\epsilon_\parallel\epsilon_\perp}q\ell_q}, \quad \ell_q = \frac{2}{\pi}\int_0^{+\infty}\frac{\mathrm{d}q_z}{(q^2+q_z^2)\epsilon(q,q_z)}. \tag{2.18}$$

In order to continuously explore the range of screening properties between metal and insulator, one may use, at the simplest level, the Thomas-Fermi model for the bulk dielectric function [82]:

$$\epsilon(q,q_z) = \epsilon_m + \frac{q_{\mathrm{TF}}^2}{q^2+q_z^2}, \tag{2.19}$$

where ϵ_m is the background dielectric constant that accounts for screening by interband transitions, and q_{TF} is the Thomas-Fermi wavevector. Qualitatively, the Thomas-Fermi model introduces a screening length for the potential: $\lambda_{\mathrm{TF}} = q_{\mathrm{TF}}^{-1}$. In an insulator, $q_{\mathrm{TF}} = 0$ and the screening length is infinite, while in a perfect metal $q_{\mathrm{TF}} \to \infty$ and the potential is screened over a very short distance below the surface. Replacing eq. (2.19) into eq. (2.18) yields the surface response function in the Thomas-Fermi model:

$$g_m(q) = \frac{\epsilon_m f_{\mathrm{TF}}(q) - \sqrt{\epsilon_\parallel \epsilon_\perp}}{\epsilon_m f_{\mathrm{TF}}(q) + \sqrt{\epsilon_\parallel \epsilon_\perp}}, \quad f_{\mathrm{TF}}(q) = \sqrt{1 + \frac{1}{\epsilon_m}\frac{q_{\mathrm{TF}}^2}{q^2}}. \tag{2.20}$$

In the limit $q_{\mathrm{TF}} \to 0$, we recover the insulator result of eq. (2.16). Conversely, if we let $q_{\mathrm{TF}} \to \infty$, we may obtain the potential in the perfect metal limit. Indeed, if $q_{\mathrm{TF}} \to \infty$, $g_m(q) = 1$. Then, eq. (2.17) becomes

$$\phi_{\mathrm{tot}}(q, 0) = \frac{e}{4\pi\epsilon_0\sqrt{\epsilon_\parallel \epsilon_\perp}}\frac{2\pi}{q}\tanh(aqh/2), \tag{2.21}$$

and the real space potential, according to eq. (2.10), is given by

$$\phi(\rho) = \frac{e}{4\pi\epsilon_0\sqrt{\epsilon_\parallel \epsilon_\perp}}\int_0^{+\infty} \mathrm{d}q\, J_0(q\rho)\tanh(aqh/2). \tag{2.22}$$

The integral may be computed in the following way. First, we introduce the notation

$$\phi(\rho) = \frac{e}{4\pi\epsilon_0\sqrt{\epsilon_\parallel \epsilon_\perp}}\frac{2}{ah}\mathcal{I}(\tilde{\rho}), \tag{2.23}$$

with $\tilde{\rho} \equiv 2\rho/ah$, and

$$\mathcal{I}(\tilde{\rho}) = \int_0^{+\infty} \mathrm{d}q\, J_0(q\tilde{\rho})\tanh(q). \tag{2.24}$$

Then, we make use of the property

$$\mathcal{I}(\tilde{\rho}) = \int_0^{+\infty} \mathrm{d}s\, \mathcal{L}[J_0(q\tilde{\rho})](s)\mathcal{L}^{-1}[\tanh(q)](s), \tag{2.25}$$

where $\mathcal{L}$ is the Laplace transform. For the Bessel function, we have $\mathcal{L}[J_0(q\tilde{\rho})](s) = 1/\sqrt{\tilde{\rho}^2 + s^2}$. The hyperbolic tangent has poles at $iq_n = i(2n+1)\pi/2, n \in \mathbb{Z}$ on the imaginary axis. Hence, its inverse Laplace transform is given by

$$\mathcal{L}^{-1}[\tanh(q)](s) = \frac{1}{2i\pi}\int_{\delta - i\infty}^{\delta + i\infty} \mathrm{d}q\, \tanh(q)e^{qs}, \tag{2.26}$$

with $\delta > 0$. This integral is computed by closing the integration path in the left complex plane, and making use of the Cauchy residue theorem:

$$\mathcal{L}^{-1}[\tanh(q)](s) = \sum_{iq_n} \mathrm{Res}_{q=iq_n}[\tanh(q)e^{qs}], \tag{2.27}$$

Since the residue of the hyperbolic tangent at the poles iq_n is 1, we obtain

$$\mathcal{L}^{-1}[\tanh(q)](s) = \sum_{n=-\infty}^{+\infty} e^{i(2n+1)\pi s/2} = 2\sum_{n=0}^{+\infty}\cos\left(\frac{2n+1}{2}\pi s\right). \tag{2.28}$$

Replacing into eq. (2.24) yields

$$\mathcal{I}(\tilde{\rho}) = 2\sum_{n=0}^{+\infty}\int_0^{+\infty} \mathrm{d}s \frac{\cos((2n+1)\pi s/2)}{\sqrt{\tilde{\rho}^2 + s^2}}. \tag{2.29}$$

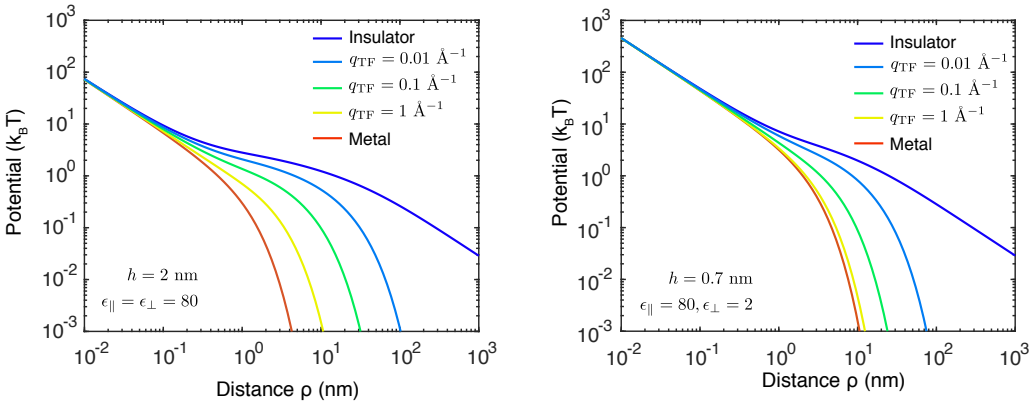

Figure 2.6

Coulomb potential created by an ion of charge e inside a nano-slit, for different models of the confining walls' dielectric response. The left panel corresponds to a slit of height $h = 2$ nm and water with isotropic permittivity, while in the left panel the slit height is 0.7 nm and water has an anisotropic dielectric response. The background dielectric constant is set to $\epsilon_m = 2$ in all instances.

Here, we may recognise the integral representation K_0, the modified Bessel function of the second kind of order 0:

$$\mathcal{I}(\tilde{\rho}) = 2\sum_{n=0}^{+\infty} K_0\left(\frac{2n+1}{2}\pi\tilde{\rho}\right). \tag{2.30}$$

Finally, we obtain for the potential in the perfect metal limit

$$\phi(\rho) = \frac{e}{\pi\epsilon_0\sqrt{\epsilon_\parallel\epsilon_\perp}ah}\sum_{n=0}^{+\infty} K_0\left((2n+1)\pi\frac{\rho}{ah}\right). \tag{2.31}$$

This result differs from the one given without proof by Kondrat and Kornyshev [79], which we find to be incorrect, since it does not reduce to an unperturbed 3D Coulomb potential in the limit $\rho \to 0$, as opposed to ours. Nevertheless, in the limit $\rho \gg h$, we recover the same asymptotic form as in [79]:

$$\phi(\rho) \approx \frac{e}{\pi\epsilon_0\sqrt{\epsilon_\parallel\epsilon_\perp}}\frac{e^{-\pi\rho/ah}}{\sqrt{2ah\rho}}. \tag{2.32}$$

In figure 2.6, we plot the Coulomb potential created by an ion in a slit-like channel for different values of the Thomas-Fermi wavevector q_{TF} of the confining walls. As soon as the wall material has conduction electrons (that is, q_{TF} is non-zero), the potential becomes exponentially screened at long distances, over the typical lengthscale ah/π, as given by eq. (2.32). In the perfect metal case $q_{TF} \to \infty$, the transition between the short distance $1/\rho$ regime and long-distance exponential regime occurs at $\rho \sim h$. However, in a realistic material with finite screening length, the transition occurs at longer distances. Before the transition to the exponentially screened regime the material behaves as an insulator with the background dielectric constant ϵ_m. For example, in the case of graphite with screening length $\lambda_{TF} \sim 1$ nm [83] ($q_{TF} \sim 0.1$ Å), the perfect metal model

significantly underestimates the Coulomb potential (figure 2.6). Overall, we conclude that the electronic properties of the confining wall material strongly impact the confined ionic interactions.

2.6 Consequences of interaction confinement

We have shown that the Coulomb interactions between ions in solution are significantly modified when the solution is confined to a channel of few-nanometre width. These effective *confined interactions* are much stronger than the bulk ones (see figures 2.2 and 2.3), and should therefore result in enhanced correlations between the ions. Taking the example of a nanotube of radius R, one may assess the importance of correlations by introducing a coupling parameter $\Gamma = e\phi((\pi R^2\rho)^{-1})/(k_BT)$, where ρ is the ion concentration inside the channel, so that $(\pi R^2\rho)^{-1}$ is the average distance between ions [12]. Let us take $R = 2$ nm, so that $\mathcal{E}_s \sim 2.5k_BT$ from eq. (2.4). An effective Coulomb potential of magnitude $\sim 5k_BT$ then extends around an ion over a distance $\xi \sim 10$ nm. Therefore, for concentrations above $\rho = 10^{-2}$ M, $\Gamma > 1$ and correlations are expected to become important.

Furthermore, the self-energy barrier that ions face upon entering a few-nanometre wide channel significantly affects the ionic concentration inside the channel As an example, consider a neutral channel in the absence of correlation effects: a barrier $\mathcal{E}_s = 4k_BT$ reduces the ionic concentration by a factor $e^{\mathcal{E}_s/(k_BT)} = 100$. We should also mention here that when entering a channel smaller than its hydrated radius, an ion pays an additional energy penalty due to the shedding of its hydration shell [84, 85]. For chloride, the total hydration energy is as high as 155 k_BT, but the hydrated radius is 0.4 nm, so that only partial dehydration arises and only for the smallest pores. For pores larger than 1 nm, we expect the self-energy to dominate the entrance barrier. We should mention that the discussion so far has been restricted to monovalent ions. Interaction confinement effects are amplified for ions of valence $Z > 1$: the self-energy, for example, scales as Z^2. This will be particularly important in Part II, where we will discuss confinement-induced many-ion effects.

Finally, we have shown that ionic interactions in confinement strongly depend on the electronic nature of the wall material: whether it is a metal, an insulator or something in between. This suggests a more general definition of interaction confinement: it is the regime where fluid transport properties depend on the channel wall material. Granted this definition, the quantum friction phenomenon described in Part III also appears as a consequence of interaction confinement as it involves the coupling of interfacial water dynamics to the electron dynamics in the channel wall.

2.7 The big picture

Interaction confinement means that the presence of a confining wall not only affects a particle's translational degrees of freedom, but also its interactions. Ions in few-nanometre-wide channels experience interaction confinement due to the dielectric contrast between water and the channel wall material. As a result, ionic interactions are enhanced in confinement compared to the bulk, leading to correlation effects that

will be discussed in Part II. These interactions strongly depend on the electronic properties of the channel wall. The effect of confining wall electronic properties on interfacial water dynamics will be discussed in Part III of this thesis.

Part II

Many-ion effects in interaction confinement

Chapter 3

Ionic Coulomb blockade as a fractional Wien effect

Contents

Recent advances in nanofluidics have allowed exploration of ion transport down to molecular scale confinement [15,24,31], yet artificial porins are still far from reaching the advanced functionalities of biological ion machinery, such as high selectivity, ionic pumping, and electrical and mechanical gating [86–88]. Part II of this thesis explores confinement-induced ionic correlations as a route towards such functionalities. In the present Chapter, we focus on the phenomenon of ionic Coulomb blockade – the ionic analogue of electronic Coulomb blockade (CB) – which amounts to single-ion transport that is tuneable by an external gate. Signatures of ionic CB has been observed indirectly in experiments [31,89,90] and simulations [91–94], but a theoretical understanding beyond the electronic analogy [95] is still lacking. Here, we show that interaction confinement in a charged nanochannel results in many-body correlated dynamics, which produce quantised and strongly non-linear ionic transport, in full agreement with molecular simulations. We find that ionic CB occurs when, upon sufficient confinement, oppositely charged ions form 'Bjerrum pairs', and the conduction proceeds through a mechanism reminiscent of Onsager's Wien effect. Our findings open the way to novel nanofluidic functionalities, such as an ionic-CB-based ion pump inspired by its electronic counterpart.

This Chapter is based on the following publication: N. Kavokine, S. Marbach, A. Siria and L. Bocquet, "Ionic Coulomb blockade as a fractional Wien effect". *Nat. Nanotech.* **14**, 573–578 (2019).

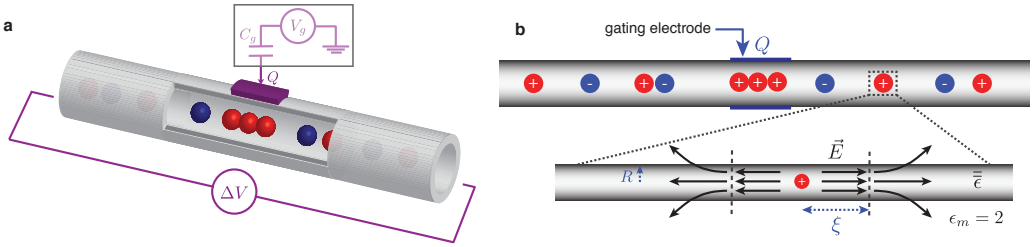

Figure 3.1

a. Sketch of an ionic Coulomb blockade configuration: an electrolyte is confined to a gated nanochannel. The tuneable surface charge Q is equivalent to a voltage applied to the gating electrode which is capacitively coupled to the channel. **b.** Schematic of the corresponding one-dimensional model. Due to confinement, ions interact through 1D-like Coulomb potentials.

3.1 General context

Coulomb blockade is a well-known condensed-matter phenomenon that is typically observed in a single electron transistor: under fixed bias, the current between source and drain peaks at quantised values of the gating voltage [96]. The origins of this effect stem from the many-body Coulomb interactions between the electrons and from the discreteness of the charge carriers [95]. Similar physical ingredients are at play in a nanoscale channel filled with a salt solution (figure 3.1): ions also interact via Coulomb forces, and a variable surface charge on the channel walls can play the role of the gating voltage. While ionic interactions in solutions are typically weaker than the thermal energy, they become much stronger in nanoscale channels due to interaction confinement, as discussed in Chapter 2. One may therefore expect to observe an "ionic Coulomb blockade", namely peaks in the ionic conductance of a nanochannel at quantised values of its surface charge. It is thus of interest that molecular dynamics simulations [91–94] and experiments [89, 90, 97] have shown what might be indirect signatures of ionic CB (though in the absence of a gating voltage), and conductance gating by a surface charge has been demonstrated in simulations of a biological ion channel model [98]. These observations remain surprising since ionic systems in water at room temperature have specific features contrasting with electronic systems which may preclude the occurrence of ionic CB. Beyond the absence of quantum effects, the fact that ions are of both signs – while electrons are only negative – results in Debye screening, which is expected to drastically weaken the many body interaction; it remains unclear under which conditions these aspects may suppress ionic transport quantisation.

Although pioneering analytical efforts have translated the results established for electrons [95] to the ionic case [98–100], a general theory for ionic CB, incorporating the unique features of ionic systems in contrast to their electronic counterparts, is still lacking. Developing such a theory is challenging, since it clearly requires to go beyond the mean-field PNP framework. The existing methods for doing so are largely restricted to equilibrium systems. There have been proposals of a field theory framework that formally takes all correlations into account in arbitrary geometry [101, 102], and that can deal with dielectric discontinuities, but applications have been restricted to a Debye-Hückel-type approximation for the electrolyte free energy [103]. Bazant, Storey and

Kornyshev [104,105] have proposed to introduce a term proportional to the Laplacian of the potential squared in the electrolyte free energy. The approach has been successful in understanding overscreening and crowding phenomena, but remains phenomenological. A method for dealing with strong correlations has been proposed by Levin [106], who incorporated ion pairs as a separate chemical species, but this approach runs into difficulties at high ionic concentrations where an ion pair becomes ill-defined. Finally, in the specific case of a one-dimensional nanotube geometry, an interacting electrolyte may be mapped onto an exactly solvable model [80, 107–109]. Recently, a general analogy between the statistical mechanics of 1D electrolytes and non-Hermitian quantum mechanics has been proposed [110].

In this Chapter, we build on the exactly solvable model approach to describe an electrolyte inside a gated nanochannel. We then extend the theory to the out-of-equilibrium regime, where it successfully accounts for the ionic CB phenomenon.

3.2 Model definition and numerical results

Our theory is based on a simple but general model of a nanochannel which confines ions in one dimension (figure 3.1a). The channel has radius R and length $L \gg R$, as opposed to nanopores of length $L \sim R$. It is filled with water, which under confinement exhibits *a priori* an anisotropic dielectric permittivity $\bar{\bar{\epsilon}}$ [73,76], and it is embedded in a membrane with low permittivity ϵ_m (whenever needed, we use $\epsilon_m = 2$). Under such conditions (see figure 3.1b), the electric field lines produced by an ion stay confined inside the channel over a characteristic length ξ, as discussed in Chapter 2. This leads to a stronger Coulomb interaction than in the bulk solution, which is well described by the exponential potential

$$V(x) = k_B T \frac{\xi}{x_T} e^{-|x|/\xi}. \tag{3.1}$$

This introduces a thermal length x_T [109], which is the typical distance between two opposite charges confined in the channel. We detail in Appendix A.1 how the parameters ξ and x_T are related to the channel geometry and to the various dielectric constants. If the permittivity of confined water is assumed to be the same as in the bulk, one has $\xi \approx 7R$ and $x_T = R^2/2\ell_B$, where $\ell_B = 0.7$ nm is the Bjerrum length in bulk water. We shall use these relations in the following, keeping in mind that taking into account the anisotropic permittivity would result in a stronger interaction for a given confinement.

A charge is imposed on the confining surface and acts as a gate on the system; here we reduce the surface charge to a point-like charge Q. The ions interact between themselves and with the surface charge through the potential given in eq. (C.34); depending on conditions, an electric field E may be applied along the channel.

Before developing an analytical theory, we confirm using (grand canonical) brownian dynamics simulations [111] that our simplified model displays the ionic CB phenomenology. Details of the simulations are given in Appendix F.1.1: the measured quantities are the ionic current and the neutralising charge $N(Q)$, defined as the total positive charge that screens the negative charge Q. Figures 3.2a and 3.2b show typical simulation results. Remarkably, we do observe signatures of ionic CB: namely, the neutralising charge $N(Q)$ is "quantised", as it increases in discrete steps as a function of Q – this can be considered an equilibrium signature of ionic CB –, and under an external electric field, the current peaks at discrete values of Q. We thus recover the same phenomenology as

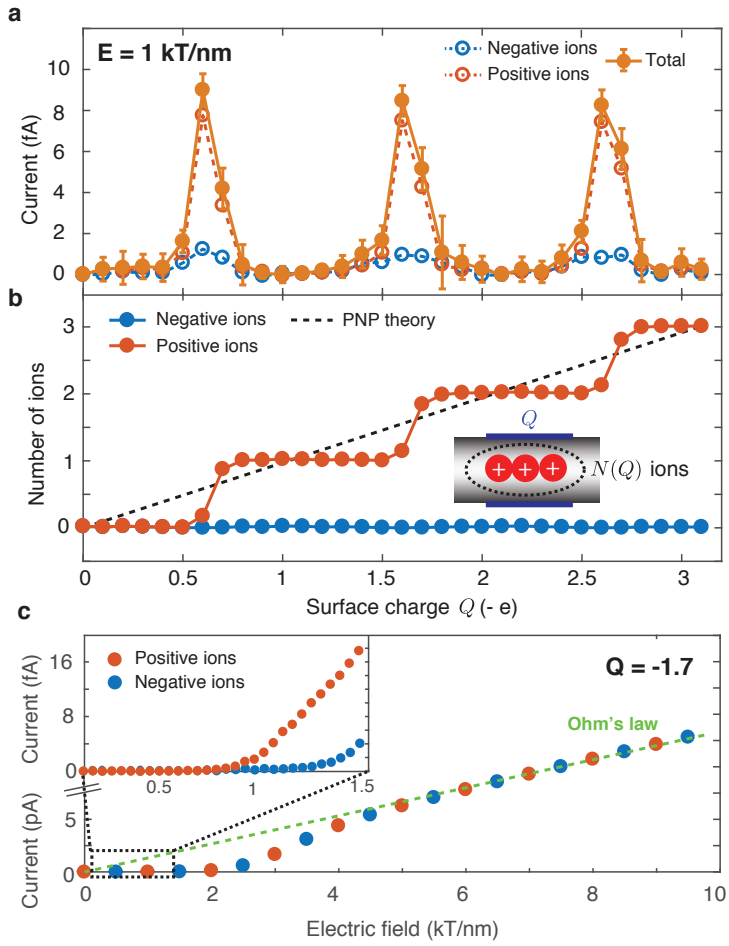

Figure 3.2

Brownian dynamics simulations of ionic CB. **a.** The ionic current through the channel, at fixed applied electric field ($E = 1\ k_BT/e/\text{nm}$), show peaks at discrete values of the surface charge. **b.** The neutralising charge $N(Q)$ – the total positive charge that screens the negative surface charge – increases in steps as a function of Q. The dashed line shows the mean-field prediction obtained from the equilibrium solution of the PNP equations, which is in complete disagreement with the simulations. **c.** Ionic current as a function of the applied electric field at fixed surface charge ($Q = -1.7$). A strongly non-linear behaviour is observed. The parameters are $x_T = 0.09$ nm, $\xi = 3.5$ nm, and salt concentration $\rho_0 = 0.44$ M. Error bars represent the standard deviation of the mean.

in simulations of nanopores [98], although in our general setting we do not assume electrostatic coupling between the channel entrances and the surface charge. Furthermore, our simulations reveal a very non-linear current-voltage characteristic (figure 3.2c), with the conductance at low voltages being suppressed with respect to the one expected from Ohm's law. Interestingly, the $I-V$ characteristic for our ionic CB system differs from its electronic counterpart, where several steps in current versus applied voltage are observed before reaching Ohm's law [96].

3.3 Fractional Wien effect theory

We now develop an analytical theory in order to understand this counterintuitive behaviour. The vision of Coulomb blockade in terms of energy barriers which has been developed for electrons in quantum dots [95], and adapted to ions in nanopores [98] cannot apply here as we consider a 1D nanochannel of arbitrary length. Moreover, the phenomenon at stake is clearly out of reach for the mean-field PNP equations discussed in Chapter 1. The PNP result for the neutralising charge is derived in Appendix C.1 and is shown in figure 3.2b: a perfectly linear behaviour for $N(Q)$ versus the surface charge Q is obtained, in contrast to the simulation results. Thus, the theoretical description of ionic CB requires to exactly solve the underlying many-body problem.

3.3.1 Equilibrium properties

To this end, we first compute the grand-canonical partition function of the confined electrolyte in the presence of the gating charge Q and interacting with the pairwise potential of eq. (C.34); the chemical potential is μ and the temperature T (we set $k_BT = 1$). The system under consideration closely resembles a 1D Coulomb gas model, which can be solved using a functional integral technique as in [107,112,113], which we extend to incorporate an arbitrary gating charge density $q(x)$. An exhaustive calculation reported in Appendix C.1 yields the partition function as

$$\Xi = \int \mathrm{d}\phi_0 \mathrm{d}\phi_L e^{-x_T(\phi_0^2+\phi_L^2)/4\xi} \mathcal{P}(\phi_L, L|\phi_0), \tag{3.2}$$

where the propagator $\mathcal{P}(\phi, x|\phi_0)$ solves

$$\frac{\partial \mathcal{P}}{\partial x} = \frac{1}{x_T}\frac{\partial^2 \mathcal{P}}{\partial \phi^2} + \left(iq\phi - \frac{x_T}{4\xi^2}\phi^2 + \frac{2z}{L}\cos\phi \right) \mathcal{P} \tag{3.3}$$

with initial condition $\mathcal{P}(\phi, 0|\phi_0) = \delta(\phi - \phi_0)$, and $z = e^{\beta\mu}$ the fugacity.

This result allows us to unveil the unconventional behaviour of the ionic system. As a first indication, the equation of state of the confined ionic gas can be exactly derived in the limit $z_T \equiv z\, x_T/L \ll 1$, corresponding to strong electrostatic interactions (with our simulation settings, $z_T = 0.02$), yielding

$$P = \frac{1}{2}\rho k_B T \times \left(1 + O(z_T^2)\right), \tag{3.4}$$

where P is the pressure and ρ is the salt density (see Appendix C.1). Thus, when the interactions are strong enough, the ionic gas of density ρ behaves as an ideal gas of

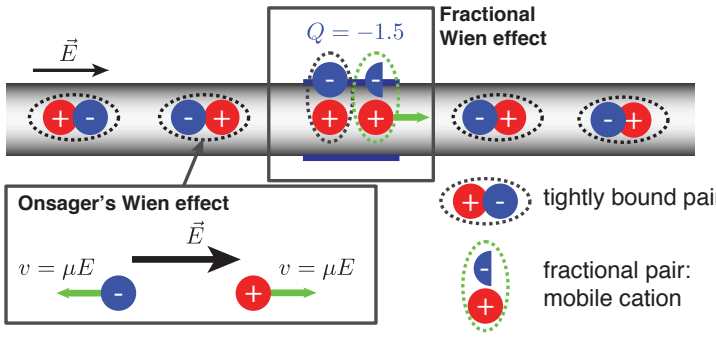

Figure 3.3

Schematic representation of Onsager's Wien effect and of the fractional Wien effect. Both correspond to non-linearities in the current-voltage characteristic due to the electric field dependence of the dissociation rate of ion pairs.

density $\rho/2$. Hence, in the channel, ions of opposite charge are actually bound together in the form of Bjerrum pairs, as confirmed by direct observation in the simulations[1]. The confined salt behaves accordingly as a weak electrolyte. We will now demonstrate that this crucial characteristic, missed by mean-field theory, is the key to explaining both the conductance gating and the strongly non-linear response under an electric field, as highlighted in figure 3.2.

3.3.2 The Wien effect

Let us first sketch a qualitative picture. In a weak electrolyte, the conduction should proceed through the second Wien effect, which was famously explained by Onsager [114, 115]. In Onsager's picture, tightly bound ion pairs cannot move under the effect of an electric field, and current can only flow when an ion pair dissociates (figure. 3.3). This picture applies to our system, except for the presence of the gating charge Q, which acts as a "defect" and affects the dissociation process of ion pairs. If Q is an integer, all the ions are tightly bound at low enough E and the conductance is vanishing. Now if Q has a fractional part, it still binds an integer number of ions, so that one of those ions may be less strongly bound than the others (for example if a charge $Q = -1.5$ binds two positive ions). This weakly bound ion may then dissociate from the surface charge under the effect of the external electric field, resulting in non-zero conductance. This qualitative picture is confirmed by direct observation in the simulations. Interestingly, once a pair dissociates, conduction occurs via a Grotthus-like mechanism, with the free ion exchanging between Bjerrum pairs. Altogether, the conduction is due to ions dissociating not from their opposite charge counterparts, but from the fractional surface charge: we thus name this new mechanism "fractional Wien effect".

In addition to the surface charge gating, the fractional Wien effect picture allows us to understand the non-linear current voltage characteristics. Indeed, at low electric fields, the conduction is due to the dissociation of fractional ion-surface charge pairs, whose dissociation rate depends on the electric field, thus the conductance acquires an

[1] Movie available at https://www.nature.com/articles/s41565-019-0425-y

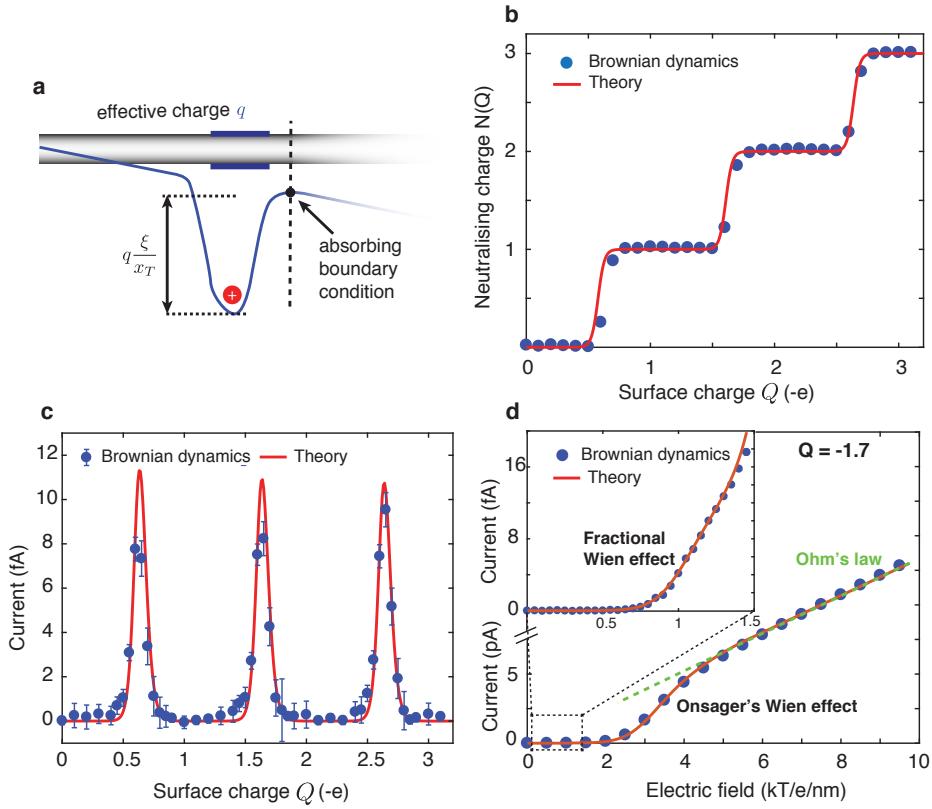

Figure 3.4

Analytical theory for the Wien effect mechanism of ionic CB. **a.** Schematic setting for the study of out-of-equilibrium Bjerrum pair dynamics. The main ingredient is the computation of the mean escape time of an ion from the potential created by an effective charge q. **b.** Neutralising charge $N(Q)$ as a function of surface charge. **c.** Positive ion current, at fixed applied electric field ($E = 1\ k_BT/e/\text{nm}$), as a function of surface charge. **d.** Current-voltage characteristic at fixed surface charge, corresponding to a conductance peak ($Q = -1.7$). Inset: zoom on the small applied electric field region. In panels b, c and d, dots are simulations results, while the solid line is the theoretical prediction from eq. (3.8) and eq. (3.5). The Wien effect theory shows quantitative agreement with simulations. Error bars represent the standard deviation of the mean.

electric field dependence. But, at sufficiently high electric fields, the Bjerrum pairs that are present in the bulk of the channel will also start dissociating, resulting in the standard ("bulk") Wien effect that was studied by Onsager. This results in another non-linearity in the $I-V$ curve, before a collapse onto Ohm's law once all the pairs have been dissociated.

3.3.3 Out-of-equilibrium theory

We now develop an out-of-equilibrium framework to quantify the fractional Wien picture that has emerged. As a first step, the exact solution (3.2) for the partition function Ξ

allows to compute the probability of the system containing a fractional ion-surface charge pair, or equivalently the average neutralising charge $N(Q)$. In the limit of an infinite channel and a point-like surface charge, we obtain $N(Q) = -(x_T/\xi)(\partial \log \Xi/\partial Q) - Q$ and a lengthy calculation reported in Appendix C.1 yields an analytical expression, which can be written in the form:

$$N(Q) = \frac{\sum_{ij} a_i a_j (j-i) e^{-\frac{\xi}{2x_T}(Q-(i-j))^2}}{\sum_{ij} a_i a_j e^{-\frac{\xi}{2x_T}(Q-(i-j))^2}} - Q. \tag{3.5}$$

The coefficients a_i are obtained as series expansions in $z_T \equiv z\, x_T/L$ (a few terms are sufficient in the limit of interest $z_T \ll 1$). The prediction in eq. (3.5) is plotted in figure 3.4b: it accounts for a quantised neutralising charge, and the agreement with simulations is excellent. Assuming strong enough interactions, one may adopt a "two-state" perspective: the surface charge Q may bind either $\lfloor Q \rfloor$ or $\lfloor Q \rfloor + 1$ counterions ($\lfloor . \rfloor$ denoting the floor function); in the latter case, a fractional ion-surface charge pair is formed. The probability of the system containing this weakly bound pair is accordingly $p(Q) = N(Q) - \lfloor Q \rfloor$.

In a second step, we study the out-of-equilibrium dynamics of a Bjerrum pair. We consider a single ion bound to an effective charge q (see figure 3.4a). Its probability distribution $P(x,t)$ is governed by the Fokker-Planck equation

$$\partial_t P = D\partial_x \left(P \partial_x \left[-qV(x) - Ex \right] \right) + D\partial_x^2 P, \tag{3.6}$$

with D the diffusion coefficient, E the applied electric field and $V(x)$ the pairwise interaction potential in eq. (C.34). Solving eq. (3.6) with an absorbing boundary condition (see figure 3.4b) yields the mean escape time for the bound ion (see Appendix C.2 and Ref. [116]):

$$\tau(q,E) = \frac{1}{D} \int_{-\infty}^{+\infty} \int_{\max(0,x)}^{\xi \log \frac{q}{E x_T}} e^{q(V(x)-V(y))+E(x-y)} \mathrm{d}y \mathrm{d}x. \tag{3.7}$$

For a bulk ion pair the effective charge q is 1, and the average lifetime of the pair is actually $\tau(1,E)/2$ since both ions are mobile; for a fractional ion-surface charge pair, $q = Q - \lfloor Q \rfloor$. In Appendix C.2, we derive the relation between the lifetime of the ion pairs and the number of free charge carriers. Combining this result with the probability $p(Q)$ of finding a weakly bound pair in the system yields an expression for the positive ion current $I^+(E)$ accounting for both the fractional and the bulk Wien effect:

$$I^+(E) = (N(Q) - \lfloor Q \rfloor) I_{Q-\lfloor Q \rfloor}(E) + I^+_{\mathrm{bulk}}(E), \tag{3.8}$$

with $I_q(E) = (L/(DE) + \tau(q,E))^{-1}$ and

$$I^+_{\mathrm{bulk}}(E) = \frac{1}{2\tau(1,E)} \left(\sqrt{1 + 2\rho D E \tau(1,E)} - 1 \right). \tag{3.9}$$

These analytical predictions for the current (eq. (3.8)), are plotted in figure 3.4d-e: they reproduce quantitatively the simulations results. Our result accounts both for the CB oscillations – enhanced conductance at quantised values of surface charge – and for the "blockade" of ionic transport in the form of the strongly nonlinear current voltage relation at low applied field. The theory fully validates the fractional Wien mechanism, highlighting that this effect originates in an interplay between many-body dynamics of ion pairs and Coulomb gas statistics.

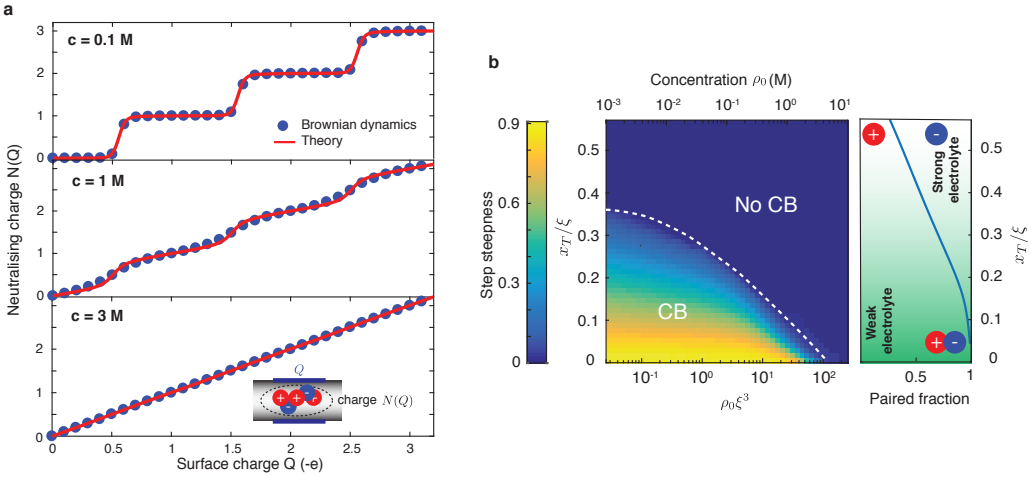

Figure 3.5

Conditions for observation of ionic Coulomb blockade. **a.** Neutralising charge $N(Q)$ as a function of the surface charge Q, as obtained from brownian dynamics simulations (dots), and the full theoretical prediction from eq. (3.5) (solid line), at different salt concentration values. CB steps disappear as the salt concentration is increased. The parameters are chosen here as $x_T = 0.18$ nm and $\xi = 7$ nm. **b.** "Phase diagram" for Coulomb blockade. The colour scale shows, as an assessment of the "strength" of ionic CB, the steepness of the steps in the neutralising charge $N(Q)$. It is defined as $1 - 1/\text{maximum slope of a step}$ and varies between 0 (no CB) to 1 (full CB). The axes correspond to the channel radius (in terms of the dimensionless quantity $x_T/\xi = R^2/2\ell_B\xi$) and to the dimensionless bulk salt concentration $\rho_0\xi^3$. On the right panel, the fraction of ion pairs in the channel is plotted as a function of x_T/ξ, at bulk concentration 0.1 M. Ion pairing is a prerequisite for ionic Coulomb blockade, *i.e.* CB occurs when the salt behaves as a weak electrolyte.

3.4 Phase diagram

Having now established a theoretical framework for ionic CB that is quantitatively validated against molecular simulations, we may use it to obtain insight into the conditions under which one may expect ionic CB. Figure 3.5a shows the prediction for the neutralising charge $N(Q)$ at increasing salt concentration values: strikingly, the CB steps disappear at high salt concentration as a result of Debye screening, again in full agreement with simulations. This is a crucial specificity of our ionic system with respect to its electronic counterpart. Going further, we build a phase diagram which displays the parameter space where ionic CB occurs (that is where $N(Q)$ versus Q displays steps), in terms of dimensionless ion density and channel size, see figure 3.5b. Ionic CB indeed disappears above a critical salt concentration for a given channel size (or x_T); Debye screening thus does prevent Coulomb blockade, though only at rather high salt concentration values (typically, more than 2 M for a 1 nm channel). Conversely, at a given salt concentration, a small enough x_T (strong enough interactions) is required for ionic CB to occur. In the limit $z_T \ll 1$, the slope of a step is given by $(\mathrm{d}N/\mathrm{d}Q)_{\max} = \xi/(4x_T) + O(z_T^4)$ (Appendix C.1). Therefore a necessary condition for observing steps is $\xi/x_T \gtrsim 4$, *i.e.* the Coulomb interaction between two ions should be greater than $\sim 4\ k_BT$. Concretely, this

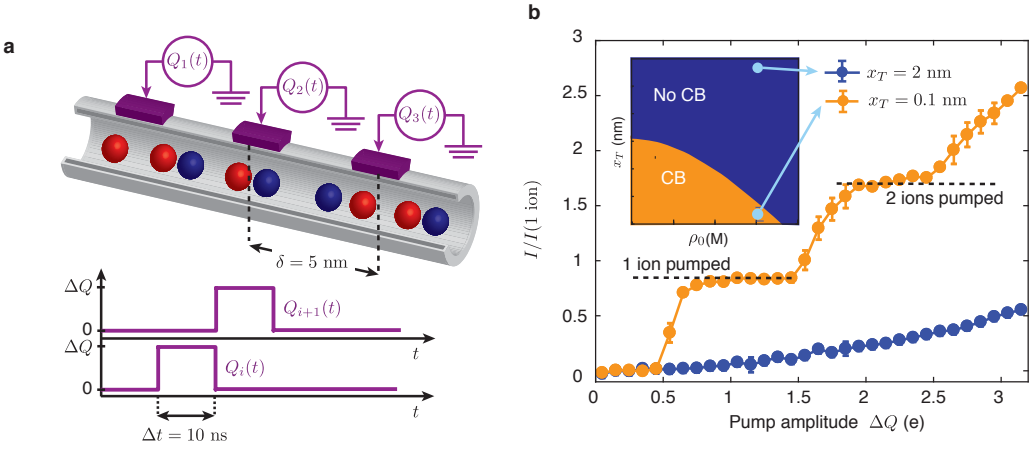

Figure 3.6

Coulomb-blockade-based ion pump. **a.** Schematic of the ion pump inspired by its electronic counterpart; time dependence of the variable surface charges $Q_i(t)$. The 125 variable charges are placed every 5 nm, and periodic boundary conditions are used. **b.** Positive ion current resulting from the pump operation (with no applied electric field), at $x_T = 0.1$ nm (CB regime), and $x_T = 2$ nm (no CB), as obtained from brownian dynamics, as a function of the pump amplitude ΔQ. The current is normalised by $I(1 \text{ ion})$, which is the current resulting from one ion moving at a velocity 5 nm/10 ns. Error bars represent the standard deviation of the mean.

corresponds to nanochannel sizes $R \lesssim 3.5\ell_B \sim 2.5$ nm for monovalent ions. For multivalent ions with valency p, the Bjerrum length increases as p^2 and this modifies accordingly the condition on the channel size. Thus, our theory demonstrates that ionic CB can actually be expected in channels that are much larger than previously considered biological nanopores [98] of radius $R \sim 0.3$ nm. Finally, the right panel of figure 3.5b shows the fraction of Bjerrum pairs as predicted by our theory (Appendix C.1): it decreases with increasing x_T, in line with the disappearance of CB steps, highlighting once more that ionic CB and Bjerrum pairing are intimately related.

3.5 Ion pump

Our modelling of Coulomb blockade opens the way to the design of new functionalities in nanofluidic systems. Beyond gated transport itself, one may also harness the control over single ions allowed by CB to develop ion pumping functionalities. Single electron pumps have been obtained by associating two CB devices in series, with their gate voltages oscillating out of phase [117]. Figure 3.6a shows an analogous ionic system, a nanochannel with variable surface charges placed along its length. We confirm using brownian dynamics simulations that such a device is capable of pumping activity. Upon appropriate modulation of the surface charges, and in the absence of applied electric field, there is indeed transport of ions along the channel; the modulation amplitude ΔQ allows one to precisely control the discrete number of ions being transported (figure 3.6b). But most importantly, the simulations highlight that the pumping fully relies on the system operating in the CB regime. Indeed, the pumping current is almost 0 at large x_T (weak

interactions, no CB), while it is significant only at small x_T (strong interactions, CB regime; see inset of figure 3.6b). This proof-of-concept confirms the importance of ionic CB as a building block for artificial devices mimicking biological functions; we leave for future work the thorough investigation of such devices.

3.6 The big picture

In this Chapter, we have presented a first consequence of interaction confinement on the ion transport in one-dimensional nanoscale channels. We predict that, if gated by a variable surface charge, a few-nanometer-wide nanotube can exhibit ionic Coulomb blockade : conduction is allowed only at discrete values of the surface charge. This quantum-like behaviour is found to have in fact a completely physico-chemical origin, in the confinement-induced ionic correlations. These lead to the formation Bjerrum pairs, and non-linear conduction proceeding through Onsager's Wien effect. We have developed an analytical theory for one-dimensional electrolytes that quantitatively accounts for ionic Coulomb blockade, which is based on the exact solution of a Coulomb-gas-type model and an escape rate approach for the dynamics of ion pairs. Ionic Coulomb blockade is a promising tool for manipulating electrolytes at the single-ion level. The theoretical methods we propose are also more general, and can be extended to a range of confined ionic systems, one of which is discussed in the next Chapter.

Chapter 4

Hodgkin-Huxley iontronics
with two-dimensional nanofluidic memristors

Contents

New energy-efficient architectures inspired by the brain are growing as an alternative to traditional von Neumann computing [118]. While existing hardware implementations use electrons as charge carriers, advances in nanofluidics have opened the possibilities for ion-based computation [11], inspired by biological neurons. In this Chapter, we show that interaction-confinement-induced correlations lead to neuromorphic behaviour in 2D electrolyes, such as those that were recently demonstrated in subnanometric slits [15–17]. Using analytical theory, backed up by molecular dynamics simulations, we demonstrate that under an electric field, ions in a nanoscale slit assemble into micelle-like clusters, whose long-timescale dynamics result in a history-dependent conductivity. We carry out molecular simulations of two such devices, reproducing the Hodgkin-Huxley neuron model [119] with experimentally-accessible biomimetic nanofluidic circuitry. The resulting system highlights spontaneous emission of voltage spikes trains, characteristic of neuromorphic activity.

This Chapter is based on the following publication: "Modelling of emergent memory and voltage spiking in ionic transport through angström-scale slits". P. Robin, N. Kavokine and L. Bocquet, *Science* (2021).[1]

[1] The molecular simulations and analytical developments presented in this Chapter have been carried out by Paul Robin, to whom I am deeply grateful for the collaboration on this project.

4.1 General context

The brain activity relies on the transport of ion species to carry out complex computations [120, 121]. As ions come with various size, shape, valence and chemical properties, they are intrinsically more versatile than electrons. This offers manifold possibilities for computational architectures beyond von Neumann's. Notably, ionic systems are best suited to implement parallel computing methods – which are crucial for energy saving [122] – since they can encode information through the fluxes of many different chemical species. Yet, biomimetic ion-based computing has not been achieved so far. This points to the need of inventing and designing artificial iontronic devices with advanced functionalities [8], incorporating experimentally-accessible molecular channels as ion conduits.

On the experimental side, considerable progress in the design of novel nanofluidic devices has been achieved over the past decade (see Chapter 1), and a milestone has been reached very recently, as confinement of an electrolyte down to a single molecular layer was demonstrated and investigated experimentally [15–17, 68]. Extremely confined systems are promising from a functional point of view, as they are most sensitive to the discrete nature of ions, and are prone to exhibit exotic transport properties that could be harnessed as building blocks of iontronic circuitry [46, 68, 123]. An example was given in Chapter 3, where a gated one-dimensional channel was shown to exhibit ionic Coulomb blockade.

In the present Chapter, we show that two-dimensional (2D) ion channels, such as the angstrometric slits introduced in Refs. [15,16,68], behave as memristors (or memory resistors) [124, 125], in that they exhibit a history-dependent conductivity. We further prove that elementary circuitry incorporating two such channels allows reproducing ion-driven voltage spiking characteristic of neuron activity [119]. This unconventional behaviour takes its root in the interaction-confinement-induced correlations in the monolayer electrolye, which cause the ions to self-associates into dense, linear clusters upon application of an electric field. The slow dynamics of these large-scale structures are at the source of the memory effect. In order to unveil these properties, we combine molecular dynamics simulations of two-dimensional electrolytes (with both explicit and implicit solvent and confining material, see figure 4.1 a and b), as well as analytical modelling beyond the traditional Poisson-Nernst-Planck (PNP) equations. Our theory ultimately leads to the design of elementary nanofluidic devices whose architecture and stimulated response mimic those of biological neurons and that could be capable of carrying out prototypic computations.

4.2 Monolayer electrolyte at equilibrium

4.2.1 Bjerrum pairing

We consider a monolayer of ions, molecularly confined in a subnanometric slit, see figure 4.1. As discussed in Chapter 2, in such strong planar confinement, ions experience not only a reduction in translational freedom, but also stronger electrostatic interactions whose nature is intermediate between that of 3D and 2D systems, which we term '$2D^+$' interactions.

We first investigate the equilibrium properties of such 2D electrolytes. Using all-atom MD simulations, we consider aqueous solutions of various salts, such as NaCl, $CaCl_2$ and

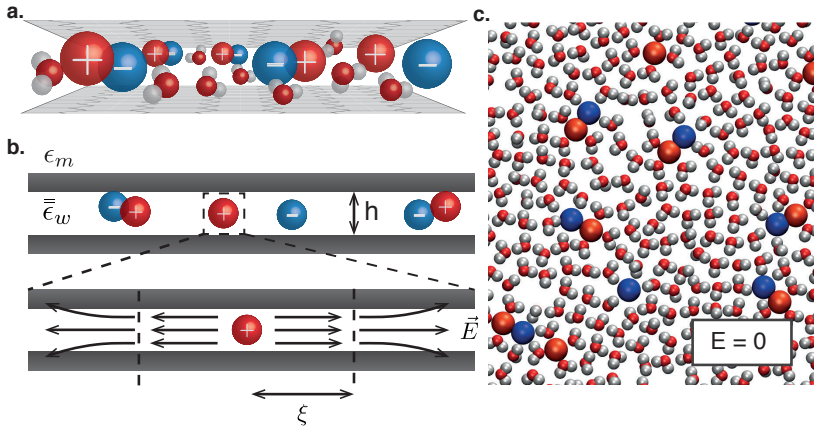

Figure 4.1

Modelling and simulation of a 2D electrolyte. **a.** Sketch of a 2D electrolyte. **b.** Sketch of the quasi-2D Coulomb gas model, with $2D^+$ Coulomb interactions given by (4.1). The electric field is confined in the channel over a length ξ due to dielectric contrast between water and the channel wall. **c.** Typical configuration of a monolayer electrolyte as observed in all-atom MD simulations. Sodium (in red) and chloride ions (in blue) form tightly bound Bjerrum pairs at room temperature in slits of height $h = 0.7\,\text{nm}$.

$CaSO_4$, confined in a narrow slit of tunable spacing $h = 0.7$, 1.0 or 1.4 nm (amounting to one, two and three water layers, respectively) made of two sheets of graphene or hexagonal boron nitride (hBN). Details of the simulations are provided in Appendix F.2. While these salts are known to be completely dissociated in bulk solutions, we find that in monolayer confinement, they form tightly bound Bjerrum pairs (see figure 4.1c) – and even triplets in the case of $CaCl_2$. Even in two- or three-layer confinement, all salts except NaCl still associate into pairs. Such pairing is consistent with the $2D^+$ confined interactions discussed in Chapter 2. The interaction energy between tow ions i and j may be expressed as

$$\beta V_{ij}(r) = -\frac{q_i q_j}{T^*} \log \frac{r}{r+\xi}, \tag{4.1}$$

where β is inverse temperature, $q_{i,j} = \pm 1$ the charge sign and $1/T^*$ a dimensionless coupling constant. The expressions of T^* and of the field escape length ξ are derived in Chpater 2, notably in the experimentally relevant case where the dielectric permittivity of confined water is anisotropic [73, 76]. In the case of a divalent salt in a slit of height $h = 0.7\,\text{nm}$ at room temperature, we find typically $T^* = 0.11$ and $\xi = 14\,\text{nm}$. The corresponding Bjerrum length ℓ_B, defined by $\beta V(\ell_\text{B}) = 1$, is 130 nm, which is much larger than the Bjerrum length in bulk water ($\ell_\text{B} = 0.7$ nm). Therefore, the interaction potential in eq. (4.1) is much stronger than its bulk counterpart $V_\text{bulk}(r) = e^2/4\pi\epsilon_0\epsilon_w r$; this qualitatively explains the confinement-induced ion pairing. The coupling constant $1/T^*$ is also proportional to Z^2/h, with Z the valence of ions, explaining why monovalent ions only forms pairs in the thinnest slits.

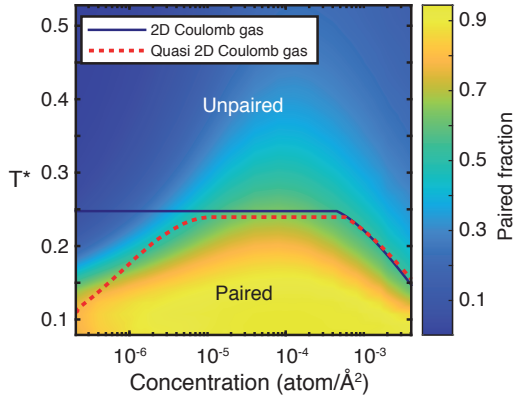

Figure 4.2

Phase diagram of a 2D electrolyte, obtained from brownian dynamics simulations. At reduced temperature $T^* = 0.25$, the system undergoes a pairing phase transition, analogous to the Kosterlitz-Thouless transition. The solid and dashed lines correspond to the mean-field prediction for the transition temperature, for an exactly 2D ($\xi = \infty$) and 2D$^+$ (finite ξ) Coulomb gas, respectively.

4.2.2 Kosterlitz-Thouless transition

In order to identify the range of effective temperatures and ionic concentrations in which Bjerrum pairing occurs (figure 4.2), we performed implicit solvent brownian dynamics (BD) simulations of a symmetric electrolyte interacting with the derived potential in eq. (4.1). At short distance ($r \ll \xi$), our interaction potential is logarithmic, and resembles a 2D Coulomb potential. The pairing transition in our monolayer electrolyte is therefore almost described by a 2D Coulomb gas model [106, 126], and is analogous to the Kosterlitz-Thouless (KT) topological phase transition [127]. However, the analogy is not perfect since the interaction potential recovers a bulk $1/r$ behavior at large distances $r \gg \xi$.

To account for these observations, we use a mean-field approach inspired by the Fuoss theory of bulk electrolytes [128], in which ion pairs are incorporated as a separate species. We are able to determine analytically the pairing transition temperature, both in the ideal 2D and our 2D$^+$ setting (figure 4.2), as detailed in Appendix D.2. Our analytical computation reproduces quantitatively the BD simulations, and the ideal 2D description turns out to be valid for all but the lowest salt concentrations. The ion pairing quasi-KT phase transition appears as a specific feature of the monolayer electrolyte. In 1D confinement there can be no phase transition [123], and in three dimensions, the ion-ion interactions are usually not strong enough for pairing to occur at room temperature [106]. Here on the contrary, our model predicts a transition temperature $T = 350\,\mathrm{K}$ for divalent salts like $CaSO_4$ in slits with $h = 1.4\,\mathrm{nm}$, or for $CaCl_2$ with $h = 0.7\,\mathrm{nm}$.

4.3 Non-linear dynamics

4.3.1 Polyelectrolytic Wien effect

Such strong ionic correlations at equilibrium are at the source of highly non-linear ion transport, as illustrated by the current-voltage characteristics obtained from MD simulations (figure 4.3). This non-linearity reveals that conduction proceeds in fact through the breaking of ion pairs. Consistently, a non-linear response is observed for $CaSO_4$, which is paired at equilibrium, unlike NaCl which does not form pairs in the considered conditions (figure 4.3).

This type of ion transport is known as the second Wien effect, which we have already encountered in the study of ionic Coulomb blockade. In contrast to the 1D case where the Wien effect was successfully described within an escape rate formalism, the present $2D^+$ geometry is best suited for an approach based on Onsager's original theory [114]. We consider a chemical equilibrium between pairs and "free" ions of the form $NaCl \leftrightarrows Na^+ + Cl^-$ (see figure 4.3). Assuming pairs dissociate with a timescale τ_d and free ions assemble into pairs with a timescale τ_a, we obtain an evolution equation for the fraction n_f of free ions not engaged in a pair:

$$\dot{n}_f = \frac{1 - n_f}{\tau_d} - \frac{n_f^2}{\tau_a}. \tag{4.2}$$

While computing the dependence of τ_d on the parameters is usually a mathematical challenge, we were able to reduce it to self-similar problem in the particular case of $2D^+$ confined electrolytes, as detailed in Appendix D.3, yielding:

$$\tau_a = \frac{T^*}{4\pi D\rho}, \tag{4.3}$$

$$\tau_d = \frac{r_0^2}{2D}\left(\frac{l_E}{r_0}\right)^{1/T^*}, \tag{4.4}$$

where the lengthscale $l_E = k_BT/ZeE$ describes the strength of the external field with respect to thermal fluctuations, D is the diffusion coefficient and r_0 is the ion radius. Because this model considers no interactions between ion pairs, we refer to it as the isolated pair (IP) model. When the steady state is reached, equation (4.2) can be solved and the ionic current reads:

$$I = N\frac{2ZeD}{k_BTL}E\frac{\tau_a}{2\tau_d}\left(\sqrt{1+\frac{2\tau_d}{\tau_a}} - 1\right) \underset{E\to 0}{\propto} E^{a_{IP}(T^*)}, \tag{4.5}$$

with L the channel length and $a_{IP}(T^*) = 1+1/2T^*$ the I-V curve exponent at low applied voltage. Surprisingly, this prediction fails to reproduce simulation results, even at very low concentrations, see figure 4.3b (solid yellow line).

The all-atom MD simulations provide some hints to understand this discrepancy. As shown in figure 4.3c, under an external electric field, ion pairs do not actually break but instead rearrange into gigantic clusters with chemistry-specific size and topology (see figure F.4 and Appendix F.2). These clusters, which we term "Bjerrum polyelectrolytes", lead to a radically new phenomenology. The formation of macrostructures indicates that ion pairs cannot be treated independently, and therefore the Wien effect dynamics are

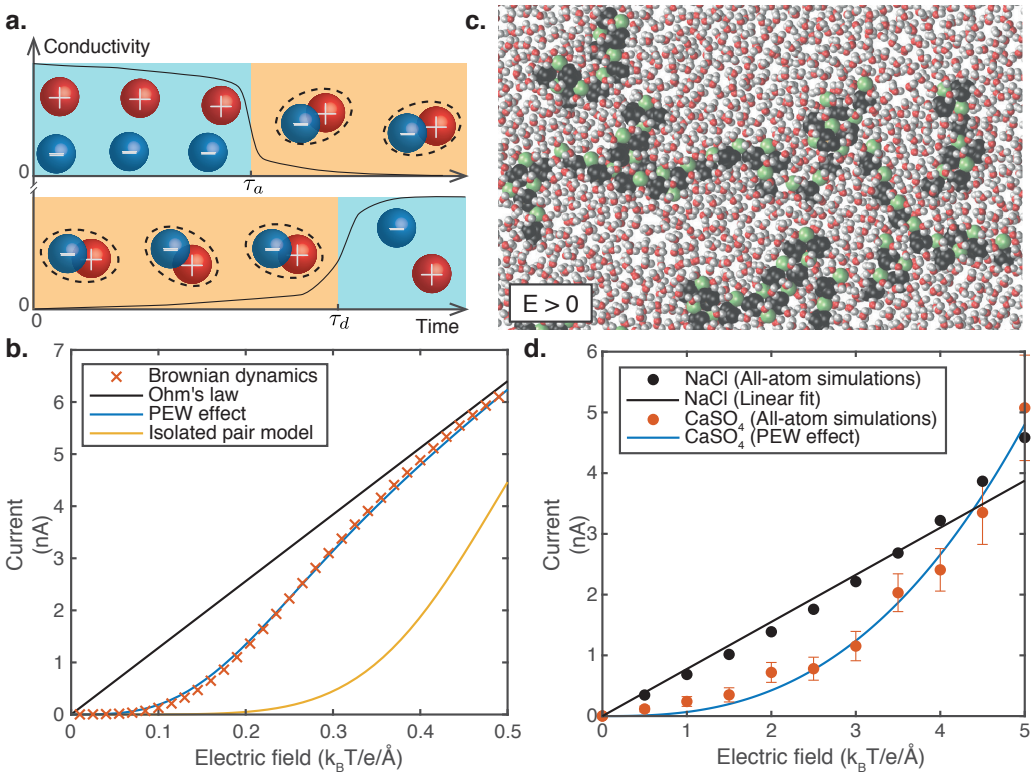

Figure 4.3

Analytical theory of the polyelectrolytic Wien (PEW) effect. **a.** Schematic representation of Onsager's Wien effect for an isolated ion pair: free ions have a lifetime of order τ_a during which they contribute to conduction, before assembling into pairs (upper panel). Pairs typically break up after a time τ_d, and do not take part in conduction (lower panel). **b.** Current-voltage characteristic of a generic divalent salt. Taking into account the formation of polyelectrolytes significantly improves the agreement with simulations (blue line, see (4.6) and (4.7)) compared the isolated pair model (yellow line, see (4.4)), for an ionic concentration $\rho = 10^{-3}\,\mathrm{atom/nm^2}$. **c.** Molecular dynamics snapshot showing the formation of Bjerrum polyelectrolytes. The salt is $CaSO_4$; calcium ion are in green and sulphate ions in black. **d.** Current-voltage characteristic of $CaSO_4$ in a 1 nm slit as obtained from all-atom simulations, compared to the power law $I \propto E^a$ of the PEW effect theory, with the predicted exponent $a = a_{PEW} = 2.6$. Sodium chloride does not form pairs in slits of that height, and exhibits a linear response.

fundamentally different from Onsager's picture. Going beyond the IP model essentially amounts to accounting for Debye screening, characterised by the Debye length $\lambda_D = \sqrt{\frac{T^*}{\rho n_f}}$. Since under a (low) electric field E, the free ions density is $n_f \sim \tau_d^{-1/2} \propto l_E^{-1/2T^*}$, then $\lambda_D \propto l_E^{1/4T^*}$ sets the size of the screening cloud around a given ion. Yet, two ions are carried away from each other if they are separated by a distance exceeding $l_E/T^* \propto l_E$ in the direction of the field, say x. For sufficiently low temperature (or sufficiently large field), $\lambda_D > l_E$ and the ionic atmosphere becomes anisotropic: it extends over l_E in the direction x and over λ_D in the perpendicular direction y. We show in Appendix D.3 that such an anisotropic screening cloud becomes unstable in the direction y above a critical electric field, explaining the formation of Bjerrum polyelectrolytes. In terms of the dynamics, this amounts to modifying the scaling exponent of the pair dissociation time according to (see Appendix D.3):

$$\tau_d = \frac{r_0^2}{2D}\left(\frac{l_E}{r_0}\right)^{1/2T^*}. \tag{4.6}$$

As per eq. (4.5), this results in a new exponent for the current versus voltage scaling:

$$I \underset{E\to 0}{\propto} E^{a_{PEW}(T^*)},\ a_{PEW}(T^*) = 1 + 1/4T^*. \tag{4.7}$$

We term this new mechanism the polyelectrolytic Wien (PEW) effect, since conduction actually occurs inside the Bjerrum polyelectrolytes. In figure 4.3b, we show that the PEW prediction is in quantitative agreement with BD simulation results, in contrast to the isolated pair model. We also compare it to results from all-atom simulations for $CaSO_4$ in figure 4.3d to demonstrate its robustness: the dynamics of the ionic assemblies are independent of the chemical nature of the salt and the confining medium or of simulation details (see figure F.4). Their formation is a direct consequence of 2D confinement.

4.3.2 Ionic memristor

The non-linear transport phenomena unveiled above set the stage for the memristor effect. The number of free ions in the system is expected to behave as an internal variable, which keeps memory of the voltage history. More formally, Eqs. (4.2) and (4.5) can be recast in the more transparent form, introducing the voltage U:

$$I = G(n_f) \times U, \tag{4.8}$$

$$\frac{\partial}{\partial t} n_f = f(n_f, U) \tag{4.9}$$

The fraction of conducting free ions, n_f, appears here indeed as an internal state variable. Furthermore, from the previous analysis, the relevant timescale governing the system's dynamics – τ_a – is much longer than usual molecular timescales, with typically $\tau_a \sim 1\,\mu s$. This points to potential memory effects in the system. Altogether, eqs. (4.8-4.9) formally define a voltage-controlled memristor, an electronic device whose resistance depends on its past [124, 125].

A further proof and hallmark of the memristor behaviour is shown in figure 4.4a, as the I-V characteristic under alternating voltage takes the form of a pinched loop for frequencies larger than a threshold f_p. The timescale $\tau_p = 1/f_p$ is found to decrease with ionic

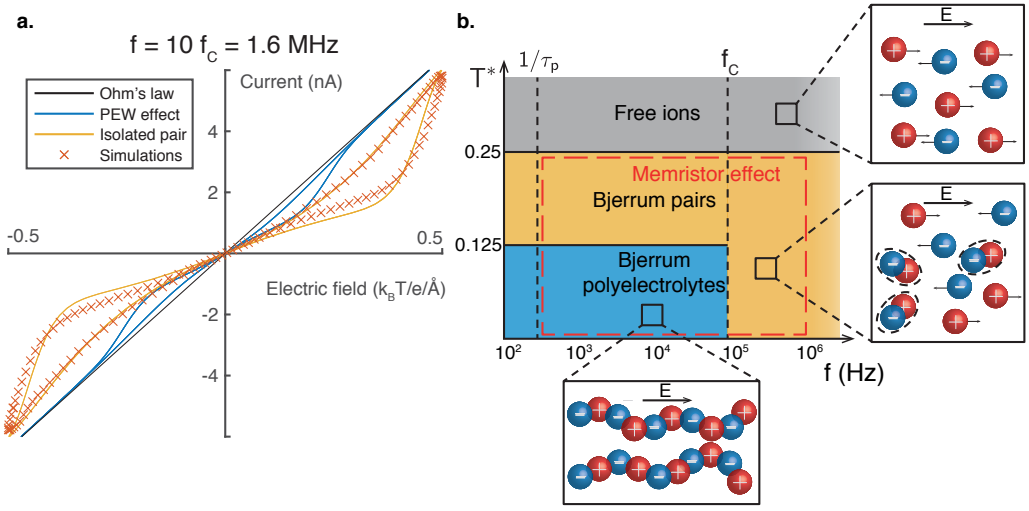

Figure 4.4

Time-dependent regime and memristor effect. **a.** "Pinched" current-voltage characteristic at high frequency (here $f = 10 f_C = 1.6\,\text{MHz}$ and $T^* = 0.11$), typical of memristive devices. Here, the IP model (yellow line, equations (4.2) and (4.4)) provides a better prediction than the PEW effect model (blue line, equations (4.2) and (4.6)), showing that Bjerrum polyelectrolytes are unstable at high frequency. **b.** Temperature-frequency diagram summarizing the existence domains of Bjerrum pairs and polyelectrolytes, for a generic salt with $r_0 = 1\,\text{Å}$, $D = 10^{-9}\,\text{m}^2\,\text{s}^{-1}$ and ionic concentration $\rho \sim 10^{-3}\,\text{at/nm}^2$.

concentration ρ, and we interpret it as a formation timescale of Bjerrum polyelectrolytes. Qualitatively, as conduction occurs through the slow formation of macrostructures, the system cannot adapt to the instantaneous value of the electric field: once the polyelectrolytes are formed, they contribute to conduction even if the field is turned off, before eventually dissolving. Going further, we compare the BD simulation results with our Wien effect theory to gain insight into the underlying physics of the memristor behaviour. We find that below a frequency f_C (here $f_C = 160$ kHz) the simulated I-V curves are well reproduced by the PEW model, while for $f > f_C$, quantitative agreement is observed with the IP model, see figure 4.4b and figure F.4. This is consistent with the observation that at high frequencies, polyelectrolytes do not have time to form and conduction proceeds through the breaking of individual pairs. The threshold frequency $f_C = 160$ kHz is found to be remarkably independent of concentration and is therefore related to the dynamics of individual Bjerrum polyelectrolytes.

While in our simulations the frequency of the alternating field is high due to numerical constraints, our model predicts that it should also be relevant in a realistic experimental setting. We show in Appendix D.4 that a memristor effect may be observed at experimentally relevant frequencies $f \sim 100$ Hz and voltages $U \sim 0.1$ V (see figure F.4). Overall a key finding of our work is therefore that an ionic memristor can be realized using $2D^+$ electrolytes confined in molecular channels. The memory effect is driven by Bjerrum pairs and polyelectrolytes, which form in all salts regardless of their chemical nature. Therefore, the memristor effect, described by equations (4.8) and (4.9), is a universal property

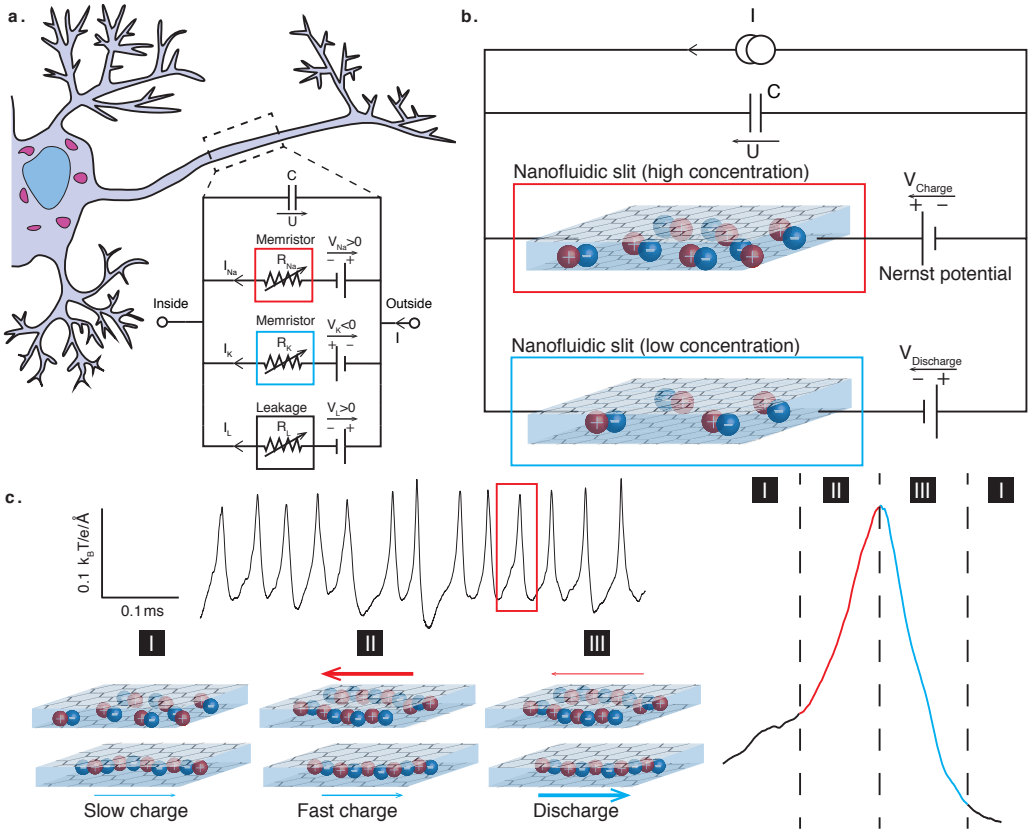

Figure 4.5

Building an artificial Hodgkin-Huxley neuron from 2D ionic memristors. **a.** Electronic representation of the Hodgkin-Huxley model, adapted from [119]. **b.** Prototype ionic machine implemented in BD simulations, exhibiting primitive neuronal behaviour. Two slits with different ionic concentrations are simulated over long timescales ($t \sim 1\,\mathrm{ms}$). Each slit is connected to a pair of reservoirs, imposing a given Nernst potential on the slit, as in the original computation by Hodgkin and Huxley. **c.** Spontaneous voltage spikes emitted by the prototype ionic machine, and qualitative explanation for the observed spiking effect.

of 2D electrolytes. We also find that optimal conditions correspond to a divalent salt with a slit height close to 1 nm, with other parameters such as the chemical structure of ions or of the confining material playing little role.

4.4 Hodgkin-Huxley neuron

We now make use of the fact that memristors are the electric equivalents of voltage-gated ion channels. As such, they may serve as components of a primitive neuron, as first pointed out by Hodgkin and Huxley [119] (figure 4.5a). Hence, it is expected that assembling several nanofluidic memristors should allow to mimic neuromorphic behavior.

To demonstrate this possibility, we perform parallel BD simulations of two monolayer electrolytes confined in two separate molecular channels, see figure 4.5b). For both electrolytes, the simulation yields the instantaneous relation between the applied voltage and resulting ionic current. A numeric circuitry is designed around the simulated molecular systems in order to reproduce the Hodgkin-Huxley model, see figure 4.5a. This includes a capacitor, and opposite sign potentials applied on each channel that account for the Nernst potentials. Altogether the circuit responds live to the MD-simulated conductance of the nanofluidic channels. Further details of the simulations are given in Appendix D.5. The outcome of these molecular simulations is shown in figure 4.5c: we observe spontaneous voltage spikes at a frequency around 10 kHz. These spikes are the hallmark of neuromorphic behaviour, obtained here from the sole properties of monolayer electrolytes.

The qualitative mechanism behind the generation of the spikes can be understood as follows. Since the two electrolytes are subject to (Nernst) potentials of opposite signs, they conduct current in opposite directions, but they are gated by the same voltage U. When U is small, only the discharging memristor is conducting, so that the capacitor receives a current $I_C < I$ and slowly charges. When U reaches a threshold value, the charging memristor starts conducting and the capacitor receives $I_C \gg I$, causing the voltage to spike up to $U \sim V_{\text{Charge}}$. Then, the discharging memristor takes over: the capacitor receives a strongly negative current, and its voltage is lowered back to 0, at which point the process can start again (see figure 4.5c). This whole process is analogous to voltage spiking in biological neurons caused by the successive opening and closing of ion channels (sodium and potassium channels in the case of the Hodgkin-Huxley model of the giant squid axon). The observed working frequency of a few kilohertz is, considering the set of parameters used in simulations, just above the threshold frequency for the memristor effect, which is therefore crucial for observing the neuromorphic behaviour.

4.5 The big picture

Two-dimensional electrolytes inside sub-nanometric slits are today an experimentally accessible nanofluidic system, where very strong interaction confinement is achieved. In this Chapter, thanks to a combination of analytical theory and molecular dynamics simulations, we have predicted that confinement-induced correlations result in very peculiar ion transport in such systems.

- The ionic interactions in 2D confinement are so strong that oppositely charged ions form tightly bound Bjerrum pairs.
- Upon application of a constant electric field, the system undergoes a dynamical phase transition and ion pairs assemble into dense clusters, which we term "Bjerrum polyelectrolyes". We develop a specific theory to describe conduction in these clusters.
- The slow dynamics of Bjerrum polyelectrolytes result in the system behaving as a memristor: a circuit component whose resistance depends on its past.
- The memristor effect can be harnessed to build elementary computational architectures with nanofluidic systems. As a proof-of-concept, we simulate two

coupled 2D electrolytes associated in a Hodgkin-Huxley cell, and show that these exhibit spontaneous voltage spikes, characteristic of neuromorphic activity.

The effects we predict are strongest with a divalent salt such as $CaSO_4$, in 7 – 10 Å confinement. Taken together, they open a promising avenue for bio-inspired computing based on nanoscale ion transport.

Part III

Many-body physics of the solid-liquid interface

Chapter 5

Quantum friction in nanoscale water flows

Contents

The peculiar flow of water in carbon nanochannels has defied understanding thus far [8], with accumulating experimental evidence for ultra-low friction, exceptionally high water flow rates, and curvature-dependent hydrodynamic slippage [19–25]. These unique properties have raised considerable interest in carbon-based membranes for desalination, molecular sieving and energy harvesting [129–131]. However, the underlying mechanism for the bizarre water-carbon friction remains a critical knowledge gap [26], with neither current theories [132], nor classical [133–136] or *ab initio* molecular dynamics simulations [137] providing satisfactory rationalisation for this singular behaviour. In this Chapter, we develop a quantum microscopic theory of the solid-liquid interface, which explicitly takes into account the electronic degrees of freedom of the solid through a non-equilibrium field theory framework. Our theory reveals a new contribution to friction, which is due to the coupling of charge fluctuations in the liquid to electronic excitations in the solid. We expect that this quantum friction, which cannot be accounted for by Born-Oppenheimer molecular dynamics, is the dominant friction mechanism for water on carbon-based materials. We demonstrate a strong difference in quantum friction between the water-graphene and water-graphite interface, due to the coupling of water Debye collective modes with a thermally excited interlayer plasmon specific to graphite. This suggests an explanation for the radius-dependent slippage of water in carbon nanotubes [23], in

terms of the nanotubes' surface electronic excitations. Our findings open the way to quantum engineering of hydrodynamic flows through the confining wall electronic properties.

This Chapter is based on the following publication: "Fluctuation-induced quantum friction in nanoscale water flows". N. Kavokine, A. Robert, M.-L. Bocquet and L. Bocquet. arXiv:2105:03413, *under review* (2021).[1]

5.1 General context

The flow rate of water through a macroscopic channel is determined solely by the channel's geometry. This is no longer true at the nanoscale, where the amount of friction between water and channel wall strongly affects the channel's permeability [138], as discussed in Chapter 1. Despite the importance of maximising flow slippage for practical applications such as filtration, understanding liquid friction on solid surfaces has remained a key fundamental challenge in fluid dynamics [26], with the water-carbon interface presenting a particularly puzzling picture [8]. Water was indeed found to exhibit very strong slippage – that is, low friction – in carbon nanotubes (CNTs) [19,20], with the slippage increasing with decreasing tube radius [23]. On the other hand, water slippage is vanishing inside the structurally similar, but electronically different, boron nitride nanotubes (BNNTs) [23], and only moderate water slippage has been reported on flat graphite surfaces [48].

These observations challenge the current theoretical understanding of the solid-liquid interface, which is based on picturing the solid as a static external potential that acts on the fluid molecules. The starting point of existing theoretical approaches is typically the Green-Kubo relation for the solid-liquid friction coefficient [139–141]:

$$\lambda = \frac{1}{\mathcal{A} k_\mathrm{B} T} \int_0^{+\infty} \langle F_x(t) F_x(0) \rangle, \tag{5.1}$$

where $F_x(t)$ is the total force that the static solid exerts on the liquid at time t of equilibrium dynamics, and $\mathcal{A}$ is the surface area. The force-force correlation function cannot in general be computed analytically, though it can be extracted from molecular dynamics simulations [135,137]. Most numerical evaluations of slippage are indeed based on equilibrium simulations and the use of eq. (5.1). The essence of these numerical results may be captured by a simple scaling estimate, which was established in [139]:

$$\lambda \sim n_w^s \frac{S_w(q_0)}{D k_\mathrm{B} T} |V_{q_0}|^2. \tag{5.2}$$

Here n_w^s is the liquid density in the interfacial layer, V_{q_0} is the interaction energy between this layer and the solid, and $S_w(q_0)$ is the structure factor of the liquid in the direction parallel to the interface.

The dissipation therefore appears to be determined by the interaction energy between the interfacial fluid layer and the solid, and by the commensurability of its molecular structure with the solid's periodic potential. Friction is then expected to be lower on

[1] The molecular dynamics simulations presented in this Chapter have been carried out by A. Robert and M.-L. Bocquet, to whom I am grateful for their collaboration on this project.

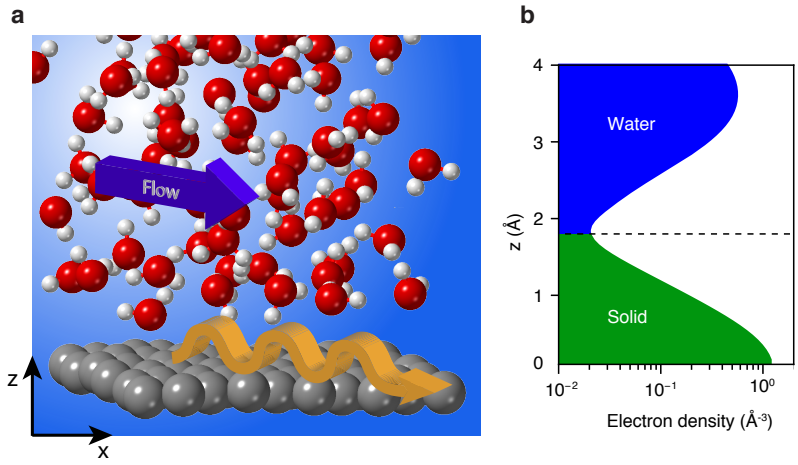

Figure 5.1

Quantum friction at the solid-liquid interface. **a**. Artist's view of the quantum friction phenomenon: water charge fluctuations couple to electronic excitations within the solid surface. **b**. Average electronic density, as obtained from density functional calculations (Appendix F.3.4, at the water-graphene interface.

surfaces that are weakly interacting with the liquid, hence more hydrophobic, consistently with a number of experiments and simulations [12, 142]. However, this classical approach involves a high degree of arbitrariness through the choice of the molecular force fields [143], leading, for instance, to a three order of magnitude spread in the reported molecular dynamics (MD) simulation results for the water friction coefficient inside sub-10 nm CNTs [134, 135, 144]. Moreover, it simply fails to account for experimental observations : in particular, the radius-dependence of friction observed for relatively large (60 nm diameter) CNTs [23], or the vast difference with BNNTs.

All this suggests that some key ingredients are missing from the current understanding of the solid-liquid interface, which might include quantum effects in nanoscale fluid dynamics. A few simulation studies have made pioneering attempts at taking into account electronic degrees of freedom at the solid-water interface, through polarisable force fields [145] or *ab initio* molecular dynamics (AIMD) [137, 146] in the Born-Oppenheimer approximation. While the latter point to some difference in water friction between graphene and boron nitride surfaces, such simulations are still insufficient to account for the whole experimental picture. In this Chapter, we introduce a theoretical description of the solid-liquid interface that fully accounts for the quantum dynamics of the solid electrons. This description reveals an analogue of interaction confinement at the solid-liquid interface, as the interfacial water dynamics appear sensitive to the confining wall's electronic properties. We predict that quantum effects do contribute to the solid-liquid friction, with the water-carbon interface being unique in many respects.

5.2 Model definition

We consider a flat solid-liquid interface lying in the (x, y) plane, as depicted in figure 5.1. We are interested in the solid-liquid friction force, which is the total force $\mathbf{F}$ that the solid exerts on the liquid in the direction parallel to the interface. It vanishes in the absence of liquid flow, while in the presence of flow it is proportional to the interfacial fluid velocity:

$$\mathbf{F}/\mathcal{A} = -\lambda\,\mathbf{v}, \tag{5.3}$$

where $\mathcal{A}$ is the area of the interface and λ is the solid-liquid friction coefficient. Equivalently, we will also consider the hydrodynamic slip length defined as $b = \eta/\lambda$, where η is the fluid viscosity. The solid interacts with the liquid through long range Coulomb forces, which result in van der Waals attraction at long range, and through short-range Pauli repulsion forces, which prevent the solid and the liquid from interpenetrating each other. In the framework of classical molecular dynamics, these are modelled in terms of a semi-empirical Lennard-Jones potential, with ad hoc molecular parameters. Our aim here is to relax this assumption and explicitly take into account the Coulomb interactions and the dynamics of the solid electrons.

5.3 Single particle friction

In order to introduce the theoretical framework, we first consider a single point charge e moving at a height h above the solid surface. As electronic degrees of freedom are taken into account, a polarisation charge arises within the solid. Dissipation then occurs in the dynamics of this polarisation charge [147].

We use cylindrical coordinates $\mathbf{r} = (\boldsymbol{\rho}, z)$, with the charge initially at $\mathbf{r}_0 = (0, h)$. It generates at every point $\mathbf{r}$ a Coulomb potential $V(\mathbf{r} - \mathbf{r}_0)$, with

$$V(\mathbf{r}) = \frac{e^2}{4\pi\epsilon_0\|\mathbf{r}\|}. \tag{5.4}$$

If the charge now moves at velocity $\mathbf{v}$, the Coulomb potential becomes time-dependent: $V(\mathbf{r}, t) = V(\mathbf{r} - (\mathbf{r}_0 + \mathbf{v}t))$. In the framework of linear response theory, the polarisation charge $\delta n(\mathbf{r}, t)$ is given by

$$\delta n(\mathbf{r}, t) = \int_{-\infty}^{+\infty} \mathrm{d}t' \int \mathrm{d}\mathbf{r}' \chi_\mathrm{e}(\mathbf{r}, \mathbf{r}', t - t') V(\mathbf{r}', t'). \tag{5.5}$$

This defines the density response function χ_e of the solid. The polarisation charge generates a Coulomb potential that acts back on the external charge. The corresponding force reads

$$\mathbf{f}(t) = -\int_{-\infty}^{+\infty} \mathrm{d}t' \int \mathrm{d}\mathbf{r}\mathrm{d}\mathbf{r}'\, \nabla_{\mathbf{r}_0} V(\mathbf{r}_0 + \mathbf{v}t - \mathbf{r}) \chi_\mathrm{e}(\mathbf{r}, \mathbf{r}', t - t') V(\mathbf{r}' - \mathbf{r}_0 - \mathbf{v}t'). \tag{5.6}$$

We assume that the solid is translationally invariant parallel to the surface, and consider only the in-plane component of the force. Then, $\chi_\mathrm{e}(\mathbf{r}, \mathbf{r}')$ depends only on $(\boldsymbol{\rho} - \boldsymbol{\rho}', z, z')$, and we may carry out Fourier transforms with respect to the in-plane coordinate $\boldsymbol{\rho}$:

$$\mathbf{f}(t) = -\int \frac{\mathrm{d}\mathbf{q}}{(2\pi)^2} (i\mathbf{q}) \int_{-\infty}^{0} \mathrm{d}z\mathrm{d}z' V_q(z + h) V_q(z' + h) \int_{-\infty}^{+\infty} \mathrm{d}t' e^{i\mathbf{q}\mathbf{v}(t-t')} \chi_\mathrm{e}(q, z, z', t - t'), \tag{5.7}$$

with

$$V_q(z) = \frac{e^2}{4\pi\epsilon_0}\frac{2\pi}{q}e^{-q|z|} \tag{5.8}$$

the 2D Fourier transform of the Coulomb potential. Identifying the Fourier transform of χ_e with respect to time, we obtain

$$\mathbf{f} = \frac{e^2}{8\pi^2\epsilon_0}\int \mathrm{d}\mathbf{q}\,\frac{i\mathbf{q}}{q}e^{-2qh}\left[\frac{-e^2}{2\epsilon_0 q}\int_{-\infty}^{0}\mathrm{d}z\mathrm{d}z'\,e^{q(z+z')}\chi_e(q,z,z',\omega=\mathbf{qv})\right]. \tag{5.9}$$

The expression in brackets defines the solid's surface response function $g_e(q,\omega=\mathbf{qv})$. Physically, $g_e(\mathbf{q},\omega)$ relates the external potential applied to the solid in the half-space $z<0$ to the induced potential in the half-space $z>0$. If the external potential is an evanescent plane wave of the form $V_{\mathrm{ext}} = V_0 e^{i(\mathbf{qr}-\omega t)}e^{qz}$, the induced potential is $V_{\mathrm{ind}} = V_0 g_e(\mathbf{q},\omega)e^{i(\mathbf{qr}-\omega t)}e^{-qz}$ (see detailed discussion in Appendix B). Using the property $g_e(q,-\omega) = g_e(q,\omega)^*$, we finally obtain that the moving charge is subject to a friction force that reads

$$\mathbf{f} = \frac{-e^2}{8\pi^2\epsilon_0}\int \mathrm{d}^2q\,\frac{\mathbf{q}}{q}e^{-2qh}\,\mathrm{Im}\,g_e(\mathbf{q},\mathbf{q}\cdot\mathbf{v}), \tag{5.10}$$

generalising the bulk result [148, 149] to interfacial friction. eq. (5.10) accounts for electronic friction, that is, friction through the generation of electronic excitations within the solid. This phenomenon has been invoked in various situations where classical nuclear degrees of freedom are coupled to an electron bath [150–154].

The mechanism outlined here for a single charged particle should in principle apply as well to a dense polar liquid such as water. An electronic contribution to hydrodynamic friction, given by the sum of electronic friction forces on each water molecule, was indeed proposed in [155, 156] to account for the radius-dependent slippage in carbon nanotubes, but the prediction disagreed with experiments by orders of magnitude. The pitfall in these estimates lies in the wrong treatment of the collective excitations of the fluid, which cannot be accounted for by a sum of individual contributions.

5.4 From particles to modes

5.4.1 General theory

We are hence required to go beyond the single-particle picture. As a first step, we formally express the dissipation resulting from water flow on a solid wall in terms of the system's many-body dynamics. To do so, we build on the general framework of fluctuation-induced forces [157, 158], which is specifically extended to account for a solid-liquid instead of a solid-solid interface. In particular, we implement a fully non-local and non-equilibrium treatment through the Schwinger-Keldysh framework of perturbation theory [159, 160].

Let us assume for concreteness that the liquid is water. We focus on the force due to the long range Coulomb interaction between the water molecules and the solid electrons, noting that we could consider the Coulomb interactions between water and the crystal lattice in a similar way. Since the dynamics of the electrons are quantum, the friction force is represented by an operator $\hat{\mathbf{F}}$, whose average value at time t is

$$\langle\hat{\mathbf{F}}(t)\rangle = -\int \mathrm{d}\mathbf{r}\,\mathrm{d}\mathbf{r}'\,\nabla_{\mathbf{r}'}V(\mathbf{r}-\mathbf{r}')\langle n_w(\mathbf{r}',t)\hat{n}_e(\mathbf{r},t)\rangle. \tag{5.11}$$

Here V is the Coulomb potential, n_w is the instantaneous charge density of water, and $\hat{n}_e$ is the electron density operator. The average is over all thermal and quantum fluctuations of the system. While the dynamics of water are well described within classical mechanics even at the molecular scale, the electron dynamics are intrinsically quantum. Hence, in order to maintain a consistent formalism, we treat the water dynamics in formally quantum way. Precisely, we represent the water charge density by a quantum field $\hat{n}_w$, which we assume to have gaussian fluctuations with prescribed correlation functions, as is done, for example, in the theory of solvation [161, 162]. The average in eq. (5.11) is then computed in the framework of many-body perturbation theory, with respect to the interaction Hamiltonian that comprises both the electron-water and electron-electron Coulomb interactions:

$$\hat{H}_{\text{int}} = \int \mathrm{d}\mathbf{r}\mathrm{d}\mathbf{r}' \hat{n}_w(\mathbf{r}', t) V(\mathbf{r} - \mathbf{r}') \hat{n}_e(\mathbf{r}, t) + \frac{1}{2} \int \mathrm{d}\mathbf{r}\mathrm{d}\mathbf{r}' \hat{n}_e(\mathbf{r}', t) V(\mathbf{r} - \mathbf{r}') \hat{n}_e(\mathbf{r}, t). \quad (5.12)$$

The main difficulty of the computation is in that it deals with a non-equilibrium steady state: for the friction force to be non-zero, we need to impose a net flow of water parallel to the interface. Accordingly, we treat the perturbative expansion in the non-equilibrium Schwinger-Keldysh framework ([160] and Appendix E.1.2). After an exhaustive computation, reported in Appendix E.1, our most general result is a Dyson equation relating the electron-water, water-water and electron-electron density correlation functions, which has the following Feynman diagram representation:

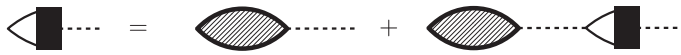

(5.13)

Here the thick solid lines represent the fully dressed electron Green's function, and the dashed lines are water density correlation functions. The electronic polarisation "bubble" is renormalised by the Coulomb interactions according to

(5.14)

Qualitatively, eqs. (5.13) and (5.14) express that electron-water correlations result from all the possible fluctuations of the water and electron densities. The friction force may then be expressed in terms of the Keldysh component of the water-electron correlation function. We stress here the generality of the result, as it applies to a fully out of equilibrium situation, and allows for overlap between the water and electron densities. Moreover, we treat the water-electron interaction beyond the mean-field approximation, as our computation allows for a self-energy correction due to the presence of water in the electron Green's functions.

The fully general but cumbersome result in eq. (5.13) can be simplified if the water and electron densities are no longer allowed to interpenetrate each other. This is a reasonable approximation as long as there is no chemisorption of water on the solid surface: then, the short-range Pauli repulsion effectively acts as an infinite potential barrier between the water and the electrons. Density functional calculations show that this is the case, for instance, at the water-graphene interface (figure 5.1b). A further simplification is obtained by considering the hydrodynamic flow profile above the solid surface. As long as the typical range of the solid-liquid interactions is smaller than the slip length, one may consider the flow velocity to be uniform, and equal to the interfacial velocity $\mathbf{v}$. Then,

expanding the friction force to linear order in $\mathbf{v}$, we obtain a closed-form expression for the friction coefficient λ. It separates into two terms: $\lambda = \lambda_{\mathrm{Cl}} + \lambda_{\mathrm{Q}}$, with

$$\lambda_{\mathrm{Cl}} = \frac{1}{8\pi^2 k_{\mathrm{B}} T} \int \mathrm{d}^2 q \, \frac{(\mathbf{q}\cdot\mathbf{v})^2}{v^2} |V_{\mathrm{e}}(\mathbf{q})|^2 \int_{-\infty}^{+\infty} \mathrm{d}t S_{\mathrm{w}}(\mathbf{q}, t) \tag{5.15}$$

and

$$v\cdot\lambda_{\mathrm{Q}} = \frac{1}{8\pi^2} \int_0^{+\infty} q\mathrm{d}q\,(\hbar q) \int_0^{+\infty} \frac{\mathrm{d}(\hbar\omega)}{k_B T} \frac{q\cdot v}{\sinh^2(\frac{\hbar\omega}{2k_{\mathrm{B}}T})} \frac{\mathrm{Im}[g_{\mathrm{e}}(q,\omega)]\,\mathrm{Im}[g_{\mathrm{w}}(q,\omega)]}{|1 - g_{\mathrm{e}}(q,\omega)\, g_{\mathrm{w}}(q,\omega)|^2}. \tag{5.16}$$

The first term (eq.(5.15)) corresponds exactly to the scaling estimate of the friction coefficient based on the classical surface roughness picture and calculated previously in refs. [135, 163]: we hence call it the classical term. In eq. (5.15), $V_{\mathrm{e}}(\mathbf{q})$ is the average Coulomb potential acting on the interfacial water layer, and $S_{\mathrm{w}}(\mathbf{q})$ is the water charge structure factor (precise definitions of these quantities are given in Appendix E.1.5). On the other hand, the second term (eq. (5.16)) is absent in the roughness-based picture, and originates from the coupled water and electron dynamics, as it involves the surface response functions of both the solid and the liquid, g_{e} and g_{w}, respectively: we call it the quantum term. A similar term is known to arise in the non-contact friction between two dielectric media separated by a vacuum gap [164–167]: it is then interpreted as a dynamic analogue of the van der Waals force. However, the expression of this van der Waals friction was rigorously established only in the case of two media with local dielectric response [168], hence it could not apply directly to the solid-liquid interface under scrutiny.

5.4.2 Toy model

Let us examine the expression for the quantum friction coefficient in eq. (5.16). A crucial observation is that it depends on the overlap between the water and electron surface excitation spectra. Hence, quantum friction cannot be seen as resulting from the interaction of individual water molecules with the solid: it is rather a consequence of the interaction between the collective charge fluctuation modes of the two media. Starting from this observation, the structure of eq. (5.16) can be given a simple interpretation in terms a quasiparticle tunnelling between harmonic modes. Let us assume that the charge fluctuations in each medium can be described by a single harmonic mode, with the same wavevector $\mathbf{q}$ and frequency $\omega_{\mathbf{q}}$. Then, the total hamiltonian of the system is

$$\hat{H} = \hbar\omega_{\mathbf{q}}(w_{\mathbf{q}}^\dagger w_{\mathbf{q}} + s_{\mathbf{q}}^\dagger s_{\mathbf{q}}) + H_{\mathrm{int}}, \qquad H_{\mathrm{int}} = V_q(w_{\mathbf{q}}^\dagger s_{\mathbf{q}} + s_{\mathbf{q}}^\dagger w_{\mathbf{q}}). \tag{5.17}$$

where V_q is a Fourier-transformed Coulomb interaction and $(w_{\mathbf{q}}^\dagger, w_{\mathbf{q}})$ and $(s_{\mathbf{q}}^\dagger, s_{\mathbf{q}})$ are the creation and anihilation operators corresponding to the water and the solid modes, respectively. Elementary excitations (quasiparticles) may tunnel back and forth between the s and w modes. We denote $|n_s, n_w\rangle$ the eigenstates of the non-interacting system. According to the Fermi golden rule, the quasiparticle tunnelling rate from mode w to mode s is

$$\begin{aligned}\gamma(w\to s) &= \frac{2\pi}{\hbar} \sum_{n_s,n_w} P_s(n_s) P_w(n_w) |\langle n_w - 1, n_s + 1 | H_{\mathrm{int}} | n_w, n_s\rangle|^2 \\ &= \frac{2\pi}{\hbar} V_q^2 \sum_{n_s,n_w} P_s(n_s) P_w(n_w) n_w(n_s+1),\end{aligned} \tag{5.18}$$

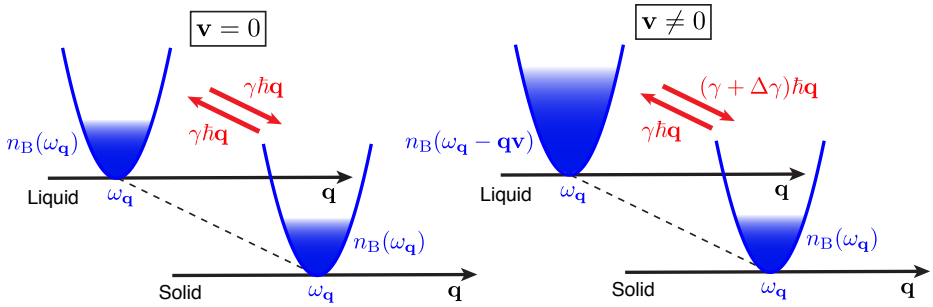

Figure 5.2

Schematic of the quantum friction mechanism, showing quasiparticle tunnelling between two surface modes. The back and forth tunnelling rates are different in the presence of flow, resulting in net momentum transfer from the liquid to the solid.

where $P_s(n_s)$ ($P_w(n_w)$) is the probability that there are n_s (n_w) quasiparticles in mode s (w). Hence, the difference between forward and backward tunnelling rates is

$$\Delta\gamma(\omega_\mathbf{q}) = \gamma(w \to s) - \gamma(s \to w) = \frac{2\pi}{\hbar} V_q^2 \sum_n n(P_w(n) - P_s(n)). \tag{5.19}$$

At equilibrium,

$$\sum_n n P_w(n) = \sum_n n P_s(n) = n_\mathrm{B}(\omega_\mathbf{q}), \tag{5.20}$$

with $n_\mathrm{B}(\omega) \equiv 1/(e^{\hbar\omega/k_B T} - 1)$ the Bose distribution, so that the tunnelling rates compensate and there is no net momentum transfer between the two media. This is no longer true when the fluid flows with velocity $\mathbf{v}$. Our full computation (Appendix E.1) shows that the flow induces a Doppler shift in the occupation of the water modes. Precisely, the w mode contains $n_\mathrm{B}(\omega_\mathbf{q} - \mathbf{q}\mathbf{v})$ quasiparticles, while the s mode still contains $n_\mathrm{B}(\omega_\mathbf{q})$ quasiparticles. This results in a difference in between the $w \to s$ and $s \to w$ tunnelling rates:

$$\Delta\gamma(\omega_\mathbf{q}) = \frac{2\pi}{\hbar} V_q^2 (n_\mathrm{B}(\omega_\mathbf{q} - \mathbf{q}\mathbf{v}) - n_\mathrm{B}(\omega_\mathbf{q})) \approx \pi V_q^2 \frac{\mathbf{q}\cdot\mathbf{v}}{k_B T} \sinh^{-2}\left(\frac{\hbar\omega_\mathbf{q}}{2k_B T}\right). \tag{5.21}$$

Such an asymmetric quasiparticle tunnelling results in a net momentum transfer, hence an elementary friction force $\mathbf{f}_\mathbf{q} = \hbar\mathbf{q}\,\Delta\gamma(\omega_\mathbf{q})$. The total friction force is then obtained by integrating over all the modes: $\mathbf{F}/\mathcal{A} = \int \mathrm{d}^2q\, \hbar\mathbf{q}\,\Delta\gamma(\omega_\mathbf{q})$. This is essentially the structure of eq. (5.16), where the frequency integral takes into account the distribution of modes at wavevector $\mathbf{q}$; the product of surface excitation spectra enforces energy conservation and contains the Coulomb interaction V_q^2. The mechanism of dissipation via asymmetric quasiparticle tunnelling between charge fluctuation modes is summarised in figure 5.2.

Based on eq. (5.16), we can now evaluate quantitatively the quantum hydrodynamic friction coefficient λ_Q. To this end, we need to determine the surface excitation spectra $\mathrm{Im}\, g_{\mathrm{w,e}}(q,\omega)$ of water, and of the electronic system under consideration. In both cases, we are only interested in the spectra at frequencies below $2k_B T/\hbar = 50$ meV or 10 THz,

because only modes that are populated at temperature T can contribute to quantum friction. However, the spectra need to be evaluated up to the highest momenta, since the contribution of modes at wavevector q to the friction coefficient scales as q^3.

5.5 Water fluctuations

Our result in eq. (5.16) involves the bare surface response function of water, which depends on the water dynamics in the absence of coupling to electronic degrees of freedom. Moreover, in the frequency range under consideration, the water dynamics are completely classical, so that classical MD simulations are well-suited for the determination of water surface response functions. Accordingly, we have carried out such simulations for water (in the SPC/E model) in contact with graphite surfaces, for which we considered two different sets of Lennard-Jones parameters [143, 169] (figure 5.3a). The surface response functions were determined from the equilibrium charge correlation functions through the fluctuation-dissipation theorem, according to the definition in eq. (B.3). Details of the simulations and analysis are given in Appendix F.3.

We first focus on results in the long wavelength limit ($q \to 0$), displayed in figure 5.3b. The surface response function should then converge to a value determined only by the bulk water dielectric permittivity $\epsilon_{\mathrm{w}}(\omega)$:

$$g_{\mathrm{w}}(0,\omega) = \frac{\epsilon_{\mathrm{w}}(\omega) - 1}{\epsilon_{\mathrm{w}}(\omega) + 1}. \tag{5.22}$$

It is then interpreted as an electromagnetic reflection coefficient (see Appendix B). We find that this limit is essentially reached for the lowest q values accessible in our simulation ($q = 0.05$ Å^{-1}). Moreover, for frequencies below 100 meV, our results agree well with the long wavelength surface response function obtained from the experimentally determined $\epsilon_{\mathrm{w}}(\omega)$ [170]. Note that by construction the mode frequencies in the surface response g_{w} are strongly blue shifted with respect to the bulk dielectric response $-\mathrm{Im}[1/\epsilon_{\mathrm{w}}(\omega)]$ by a factor of $\epsilon_{\mathrm{w}}(0)/2 \approx 40$.

The relation with the bulk dielectric function in eq. (5.22) implies that the features in $g_{\mathrm{w}}(q,\omega)$ can be analysed in terms of the well-known features of the bulk water dielectric response [171]. The low-energy surface response of water is dominated by the Debye mode, which corresponds to the wide feature in the spectrum, spanning about three decades in frequency between 0.1 meV and 100 meV. This mode is a general feature of polar liquids and corresponds to the collective relaxation of molecular dipoles. However, in water, it has recently been assigned a more complex microscopic origin, involving the migration of defects in the hydrogen bond network [172]. The sharp peak at around 100 meV corresponds to the libration mode, which involves rotation of the water molecules without displacement of their centre of mass [149].

The water surface response function shows little dispersion as the momentum q is increased (figures 5.3 and F.5), and only small variations are found between the two models for the graphite surfaces. At large momenta ($q \geq 1$ Å^{-1}), the surface response function shows an exponential decrease, which we attribute to the depletion of water near the hydrophobic surface. We find that, for the purposes of calculation, $g_{\mathrm{w}}(q,\omega)$ is well represented by the sum of two Debye peaks at $\omega_{\mathrm{D},1} = 1.5$ meV and $\omega_{\mathrm{D},2} = 20$ meV, with

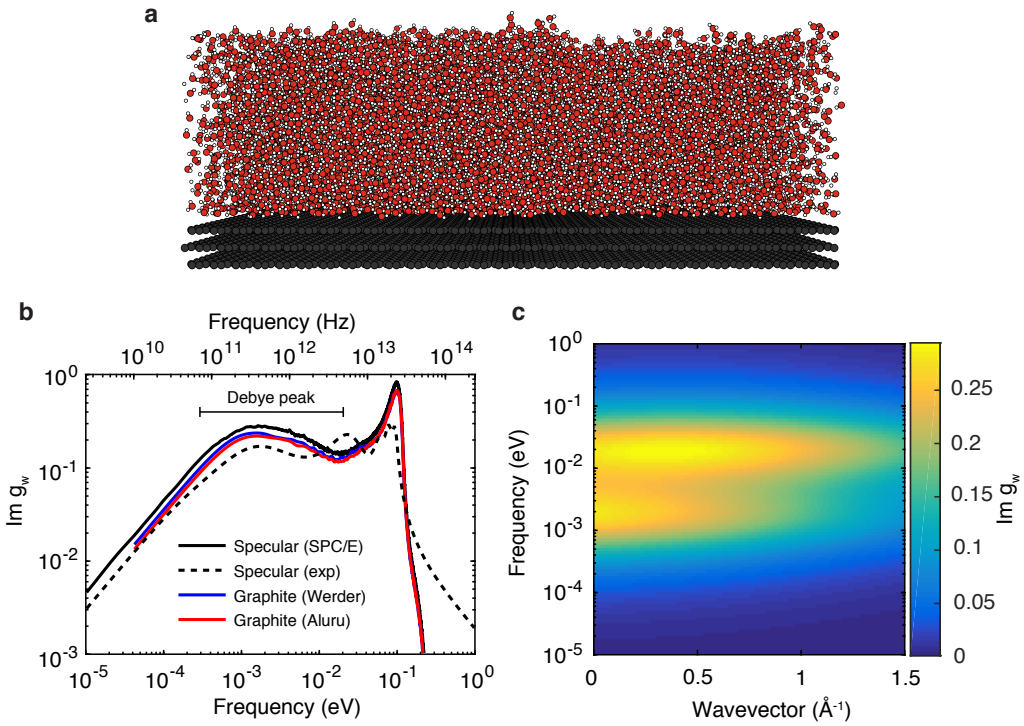

Figure 5.3

Surface dielectric response of water. **a**. Snapshot of the MD simulation used for determining the water surface response function. **b**. Surface response function of water in the long wavelength limit. The results from surface simulations agree with the long wavelength limit obtained from the bulk dielectric function (eq. (5.22)). **c**. Surface response function of water in energy-momentum space, after fitting the simulation data with two Debye peaks (see text).

momentum-dependent oscillator strengths:

$$g_{\mathrm{w}}(q,\omega) = \frac{f_1(q)}{1 - i\omega/\omega_{\mathrm{D},1}} + \frac{f_2(q)}{1 - i\omega/\omega_{\mathrm{D},2}}. \tag{5.23}$$

Analytical expressions for $f_1(q)$ and $f_2(q)$ are given in Appendix F.3; at large q, $f_1(q) + f_2(q) \propto e^{-2qd}$, with $d = 0.95$ Å.

5.6 Jellium model

We now examine the surface excitations in the solid and first explore a generic electronic system. A solid has low energy electronic excitations if contains free charge carriers, but the precise location of these excitations in energy-momentum space depends strongly on the conduction band characteristics. The simplest way to account for this dependence for a wide range of parameters is in the framework of the jellium model. In the jellium model, the nuclei and core electrons are assimilated to a semi-infinite positive background,

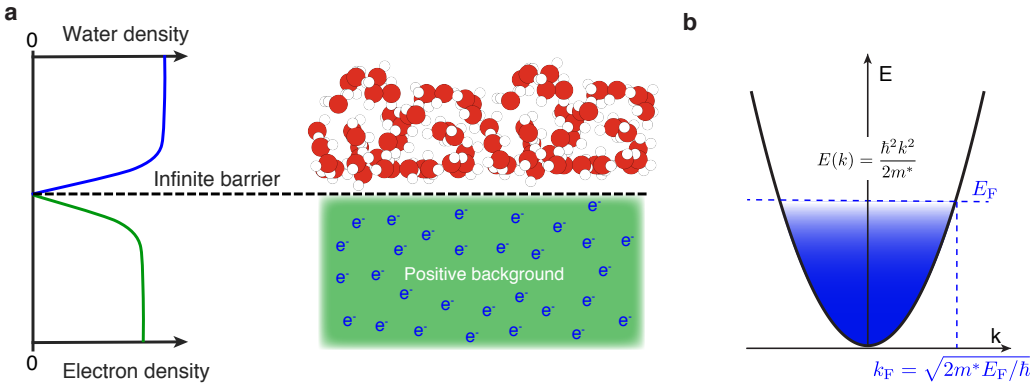

Figure 5.4

a. Schematic of the infinite barrier jellium model: the water and solid electrons are separated by an infinite potential barrier. **b**. Band structure for the jellium model: a single parabolic band with effective mass m^*.

while the conduction electrons behave as free electrons (figure 5.4a), so that they occupy a parabolic band: $E(k) = \hbar^2 k^2/(2m^*)$. The electronic structure is then completely determined by two parameters: the effective mass m^* appearing in the electron dispersion, and the Fermi energy E_F up to which the band is filled, figure 5.4b.

In general, in the jellium model, electrons are allowed to spill over the positive background edge [173]. However, in the presence of water, the spill-over is limited by the Pauli repulsion between the water and the surface electrons (figure 5.1b), so that the infinite barrier jellium model appears better suited to describing the electronic system under scrutiny. The infinite barrier jellium presents furthermore a technical advantage, as it may be treated within the specular reflection (SR) approximation, with only small quantitative differences with respect to the exact semi-infinite computation [174]. The SR approximation allows one to express the surface response of a system in terms of its bulk response. Precisely, the non-interacting density-density response function of the semi-infinite system $\chi^0(q, z, z', \omega)$ is assumed to satisfy

$$\chi^0(q, z, z', \omega) \simeq \chi^0_B(q, z - z', \omega) + \chi^0_B(q, z + z', \omega), \tag{5.24}$$

where χ^0_B is its bulk counterpart. Then, the surface response function can be obtained according to (see [175] and Appendix B.4)

$$g_e(q, \omega) = \frac{1 - q\ell_q(\omega)}{1 + q\ell_q(\omega)}, \quad \ell_q(\omega) = \frac{2}{\pi} \int_0^{+\infty} \frac{dq_z}{(q^2 + q_z^2)\epsilon(q, q_z, \omega)}, \tag{5.25}$$

where $\epsilon(q, q_z, \omega) = 1 - \frac{e^2}{\epsilon_0(q^2+q_z^2)} \chi^0_B(q, q_z, \omega)$ is the bulk system's dielectric function. The bulk dielectric function can in turn be obtained from the band dispersion and Fermi energy in a standard way (Appendix B and Appendix E.2).

A typical result for the jellium surface response function is shown in figure 5.5a. It presents two types of features: incoherent particle-hole excitations, and a collective surface plasmon mode. At zero energy, particle-hole excitations are present up to $q = 2k_F$, with

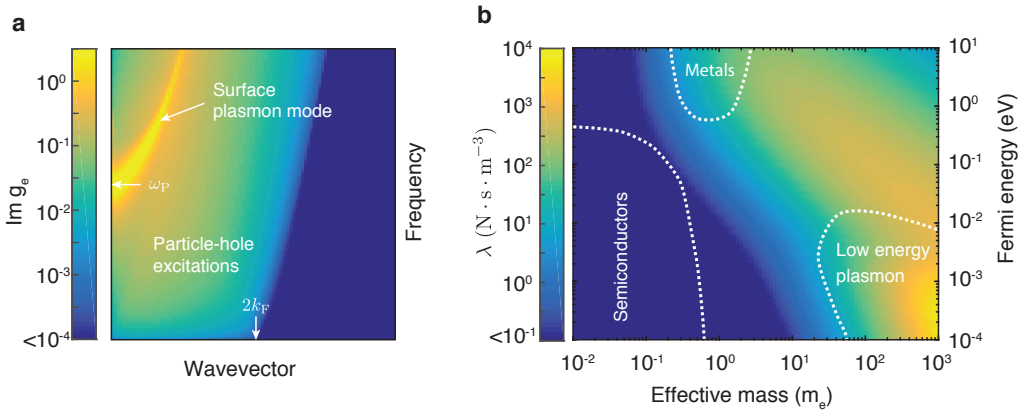

Figure 5.5

a. Surface response function for a semi-infinite jellium ($r_s = 5$) in energy-momentum space. **b**. Quantum friction coefficient for water on a jellium surface, as a function of the jellium Fermi energy and effective mass (in units of electron mass).

$k_F = \sqrt{2m^* E_F/\hbar}$ the Fermi momentum. The long wavelength surface plasmon frequency ω_P scales as $(m^*)^{1/4} E_F^{3/4}$. It shows a positive dispersion, and remains visible in the spectrum up to a momentum $q_{max} \approx k_F(\sqrt{1 + 2\hbar\omega_P/E_F} - 1)$, above which it enters the particle-hole continuum and becomes Landau-damped.

Having determined the surface response functions for water and for the jellium electrons, we may compute the quantum friction coefficient of water according to eq. (5.16), for a range of Fermi energy and effective mass values. Result are shown in figure 5.5b. The friction coefficient λ_Q is given in the standard unit N · s · m^{-3} ($\lambda = 10^5$ N · s · m^{-3} corresponding to a slip length of 10 nm for water).

Generally, the quantum contribution to friction is found to be non-negligible when the electronic system has excitations at low energy and high momentum. For instance, we find it to be very small for water on semiconductor surfaces, which, for our purpose, can be described by a jellium model with low Fermi energy and effective mass, regardless of the nature (electron or hole) of the charge carriers. In such systems, electronic excitations are restricted to very small momenta, and we expect the hydrodynamic friction to be dominated either by the classical roughness term [135, 139] or by the optical phonon contribution (Appendix E.2.3).

On metal surfaces, with high Fermi energy (1 - 10 eV) and effective mass close to unity, we find $\lambda_Q \sim 10^2$ N · s · m^{-3}, which is two orders of magnitude lower than typical hydrodynamic friction coefficients. There are, to our knowledge, no experimental measurements of water slip length on atomically smooth metal surfaces. If dominated by the quantum contribution, we would expect such surfaces to exhibit very high slippage. The highest values of quantum friction coefficient in the (m^*, E_F) parameter space are obtained in the region of low Fermi energy and high effective mass. In this region, the electronic surface plasmon mode is at low enough energy ($\sim$ 10 meV) and high enough momenta ($\sim$ 0.5 Å^{-1}) to couple with the Debye peak of water: the resonant coupling between these two modes results in a particular friction enhancement (see figure E.2).

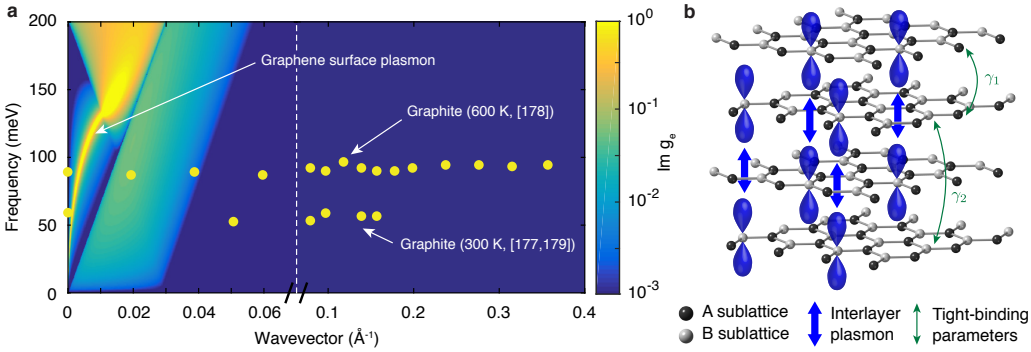

Figure 5.6

Surface excitations of carbon-based materials. **a**. Surface response function of doped graphene ($E_\mathrm{F} = 0.1$ eV) in energy-momentum space, and experimental data for the graphite surface plasmon mode [177–179]. **b**. Schematic of the electron movement corresponding to the graphite surface plasmon, and definition of the interlayer coupling parameters.

5.7 Water-carbon interface

We now examine specifically the water-carbon interface. In the ideal case where the solid is a single graphene sheet, its surface response function can be calculated analytically ([176] and Appendix E.3.1). The result is plotted in figure 5.6a, considering a doping level $E_F = 0.1$ eV. Graphene is found to have low energy excitations ($\omega \lesssim 100$ meV) only at very small momenta ($q \lesssim 0.05$ Å^{-1}). An intra-layer plasmon mode is present, but it displays a very steep square root dispersion at small momenta. The quantum contribution to the water friction coefficient, evaluated with eq. (5.16), is accordingly found to be very small, below 10^0 N·s·m^{-3}, whatever the doping level, much like in the case of semiconductors treated within the jellium model.

The situation, however, is drastically different for water on a semi-infinite graphite surface, made up of a staggered stack of graphene sheets (figure 5.6b). In such an arrangement, electrons acquire an extra degree of freedom compared to graphene, as they may tunnel between the stacked sheets. In particular, the coupling between second nearest layers is associated with a bandwidth $4\gamma_2 = 40$ meV. It is therefore not surprising that experimentally, a strong effect of this interlayer coupling on the graphite low energy excitations was observed. In electron energy loss spectroscopy, graphite was found to exhibit a surface plasmon mode, polarised perpendicularly to the layers, at $\omega_\mathrm{P} = 50$ meV (at 300 K), with a very flat dispersion in the measured momentum range, which was up to $q_\mathrm{max} = 0.2$ Å^{-1} at 300 K [179] and $q_\mathrm{max} = 0.4$ Å^{-1} at 600 K [178] (see figure 5.6a). A similar plasmon peak was also observed in inelastic electron tunnelling spectroscopy [180]. Based on our study of the jellium model, we expect this low-energy plasmon of graphite to strongly interact with the water Debye mode, resulting in an enhancement of quantum friction. This enhancement may be assessed by describing the plasmon contribution to the graphite surface response in terms of a Drude model:

$$g_\mathrm{e}(q,\omega) = \frac{\omega_\mathrm{P}^2}{\omega_\mathrm{P}^2 - \omega^2 - 2i\gamma\omega}\theta(q - q_\mathrm{max}), \tag{5.26}$$

with $\gamma \sim 25$ meV the surface plasmon width [177,178], and θ the Heaviside step function. Using this expression in eq. (5.16), we obtain a water quantum friction coefficient $\lambda = 0.4 \times 10^3$ N $\cdot$ s $\cdot$ m^{-3} for $q_{\max} = 0.2$ Å^{-1} and $\lambda = 5 \times 10^3$ N $\cdot$ s $\cdot$ m^{-3} for $q_{\max} = 0.4$ Å^{-1}, which is indeed orders of magnitude larger than the expectation for graphene, and non-negligible compared to experimentally measured hydrodynamic friction coefficients: $\lambda \approx 2 \times 10^4 - 10^5$ N $\cdot$ s $\cdot$ m^{-3} on graphite surfaces [15,48] and $\lambda \approx 3 \times 10^4$ N $\cdot$ s $\cdot$ m^{-3} in carbon nanotubes with large (50 nm) radius [23], corresponding to hydrodynamic slip lengths in the range of a few tens of nanometers.

Going beyond a phenomenological treatment for the water-graphite quantum friction is particularly challenging. Indeed the numerical treatment of excitations at low energies and high momenta within the complex graphite band structure [181] requires a very large number of k points, and a very large unit cell comprising more than 100 layers would be needed to avoid finite size effects [182]. This is likely to be the reason why, to our knowledge, there is no detailed theoretical study of the graphite terahertz surface plasmon. Nevertheless, we propose a simplified model in order to extract the essential physical ingredients at play in the graphite surface response. At a qualitative level, the free charge carriers that contribute to the low energy plasmon are located mainly on the B sublattice [183] (figure 5.6b). The flat plasmon dispersion has been attributed to the shape of the bands containing those free carriers [178]. As a consequence of interlayer coupling, these are nearly flat up to parallel momentum $k \sim \gamma_1/v_{\mathrm{F}} = 0.06{-}0.11$ Å^{-1}, with γ_1 the nearest-neighbour interlayer coupling parameter (figure 5.6b) and v_{F} the graphene Fermi velocity. If the electron dispersion is flat parallel to the layers, then the graphite can be pictured as an array of independent 1D chains extending perpendicular to the layers, at least within a certain momentum range. This assembly of localised oscillators are then expected to have excitations whose energy does not depend on wavevector, that is a dispersionless mode.

Based on this qualitative idea, we propose a simplified model for the graphite surface response. We consider only the atoms on the B sublattice, which form an assembly of tight-binding chains with coupling parameter $\gamma_2 = 10$ meV [184]. At sufficiently large momenta ($q \gtrsim 1/(2c) = 0.14$ Å^{-1}), we may consider that the external field acts only on the topmost (surface) atoms. We then compute the local density response of the topmost atom a of a 1D chain $\delta n_a(q,\omega) = \chi_a(q,\omega)\phi_a(q,\omega)$, where ϕ_a is the potential acting on atom a (see Appendix E.3.2). Then, treating the Coulomb interactions between the chains in the random phase approximation, we obtain the graphite surface response function as

$$g_{\mathrm{e}}(q,\omega) = \frac{n_{\mathrm{s}} v_q \chi_a(\omega)}{n_{\mathrm{s}} v_q \chi_a(\omega) - 1}, \tag{5.27}$$

where $v_q = \frac{e^2}{4\pi\epsilon_0}\frac{2\pi}{q}$ is the 2D Coulomb potential and n_{s} is the density of charge carriers contributing to the low energy mode. Our simple model accounts indeed for an excitation continuum around $\omega = 40$ meV, whose intensity slowly decays with momentum (figure E.4). If we use for n_{s} the free carrier density in graphite at 300 K ($n_s = 2.3 \times 10^{12}$ cm^{-2} [185]), we find a friction coefficient $\lambda_{\mathrm{Q}} = 1.8 \times 10^4$ N $\cdot$ s $\cdot$ m^{-3}, slightly larger than the Drude model estimates, and within the range of experimentally measured water friction coefficients (figure 5.8).

Going further, we find that the band flattening which is at the root of the 1D chain picture is enhanced in the presence of water. Indeed, we are able to evaluate the lowest order self-energy correction the electron Green's functions in graphene (Appendix E.3.3):

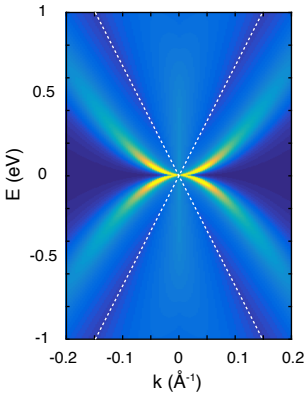

Figure 5.7

Spectral function (in arbitrary units) in energy-momentum space for graphene in the presence of water. The white dashed lines indicate the position of the bare bands.

the resulting renormalised spectral density is shown in figure 5.7. We find that, upon coupling with the water Debye mode, the graphene band velocity is reduced, so that more states become available at low energy and high momentum. We expect that a qualitatively similar renormalisation occurs in graphite. Hence, in our 1D chain model, the carrier density n_s should increase in the presence of water with respect to bare graphite, yielding quantum friction coefficients in the range $\lambda_Q \sim 10^4 - 10^5$ N $\cdot$ s $\cdot$ m^{-3} (figure 5.8a), well in agreement with the experimentally measured total hydrodynamic friction (figure 5.8b).

Overall, our theory suggests that quantum friction may be the dominant mechanism for the hydrodynamic friction on atomically smooth carbon surfaces. This is in line with the observation that, in classical MD simulations, the water friction coefficient on graphite is typically underestimated with respect to the experimental values [135]. Furthermore, the strong difference in quantum friction that we find between graphene and graphite suggests an explanation for the radius-dependent slippage of water in carbon nanotubes. It is crucial that the experiments in [23] are carried out with multiwall carbon nanotubes. In such nanotubes, the interlayer coupling is known to strongly depend on radius: a 50 nm radius tube has locally a graphite-like structure, while in a 10 nm radius tube the shells are completely decoupled [186]. Therefore, in large radius nanotubes, water is subject to graphite-like high quantum friction, while in smaller radius nanotubes water experiences graphene-like low friction.

The quantitative relevance of this argument can be checked, at the simplest level, in the framework of the Franklin model [187, 188], which relates the probability p of two layers being misaligned in a graphite structure to the average interlayer spacing d, which is known from experiment as a function of the tube radius R [186]: $d(R) = 3.44 - 0.086 \cdot (1 - p^2)$ (Å). We may then assume that the electron density n_s in eq. (5.27) scales according to $n_s(R) = n_s^0(1 - p(R))$, and we choose $n_s^0 = 10^{13}$ cm^{-2} so that $\lambda(R \to \infty) = 4.4 \times 10^4$ N $\cdot$ s $\cdot$ m^{-3}. The resulting prediction for the slip length $b = \eta/\lambda$, with η the water viscosity, is shown in figure 5.8b. Overall the predicted radius dependence is found to be in good agreement with the experimental data. We note that if the inner shell tubes are semiconducting, the radius-dependent band gap $E_g(R) = (2/3)v_F/R$ [189] may also reduce the number of charge carriers contributing to low energy excitations: we then expect a scaling $n_s(R) = n_s^0 e^{-E_g(R)/k_B T}$. Such a scaling also provides reasonable agreement with the data (figure 5.8b). While the details of electronic excitations in multiwall carbon nanotubes are hard to investigate theoretically, our theory strongly

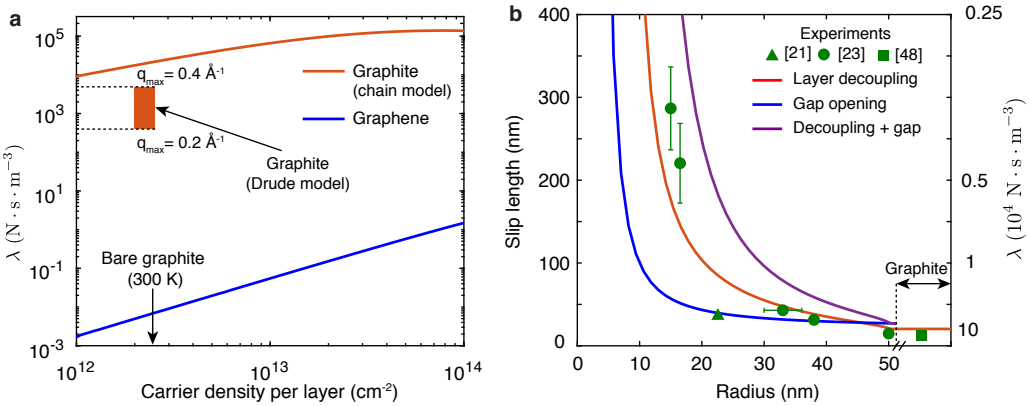

Figure 5.8

Water-carbon quantum friction. **a**. Quantum friction coefficient for water on graphene and graphite as a function of charge carrier density. For graphene, the carrier density is determined by the doping level. For graphite, the friction coefficient is determined from the 1D chain model (eq. (5.27)), where the carrier density corresponds to the parameter n_s. **b**. Water slip length in multiwall carbon nanotube as a function of inner tube radius. The green symbols are experimental data from refs. [21,23,48], and the full lines are theoretical predictions, corresponding to different models for the radius dependence of n_s in eq. (5.27).

suggests that quantum friction is a key ingredient for determining the water slip length in these systems.

5.8 Discussion

Our theory explains why the water-carbon couple is indeed bizarre [8]. We are able to rationalise the unique friction properties of water on carbon surfaces, as well as the puzzling radius dependence of slippage in carbon nanotubes, in terms of a quantum contribution to the hydrodynamic friction. We find that water friction is not anomalously low on graphene: it is rather anomalously high on graphite. This anomaly is shown to have a quantum origin, in the coupling of a water collective mode to a peculiar terahertz plasmon specific to graphite.

A similar fluctuation-induced contribution to friction has been predicted for two solids separated by a vacuum gap [158], yet in the case of solids such contributions are measurable only in a non-contact configuration [190]. In contrast, thanks to the amorphous nature of water, we find that quantum friction may be the dominant contribution for water friction on atomically smooth surfaces, provided that these have electronic excitations at low energy ($\omega \lesssim 100$ meV) and high momenta ($q \sim 0.5$ Å^{-1}), which may couple to the Debye mode of water. We expect a similar quantum contribution to exist in the friction of polar organic solvents [191,192] or room-temperature ionic liquids [193] since they also exhibit a Debye mode.

We stress that quantum friction is altogether beyond the reach of standard *ab initio* MD simulations [137,146], since it is an effect of electronic excitations beyond the Born-Oppenheimer (BO) approximation. At the water-carbon interface, the breakdown of the

BO approximation is particularly strong: this is in line with the recent observation of non-BO effects on the graphene optical phonon frequencies [194]. While *ab initio* MD provides precious information on the static properties of solid-liquid interfaces, our results indicate that studying the dynamics of these interfaces requires novel simulation methods. Furthermore, the strong self-energy corrections that we find for graphene interacting with water collective modes suggest that water-graphene systems should be treated beyond the single water molecule and at the GW level.

The quantum friction phenomenon may be viewed as an extension of the idea of interaction confinement to the solid-liquid interface. Indeed, in Part II of this thesis, we explored the physics of strongly confined electrolytes whose interactions were sensitive to the microscopic nature of the channel walls, and in particular to their dielectric screening properties. Here, we find that the many-body dynamics of interfacial water are also sensitive to the nature of the confining wall, but through much more subtle time-dependent response properties. As such, interaction confinement may actually affect fluid transport in fairly large channels (~ 30 nm radius), as soon as the flow rate depends strongly on wall slippage.

Ultimately, our findings present a new avenue for controlling nanoscale water flows with the vastly tuneable electronic properties of carbon-based confining walls. A particularly promising material in this respect is twisted bilayer graphene, which was recently predicted to exhibit a nearly dispersionless plasmon mode at terahertz frequencies [195] for twist angles $\lesssim 2°$.

5.9 The big picture

In this Chapter, we have developed a new theoretical description of the solid-liquid interface, that takes into account the electronic degrees of freedom of the solid at a quantum level. Our theory predicts a quantum contribution to the hydrodynamic friction coefficient, which is due to the coupling of water charge fluctuations to electronic excitations in the solid. This quantum contribution is significant when the solid has excitations at low energy ($\omega \lesssim 100$ meV) and high momenta ($q \sim 0.5$ Å^{-1}), so that they may interact with the water Debye mode. While quantum friction is very small for water on graphene, it is likely to be the dominant friction mechanism for water on graphite, because water fluctuations efficiently couple to the electron movement in between the graphene layers. This striking difference suggests an explanation for the radius-dependent water slippage in multiwall carbon nanotubes, in terms of their interlayer electronic excitations. Our results shed some light on the long-standing mystery of water-carbon friction, and reveal a non-trivial quantum effect in nanoscale fluid dynamics.

Part IV

Experimental investigations of nanoscale fluid transport

Chapter 6

Direct measurement of water slippage in two-dimensional nanochannels

Contents

Water and carbon form a bizarre couple [8]: in numerous instances, carbon-based pores outperform alternative materials in terms of water permeability or other transport characteristics [19–25]. The origins of this superior performance are so far not understood [26], and are the subject of ongoing theoretical efforts: for instance, in Chapter 5, we proposed that quantum friction at the water-carbon interface might be an essential ingredient of the peculiar phenomenology. In this context, there is a crucial need for experimental measurements of slippage at the water-carbon interface. While numerous permeability measurements have been carried out with carbon-based membranes [19,20,22], there are only very few studies that met the considerable challenge of carrying out such measurements in a controlled nanochannel geometry, which is best suited for benchmarking theoretical predictions [23,196]. Here, we present the first direct measurements of water slippage in two-dimensional nanochannels [15], using a specific fluorescence-based technique and an in-house confocal microscopy setup. This work is still ongoing at the time of writing of this Chapter. We will report preliminary results for channels of height $h = 15$ nm and $h = 10$ nm, which suggest that our measurement technique should have enough sensitivity to probe nanochannels down to the molecular scale.

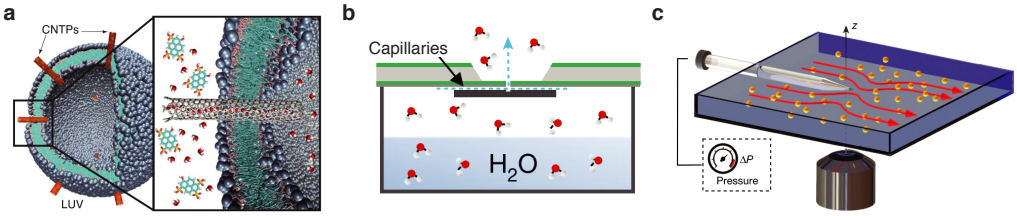

Figure 6.1

Flow measurement techniques in nanofluidics. **a.** Cartoon of a lipid vesicle with embedded carbon nanotubes porins (CNTPs). The flow rate is measured by monitoring the osmotically induced swelling of vesicles through light scattering. Reproduced from [24]. **b.** Schematic of the weight loss measurement setup employed in [15]. **c.** Schematic representation of the flow rate measurement through a nanotube, using a Landau-Squire jet. Reproduced from [23].

I am grateful to V. Kalangi, who fabricated the nanofluidic devices and carried out the fluorescence measurements, for his collaboration on this project. My contribution amounts to developing the confocal microscopy setup and performing the data analysis.

6.1 General context

The flow rate of water through a slit-like channel of length $d = 10$ μm, width $L = 200$ nm and height $h = 10$ nm, under a pressure drop $\Delta P = 1$ bar, is $Q = 10^{-16}$ L$\cdot$s^{-1}, assuming a no-slip boundary condition at the channel walls (see Chapter 1). The measurement of such tiny flow rates is inaccessible to conventional flow sensors, and several specific methods have been developed to overcome this challenge.

An obvious solution is to measure the flow through multiple channels at once. This requires, however, the ability to isolate a large number of identical channels and control for leakage. Such constraints are easiest to satisfy in the case of biological channels: channels with a given amino acid sequence may be expressed and purified, and they insert into phospholipid membranes spontaneously and without leaks. The osmotic-flow-induced swelling of reconstituted lipid vesicles embedded with channels has been used to measure the permeability of, for instance, aquaporin [197]. The same method was recently applied to the permeability of tiny carbon nanotubes (0.8 nm in diameter), that also spontaneously insert into lipid membranes [24] (figure 6.1a). Alternatively, the flow rate could be inferred by measuring the ion concentration profile in the vicinity of a membrane embedded with ion channels using microelectrodes [198, 199].

For a single single tube-like channel, the only technique with enough sensitivity for nanoscale channel dimensions was proposed by Secchi *et al.* [23]. It relies on the properties of the flow induced by the jet that emerges from a nanotube into a macroscopic reservoir [196], the so called Landau-Squire flow (figure 6.1c). At low Reynolds number, the Stokes equation in the reservoir enforces diffusion of the fluid momentum. Therefore, the fluid velocity scales as the rate of momentum transfer from the tube to the reservoir, $F \sim \eta R \bar{v}$, and not as the rate of mass transfer $Q_m \sim \rho R^2 \bar{v}$. Thus, as opposed to the tube flow rate which scales as the tube radius squared, the flow velocity in the reservoir scales linearly with the tube radius. Moreover, the diffusive behaviour imposes a $1/r$

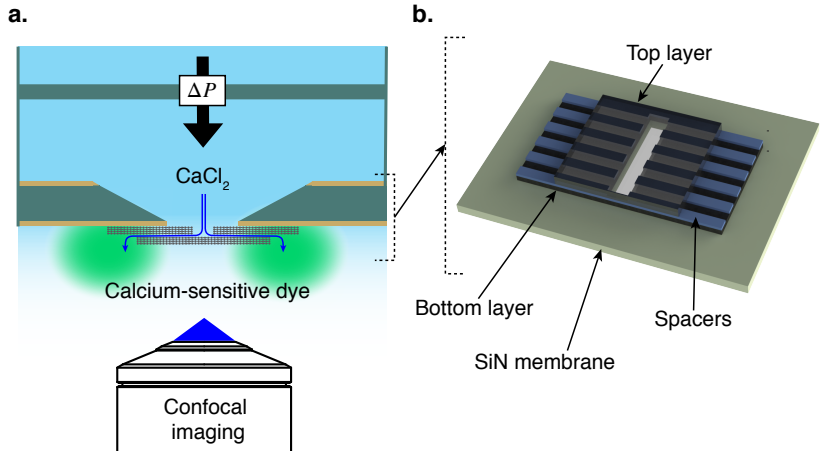

Figure 6.2

Setup for water flow measurement in two-dimensional nanochannels. **a.** Schematic of flow detection by fluorescence imaging of a calcium-sensitive dye. **b.** Schematic of the nanofluidic device under study (courtesy of T. Emmerich).

decay of the flow profile away from the tube, which allows for a measurable flow over tens of micrometers. By analysing the flow profile, Secchi *et al.* could detect flow rates down to 10^{-14} L $\cdot$ s^{-1}. An application of the Landau-Squire technique for measuring electro-osmotic flow was first proposed in ref. [200], where the flow-induced rotation of a particle held in an optical trap was monitored in order to obtain electro-osmotic flow rates down to a few pL $\cdot$ s^{-1}.

The geometry of the recently developed slit-like channels is unsuitable for Landau-Squire measurements, and existing measurements of their hydrodynamic permeability rely on a weight loss technique [15]. The channels are set up to provide the only pathway out of a water reservoir, which is placed on a balance (figure 6.1b). Capillary condensation ensures that water is liquid inside the channels, therefore the evaporation rate, as given by the weight loss, is a measure of the liquid water flow rate through the channels. Radha *et al.* [15] monitored the weight loss for several days in order to obtain flow rates down to 10^{-12} L $\cdot$ s^{-1}. However, with such evaporation measurements, the driving force is not exactly known, as it is a combination of capillary pressure and disjoining pressure [9], so that the measured flow rates could not be directly related to confined fluid properties such as slip length.

In this Chapter, we present a direct measurement of the water flow through two-dimensional nanochannels under an imposed pressure drop in-between two reservoirs, which relies on a fluorescence-based technique for flow detection, and develop a theoretical model to extract the water slip length from the fluorescence data.

6.2 Experimental setup

6.2.1 Device fabrication

The nanofluidic devices (figure 6.2b) were fabricated by van der Waals assembly, following the method described in [15]. The devices are composed of two graphite flakes (the "top layer" and the "bottom layer"), separated by graphene "spacers" of chosen thickness, obtained by patterning a graphite flake through electron beam lithography and oxygen plasma etching. The graphite structure is deposited on a silicon nitride (SiN) membrane. An aperture is etched in the SiN membrane and in the bottom graphite layer, so that water may flow between the two sides of the membrane only through the graphite channels.

6.2.2 Flow measurement

The advection of fluorescent molecules by fluid flow has been widely used as a mean of optically detecting fluid transport [201, 202]. However, such methods are not directly applicable to nanoscale fluid transport measurements, since the molecular size of a fluorescent dye may be on the scale of the channel opening. To circumvent this issue, we use fluorescence to detect *ion transport*, instead of dye transport, through the nanochannel. As shown in figure 6.2a, a calcium chloride solution is placed in the top reservoir, while the bottom reservoir contains a solution of a specific dye, whose fluorescence is enhanced (about 100-fold) in the presence of calcium (Fluo-4FF). The pressure-driven flow through the nanochannel results in a fluorescence increase due to the calcium influx to the bottom reservoir. The signal from the calcium-bound dye near the channel mouth is separated from the background thanks to optical sectioning by a confocal microscope.

6.2.3 Optical setup

Fluorescence imaging is done using a confocal microscope that I developed during my PhD (figure 6.3). The microscope is built around an Olympus IX-83 body. Fluorescence is excited using a blue laser (Coherent Obis, 488 nm, 60 mW). The beam is expanded up to ~ 5 mm diameter, and projected onto a pair of scanning mirrors (Thorlabs GVS-202). The scanning mirrors are then imaged onto the back focal plane of the objective (Olympus LUMPlanFI, NA = 0.9, 60x, water immersion) by a scan lens / tube lens system (Thorlabs SL50-CLS2 and TTL200-CLS2). The fluorescence from the sample back along the excitation path up to the scanning mirrors, at which point it is separated from the excitation using a dichroic mirror (Semrock Di03-R488-t3), and an emission filter. The fluorescence is then focused onto a 50 μm pinhole for optical sectioning, and re-imaged onto the opening of an avalanche photodiode (MPD, PD-100-CTE). The photon-counter output of the photodiode is connected to a DAQ card (NI PCIe-6363), and the microscope is operated by a custom Labview software.

6.3 Theory

In this section, we develop a theoretical description of the experimental configuration, in order to extract the water flow rate in the nanochannels from the measured fluorescence profiles. We first examine the hydrodynamic flow that is induced in the reservoirs,

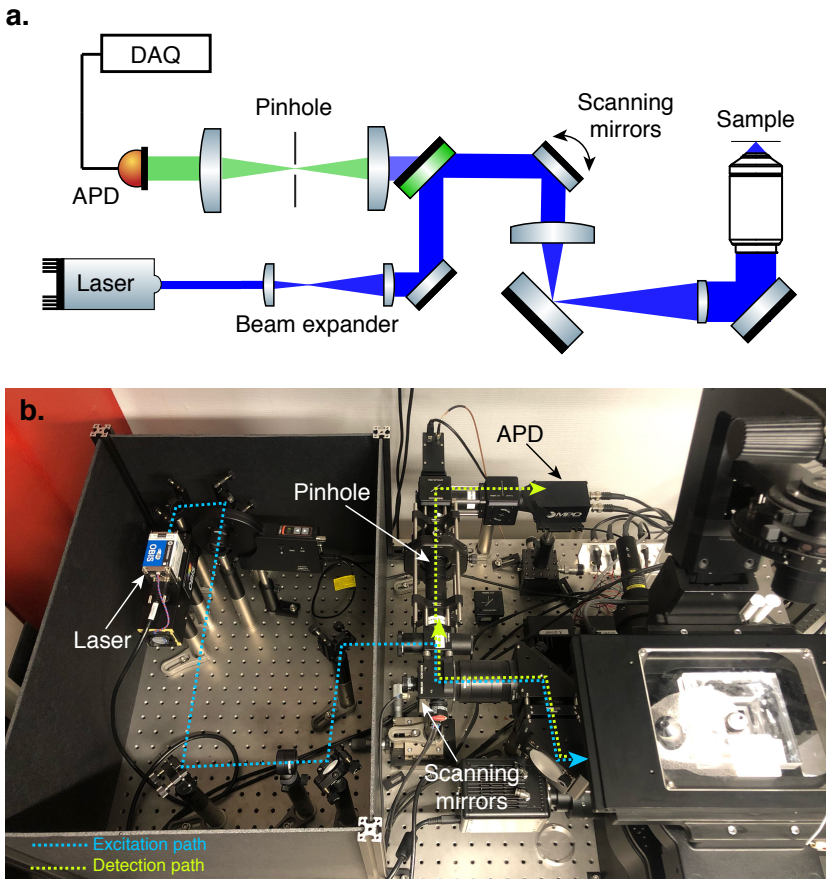

Figure 6.3

Confocal microscopy setup. Simplified schematic of the optical path (**a.**), and photograph of the setup (**b.**).

and then focus on the full reaction-diffusion problem corresponding to the fluorescence measurement.

6.3.1 Flow through a one-dimensional aperture

Consider the flow emerging from an infinitely thin slit into a semi-infinite reservoir (see figure 6.4). It has been shown by Jeffery and Hamel [203–205] that the full non-linear Navier-Stokes equation has a purely radial solution in this geometry. Since we are interested in the limit of very low Reynolds number, here we reproduce their solution discarding the non-linear terms.

For a radial velocity field $\mathbf{u} = u(r, \theta)\, \mathbf{e}_r$, the continuity equation imposes $\partial(ru)/\partial r = 0$ and therefore $u = F(\theta)/r$. The Stokes equation reads

$$\eta \nabla^2 \mathbf{u} - \nabla p = 0. \tag{6.1}$$

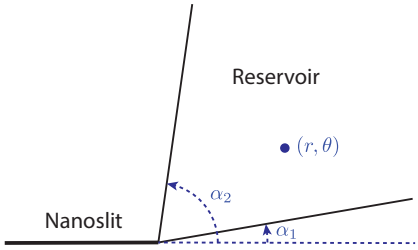

Figure 6.4

The geometry under consideration.

Its two components are

$$\frac{\partial p}{\partial r} = \eta \frac{F''(\theta)}{r^3} \tag{6.2}$$

and

$$\frac{\partial p}{\partial \theta} = \frac{2\eta F'(\theta)}{r^2}. \tag{6.3}$$

Integrating (6.3) with respect to θ, we obtain

$$p = \frac{2\eta F(\theta)}{r^2} + S(r), \tag{6.4}$$

with $S(r)$ an arbitrary function of r. Substituting into (6.2),

$$-\frac{4\eta F(\theta)}{r^3} + S'(r) = \eta \frac{F''(\theta)}{r^3}. \tag{6.5}$$

Multiplying by r^3, on notices that $r^3 S'(r)$ must be a constant, which we denote ηC. Therefore, F satisfies the ordinary differential equation

$$F'' + 4F = C, \tag{6.6}$$

with the no-slip boundary conditions imposing $F(\alpha_{1,2}) = 0$. One must also impose the total flow rate per unit length. If the fluid velocity in the slit is v and its height is h, then one has

$$\int_{\alpha_1}^{\alpha_2} F(\theta)\, \mathrm{d}\theta = vh. \tag{6.7}$$

In the following we specialise to the case $\alpha_1 = 0$ and $\alpha_2 = \pi/2$. Then, the velocity field satisfying the boundary conditions is

$$\mathbf{u} = vh \frac{\sin(2\theta)}{r}\, \mathbf{e}_r. \tag{6.8}$$

If $\alpha_1 = -\pi/2$ and $\alpha_2 = \pi/2$, the solution is

$$\mathbf{u} = \frac{vh}{\pi} \frac{1 + \cos(2\theta)}{r}\, \mathbf{e}_r. \tag{6.9}$$

One remark needs to be made concerning these particularly simple solutions. With the assumption of an infinitely thin slit, we have been able to specify the total flow rate, but not the momentum transferred to the reservoir. In fact, the momentum transfer has been imposed by the requirement that the flow is purely radial. Such an approximation should

be best for small apertures $\alpha_2 - \alpha_1$, and it breaks down for very large apertures (typically $\alpha_2 - \alpha_1 \sim 2\pi$, the Landau-Squire configuration), where one must relax the assumption of purely radial flow. In our experimental configuration, $\alpha_2 - \alpha_1 \approx \pi$, so that the radial assumption may be around its limit of validity, but the details of the flow profile will not be important in the reaction-diffusion problem, which we solve in the limit of low Peclet number.

6.3.2 Reaction-diffusion problem

Governing equations

We now consider the experimental geometry with a channel of length d connecting two reservoirs. Since the top and bottom layers are thin on the scale of the imaging (< 1 μm), we will assume $\alpha_2 - \alpha_1 = \pi$ in the reservoirs. This will introduce some error on the concentrations very close to the channel mouth, but we will find in the end that such fine details of the geometry are unimportant.

We have just determined the flow field $\mathbf{u}$ in the reservoirs, while inside the channel it is given by the Poiseuille law. This flow advects calcium ions Ca that react with the dye F to form the fluorescent complex CaF whose concentration profile we wish to determine. The reaction is

$$\mathrm{Ca} + \mathrm{F} \leftrightharpoons \mathrm{CaF}. \tag{6.10}$$

We denote k_+ and k_- the forward and backward rate constants, respectively. In principle, we need to solve three coupled advection-diffusion-reaction equations for the three chemical species:

$$-D_{\mathrm{Ca}}\nabla^2[\mathrm{Ca}] + \nabla(\mathbf{u}\cdot[\mathrm{Ca}]) = -k_+[\mathrm{Ca}][\mathrm{F}] + k_-[\mathrm{CaF}] \tag{6.11}$$

$$-D_{\mathrm{CaF}}\nabla^2[\mathrm{CaF}] + \nabla(\mathbf{u}\cdot[\mathrm{CaF}]) = k_+[\mathrm{Ca}][\mathrm{F}] - k_-[\mathrm{CaF}] \tag{6.12}$$

$$-D_{\mathrm{F}}\nabla^2[\mathrm{F}] + \nabla(\mathbf{u}\cdot[\mathrm{F}]) = -k_+[\mathrm{Ca}][\mathrm{F}] + k_-[\mathrm{CaF}] \tag{6.13}$$

Pure diffusion case

We first solve the problem in the absence of flow: we set $\mathbf{u} = 0$ in the governing equations. We introduce two reduced concentration variables:

$$c = \frac{D_{\mathrm{Ca}}[\mathrm{Ca}] + D_{\mathrm{CaF}}[\mathrm{CaF}]}{D_{\mathrm{Ca}}} \quad \text{and} \quad f = \frac{D_{\mathrm{F}}[\mathrm{F}] + D_{\mathrm{CaF}}[\mathrm{CaF}]}{D_{\mathrm{F}}}. \tag{6.14}$$

They satisfy diffusion equations: $\nabla^2 c = 0$ and $\nabla^2 f = 0$. We will solve these separately in the two reservoirs and in the channel, and then stitch the solutions together. We focus on the equation for c, the one for f being completely analogous. We denote J the total flux of c that is constant across the system, and $\bar{J} = J/D_{\mathrm{Ca}}$.

Solution in the reservoirs Expanding the Laplace operator, the diffusion equation reads

$$\left[\frac{\partial^2}{\partial r^2} + \frac{1}{r}\frac{\partial}{\partial r} + \frac{1}{r^2}\frac{\partial^2}{\partial \theta^2} + \frac{\partial^2}{\partial z^2}\right] c = 0 \tag{6.15}$$

We have introduced explicitly the dimension z along the width of the channels. The reason is that we need to take into account the finite width L of the channels: if it is

assumed infinite, the 2D diffusion equation yields a diverging logarithmic solution. We impose no flux through the boundaries, that is $\partial_\theta c|_{\theta=\alpha_1,\alpha_2} = 0$. This can be satisfied by taking c independent of θ. Then, we may solve the Laplace equation through a Fourier transform. We introduce

$$\tilde{c}(r,k) = \int_{-\infty}^{+\infty} \mathrm{d}z\, c(r,z) e^{-ikz}, \tag{6.16}$$

which satisfies

$$\frac{\partial^2 \tilde{c}}{\partial r^2} + \frac{1}{r}\frac{\partial \tilde{c}}{\partial r} - k^2 \tilde{c} = 0. \tag{6.17}$$

This is a modified Bessel equation, whose well-behaved (at $r \to \infty$) solution is the modified Bessel function of the second kind K_0. Precisely, we obtain

$$c(r,z) = \text{const} + \int_{-\infty}^{+\infty} \mathrm{d}k\, e^{ikz} A(k) K_0(|k|r), \tag{6.18}$$

with $A(k)$ an arbitrary function of k, determined by the boundary conditions. In the bottom reservoir $c(\mathbf{r} \to \infty) = 0$, therefore const $= 0$. We also need to impose that as $r \to 0$ the positive flux J comes out of an aperture of length L.

$$\lim_{r\to 0}[-r\partial_r c(r,z)] = \frac{\bar{J}}{\alpha L}\theta(|z| - L/2), \tag{6.19}$$

with $\alpha = \alpha_2 - \alpha_1$. Using that $K_0'(x) = -K_1(x)$ and $K_1(x) \sim 1/x$ at small x, we find

$$\lim_{r\to 0}[-r\partial_r c(r,z)] = \int \mathrm{d}k A(k) e^{ikz}, \tag{6.20}$$

so that

$$A(k) = \frac{\bar{J}}{2\pi\alpha L}\int_{-\infty}^{+\infty} \mathrm{d}z\, \theta(|z| - L/2) e^{-ikz} = \frac{\bar{J}}{\pi\alpha L}\frac{\sin(kL/2)}{k}. \tag{6.21}$$

Finally, the solution for $c(r,z)$ reads

$$c(r,z) = \frac{\bar{J}}{\pi\alpha L}\int_{-\infty}^{+\infty} \frac{\mathrm{d}k}{k} e^{ikz} \sin(kL/2) K_0(|k|r). \tag{6.22}$$

At $z = 0$, the Fourier transform may be computed analytically:

$$c(r,0) = \frac{\bar{J}}{\alpha L}\,\mathrm{Arcsinh}\left(\frac{L}{2r}\right). \tag{6.23}$$

The behaviour of the solution may be readily analysed recalling that $\mathrm{Arcsinh}(x) = \log(x + \sqrt{x^2+1})$. At small r, the solution behaves as $\log r$, as expected in a 2D geometry. At increasing r, the solution transitions to a 3D behaviour, and ends up scaling as $1/r$:

$$c(r \to \infty, 0) \sim \frac{\bar{J}}{2\alpha r}. \tag{6.24}$$

This limiting behaviour is consistent with flux conservation, as it corresponds to a flux J through a portion of sphere of angle α.

Similarly, we may determine in the top reservoir

$$c(r,0) = [\mathrm{Ca}]_0 - \frac{\bar{J}}{\alpha L}\,\mathrm{Arcsinh}\left(\frac{L}{2r}\right). \tag{6.25}$$

In the exact same way, we obtain the solutions for f. We call $-J'$ the constant flux of f, and $\bar{J}' \equiv J'/D_F$. Then, in the bottom reservoir

$$f(r,0) = [\mathrm{F}]_0 - \frac{\bar{J}'}{\alpha L}\,\mathrm{Arcsinh}\left(\frac{L}{2r}\right), \tag{6.26}$$

and in the top reservoir

$$f(r,0) = \frac{\bar{J}'}{\alpha L}\,\mathrm{Arcsinh}\left(\frac{L}{2r}\right). \tag{6.27}$$

Solution in the channel In the channel, we neglect any edge effects and simply consider 1D diffusion. Then the concentration profiles are linear:

$$c(x) = c(0) - \tfrac{\bar{J}}{\lambda L h}x \quad \text{and} \quad f(x) = f(d) + \tfrac{\bar{J}'}{\lambda L h}(x-d). \tag{6.28}$$

The factor λ accounts for the fact that there are spacers between the channels, and the actual width available to the flow is therefore less than L. It may also account for some channels being closed. Let w be the width of an individual channel, s the width of a spacer, N the number of open channels and μ the fraction of open channels. Then

$$\lambda = \frac{\mu N w}{N(w+s)}. \tag{6.29}$$

We may now determine the unknown fluxes J and J' by stitching the solutions at the channel boundaries. We assume that we need to match $c(0)$ in the channel and $c(r=h,0)$ in the top reservoir. The choice $r=h$ is arbitrary up to a constant of order 1, whose choice does not alter the final result. Similarly, we impose $c(d)$ to match $c(r=h,0)$ in the bottom reservoir. This yields a self-consistent equation for $\bar{J}$:

$$[\mathrm{Ca}]_0 - \frac{\bar{J}}{\alpha L}\,\mathrm{Arcsinh}\left(\frac{L}{2h}\right) - \frac{\bar{J}}{\lambda L h}d = \frac{\bar{J}}{\alpha L}\,\mathrm{Arcsinh}\left(\frac{L}{2h}\right). \tag{6.30}$$

Since $h \ll L$, we may simplify $\mathrm{Arcsinh}(L/2h) \approx \log(L/h)$, and we set $\alpha = \pi$. We obtain

$$\bar{J} = L\,\frac{\lambda(h/d)[\mathrm{Ca}]_0}{1 + \dfrac{2}{\pi}\dfrac{\lambda h}{d}\log(L/h)}. \tag{6.31}$$

With the experimental parameters, $(2h/\pi d)\log(L/h) = 4\times10^{-3}$ and it may be safely neglected in the denominator. We may then use the simple result

$$\bar{J} = \frac{\lambda L h}{d}[\mathrm{Ca}]_0. \tag{6.32}$$

Extension to non-zero flow

In the presence of flow, the advection terms are no longer zero, and the reduced variables c and f in principle no longer satisfy simple diffusion equations. Nevertheless, in the reservoirs, one may check that the advection terms are in fact negligible. Upon normalising by the relevant diffusion coefficient, in the reservoir, the advection-diffusion operator becomes

$$\frac{\partial^2}{\partial r^2} + \left[(1 - \frac{\mathrm{Pe}}{\pi}(1 + \cos(2\theta))\right] \frac{1}{r}\frac{\partial}{\partial r} + \frac{1}{r^2}\frac{\partial^2}{\partial \theta^2} + \frac{\partial^2}{\partial z^2}, \tag{6.33}$$

with $\mathrm{Pe} = \frac{vh}{D}$ a Peclet number: we have made use of the flow field obtained in section 6.3.1. One expects a velocity v of at most 1 $\mathrm{mm \cdot s^{-1}}$, and for $D \sim 10^{-10}$ $\mathrm{m^2 \cdot s^{-1}}$ and $h = 10$ nm this amounts to $\mathrm{Pe} \sim 10^{-1}$. Therefore, to a good approximation, one may neglect the advection terms in the reservoirs.

On the other hand, in the channel, one has to fully take advection into account. But even in a 1D geometry, the three coupled non-linear differential equations can only be solved numerically. We may nevertheless proceed analytically under the assumption that the chemical reaction can be neglected inside the channel. This is expected to be reasonable, since in the pure diffusion case, the dye concentration becomes negligible beyond 1 μm inside the channel. This is on the scale of the geometrical details such as the thickness of the graphite layers and the exact shape of the channel mouth, which we find to drop out at the end of the computation. The assumption will still be checked numerically in the final version of this work.

If there is no chemical reaction in the channel we may write the advection-diffusion equation for the calcium ions:

$$-D_{\mathrm{Ca}}\frac{\mathrm{d[Ca]}}{\mathrm{d}x} + v[\mathrm{Ca}] = \frac{J}{\lambda L h}. \tag{6.34}$$

We introduce the Peclet number $\mathrm{Pe} = vh/D_{\mathrm{Ca}}$, so that

$$\frac{\mathrm{d[Ca]}}{\mathrm{d}x} - \frac{\mathrm{Pe}}{h}[\mathrm{Ca}] = -\frac{\bar{J}}{\lambda h L}. \tag{6.35}$$

This is solved by

$$[\mathrm{Ca}](x) = \frac{\bar{J}}{\lambda \mathrm{Pe} L}\left(1 - e^{\mathrm{Pe}\, x/h}\right) + c(0)e^{\mathrm{Pe}\, x/h}. \tag{6.36}$$

We may now apply the same stitching procedure as in the pure diffusion case to determine J. We obtain

$$\bar{J} = \frac{L[\mathrm{Ca}]_0}{(1/\pi)\log(L/h)(1 + e^{-\mathrm{Pe}\, d/h}) - \frac{1}{\lambda \mathrm{Pe}}(e^{-\mathrm{Pe}\, d/h} - 1)}. \tag{6.37}$$

This may be simplified to linear order in the Peclet number:

$$\bar{J} = \frac{\lambda h L}{d}[\mathrm{Ca}]_0\left(1 + \frac{d}{2h}\mathrm{Pe}\right). \tag{6.38}$$

Far away from the channels, all the calcium has been bound to the dye and

$$[\mathrm{CaF}] \approx \frac{D_{\mathrm{CaF}}}{D_{\mathrm{Ca}}}\frac{\bar{J}}{2\pi r}. \tag{6.39}$$

By fitting this long distance behaviour, one can determine $\bar{J}$. Then,

$$\frac{\bar{J}(\mathrm{Pe})}{\bar{J}(\mathrm{Pe}=0)} = 1 + \frac{d}{2h}\mathrm{Pe}. \tag{6.40}$$

We may explicit the Peclet number as a function of the pressure drop ΔP and slip length b:

$$\mathrm{Pe} = \frac{\Delta P h^3}{12\eta d D_{\mathrm{Ca}}}\left(1 + \frac{6b}{h}\right). \tag{6.41}$$

Then, the relevant result for analysing the experimental data is

$$\frac{\bar{J}(\mathrm{Pe})}{\bar{J}(\mathrm{Pe}=0)} = 1 + \frac{\Delta P h^2}{24\eta D_{\mathrm{Ca}}}\left(1 + \frac{6b}{h}\right). \tag{6.42}$$

Remarkably, we find that the long-distance scaling of the fluorescence intensity depends on very few parameters, and is insensitive to the geometric details of the channels, and even to the number of channels. Therefore, we expect eq. (6.42) to provide a robust method for extracting the hydrodynamic slip length from fluorescence data.

6.4 Preliminary results

Fluorescence flow measurements have so far been carried out with two nanofluidic devices. Device 1 had $N = 80$ channels of height $h = 15$ nm and length $d = 10$ μm, while Device 2 had $N = 30$ channels of height $h = 10$ nm and length $d = 10$ μm. Figure 6.5a shows fluorescence images of Device 2 at increasing values of pressure drop imposed across the membrane: a corresponding increase in fluorescence intensity is clearly visible.

The main prediction of the model established in section 6.3 is a $1/r$ scaling of the fluorescence intensity at large distance r away from the channels (eq. (6.39)), which can be directly related to the Peclet number, and therefore to the slip length of water inside the channels (eq. (6.42)).

For comparison with the model, the measured fluorescence intensity was radially averaged (over half a circle) on each side of the device. Typical radially-averaged fluorescence profiles, plotted as a function of the inverse distance $1/r$, are shown in figure 6.5b: a linear behaviour is indeed observed, consistently with the model predictions. Fitting of this linear regime allowed us to extract the flux $\bar{J}$ (eq. (6.39)), for increasing values of the pressure drop ΔP. As shown in figure 6.5c, for both devices, $\bar{J}$ shows roughly linear behaviour as a function of ΔP, in line with the prediction of eq. (6.42). According to our theory, the slope of $\bar{J}(\Delta P)/\bar{J}(\Delta P = 0)$ versus ΔP gives access to the slip length of water inside the channels, see dashed lines in figure 6.5c. While for both devices the observed increase of $\bar{J}$ with ΔP is faster than what would be expected in the absence of slippage, the data can be described by introducing only a very small slip length $b \sim 1 - 4$ nm.

6.5 Discussion

The water slip length on graphite extracted from our preliminary measurements is broadly consistent with the previously reported value $b \approx 6 - 10$ nm, measured by surface force

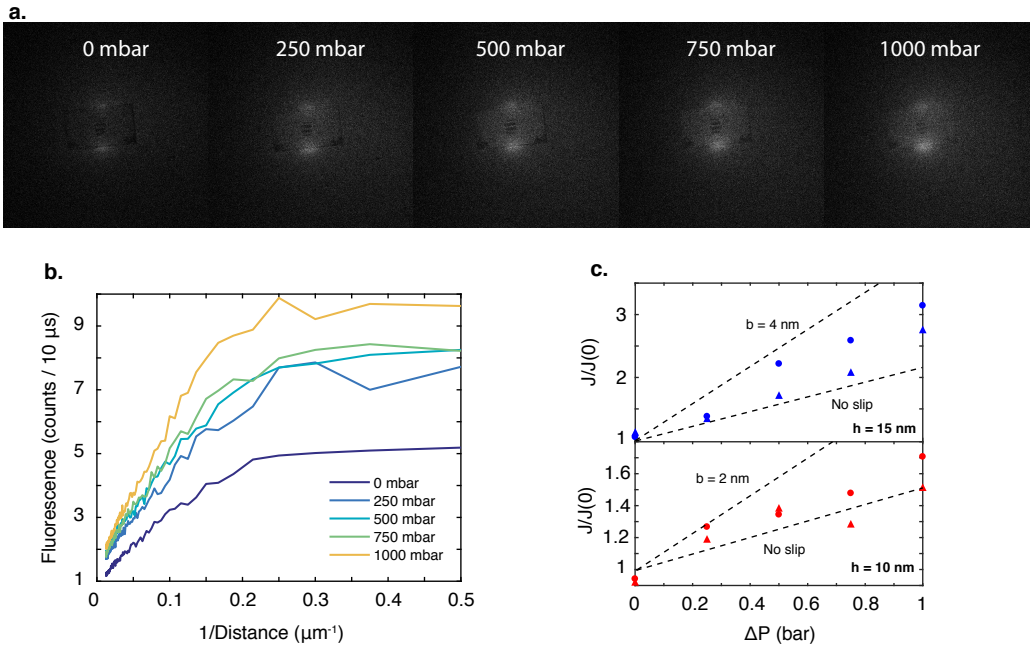

Figure 6.5

Preliminary results of water flow measurements across two-dimensional graphite channels. **a.** Confocal fluorescence images of Device 2 ($h = 10$ nm) under increasing pressure drops. The calcium concentration in the top reservoir is $[\mathrm{Ca}]_0 = 15$ mM and the dye concentration in the bottom reservoir in $[\mathrm{F}]_0 = 100$ μm. **b.** Radially-averaged fluorescence profiles corresponding to the images in **a** (top channels). **c.** Normalised flux $\bar{J}$ (see eq. (6.39)) obtained by fitting the long-distance behaviour of the fluorescence, for both devices. The dashed lines correspond to the prediction of eq. (6.42). For device 1, the top reservoir calcium concentration was $[\mathrm{Ca}]_0 = 10$ mM. The two symbols (triangle and circle) correspond to the two sides of the devices.

apparatus [48]. However, our measurements still require careful benchmarking – notably with boron nitride instead of graphite channels – and the contribution of diffusio-osmosis to the measured water flux remains to be assessed. Nevertheless, the results presented in figure 6.5 provide a proof of principle that our fluorescence technique should allow for the measurement of flow rates in two-dimensional channels down to the molecular scale. Indeed, the radially averaged fluorescence profiles obtained with 10 nm wide channels show a signal to noise ratio of nearly 100, so that we expect the flow through 1 nm wide channels to still be measurable, even under the conservative assumption of the signal scaling as h^2.

While in 10 to 15 nm wide channels water is expected to have essentially bulk-like behaviour, in few-nanometre confinement the onset of water structuring is expected to significantly affect the channel permeability. For instance, in the experiments of Radha *et al.*, the evaporation rate of water through two-dimensional channels was unexpectedly found to display a maximum at around 2 nm channel width [15]. The interpretation of these evaporation experiments is difficult, since the driving force of the flow – a combination of capillary pressure and disjoining pressure – is not exactly known. Hence, the

measurement of water flow rate in nanometre-scale channels under imposed pressure drop will be crucial to shed some light on these peculiar results. Moreover, such measurements will be a much-needed testing ground for our theory of quantum friction, which may be extended to a nanoslit configuration so as to predict the dependence of a graphitic channel's permeability on confinement width.

6.6 The big picture

In this Chapter, we have presented direct optical measurements of water slip length in two-dimensional graphite nanochannels. The measurement technique is based on detecting the pressure-driven flow of calcium ions through the channel thanks to a calcium-sensitive dye, whose fluorescence is imaged by confocal microscopy. A dedicated theoretical model links the shape of the measured fluorescence profiles to the water slip length inside the channels, and preliminary results yield slip lengths $b \sim 1 - 4$ nm for water on graphite. We expect our method to be applicable to nanometre-scale channels, where it would allow us, for instance, to directly test the predictions of the quantum friction theory developed in Chapter 5.

Chapter 7

Ultrafast photomechanical transduction through thermophoretic implosion

a.k.a. the Jedi experiment.

Contents

Since the historical experiments of Crookes, the direct manipulation of matter by light has been both a challenge and a source of scientific debate. In this Chapter, we show that laser illumination allows to displace a vial of nanoparticle solution over centimetre-scale distances. Cantilever-based force measurements show that the movement is due to millisecond long force spikes, which are synchronised with a sound emission. We observe that the nanoparticles undergo negative thermophoresis, while ultrafast imaging reveals that the force spikes are followed by the explosive growth of a bubble in the solution. We propose a mechanism accounting for the propulsion based on a thermophoretic instability of the nanoparticle cloud, analogous to the Jeans instability that occurs in gravitational systems. Our experiments demonstrate a new type of laser propulsion, and a remarkably violent actuation of soft matter, reminiscent of the strategy used by certain plants to propel their spores.

This Chapter is based on the following publication: N. Kavokine, S. Zou, R. Liu, A. Niguès, B. Zou and L. Bocquet. "Ultrafast photomechanical transduction through thermophoretic implosion". *Nat. Commun.* **11**, 50 (2020).[1]

All movies are available at https://www.nature.com/articles/s41467-019-13912-w#Sec13.

7.1 General context

In 1874, William Crookes observed that a light-absorbing vane placed in a vacuum-filled glass bulb would rotate when exposed to sunlight, and interpreted the results as the effect of radiation pressure [206]. Crookes' interpretation was the cause of much debate at the time, and it is five years later that Maxwell proposed the currently accepted explanation: the vane actually rotates due to thermophoresis of the residual gas molecules in the bulb [207]. Since then, a variety of methods for propelling macroscopic objects with light have been proposed [208], involving, if not radiation pressure [209,210], the light-induced ejection of matter, resulting in propulsion through momentum conservation [211–213]. However, the potential of thermophoresis – the driving mechanism in Crookes' experiment – for macroscopic light-induced propulsion has hardly been explored since the nineteenth century. While light-induced self-thermophoresis has been highlighted as a means of controlled optical manipulation of individual colloids [214, 215], light-induced thermal gradients have been overlooked as a means of macroscopic actuation.

We describe in this Chapter a macroscopic system that is propelled over centimetre-scale distances by the sole action of light, yet without any exchange of matter with the surrounding medium; we show that the propulsion mechanism is based on light-induced thermophoresis. The light-induced propulsion effect was serendipitously observed by our collaborators at the Beijing Institute of Technology. The observation was so intriguing that I took the time during my primarily theoretical PhD to develop an experimental setup, so as to characterise the effect and ultimately propose an explanation. This work, although seemingly unrelated to the primary subject of my thesis, does in fact involve a many-body effect in almost-nanoscale fluid dynamics.

7.2 Methods

7.2.1 Nanoparticle synthesis and characterisation

The PbS nanoparticles used in all experiments were synthesised following a typical hot-injection method, involving injection of a sulfur precursor into a lead precursor in an organic solvent. All the syntheses were carried out under air-free conditions using a standard Schlenk-line setup. PbS quantum dots purchased from Merck exhibited the same behaviour as the in-house-synthesised ones. Transmission electron microscopy (TEM, JEOL-2100F) was used to visualise the nanoparticles. Their crystal structure was obtained by the X-ray diffraction (XRD, D8-Advance X-ray diffractometer). The absorption spectra in cyclohexane were recorded using a Shimadzu UV-3600 spectrometer.

[1] The photomechanical effect discussed in this Chapter was originally observed by B. Zou and colleagues at the Beijing Institute of Technology, to whom I am grateful for sharing their intriguing discovery.

7.2.2 Force measurement setup

A schematic of our force measurement setup is given in figure 7.2. A Sheaumann HF-975-7500-25C fibre-coupled laser diode, powered by an Arroyo LaserSource controller, was used for actuating the system. The vial or spectroscopic cuvette were glued to a 3 cm long metal cantilever (made from a metal ruler). A small mirror was glued to the other side of the cantilever. A low power red laser was reflected on the small mirror, and directed onto a quadrant photodiode (Thorlabs, PDQ80A). Laser illumination above the threshold power (see figure 7.4c) resulted in force spikes which induced deflection of the cantilever in the 10 μm range. The deflection of the cantilever could be translated into a force thanks to calibration with a Novatech F329 load cell. The resolution in cantilever deflection was below 100 nm, and the time resolution was given by the photodiode bandwidth (150 kHz). In all experiments, the excitation laser fibre tip was placed at exactly 1 mm from the vial wall using a stepper motor, and 2 mm above the vial bottom. The analog control of the laser power, camera triggers and force and sound measurements were synchronised using a National Instruments DAQ card (NI USB-6363) and a custom Labview software.

7.2.3 Imaging

High speed imaging was performed using a Phantom v642 or a Hamamatsu Orca Flash 4.0 camera, and either a Nikon 50 mm macro lens, or a Thorlabs MVL12X3Z 12X zoom lens, with coaxial illumination from an Olympus U-HGLGPS (130 W) light source. Thermal imaging was performed using a FLIR Q655sc infrared camera.

7.3 Results

7.3.1 The photomechanical effect

Our system consists of a closed vial containing 1 mL of a concentrated solution of lead sulphide (PbS) nanoparticles in cyclohexane. The particles have an average diameter of 8 nm and strong absorption in the near-infrared. We observe that when illuminated with a $\sim$ 1.5 W, 975 nm laser, the vial suddenly "jumps" away from the laser source (figure 7.1a, movie 1), over a few millimetres. The typical velocity of the vial during a jump is about 1 cm $\cdot$ s^{-1}, corresponding to a mechanical work around 30 μJ. After one such jump, the vial falls out of range of the laser, which diverges from a fibre tip. Moving the fibre tip closer to the vial results in another jump, and the process can thus go on, yielding propulsion of the vial over several centimetres. In the experiment shown in figure 7.1, an average speed of 1 mm $\cdot$ s^{-1} was obtained (figures 7.1b and 7.1c, movie 2), which was essentially limited by the rate of laser repositioning.

7.3.2 Macroscopic characterisation

In order to characterise this intriguing phenomenon, we built a force-measurement setup based on a cantilever, whose deflection is monitored using a quadrant photodiode (figure 7.2). The vial was glued on the cantilever and its deflection was recorded as a function of time upon application of the laser light. Then, knowing the cantilever stiffness , we could translate the observed deflection into the horizontal component of the force exerted on the vial-cantilever system. A typical measurement is shown in figure 7.3: the cantilever registers a series of force spikes which starts when the laser is switched on; it ceases as soon as it is switched off. Each force spike is accompanied by the emission of

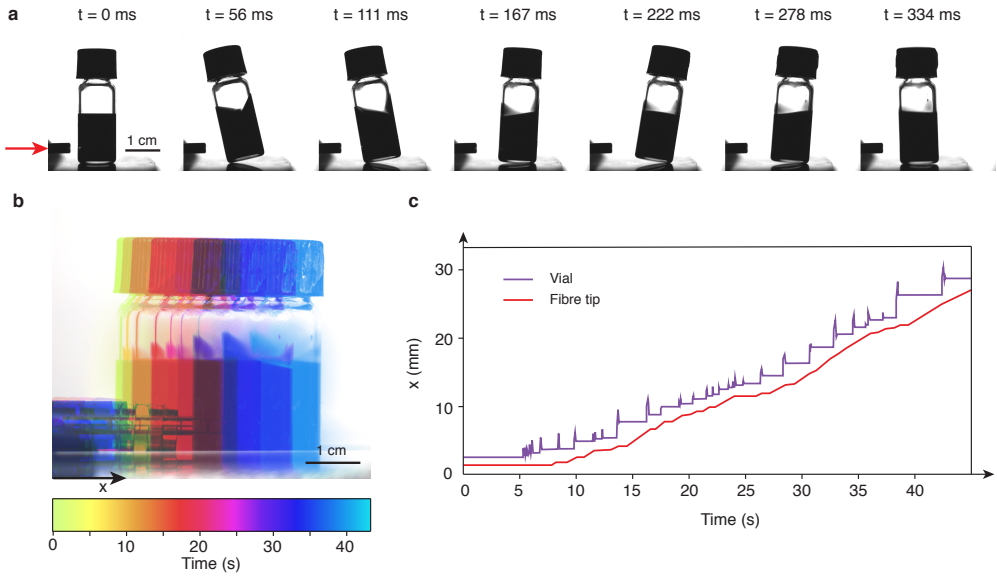

Figure 7.1

A vial filled with a lead sulphide nanoparticle solution is propelled by a near-infrared laser. **a.** Snapshots of the vial motion during one laser-induced jump. The red arrow indicates the propagation direction of the laser. **b.** Temporal colour-code projection of the large scale vial motion obtained when the fiber tip is kept at an approximately constant distance from the vial. The image is a superposition of ten snapshots of the vial motion, with the colour encoding time. **c.** Vial and fibre tip position as a function of time corresponding to the large-scale motion shown in panel b.

audible sound (figure 7.3), and $\sim 97\%$ of the recorded sound spikes match a force spike. A typical force spike lasts around 5 ms and contains several oscillations of the force between positive and negative values (figure 7.3, inset). Note that a positive force is oriented here along the direction of propagation of the laser and the initial increase of the force is always towards positive values. Varying the laser power, one observes that the force spikes are triggered only above a threshold power, as shown in figure 7.4a; above the threshold, the average spike frequency (that is the number of spikes per unit time) increases with increasing power. The threshold laser power depends on particle concentration: the lower the concentration the higher the threshold. For a 2 % in weight particle concentration,

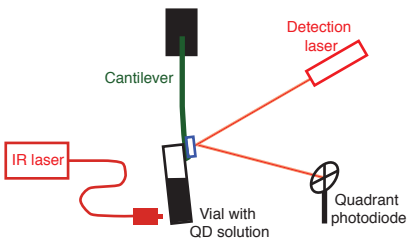

Figure 7.2

Schematic of the force measurement setup. The vial is suspended on a cantilever; a low power laser and a quadrant photodiode are used to monitor the cantilever position as a function of time.

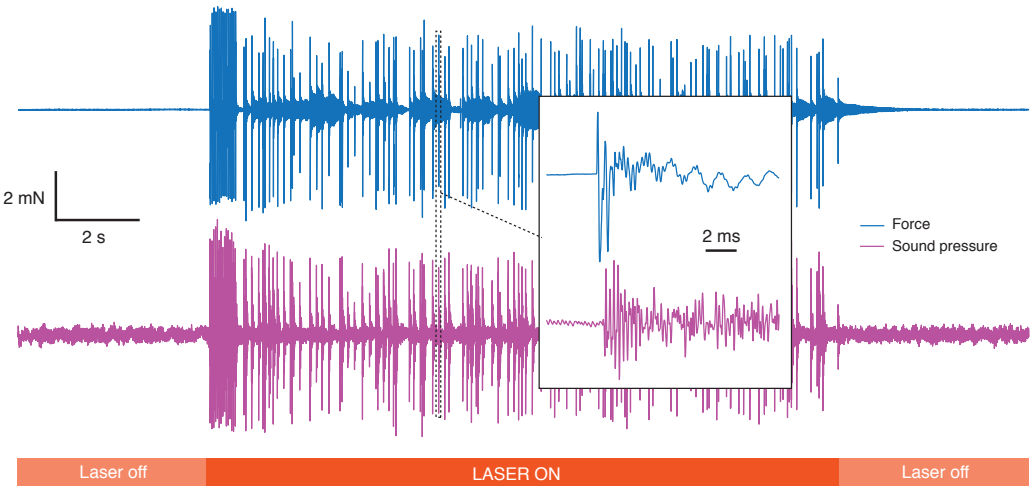

Figure 7.3

Typical force and sound pressure versus time measurement. The particle concentration is 6.4 wt % and the laser power is 1.5 W. Inset: zoom on a single force spike and the corresponding spike in sound pressure.

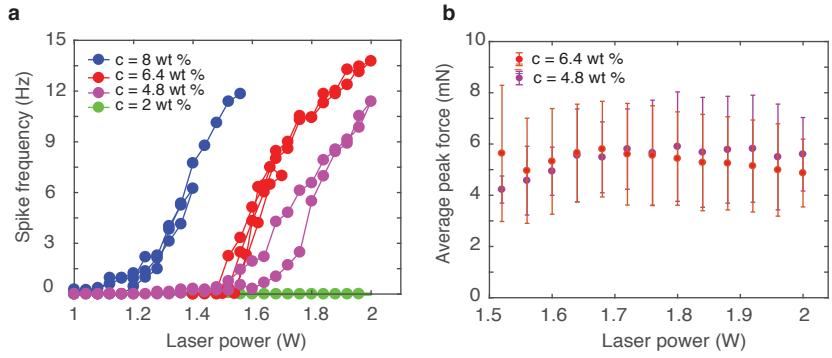

Figure 7.4

a. Frequency of the force spikes as a function of laser power, for different particle concentrations. Spikes are observed above a critical laser power, which increases with decreasing concentration. **b.** Average peak force as a function of laser power, for two different particle concentrations. Error bars represent the standard deviation.

no spikes were observed up to 7 W laser power. The average amplitude of a spike is around 6 mN; remarkably, it does not have any appreciable dependence on laser power or particle concentration (figure 7.4d).

7.3.3 Microscopic mechanism

We investigated the origin of the photomechanical effect in light of the macroscopic characterisation described above. Radiation pressure could clearly be ruled out since it acts continuously and not in spikes; moreover, one can estimate the radiation pressure in our system at a value around 5 nano-Newton, which is orders of magnitude below the forces that are measured, in the several milli-Newton range. Furthermore, the vial is sealed and can hardly be expected to exchange matter with the surrounding medium. Thus, the momentum of the vial and solution it contains must be conserved, and if the vial moves away from the laser, then the fluid inside must acquire momentum towards the laser. In order to understand how the fluid acquires this momentum, we placed the nanoparticle solution in a 1 mm thick spectroscopic cuvette, and synchronised the force measurement with high-speed imaging of the laser-illuminated region. The results are presented in figure 7.5.

As opposed to the large vial, where force spikes could be observed indefinitely (we observed no change in behaviour for up to 30 seconds), in the thin spectroscopic cuvette the spiking ceased after less than a second of illumination (figure 7.5b). After about 10 seconds, imaging of the illuminated region revealed the formation of a solid aggregate (figure 7.5c and movies 3, 4), due to the PbS particles accumulating next to the cuvette wall, somehow "jamming" the spiking mechanism. Therefore, there is a particle-laser interaction that causes the particles to migrate towards the laser. Such migration could be due to the direct interaction of the particles with the laser electric field: the phenomenon in question would be dielectrophoresis [216]. However, one can estimate the dielectrophoretic migration velocity in our system as less than 1 nm per hour, hence the contribution of dielectrophoretic driving is negligible. On the other hand, one could expect the particle migration to be the result of temperature driving, since the particles have strong absorption at the laser wavelength. Indeed, when performing infrared imaging (see movie 5) we observe temperature differences of up to 30 K across the system, and the temperature gradient reaches up to 2 $\mathrm{K}\cdot\mathrm{mm}^{-1}$. We expect such temperature differences to drive particle motion through thermophoresis; here negative thermophoresis since particles move towards higher temperatures. The particle flux $j(\mathbf{r})$ due to thermophoresis is characterised by the Soret coefficient S, defined by:

$$j(\mathbf{r}) = -DS\rho(\mathbf{r})\nabla T(\mathbf{r}), \tag{7.1}$$

where D is the particle diffusion coefficient and $\rho(\mathbf{r})$ is the particle concentration [217,218]. Thermal imaging combined with monitoring of the aggregate size as a function of time allowed us to make a rough estimate of the Soret coefficient of the PbS particles, yielding $S \approx -4\ \mathrm{K}^{-1}$. To our knowledge there have been no reported measurements of the Soret coefficient for PbS particles in cyclohexane. For a more common experimental system, polystyrene particles in water, Soret coefficient values ranging from -1.5 to $+40\ \mathrm{K}^{-1}$ have been reported [217–221], depending on conditions and particle size. Our estimate is therefore not unreasonable with regard to this range, and corresponds to quite strong negative thermophoresis.

Furthermore, high speed imaging of the solution revealed another striking phenomenon. We observed that every force spike is accompanied by the explosive formation of a bubble next to the cuvette wall (figure 7.5a, movie 3). The bubble grows in about 0.5 ms and collapses as rapidly, which could be a signature of either cavitation [222, 223] or explosive boiling [224, 225]; in that case our bubble would be analogous to a plasmonic

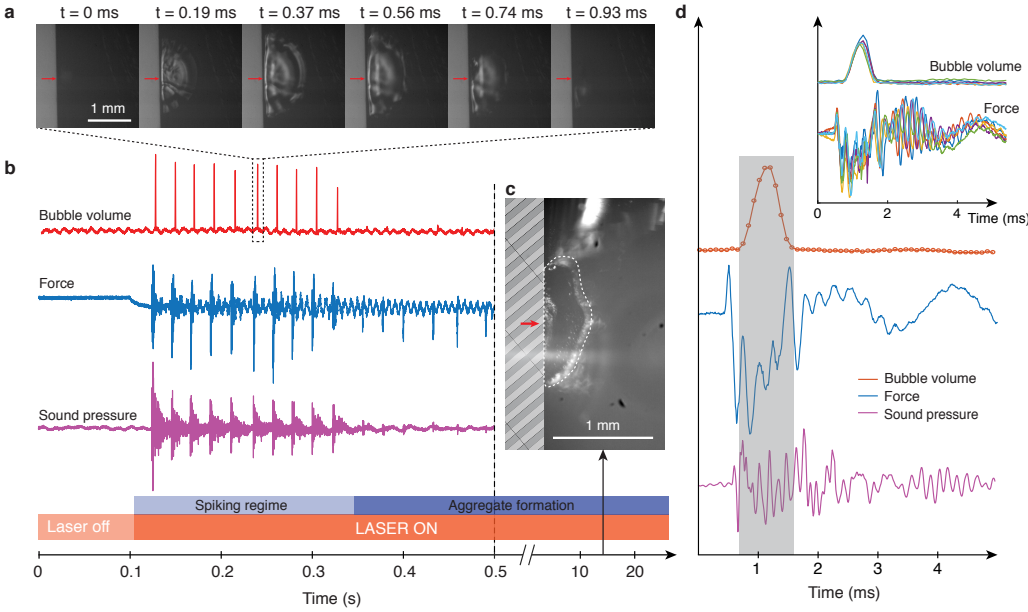

Figure 7.5

Microscopic investigation of the origin of the photomechanical effect. The four panels show results of simultaneous measurement of force and sound pressure, coupled to ultrafast imaging (11 000 fps), in a 1 mm thick spectroscopic cuvette. **a.** High speed photography snapshots of the dynamics of a bubble growing and collapsing upon laser illumination. The red arrow indicates the laser impact point. **b.** Typical recording of force and sound versus time, and of the volume of the bubble in solution as determined by optical imaging. **c.** Image of the particle aggregate that becomes visible after about 10 s illumination. The red arrow shows the impact point of the laser, the grey striped rectangle emphasises the cuvette wall, and the dashed white line highlights the aggregate in the image. **d.** Bubble volume, force, and sound pressure versus time, averaged over the first six spikes shown in panel b. The grey rectangle is a guide to the eye highlighting that the onset of the force spike precedes bubble growth. Inset: aligned time traces of six force spikes, showing very reproducible synchronisation with the bubble dynamics.

bubble [226]. One could expect these violent bubble dynamics to be the cause of the observed photomechanical effect. However, careful time-resolution of the dynamics contradicts this hypothesis. Indeed, the bubble growth results in fluid moving away from the laser, which should trigger macroscopic motion of the vial towards the laser through momentum conservation. This is in contradiction with the macroscopic observation that the vial always moves away from the laser source. Now, one could argue that the bubble dynamics may still be responsible for the vial motion if the necessary momentum was released during bubble collapse. However, this scenario is again contradicted by the experimental observations, since high speed imaging shows that the vial takes off while the bubble is still growing (movie 1). A further confirmation of this macroscopic observation is provided by the parallel high-speed imaging and force measurement (figure 7.5d), whose synchronisation we ensured down to one camera frame (90 μs). The time traces of the various measured quantities were found to be very reproducible over several spikes (see

figure 7.5d, inset), in terms of shape, time delay and order of occurence. Thus, the measurement unambiguously shows that the onset of the force spike precedes bubble collapse, and even precedes bubble growth; moreover, the spike contains oscillations on a timescale which is about three times faster than the bubble dynamics. Hence the bubble seems to arise as a collateral consequence of another phenomenon that is actually responsible for the photomechanical effect.

7.3.4 The thermophoretic instability

Based on these various observations – and the dismissal of several scenarios –, we propose a physical origin for the photomechanical effect, which is based on a collapsing instability of the colloidal suspension. The key point in our reasoning is that the thermophoretic force that drives the particles towards the laser also induces their mutual attraction. It was proposed theoretically that such a thermophoretic attraction could lead to an instability, analogous to the Jeans instability observed in gravitational systems [227,228], as we detail in the following.

Assuming for simplicity that all the particles at positions $\mathbf{r}_j$ are illuminated with intensity I, each particle behaves as a point heat source and the temperature field satisfies $\kappa\Delta T(\mathbf{r}) = 4\pi\sigma I \sum_j \delta(\mathbf{r}-\mathbf{r}_j)$, where σ is the particle absorption cross-section and κ the thermal conductivity of the solvent. This leads immediately to a temperature field which depends on the colloidal structure according to

$$T(\mathbf{r}) = T_0 + \frac{\sigma I}{\kappa}\sum_j \frac{1}{|\mathbf{r}-\mathbf{r}_j|}, \tag{7.2}$$

where T_0 is the temperature far away from the laser. Now if the particles undergo thermophoresis characterised by the Soret coefficient S, then the particle flux, given by eq. (7.1), can be rewritten introducing the effective potential $\mathcal{V}_{\text{eff}}(\mathbf{r})$ which represents the "thermophoretic interaction":

$$\mathbf{j}(\mathbf{r}) = -DS\rho(\mathbf{r})\nabla T(\mathbf{r}) \equiv \frac{D}{k_{\text{B}}T_0}\rho(\mathbf{r})(-\nabla\mathcal{V}_{\text{eff}})(\mathbf{r}), \tag{7.3}$$

with

$$\mathcal{V}_{\text{eff}}(\mathbf{r}) = -\mathcal{G}\sum_j \frac{1}{|\mathbf{r}-\mathbf{r}_j|}, \tag{7.4}$$

and $\mathcal{G} \equiv k_{\text{B}}T_0|S|\sigma I/\kappa$. Therefore, the laser-induced thermophoresis results in the particles interacting with a $1/r$ attractive potential (S is negative), which is analogous to a gravitational potential, and $\mathcal{G}$ plays the role of a gravitational constant. Now, an ensemble of particles – say a cloud of radius R – with gravitational interactions is known to undergo a Jeans instability when it exceeds a critical mass [229]: quantitatively, the cloud collapses to a point when the gravitational energy per particle exceeds the thermal energy:

$$\rho R^2\mathcal{G} \sim k_{\text{B}}T_0. \tag{7.5}$$

Such a collapsing instability explains the formation of stars from clouds of interstellar dust [230]. The profound analogy between gravitational and certain types of colloidal interactions was first noted by Keller and Segel in the case of chemotactic bacteria [231, 232]: when bacteria are attracted by a molecule that they themselves produce,

they may collapse on each other to form dense aggregates. Similar behaviour was later highlighted with diffusiophoretic [233,234], or even capillary [235] interactions, and more recently predicted theoretically for thermophoretic interactions such as the ones considered here [227, 228]. It is therefore likely that the analog of Jeans' instability with thermophoretic interactions explains the brutal force release that we observe. This is further supported by the scaling law argument we develop in the following.

The dynamics of the thermophoretic collapse couple the particle transport in the pseudo-gravitational field to the fluid dynamics. The latter is described with a Navier-Stokes equation:

$$\mu_s[\partial_t \mathbf{v} + (\mathbf{v}\cdot\nabla)\mathbf{v}] = -\nabla p + \rho(-\nabla\mathcal{V}_{\text{eff}}) + \eta\Delta\mathbf{v}, \tag{7.6}$$

where $\mathbf{v}$ is the velocity field, p is the pressure, and μ_s and η the suspension mass density and viscosity, respectively. The driving term $\rho(-\nabla\mathcal{V}_{\text{eff}})$ takes its origin in the thermophoretic interaction introduced above. Solving this equation in the presence of the thermophoretic interaction represents a formidable challenge, but one may propose some scaling relations for the collapse dynamics. First, the observations indicate that the collapse occurs over a short time-scale, of the order of 100 μs (figure 7.5b). This suggests that the Reynolds number associated with the collapse is relatively large: indeed, using a millimetric size for the collapsing region, one can estimate $\mathcal{R}e \approx 10$; thus the dynamics are dominated by the transient (inertial) terms in the Navier-Stokes equation, while viscous terms should be small. As a further note, one may remark that the viscous (shear) term cancels for an incompressible flow with spherical symmetry as expected in the present geometry, hence discarding viscosity effects on a more general ground. The collapse thus results from the balance between the transient inertial term $\mu_s R^3\dot{\mathbf{v}} \sim \mu_s R^4/\tau^2$ (integrated over the size $R \sim 1$ mm of the collapsing cloud) and the total thermophoretic force $\sim \rho R^3(-\nabla\mathcal{V}_{\text{eff}})$, with $\mathcal{V}_{\text{eff}}$ the thermophoretic interaction potential defined in eq. (7.3). Since the pseudo-gravitational potential results from the sum of the interactions of particles within the sphere of radius R, one estimates $\mathcal{V}_{\text{eff}} \approx -\rho R^3 \frac{\mathcal{G}}{R}$. This leads to a scaling law for the timescale τ of the collapse, as

$$\mu_s \cdot \frac{R^4}{\tau^2} \sim \rho^2 \mathcal{G} R^5 \sim \rho R^2 k_B T_0 \tag{7.7}$$

hence

$$\tau \sim \sqrt{\frac{\mu_s R^2}{\rho k_B T_0}}, \tag{7.8}$$

Due to the thermophoretic attraction, the density in the illuminated region is expected to be close to the close packing density of the PbS particles, so that assuming $\rho \sim 10^{24}$ m^{-3}, we find $\tau \sim 100$ μs. This estimate is indeed in good agreement with the experimental result and justifies a posteriori the inertial assumptions on the dynamics. As a further prediction, the force generated in the collapse can be estimated as the collapsing mass times its acceleration:

$$F \sim m\rho R^3 \frac{R}{\tau^2} = \frac{m\rho^2}{\mu_s} k_B T_0 R^2. \tag{7.9}$$

We find $F \sim 40$ mN, which is again compatible with the experimentally observed range.

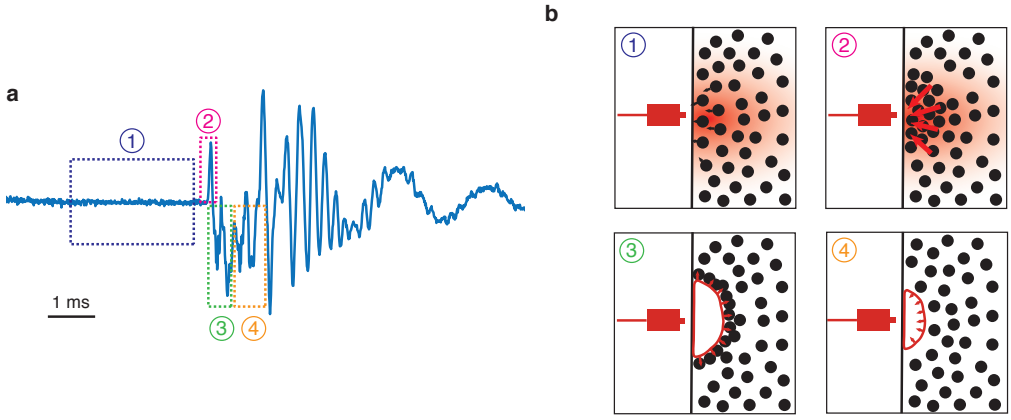

Figure 7.6

Schematic mechanism of the photomechanical effect. **a.** Force versus time signal corresponding to a force spike. The four dashed rectangles correspond to the four steps in the proposed mechanism for the generation of a spike. **b.** Schematics for the four steps highlighted in panel a. The black circles correspond to PbS particles and the red colour represents a temperature gradient. (1) Phoretic motion of the particles towards the laser source. (2) Jeans instability, resulting in brutal force release. (3) Explosive growth of a bubble, which disperses the accumulated particles. (4) Collapse of the bubble and return to the initial state.

7.4 Discussion

The above considerations allow us to propose a complete scenario for the origin of the photomechanical effect, which is summarised in figure 7.6. The PbS particles absorb the laser light and become point heat sources. They undergo negative thermophoresis and thus migrate towards the laser source. The particle density increases in the illuminated region, up to the point where the Jeans instability occurs, resulting in collective motion of the particles towards the laser, giving the whole vial momentum away from the laser. The "gravitational" collapse is expected to result in a temperature increase and pressure decrease near the wall of the vial, resulting from the increase in the particle concentration and their rapid motion, respectively. This triggers a cavitation event, with a bubble explosively growing and then collapsing next to the wall. The resulting dynamics disperse the particles that have accumulated near the wall [223,236], so that the process can start again and result in a new propulsion event. We expect that the momentum of the particles is transmitted to the vial wall, resulting in the propagation of a shock wave through the glass, which would be responsible for the oscillations observed in the force spikes and the sound: the observed oscillation frequencies were different in the vial and the spectroscopic cuvette. When the vial stands freely on a substrate, the momentum carried by the shock wave can be transmitted to the substrate and then back to the vial so that it takes off: this momentum transfer is similar to what occurs in the propulsion of the Mexican jumping beans [237]. We thus expect only the first positive force peak to matter: the subsequent oscillations contained in the spike (figure 7.6a) occur when the vial is already in the air and they cannot therefore contribute to propulsion.

We have demonstrated the propulsion of a macroscopic object by the sole action of

light through a novel mechanism involving negative thermophoresis as a key ingredient. A 1.5 W laser illumination is sufficient to propel a vial weighing 3.5 grams at a 1 $mm \cdot s^{-1}$ average speed. Remarkably, it is the interplay between three different phenomena – thermophoretic migration, the Jeans instability and bubble cavitation –, that results in the system propelling itself through repeatable, discrete force spikes. We believe it is also remarkable that a "soft" system, whose dynamics are usually viscous, actually exhibits ultrafast transport, way beyond the viscous timescale. The slow energy accumulation followed by a fast release is reminiscent of the process used by certain plants, such as the fern, to propel their spores [238]. Our novel mechanism for soft matter actuation could therefore be of interest for mimicking certain bio-inspired functionalities.

7.5 The big picture

In this Chapter, we studied a peculiar photomechanical effect: a vial filled with a concentrated colloidal suspension is propelled upon near-infrared laser illumination. Thanks to a dedicated experimental setup that combined cantilever-based force measurements and ultrafast imaging, we were able to propose a complete mechanism for the propulsion, which is summarised in figure 7.6. The key ingredients are thermophoretic migration of the colloidal particles towards the illuminated spot, and a collapsing instability of the particle cloud.

Conclusion and perspectives

In this thesis, I have explored several phenomena in nanoscale fluid transport that are beyond the reach of the well-established continuum and mean-field theories. These phenomena are the consequences of many-body effects – that is, inter-particle correlations – in the ion and fluid dynamics under nanometre-scale confinement.

Why many-body effects? We have shown in Chapter 2 that many-body effects are enhanced at the nanoscale due to *interaction confinement*: the presence of a confining wall affects not only the particles' translational degrees of freedom, but also their interactions and hence their dynamics. The way in which the wall affects interactions is essentially determined by its electromagnetic response. Hence, the fluid dynamics in a sufficiently small channel may be expected to depend on the wall material's electronic properties, and even couple to its electron dynamics. This general principle establishes a crucial distinction between nanofluidics and macroscopic hydrodynamics, where a wall is nothing more than a boundary condition. This thesis has been largely devoted to exploring the potential consequences of such a distinction.

Many-ion phenomena. In part II of this thesis, we predict that interaction confinement significantly affects nanoscale ion transport. Due to the contrast in dielectric screening properties between water and typical channel materials, ions in confinement interact much stronger than in the bulk, leading to enhanced ionic correlations. Correlations are in fact so strong that oppositely charged ions may pair up in nanometre-scale 1D or 2D confinement. This Bjerrum pairing leads to many-body effects in the ion dynamics. In 1D geometry, we predict an ionic Coulomb blockade phenomenon, where ion transport becomes "quantised" upon gating by a variable surface charge. In 2D confinement, a dynamic clustering transition of the Bjerrum pairs gives rise to memory effects in the system, and potentially neuromorphic behaviour. Overall, we find that ions in interaction confinement have striking properties that are completely beyond mean-field descriptions. We develop a range of specific theoretical tools to tackle these systems: from revisiting Onsager's theory of the Wien effect, to implementing an exactly solvable model in one dimension.

Many-body quantum friction. In part III of this thesis, we take the idea of interaction confinement further, by looking at its consequences on the dynamics of the solid-liquid interface. While ion dynamics are sensitive to the channel wall's electronic properties on the nanometre scale, where these can be described in terms of local dielectric response, the dynamics of interfacial water involve lengthscales that may be on the order of the Fermi wavelength of the wall material's conduction electrons. Moreover, in terms of time scales,

the terahertz frequencies associated with the water molecules' thermal motion may be in the range of electronic plasma frequencies of materials with low electronic density, and non-trivial water-electron couplings beyond the Born-Oppenheimer approximation may be expected. By developing a many-body quantum theory of the solid-liquid interface, we find that such couplings do indeed occur, and are responsible for a supplementary contribution to hydrodynamic friction that we call quantum friction. This quantum contribution may explain some of the peculiar properties of the water-carbon interface, in particular the radius-dependent slippage in carbon nanotubes. Thus, strikingly, the most subtle consequences of interaction confinement are measurable in fairly large channels: the radius dependence of slippage is observed in nanotubes with radii in the range $10-30$ nm.

What about experiments? The theoretical investigations developed in this thesis are largely motivated by the recent progress in fabrication technology, which has finally placed well-controlled nanofluidic systems with molecular-scale confinement within our reach. It is therefore reasonable to hope for an experimental insight into the theoretical predictions of this thesis in the near future, and several preliminary results are encouraging in this respect. For instance, non-linear current-voltage characteristics have been observed for ion transport in 2 nm diameter carbon nanotubes, and may be the signature of confinement-induced ionic correlations [44]. Moreover, an observation of ionic Coulomb blockade in MoS_2 nanopores has recently been claimed: the authors measured conductance gating by a light-controlled variable surface charge [239] (the findings have not yet been peer-reviewed). Finally, the ongoing measurements of water slippage in two-dimensional nanochannels, described in Chapter 5, will provide an ideal testing ground for our theory of quantum hydrodynamic friction, thanks to the possibility of tuning the confinement width and wall materials.

So what ? We have learned that liquids have some peculiar correlated dynamics when confined to the nanometre scale. Apart from filling up the pages of a thesis, this opens a range of exciting perspectives. The exotic ion transport phenomena that result from interaction confinement open new avenues in the field of iontronics, that is, computations based on ions. Ion transport is used by the human brain to carry out computations that are too complex for any artificial computer to handle, and with orders of magnitude lower energy consumption. The exact reasons which make biological computations so efficient are unclear, and the development of elementary ion-based computing devices may be expected to shed light on this fundamental question. Pioneering work in this direction is currently in the hands of my fellow PhD students, Théo Emmerich and Paul Robin.

The whole principle of interaction confinement, and in particular the quantum friction phenomenon, establishes a new bridge between hard and soft condensed matter. This was envisioned already in our group's 2016 paper on radius-dependent slippage in nanotubes [23]: *The unexpected slippage behaviour inside CNTs and BNNTs points to a hitherto not appreciated link between hydrodynamic flow and the electronic structure of the confining material. This opens up a new avenue for research that could bridge the gap between hard and soft condensed matter physics.* While the 2016 paper laid the foundation with a crucial experimental result, this thesis begins to build the bridge with equations, which point to non-trivial quantum effects in solid-liquid friction. I hope that the theoretical framework presented in Chapter 5 can help unveil new quantum effects at the solid-liquid interface, whether it is frictional behaviour – the single-file water configu-

ration shows particular promise in this respect – or other related effects such as Coulomb drag [240,241]. Beyond the fundamental interest, these phenomena could potentially lead to radically new ways of controlling fluid transport at the nanoscale.

Appendices

Appendix A

Ionic interactions in confinement

Contents

A.1 1D channel: nanotube

We consider the nanochannel of radius R in cylindrical coordinates (r, z). We denote $\bar{\bar{\epsilon}}$ the dielectric permittivity tensor. We place a point charge Ze at $(r, z) = (0, 0)$ and solve the Poisson equation for the electrostatic potential ϕ, which reads

$$\nabla \left(\bar{\bar{\epsilon}} \cdot \nabla \phi \right) = -\frac{Ze}{\epsilon_0} \frac{\delta(r)\delta(z)}{2\pi r}. \tag{A.1}$$

The tensor $\bar{\bar{\epsilon}}$ is diagonal in cylindrical coordinates,

$$\bar{\bar{\epsilon}} = \begin{pmatrix} \epsilon_r & 0 & 0 \\ 0 & \epsilon_\theta & 0 \\ 0 & 0 & \epsilon_z \end{pmatrix}. \tag{A.2}$$

Inside the channel ($r < R$), the permittivity is that of water and therefore $\epsilon_r = \epsilon_\theta = \epsilon_\perp$ and $\epsilon_z = \epsilon_\parallel$. Outside the channel, we assume an isotropic permittivity ϵ_m, so that $\epsilon_r = \epsilon_\theta = \epsilon_z = \epsilon_m$.

We may expand eq. (A.1) as

$$\epsilon_r \partial_r^2 \phi + \frac{\epsilon_r}{r} \partial_r \phi + \epsilon_z \partial_z^2 \phi = -\frac{Ze}{\epsilon_0} \frac{\delta(r)\delta(z)}{2\pi r}. \tag{A.3}$$

We now define the Fourier-transformed potential $\tilde{\phi}(r, q)$ by

$$\phi(r, z) = \frac{1}{2\pi^2} \int_0^\infty \mathrm{d}q \, \tilde{\phi}(q, r) \cos(qz), \tag{A.4}$$

and eq. (A.3) in Fourier space reads

$$\partial_r^2 \tilde{\phi} + \frac{1}{r} \partial_r \tilde{\phi} - \left(q \sqrt{\frac{\epsilon_z}{\epsilon_r}} \right)^2 \tilde{\phi} = -\frac{Ze}{\epsilon_0 \epsilon_r} \frac{\delta(r)}{r}. \tag{A.5}$$

We look for solutions of (A.5) separately in the regions $r < R$ and $r > R$. The solutions are given by:

$$\begin{aligned} r < R: &\quad \tilde{\phi}_<(q,r) = AI_0\left(qr\sqrt{\epsilon_\parallel/\epsilon_\perp}\right) + BK_0\left(qr\sqrt{\epsilon_\parallel/\epsilon_\perp}\right) \\ r > R: &\quad \tilde{\phi}_>(q,r) = CI_0(qr) + DK_0(qr) \end{aligned} \tag{A.6}$$

where A, B, C, D are four constants and I_0 and K_0 are the modified Bessel functions. Since I_0 diverges at infinity, we immediately set $C = 0$. We now determine the boundary conditions at $r = 0$ and $r = R$. The continuity of the potential at $r = R$ implies

$$AI_0\left(qR\sqrt{\epsilon_\parallel/\epsilon_\perp}\right) + BK_0\left(qR\sqrt{\epsilon_\parallel/\epsilon_\perp}\right) = DK_0(qR). \tag{A.7}$$

To determine the condition on the electric field at $r = 0$, we integrate eq. (A.5) over an interval $[r = -\lambda; r = \lambda]$:

$$\int_{-\lambda}^{\lambda} \mathrm{d}r\,(r\partial_r^2 + \partial_r)\tilde{\phi}_<(q,r) - \left(k\sqrt{\epsilon_\parallel/\epsilon_\perp}\right)^2 \int_{-\lambda}^{\lambda} \mathrm{d}r\, r\tilde{\phi}_<(q,r) = -\frac{Ze}{\epsilon_0\epsilon_\perp}\int_{-\lambda}^{\lambda}\delta(r)\mathrm{d}r. \tag{A.8}$$

Recalling that $(r\partial_r^2 + \partial_r) = \partial_r(r\partial_r)$ and letting λ go to 0, we obtain the condition

$$\lim_{r\to 0}\left[r\partial_r\tilde{\phi}_<(q,r)\right] = -\frac{Ze}{\epsilon_0\epsilon_\perp}. \tag{A.9}$$

Applying the same procedure at $r = R$, we obtain

$$\epsilon_\perp\,\partial_r\tilde{\phi}_<\Big|_{r=R} = \epsilon_m\,\partial_r\tilde{\phi}_>\Big|_{r=R}. \tag{A.10}$$

In terms of the solution (A.6), the condition (A.9) reads

$$q\sqrt{\frac{\epsilon_\parallel}{\epsilon_\perp}}\cdot B\cdot\lim_{r\to 0}\left[rK_1\left(qr\sqrt{\frac{\epsilon_\parallel}{\epsilon_\perp}}\right)\right] = \frac{Ze}{\epsilon_0\epsilon_\perp}, \tag{A.11}$$

and since $K_1(x) \underset{x\to 0}{\sim} 1/x$, this yields

$$B = \frac{Ze}{\epsilon_0\epsilon_\perp}. \tag{A.12}$$

Similarly, the condition (A.10) implies

$$\sqrt{\epsilon_\perp\epsilon_\parallel}\cdot\left[AI_1\left(qR\sqrt{\epsilon_\parallel/\epsilon_\perp}\right) - BK_1\left(qR\sqrt{\epsilon_\parallel/\epsilon_\perp}\right)\right] = -\epsilon_m DK_1(qR). \tag{A.13}$$

Solving together eqs. (A.7), (A.12) and (A.13) yields the constants A, B, C and the expression for the Fourier-transformed potential inside the channel:

$$\begin{aligned} \tilde{\phi}_<(q,r) = &\frac{\sqrt{\epsilon_\perp\epsilon_\parallel}K_1\left(qR\sqrt{\epsilon_\parallel/\epsilon_\perp}\right)K_0(qR) - \epsilon_m K_1(qR)K_0\left(qR\sqrt{\epsilon_\parallel/\epsilon_\perp}\right)}{\sqrt{\epsilon_\perp\epsilon_\parallel}K_0\left(qR\sqrt{\epsilon_\parallel/\epsilon_\perp}\right)I_1(qR) + \epsilon_m K_1\left(qR\sqrt{\epsilon_\parallel/\epsilon_\perp}\right)I_0(qR)}\cdot\frac{ZeI_0\left(qr\sqrt{\epsilon_\parallel/\epsilon_\perp}\right)}{\epsilon_0\epsilon_\perp}\cdots \\ &+\frac{Ze}{\epsilon_0\epsilon_\perp}\cdot K_0\left(qr\sqrt{\epsilon_\parallel/\epsilon_\perp}\right). \end{aligned} \tag{A.14}$$

Setting $\epsilon_\parallel = \epsilon_\perp$ one recovers the result obtained for example by Teber [70]. We may now follow ref. [70] in identifying the first term in eq. (A.14) as the contribution of the polarisation charges in the confining medium and the second term as the usual $1/r$ Coulomb potential. Indeed, upon reverse Fourier transformation, it yields a contribution

$$\phi_0(r,z) = \frac{q}{4\pi\epsilon_0\sqrt{(z\epsilon_\perp)^2 + (r\sqrt{\epsilon_\parallel\epsilon_\perp})^2}}, \tag{A.15}$$

which dominates the potential $\phi(r,z)$ at short distances $r \ll R$. Thus, interestingly, it is the radial permittivity that matters for the short-range interaction along the longitudinal direction.

Now at distances $r \gg R$, one needs only to consider the contribution of small wavevectors q (such that $qR \ll 1$) in eq. (A.4). We set $\kappa \equiv qR$ and expand the denominator of eq. (A.14) at small κ. We obtain:

$$\begin{aligned}&\sqrt{\epsilon_\perp\epsilon_\parallel}K_0\left(\kappa\sqrt{\epsilon_\parallel/\epsilon_\perp}\right)I_1(\kappa) + \epsilon_m K_1\left(\kappa\sqrt{\epsilon_\parallel/\epsilon_\perp}\right)I_0(\kappa) = \\ &\frac{\epsilon_m}{\kappa}\sqrt{\frac{\epsilon_\perp}{\epsilon_\parallel}}\left[1 + \frac{\kappa^2}{4\epsilon_m\epsilon_\perp}\left(\epsilon_m(\epsilon_\perp - \epsilon_\parallel) + 2\gamma\epsilon_\parallel(\epsilon_m - \epsilon_\perp) + 2\epsilon_\parallel(\epsilon_m - \epsilon_\perp)\log\left(\frac{\kappa}{2}\sqrt{\frac{\epsilon_\parallel}{\epsilon_\perp}}\right)\right) + o(\kappa^2)\right],\end{aligned} \tag{A.16}$$

where γ is Euler's gamma constant. In order to be able to compute the reverse Fourier transform, Teber proposes to introduce a characteristic length ξ such that the term in brackets in eq. (A.16) may be simplified as $1 + (\kappa\xi/R)^2$. Enforcing that the bracket should equal 2 when $\kappa = R/\xi$, one obtains an implicit equation for ξ, which reads in our anisotropic permittivity case

$$\frac{\xi^2}{R^2} = \frac{1}{4\epsilon_m\epsilon_\perp}\left[\epsilon_m(\epsilon_\perp - \epsilon_\parallel) + 2\epsilon_\parallel(\epsilon_m - \epsilon_\perp)\left(\gamma - \log\left(\frac{2\xi}{R}\sqrt{\frac{\epsilon_\perp}{\epsilon_\parallel}}\right)\right)\right]. \tag{A.17}$$

Setting $\epsilon_\perp = \epsilon_\parallel = \epsilon_w$ and assuming $\epsilon_m \ll \epsilon_w$, one recovers

$$\frac{\xi^2}{R^2} = \frac{\epsilon_w}{2\epsilon_m}\left[\log\left(\frac{2\xi}{R} - \gamma\right)\right], \tag{A.18}$$

which is eq. (7) of ref. [70]. Provided that the above approximation scheme holds in the anisotropic permittivity case, one obtains the potential along the z direction as

$$\begin{aligned}&\phi(0,z) = \phi_0(0,z) + \frac{Ze}{2\pi^2\epsilon_0 R}\frac{\sqrt{\epsilon_\parallel}}{\epsilon_m\epsilon_\perp\sqrt{\epsilon_\perp}}\ldots \\ &\int_0^{+\infty} \mathrm{d}\kappa\,\kappa\cdot\frac{\sqrt{\epsilon_\perp\epsilon_\parallel}K_1\left(\kappa\sqrt{\epsilon_\parallel/\epsilon_\perp}\right)K_0(\kappa) - \epsilon_m K_0\left(\kappa\sqrt{\epsilon_\parallel/\epsilon_\perp}\right)K_1(\kappa)}{1 + (\kappa\xi/R)^2}\cos(\kappa z/R).\end{aligned} \tag{A.19}$$

Teber identifies the length ξ as the point of transition between a 1D-like linear Coulomb potential and a $1/r$ tail. He thereby approximates the potential as

$$\phi(0,z) = \frac{\xi}{x_T}e^{-|z|/\xi}, \tag{A.20}$$

where $x_T \approx R^2/(2\ell_B)$, with ℓ_B is the Bjerrum length for an isotropic water permittivity ϵ_w. In the case of a not too strongly anisotropic permittivity, one may use our eq. (A.17)

to compute a corrected value of ξ. However, if the permittivity is strongly anisotropic there is no solution to eq. (A.17). Hence one may not use the exponential approximation directly: qualitatively, it is the short-range $1/r$ term in the potential that dominates over the 1D term that comes from the image charges. Nevertheless, it is possible to find parameters ξ and x_T such that the exponential form (A.20) reasonably reproduces at few-nm separations that are relevant in the discussion on many-body effects, in particular the Coulomb blockade phenomenon.

A.2 2D channel: nano-slit

In this section, we establish an analytical representation for the Coulomb potential created by an ion placed in the middle of a nano-slit of heigh h[1]. We start from eq. (2.17), which gives the Fourier-transformed Coulomb potential in terms of the confining medium's surface response function g_m:

$$\phi_{\text{tot}}(q,0) = \frac{e}{4\pi\epsilon_0\sqrt{\epsilon_\parallel\epsilon_\perp}}\frac{2\pi}{q}\left(1 - \frac{2g_m e^{-aqh}}{1+g_m e^{-aqh}}\right). \tag{A.21}$$

At distances $\rho \gg h$, we may consider only the contribution of the potential induced by the polarisation charges:

$$\phi(q,0) = \frac{e}{4\pi\epsilon_0\sqrt{\epsilon_\parallel\epsilon_\perp}}\frac{2\pi}{q}\left(-\frac{2g_m e^{-aqh}}{1+g_m e^{-aqh}}\right). \tag{A.22}$$

We then expand the denominator, according to

$$\phi(q,0) = \frac{e}{4\pi\epsilon_0\sqrt{\epsilon_\parallel\epsilon_\perp}}\frac{4\pi}{q}\sum_{n=1}^{+\infty}(-1)^n g_m^n e^{-nqah}. \tag{A.23}$$

This allows us to compute the real-space potential according to

$$\phi(\rho) = \int_0^{+\infty}\frac{\mathrm{d}q}{2\pi}\,qJ_0(q\rho)\phi(q,0) = \frac{e}{2\pi\epsilon_0\sqrt{\epsilon_\parallel\epsilon_\perp}}\sum_{n=1}^{+\infty}\frac{(-g_m)^n}{\sqrt{\rho^2+a^2h^2n^2}}. \tag{A.24}$$

We recall that

$$g_m = \frac{\epsilon_m - \sqrt{\epsilon_\parallel\epsilon_\perp}}{\epsilon_m + \sqrt{\epsilon_\parallel\epsilon_\perp}} < 0, \tag{A.25}$$

in the case under consideration where $\epsilon_m \ll \sqrt{\epsilon_\parallel\epsilon_\perp}$. We may then heuristically approximate the sum by the corresponding integral:

$$\phi(\rho) \simeq \frac{e}{4\pi\epsilon_0\epsilon_\parallel h}\int_0^\infty \frac{\gamma^u\,\mathrm{d}u}{\sqrt{\rho^2/a^2h^2+u^2}}, \tag{A.26}$$

with $\gamma = -g_m$. We obtain:

$$\phi(\rho) \simeq \frac{e}{4\pi\epsilon_0\epsilon_\parallel h}\left[-J_0\left(\frac{\rho|\log\gamma|}{ah}\right)\log\left(\frac{\rho|\log\gamma|}{2ah}\right) + \frac{1}{2}\pi H_0\left(\frac{\rho|\log\gamma|}{ah}\right) - f\left(-\frac{\rho^2\log^2\gamma}{4a^2h^2}\right)\right], \tag{A.27}$$

[1] I am indebted to P. Robin for carrying out this computation

where H_0 is the Struve function of zeroth order and f can be expressed in terms of the hypergeometric confluent function ${}_0F_1$ and Euler's gamma function:

$$f(x) = \left(\frac{\partial}{\partial a} \frac{{}_0F_1(a,x)}{\Gamma(a)} \right)_{a=1}. \tag{A.28}$$

We can identify the lengthscale:

$$\xi = \frac{ah}{|\log \gamma|} \simeq \frac{\epsilon_\parallel}{2\epsilon_m} h \tag{A.29}$$

where we recall that $a = \sqrt{\epsilon_\parallel / \epsilon_\perp}$. The appearance of the lengthscale ξ suggests the further approximation of the potential according to

$$\phi(\rho) \simeq \frac{-e\mathcal{K}}{2\pi\epsilon_0\epsilon_\parallel h} \log\left(\frac{\rho}{\rho + \xi} \right), \tag{A.30}$$

which strongly ressembles a 2D Coulomb potential screened by a dielectric constant $\epsilon_\parallel$. The dimensionless constant of order unity $\mathcal{K} \simeq 1.11$ is a geometric factor that depends very weakly on other parameters. This analytical approximation reproduces very well the exact result as shown in figure 2.3.

Appendix B

Surface response functions

Contents

B.1 Definition

Consider a semi-infinite medium occupying the half-space $z < 0$, while the half-space $z > 0$ is filled with vacuum. We define its density-density response function χ as the linear response function relating the induced charge density δn to the externally applied potential ϕ_{ext} (in energy units):

$$\delta n(\mathbf{r}, t) = \int_{-\infty}^{+\infty} \mathrm{d}t' \int \mathrm{d}\mathbf{r}' \chi(\mathbf{r}, \mathbf{r}', t - t') \phi_{\text{ext}}(\mathbf{r}', t'). \tag{B.1}$$

If the medium is translationally invariant parallel to the surface, we introduce cylindrical coordinates $\mathbf{r} \equiv (\boldsymbol{\rho}, z)$; and the space-time Fourier transform

$$\chi(q, z, z', \omega) = \int \mathrm{d}(\boldsymbol{\rho} - \boldsymbol{\rho}') \int_{-\infty}^{+\infty} \mathrm{d}(t - t') e^{-i\mathbf{q}(\boldsymbol{\rho} - \boldsymbol{\rho}')} e^{-i\omega(t - t')} \chi(\boldsymbol{\rho} - \boldsymbol{\rho}', z, z', t - t'). \tag{B.2}$$

The surface response function is then defined according to

$$g(q, \omega) = -\frac{e^2}{2\epsilon_0 q} \int_{-\infty}^{0} \mathrm{d}z \mathrm{d}z' \, e^{q(z+z')} \chi(q, z, z', \omega). \tag{B.3}$$

B.2 Long wavelength limit

It appears from the definition (B.3) that the surface response function plays the role of a reflection coefficient for evanescent plane waves. Suppose the medium is subject to an evanescent plane wave at frequency ω, of the form $\phi_{\text{ext}}(\boldsymbol{\rho}, z, \omega) = \phi_0 e^{i\mathbf{q}\boldsymbol{\rho}} e^{qz}$. Its space-time Fourier transform is $\phi_{\text{ext}}(z, q, \omega) = \phi_0 e^{qz}$. Then, the induced charge density is

$$\delta n(q, z, \omega) = \phi_0 \int_{-\infty}^{0} \mathrm{d}z' \chi_q(z, z', \omega) e^{qz'}, \tag{B.4}$$

and the induced potential at a distance z above the medium is

$$\phi_{\text{ind}}(q,z,\omega) = \phi_0 \int_{-\infty}^{0} \mathrm{d}z'\mathrm{d}z''\chi(q,z',z'',\omega)e^{qz'}\frac{e^2}{4\pi\epsilon_0}\frac{2\pi}{q}e^{-q(z-z")} = -g(q,\omega)\phi_0 e^{-qz}, \tag{B.5}$$

or, in real space, $\phi_{\text{ind}}(\rho,z,t) = -\phi_0 g(q,\omega)e^{i(\mathbf{q}\boldsymbol{\rho}-\omega t)}e^{-qz}$.

Given this interpretation, g may be readily evaluated in the long wavelength limit, where the medium may be assumed to have a local dielectric response $\epsilon(\omega)$. In that case, inside the medium, there may be no induced charges (except on the surface), and the potential therefore solves the Laplace equation. Since it must vanish at $-\infty$, it is of the form $\phi_m(q,z) = \phi_m e^{qz}$. Outside the medium, the potential is the sum of the external potential and the induced potential. Since the Laplace equation holds, the outside potential reads

$$\phi(q,z) = \phi_{\text{ext}}e^{qz} + \phi_{\text{ind}}e^{-qz}. \tag{B.6}$$

Now, we must enforce boundary conditions on the interface. These are given by continuity of the potential and of the displacement field $\mathbf{D} = -\epsilon_0\epsilon(\omega)\nabla\phi$. The boundary conditions read

$$\begin{aligned} \phi_{\text{ext}} + \phi_{\text{ind}} &= \phi_m \\ \phi_{\text{ext}} - \phi_{\text{ind}} &= \epsilon(\omega)\phi_m. \end{aligned} \tag{B.7}$$

Hence we obtain $\phi_{\text{ind}} = \phi_{\text{ext}}(1-\epsilon(\omega))/(\epsilon(\omega)+1)$, and therefore the expression of g in the long wavelength limit:

$$g(q\to 0,\omega) = \frac{\epsilon(\omega)-1}{\epsilon(\omega)+1}. \tag{B.8}$$

If one further takes into account the screening of the indued potential in the half-space $z>0$ by a local dielectric constant ϵ_w, then through a similar enforcement of boundary conditions this expression is generalised to

$$g(q\to 0,\omega) = \frac{\epsilon(\omega)-\epsilon_w}{\epsilon(\omega)+\epsilon_w}. \tag{B.9}$$

B.3 General case

In general, computing the surface response requires the knowledge of the density response function $\chi(q,z,z',\omega)$ for a semi-infinite medium. For a liquid, it can be determined directly from classical molecular dynamics (MD) simulations (see Appendix F). For an electronic system, it can be computed within different analytical or numerical frameworks with varying degrees of accuracy. The simplest treatment (self-consistent Hartree, or RPA) that takes into account electron-electron interactions requires to solve the following Dyson equation (see Appendix E):

$$\chi(q,z,z',\omega) = \chi^0(q,z,z',\omega) + \int \mathrm{d}z_1\mathrm{d}z_2\,\chi^0(q,z,z_1,\omega)V_q(z_1-z_2)\chi(q,z_2,z',\omega), \tag{B.10}$$

where $V_q(z) = (e^2/2\epsilon_0 q)e^{-q|z|}$ is the Fourier-transformed Coulomb potential. Here χ^0 is the non-interacting density response function: it determines the electrons' response to an

external potential ϕ_{ext} with the electron-electron interactions switched off. Solving the one-electron Schrödinger equation to first order in the perturbation ϕ_{ext} yields [242]:

$$\chi^0(\mathbf{r},t,\mathbf{r}',t') = -\frac{i}{\hbar}\theta(t-t')\text{Tr}(\rho_0[n(\mathbf{r},t),n(\mathbf{r}',t')]), \tag{B.11}$$

where ρ_0 is the non-interacting density matrix, and the density operators are in the Heisenberg picture with respect to the non-interacting hamiltonian H_0:

$$n(\mathbf{r},t) = e^{iH_0t/\hbar}n(\mathbf{r})e^{-iH_0t/\hbar}. \tag{B.12}$$

We denote $|\lambda\rangle$ the eigenstates and E_λ the corresponding energies of the unperturbed non-interacting system:

$$H_0|\lambda\rangle = E_\lambda|\lambda\rangle. \tag{B.13}$$

Then, the non-interacting density matrix is

$$\rho_0 = \sum_\lambda n_{\text{F}}(E_\lambda)|\lambda\rangle\langle\lambda|, \tag{B.14}$$

where n_{F} is the Fermi-Dirac distribution. Inserting the resolution of the identity $\hat{I} = \sum_\lambda |\lambda\rangle\langle\lambda|$ into eq. (B.11), one obtains

$$\chi^0(\mathbf{r},t,\mathbf{r}',t') = -\frac{i}{\hbar}\sum_{\lambda\lambda'}(n_{\text{F}}(E_\lambda)-n_{\text{F}}(E'_\lambda))\langle\lambda|n(\mathbf{r})|\lambda'\rangle\langle\lambda'|n(\mathbf{r}')|\lambda\rangle e^{\frac{i}{\hbar}(E_\lambda-E_{\lambda'})(t-t')}. \tag{B.15}$$

Fourier transformation with respect to time then yields

$$\chi^0(\mathbf{r},\mathbf{r}',\omega) = -\frac{i}{\hbar}\sum_{\lambda\lambda'}\frac{n_{\text{F}}(E_\lambda)-n_{\text{F}}(E'_\lambda)}{E_\lambda-E_{\lambda'}+\hbar\omega+i\delta}\langle\lambda|n(\mathbf{r})|\lambda'\rangle\langle\lambda'|n(\mathbf{r}')|\lambda\rangle, \tag{B.16}$$

with $\delta \to 0^+$. If we introduce the position representation eigenfunctions $\psi_\lambda(\mathbf{r})$, then the density operator is decomposed according to

$$n(\mathbf{r}) = \sum_{\lambda_1\lambda_2}\psi^*_{\lambda_2}(\mathbf{r})\psi_{\lambda_1}(\mathbf{r})|\lambda_2\rangle\langle\lambda_1|, \tag{B.17}$$

so that finally

$$\chi^0(\mathbf{r},\mathbf{r}',\omega) = \sum_{\lambda,\lambda'}\frac{n_{\text{F}}(E_\lambda)-n_{\text{F}}(E_{\lambda'})}{E_\lambda-E_{\lambda'}+\hbar\omega+i\delta}\,\psi^*_\lambda(\mathbf{r})\psi_{\lambda'}(\mathbf{r})\psi^*_{\lambda'}(\mathbf{r}')\psi_\lambda(\mathbf{r}'). \tag{B.18}$$

Thus, the non-interacting density response function can in principle be computed if the eigenstates and eigenenergies of the non-interacting system are known, and then the surface response function can be obtained in the framework of RPA.

B.4 Specular reflection approximation

Even if χ_0 is known, eq. (B.10) must be solved numerically for every value of q and ω. A considerable simplification is achieved within the so-called specular reflection (SR)

approximation, which allows one to solve (B.10) analytically and express the surface response in terms of the bulk response. The SR approximation sets

$$\chi^0(q,z,z',\omega) = \chi^0_{\mathrm{B}}(q,z-z',\omega) + \chi^0_{\mathrm{B}}(q,z+z',\omega), \tag{B.19}$$

where χ^0_{B} is the bulk system's non-interacting density response. This ansatz does not correspond to any particular form of the wavefunctions in eq. (B.18). It imposes phenomenologically that in the presence of a surface, the points z and z' may either interact directly, or through a specular reflection from the surface at $z = 0$. It can be shown that the SR approximation thus amounts to neglecting quantum interference between electrons impinging on and electrons reflected from the surface [175].

Inserting eq. (B.19) into eq. (B.10) and carrying out Fourier transforms along the vertical direction (the computation is detailed, for example, in [175]), one obtains:

$$g(q,\omega) = \frac{1-q\ell_q(\omega)}{1+q\ell_q(\omega)}, \quad \ell_q(\omega) = \frac{2}{\pi}\int_0^{+\infty} \frac{\mathrm{d}q_z}{(q^2+q_z^2)\epsilon(q,q_z,\omega)}, \tag{B.20}$$

where $\epsilon(q,q_z,\omega) = 1 - \frac{e^2}{\epsilon_0(q^2+q_z^2)}\chi^0_{\mathrm{B}}(q,q_z,\omega)$ is the bulk system's dielectric function. The bulk non-interacting density response function is obtained from the Fourier-transformed eq. (B.18):

$$\chi^0_{\mathrm{B}}(q,q_z,\omega) = \sum_{\nu,\nu'}\int_{\mathrm{BZ}} \frac{\mathrm{d}^3k}{4\pi^3} |\langle \mathbf{k}+\mathbf{q},\nu|e^{i\mathbf{q}\cdot\mathbf{r}}|\mathbf{k},\nu'\rangle|^2 \frac{n_{\mathrm{F}}[E_\nu(\mathbf{k}+\mathbf{q})] - n_{\mathrm{F}}[E_{\nu'}(\mathbf{k})]}{E_\nu(\mathbf{k}+\mathbf{q}) - E_{\nu'}(\mathbf{k}) - \hbar(\omega+i\delta)}, \tag{B.21}$$

where we have re-labeled the states $\lambda \mapsto (\mathbf{k},\nu)$, with ν a band index and $\mathbf{k}$ a vector within the (three-dimensional) first Brillouin zone.

For completeness, we provide here an additional derivation of eq. (B.20), which has the advantage of being computationally simpler than the one reported in [175]. It is based on the work of Ritchie and Marusak [81], who first proposed the SR approximation in their study of surface plasmons. The idea is that, when eq. (B.19) is enforced, the *shape* of the density response of the semi-infinite medium to the potential $\phi_{\mathrm{ext}}(q,z,\omega) = \phi_{\mathrm{ext}}e^{qz}$ is the same as the *shape* of the density response of an infinite medium to a symmetrised potential $\phi_{\mathrm{eff}}(q,z,\omega) = \phi_{\mathrm{eff}}e^{-q|z|}$. The amplitude ϕ_{eff} is a priori non known, and it is determined by enforcing Maxwell boundary conditions at the interface.

In the following, we will drop the frequency ω which plays no role in the computation. In response to the potential ϕ_{eff}, the induced charge density in the infinite medium reads

$$\delta n(q,z) = \phi_{\mathrm{eff}}\int_{-\infty}^{+\infty} \mathrm{d}z' \chi_{\mathrm{B}}(q,z-z')e^{-q|z'|} \tag{B.22}$$

$$= \phi_{\mathrm{eff}}\frac{1}{2\pi}\int_{-\infty}^{+\infty} \mathrm{d}q_z \chi_{\mathrm{B}}(q,q_z)e^{iq_z z}\int_{-\infty}^{+\infty} \mathrm{d}z' e^{-q|z'|}e^{-iq_z z'} \tag{B.23}$$

$$= \phi_{\mathrm{eff}}\frac{q}{\pi}\int_{-\infty}^{+\infty} \mathrm{d}q_z \frac{\chi_{\mathrm{B}}(q,q_z)}{q^2+q_z^2}e^{iq_z z}. \tag{B.24}$$

The induced potential $\phi_{\mathrm{ind,m}}$ (not to be confused with the induced potential $\phi_{\mathrm{ind}}e^{-qz}$

outside the medium) is

$$\phi_{\mathrm{ind,m}}(q,z) = \int_{-\infty}^{+\infty} \mathrm{d}z'\, \delta n(q,z') \frac{e^2}{4\pi\epsilon_0} \frac{2\pi}{q} e^{-q|z-z'|} \tag{B.25}$$

$$= 2\phi_{\mathrm{eff}} \frac{e^2}{4\pi\epsilon_0} \int_{-\infty}^{+\infty} \mathrm{d}q_z \frac{\chi_{\mathrm{B}}(q,q_z)}{q^2+q_z^2} e^{iq_z z} \int_{-\infty}^{+\infty} \mathrm{d}z' e^{-q|z-z'|} e^{iq_z z'} \tag{B.26}$$

$$= 4\phi_{\mathrm{eff}} \frac{e^2}{4\pi\epsilon_0} \int_{-\infty}^{+\infty} \mathrm{d}q_z \frac{q\chi_{\mathrm{B}}(q,q_z)}{(q^2+q_z^2)^2} e^{iq_z z}. \tag{B.27}$$

At this point, we may introduce the bulk dielectric function $\epsilon(q,q_z)$. For the bulk interacting density response function, the RPA Dyson equation (B.10) reduces to

$$\chi_{\mathrm{B}}(q,q_z) = \frac{\chi^0_{\mathrm{B}}(q,q_z)}{1 - \frac{e^2}{\epsilon_0(q^2+q_z^2)}\chi^0_{\mathrm{B}}(q,q_z)}. \tag{B.28}$$

The dielectric function being defined according to $\epsilon(q,q_z) = 1 - \frac{e^2}{\epsilon_0(q^2+q_z^2)}\chi^0_{\mathrm{B}}(q,q_z)$, we have the relation

$$\chi_{\mathrm{B}}(q,q_z) = \frac{\epsilon_0(q_z^2+q^2)}{e^2}\left(\frac{1}{\epsilon(q,q_z)} - 1\right). \tag{B.29}$$

When inserting this relation into eq. (B.27), we need to compute the integral

$$I(q) = \int_{-\infty}^{+\infty} \mathrm{d}q_z \frac{e^{iq_z z}}{q^2+q_z^2} = \frac{1}{q}\int_{-\infty}^{+\infty} \mathrm{d}u \frac{e^{iuqz}}{1+u^2}. \tag{B.30}$$

Specialising to the case $z<0$, and noticing that the integrand has poles at i and $-i$, we may close the integration path in the lower complex plane, so that

$$I(q) = -\frac{2i\pi}{q} \operatorname*{Res}_{u=-i}\left[\frac{e^{iuqz}}{1+u^2}\right] = \frac{\pi}{q}e^{qz}. \tag{B.31}$$

Finally,

$$\phi_{\mathrm{ind,m}}(q,z) = \phi_{\mathrm{eff}}\left(\frac{q}{\pi}\int_{-\infty}^{+\infty} \frac{e^{iq_z z}}{(q^2+q_z^2)\epsilon(q,q_z)} - e^{qz}\right), \tag{B.32}$$

so that the total potential in the half-space $z<0$ is

$$\phi_m(q,z) = \phi_{\mathrm{eff}}e^{qz} + \phi_{\mathrm{ind,m}}(q,z) = \phi_{\mathrm{eff}}\frac{q}{\pi}\int_{-\infty}^{+\infty} \frac{e^{iq_z z}}{(q^2+q_z^2)\epsilon(q,q_z)}. \tag{B.33}$$

We now need to determine ϕ_{eff} in the actual semi-infinite medium by enforcing the boundary conditions at the surface, which are, as in the local case (section 3.1), continuity of the potential and of the displacement field. Outside the medium, we may still express the potential as $\phi_{\mathrm{ext}}e^{qz} + \phi_{\mathrm{ind}}e^{-qz}$: the sum of the actual potential we are applying and the potential induced by the medium. The displacement field is produced only by the external charges, hence $\mathbf{D}(q,z) = -\epsilon_0\nabla\phi_{\mathrm{eff}}(q,z)$ in the half-space $z<0$, so that the boundary conditions read:

$$\begin{aligned} \phi_{\mathrm{ext}} + \phi_{\mathrm{ind}} &= q\ell_q\phi_{\mathrm{eff}} \\ \phi_{\mathrm{ext}} - \phi_{\mathrm{ind}} &= \phi_{\mathrm{eff}}. \end{aligned} \tag{B.34}$$

We deduce

$$\phi_{\text{ind}} = \frac{q\ell_q - 1}{q\ell_q + 1}\phi_{\text{ext}}, \tag{B.35}$$

and, given that $\phi_{\text{ind}} = -g(q,\omega)\phi_{\text{ext}}$ (see section B.2), we recover eq. (B.20). As in the long wavelength limit, if we take into account screening of the induced potential by a local dielectric medium of permittivity ϵ_w at $z > 0$, the result generalises to

$$g(q,\omega) = \frac{1 - \epsilon_w q\ell_q(\omega)}{1 + \epsilon_w q\ell_q(\omega)}. \tag{B.36}$$

Appendix C

Theory of ionic Coulomb blockade

Contents

C.1 Equilibrium properties: Coulomb gas theory

Our computation is inspired by the original solution of the 1D Coulomb gas model by Lenard and Edwards [112], and subsequent studies by Demery, Dean and coworkers [113, 243–245], as well as Shklovskii and coworkers [107, 109].

C.1.1 Model definition

We consider a one-dimensional lattice with sites $1, \ldots, M$ as a model for the nanochannel of radius R and length L. Each lattice site i carries a spin S_i, which takes the values $\{0, 1, -1\}$, corresponding respectively to no ion, a positive ion, or a negative ion occupying the site. We model the surface charge distribution as an extra fixed charge q_i added at each lattice site. The spins interact with the Hamiltonian

$$\mathcal{H}(\{S_i\}) = \frac{\xi}{2x_T} \sum_{i,j=1}^{M} (S_i + q_i)(S_j + q_j) e^{-|i-j|/\xi} \equiv \frac{1}{2x_T} (S+q)^T C (S+q), \tag{C.1}$$

where we have taken $k_BT = 1$. The system is in contact with a particle reservoir with bulk density ρ_0. Here the parameters ξ and x_T are dimensionless, expressed in number of lattice sites. Their relationship to the geometrical parameters is discussed in Appendix A.1.

C.1.2 General solution

The grand partition function is given by

$$\Xi = \sum_{S_1,\dots,S_M} z^{\sum_i |S_i|} e^{-\frac{1}{2x_T}(S+q)^T C (S+q)}, \tag{C.2}$$

with $z = \rho_0 \pi R^2 L/M$ the fugacity. The matrix C can be analytically inverted:

$$C^{-1} = \frac{1}{2\xi \sinh(1/\xi)} \cdot \begin{pmatrix} e^{1/\xi} & -1 & 0 & 0 & \dots & 0 & 0 \\ -1 & 2\cosh(1/\xi) & -1 & 0 & \dots & 0 & 0 \\ \vdots & \ddots & \ddots & \ddots & & \vdots & \vdots \\ \vdots & & \ddots & \ddots & \ddots & \vdots & \vdots \\ \vdots & & & \ddots & \ddots & \ddots & \vdots \\ 0 & 0 & \dots & 0 & -1 & 2\cosh(1/\xi) & -1 \\ 0 & 0 & \dots & \dots & 0 & -1 & e^{1/\xi} \end{pmatrix}. \tag{C.3}$$

Hence we can carry out a Hubbard-Stratonovich transformation, that is rewrite the partition function as a gaussian integral, introducing the integration variable ϕ:

$$\Xi = \sqrt{\frac{x_T^M}{(2\pi)^M \det(C)}} \cdot \sum_{S_1,\dots,S_M} z^{\sum_i |S_i|} \int \mathrm{d}\phi e^{-\frac{x_T}{2}\phi^T C^{-1}\phi + i(S+q)^T\phi}, \tag{C.4}$$

with $\det(C) = \frac{e^{1/\xi}}{2\sinh(1/\xi)} \cdot \left[\xi(1-e^{-2/\xi})\right]^M$. After performing the sum over the spins, which is now decoupled, we obtain

$$\Xi = \sqrt{\frac{x_T^M}{(2\pi)^M \det(C)}} \cdot \int \mathrm{d}\phi_1 \dots \mathrm{d}\phi_M \prod_{j=1}^{M} (1 + 2z\cos\phi_j) \prod_{j=1}^{M} e^{iq_j\phi_j} \dots$$
$$\exp\left(-\frac{x_T}{4\xi\sinh(1/\xi)} \left[\sum_{j=1}^{M-1} (\phi_{j+1} - \phi_j)^2 + 2(\cosh(1/\xi) - 1) \sum_{j=2}^{M-1} \phi_j^2 + (e^{1/\xi} - 1)(\phi_1^2 + \phi_M^2) \right] \right). \tag{C.5}$$

We now take a continuum limit of the lattice model. We call a the physical lattice spacing and let $\tilde{\xi} = a\xi$, $\tilde{x}_T = a x_T$ and $\tilde{z} = Mz$. We then let $a \to 0$ and $M \to \infty$ while keeping the physical length of the system $L = aM$ constant. We then drop the tilde sign to lighten the notation and obtain

$$\Xi = \int \mathrm{d}\phi(0) e^{-x_T\phi(0)^2/4\xi} \int [\mathrm{d}\phi] e^{-S[\phi]} \int \mathrm{d}\phi(L) e^{-x_T\phi(L)^2/4\xi} \tag{C.6}$$

with

$$S[\phi] = \int_0^L \mathrm{d}x \left[\frac{x_T}{4} \left(\frac{\mathrm{d}\phi}{\mathrm{d}x} \right)^2 + \frac{x_T}{4\xi^2}\phi(x)^2 - iq(x)\phi(x) - \frac{2z}{L}\cos\phi(x) \right] \equiv \int_0^L \mathcal{L}(\phi, \dot{\phi}). \tag{C.7}$$

$q(x)$ is the one-dimensional density corresponding to the surface charge, and we have changed the notation to $z \equiv \pi R^2 L \rho_0$. At this point ξ and x_T have the dimension of length. The path integral measure is defined as

$$[\mathrm{d}\phi] = \lim_{\substack{a\to 0 \\ M\to\infty \\ L=aM}} \left[\prod_{j=1}^{M} \sqrt{\frac{x_T}{4\pi a}} \mathrm{d}\phi_j \right]. \tag{C.8}$$

We now define the propagator $P(\phi, x|\phi_0, 0)$, or simply $P(\phi, x)$, as

$$P(\phi, x) = \int \mathrm{d}\phi(x)\delta(\phi(x) - \phi) \int [\mathrm{d}\phi] e^{-\int_0^x \mathcal{L}(\phi,\dot{\phi})} \int \mathrm{d}\phi(0)\delta(\phi(0) - \phi_0). \tag{C.9}$$

Considering an infinitesimal displacement Δx,

$$\begin{aligned} P(\phi, x) = \sqrt{\frac{x_T}{4\pi\Delta x}} \int \mathrm{d}(\Delta\phi) P(\phi - \Delta\phi, x - \Delta x) \dots \\ \dots \exp\left(- \int_{x-\Delta x}^{x} \mathrm{d}x' \left[\frac{x_T}{4} \left(\frac{\Delta\phi}{\Delta x} \right)^2 + \frac{x_T}{4\xi^2}\phi^2 - iq(x)\phi - \frac{2z}{L}\cos\phi \right] \right). \end{aligned} \tag{C.10}$$

Expanding the propagator as $P(\phi - \Delta\phi, x - \Delta x) = P(\phi, x) - \Delta x \partial P/\partial x - \Delta\phi \partial P/\partial\phi + (1/2)(\Delta\phi^2)\partial^2 P/\partial\phi^2$, and carrying out the gaussian integrals, we obtain

$$\begin{aligned} P(\phi, x) = \left(P(\phi, x) - \Delta x \frac{\partial P}{\partial x} + O(\Delta x^2) \right) \left(1 - \Delta x \left[\frac{x_T}{4\xi^2}\phi^2 - iq(x)\phi - \frac{2z}{L}\cos\phi \right] + O(\Delta x^2) \right) \\ + \frac{\Delta x}{x_T} \frac{\partial^2 P}{\partial x^2} (1 + O(\Delta x)). \end{aligned} \tag{C.11}$$

$P(\phi, x)$ thus solves the partial differential equation

$$\frac{\partial P}{\partial x} = \frac{1}{x_T} \frac{\partial^2 P}{\partial \phi^2} + \left(iq\phi - \frac{x_T}{4\xi^2}\phi^2 + \frac{2z}{L}\cos\phi \right) P, \tag{C.12}$$

with initial condition $P(\phi, 0) = \delta(\phi - \phi_0)$ which is the equivalent of a Schrödinger equation for the path integral representation (C.6). The partition function can thus be computed as

$$\Xi = \int \mathrm{d}\phi(L) e^{-x_T \phi^2/4\xi} P(\phi, L|f_0), \tag{C.13}$$

where $P(\phi, L|f_0)$ is the solution of (C.12) with initial condition $P(\phi, 0) = f_0(\phi) \equiv e^{-x_T\phi^2/4\xi}$, which can be easily obtained by finite difference numerical integration.

C.1.3 Observables

In the lattice model, the probability to find, say, a positive ion at position k, can be computed by replacing a factor $(1+2z\cos\phi_k)$ by $ze^{i\phi_k}$:

$$\langle \rho_k^+ \rangle = \frac{1}{\Xi}\int \mathrm{d}\phi_1 \dots \mathrm{d}\phi_M \prod_{j\neq k}(1+2z\cos\phi_j) z e^{i\phi_k} \prod_{j=1}^{M} e^{iq\phi_j} \dots$$
$$\exp\left(-\frac{x_T}{4\xi\sinh(1/\xi)}\left[\sum_{j=1}^{M-1}(\phi_{j+1}-\phi_j)^2 + 2(\cosh(1/\xi)-1)\sum_{j=2}^{M-1}\phi_j^2 + (e^{1/\xi}-1)(\phi_1^2+\phi_M^2)\right]\right). \tag{C.14}$$

Thus, taking the continuum limit, one can compute the average positive ion density by inserting the operator $ze^{i\phi}$ at position x:

$$\langle \rho^+(x)\rangle = \frac{1}{\Xi}\int \mathrm{d}\phi(0)\mathrm{d}\phi(x)\mathrm{d}\phi(L) e^{-x_T\phi(0)^2/4\xi} P(\phi(x),x|\phi(0),0)\dots$$
$$\dots z e^{i\phi(x)} P(\phi(L),L|\phi(x),x) e^{-x_T\phi(L)^2/4\xi}, \tag{C.15}$$

which can again be obtained by finite differences. Let us now compute the electrostatic potential Φ at a lattice point j_0. One has

$$\begin{aligned}\frac{\partial \Xi}{\partial q_{j_0}} &= \sum_{S_1,\dots,S_M}\left[-\frac{1}{x_T}\sum_i (S_i+q_i)C_{ij_0}\right] z^{\sum_i |S_i|} e^{-\mathcal{H}(\{S_i\})} \\ &= \sum_{S_1,\dots,S_M}\left[-\frac{\xi}{x_T}\sum_i (S_i+q_i)e^{-|i-j_0|}\right] z^{\sum_i |S_i|} e^{-\mathcal{H}(\{S_i\})} \equiv -\langle \Phi_{j_0}\rangle \cdot \Xi\end{aligned} \tag{C.16}$$

Now looking at eq. (C.5), differentiating Ξ with respect to q_{j_0} corresponds to inserting a factor $i\phi_{j_0}$, thus in the continuum limit the electrostatic potential is computed by inserting an operator $-i\phi$:

$$\langle \Phi(x)\rangle = \frac{1}{\Xi}\int \mathrm{d}\phi(0)\mathrm{d}\phi(x)\mathrm{d}\phi(L) e^{-x_T\phi(0)^2/4\xi} P(\phi(x),x|\phi(0),0)\dots$$
$$\dots (-i\phi(x)) P(\phi(L),L|\phi(x),x) e^{-x_T\phi(L)^2/4\xi}. \tag{C.17}$$

C.1.4 Effect of ion valence

So far we have only considered monovalent ions. Ions of valence p could be taken into account by having the spins S_i take the values $\{p,0,-p\}$ instead of $\{1,0,-1\}$. The action (C.7) then becomes

$$S[\phi] = \int_0^L \mathrm{d}x \left[\frac{x_T}{4}\left(\frac{\mathrm{d}\phi}{\mathrm{d}x}\right)^2 + \frac{x_T}{4\xi^2}\phi(x)^2 - iq(x)\phi(x) - \frac{2z}{L}\cos p\phi(x)\right], \tag{C.18}$$

or, after a change of variable,

$$S[\phi] = \int_0^L \mathrm{d}x \left[\frac{(x_T/p^2)}{4}\left(\frac{\mathrm{d}\phi}{\mathrm{d}x}\right)^2 + \frac{(x_T/q^2)}{4\xi^2}\phi(x)^2 - i(q(x)/p)\phi(x) - \frac{2z}{L}\cos\phi(x)\right]. \tag{C.19}$$

Thus any property for ions of valence p will be the same as for ions with valence 1, with p^2 times stronger interactions and p times smaller surface charge.

C.1.5 Mean-field approximation

The mean-field version of the Coulomb gas model is obtained by taking a saddle point approximation in path integral (C.6). Minimising the action (C.7) with respect to the function $\phi(x)$, we obtain a differential equation for $\phi(x)$:

$$\frac{x_T}{2}\frac{\mathrm{d}^2\phi}{\mathrm{d}x^2} = \frac{x_T}{2\xi^2}\phi - iq + \frac{2z}{L}\sin\phi. \tag{C.20}$$

Following the argument in section C.1.3, we identify the dimensionless electrical potential as $\Phi = -i\phi$. Thus Φ satisfies

$$\left(\frac{\mathrm{d}^2}{\mathrm{d}x^2} - \frac{1}{\xi^2}\right)\Phi = -\frac{2q}{x_T} + \frac{4z}{Lx_T}\sinh\Phi. \tag{C.21}$$

Now using $x_T = R^2/(2\ell_B) = 2\pi\epsilon_0\epsilon_w R^2/e^2$ (we still take $k_BT = 1$) and $z = \rho_0\pi R^2 L$, we obtain

$$\left(\frac{\mathrm{d}^2}{\mathrm{d}x^2} - \frac{1}{\xi^2}\right)\Phi(x) = -\frac{q(x)}{\epsilon_w\epsilon_0} + \frac{2\rho_0}{\epsilon_w\epsilon_0}\sinh\Phi(x). \tag{C.22}$$

This the equivalent of the Poisson-Boltzmann equation (that is, the Poisson-Nernst-Planck equations at equilibrium) for our system. The dashed black line in figure 3.2a corresponds to the numerical solution of eq. (C.22). It could have also been derived in the standard way from the Boltzmann distribution of ions in the electrostatic potential Φ, which solves the modified Poisson equation $(\mathrm{d}^2/\mathrm{d}x^2 - 1/\xi^2)\Phi = -\rho_c/(\epsilon_w\epsilon_0)$, with ρ_c the charge density.

C.1.6 Self-energy

An ion confined in the channel creates an electric field $\mathbf{E}(x)$ such that $|E(x)| = e^{-|x|/\xi}/x_T$. Thus, it has an electrostatic self-energy

$$E_s = \pi R^2 \int \mathrm{d}x \frac{\epsilon}{2} E(x)^2 = \pi R^2 \frac{\epsilon}{2x_T^2}\xi = \frac{\xi}{2x_T}. \tag{C.23}$$

One can check that this self-energy is taken into account in the hamiltonian (C.1): each particle contributes $\frac{\xi}{2x_T}$ to the system's energy.

C.1.7 Fourier space and thermodynamic limit

In practice, equation (C.12), is most easily solved in Fourier space. We define

$$\tilde{P}(k,x) = \frac{1}{\sqrt{2\pi}}\int \mathrm{d}\phi e^{-ik\phi}P(\phi,x). \tag{C.24}$$

Then $\tilde{P}(k,x)$ satisfies

$$\frac{\partial\tilde{P}}{\partial x} = -\frac{k^2}{x_T}\tilde{P} - q\frac{\partial\tilde{P}}{\partial k} + \frac{x_T}{4\xi^2}\frac{\partial^2\tilde{P}}{\partial k^2} + \frac{z}{L}\left[\tilde{P}(k+1,x) + \tilde{P}(k-1,x)\right], \tag{C.25}$$

or, defining $\tilde{x} \equiv x/x_T$ (and $\tilde{L} \equiv L/x_T$),

$$\frac{\partial \tilde{P}}{\partial \tilde{x}} = -k^2 \tilde{P} - q x_T \frac{\partial \tilde{P}}{\partial k} + \frac{x_T^2}{4\xi^2} \frac{\partial^2 \tilde{P}}{\partial k^2} + z_T \left[\tilde{P}(k+1, \tilde{x}) + \tilde{P}(k-1, \tilde{x}) \right]. \tag{C.26}$$

qx_T is the number of surface charges per length x_T, and $z_T = \rho_0 \pi R^2 x_T$ is the number of ions per length x_T if the density in the channel was the same as in the reservoir.

The term proportional to $\partial \tilde{P}/\partial k$ in eq. (C.26) is an advection term: it induces a drift in k space, by an amount which equals the total surface charge Q. We assume from now on that the distribution $q(x)$ is reduced to a point: $q(x) = Q\delta(x - L/2)$, or, after the change of variable, $q(\tilde{x}) = (Q/x_T)\delta(\tilde{x} - \tilde{L}/2)$. Then, the effect of the advection term is an infinitely fast shift by an amount Q, that is the action of an operator

$$S_Q : f \mapsto (g : k \mapsto f(k - Q)). \tag{C.27}$$

Let us also define the operator $\mathcal{T}$ such that

$$[\mathcal{T}(\tilde{P})](k) = -k^2 \tilde{P} + \frac{x_T^2}{4\xi^2} \frac{\partial^2 \tilde{P}}{\partial k^2} + z_T \left[\tilde{P}(k+1, \tilde{x}) + \tilde{P}(k-1, \tilde{x}) \right], \tag{C.28}$$

which plays the role of a functional transfer matrix. Recalling eq. (C.13), the partition function then reads

$$\Xi = \langle f_0 | e^{\frac{\tilde{L}}{2}\mathcal{T}} S_Q e^{\frac{\tilde{L}}{2}\mathcal{T}} | f_0 \rangle \tag{C.29}$$

with $f_0(k) = e^{-\xi k^2/x_T}$ and $\langle f(k) | g(k) \rangle \equiv \int \mathrm{d}k f^*(k) g(k)$.

Now in the limit $L \to \infty$, we may consider the largest eigenvalue λ of the operator $\mathcal{T}$, and the associated eigenfunction χ:

$$[\mathcal{T}(\chi)](k) = \lambda \chi(k). \tag{C.30}$$

Then, up to an exponentially small correction,

$$\Xi = |\langle f_0 | \chi \rangle|^2 \langle \chi(k) | \chi(k - Q) \rangle e^{\lambda \tilde{L}}. \tag{C.31}$$

C.1.8 Observables in the thermodynamic limit

The insertion of $e^{i\phi}$ in direct space is the equivalent of a unit shift in Fourier space. Hence the ion density at a point $\tilde{x}$ (assuming for simplicity $\tilde{x} < \tilde{L}/2$) is given by

$$\langle \rho_\pm(\tilde{x}) \rangle = z_T \frac{\langle \chi(k - Q) | [e^{-(\tilde{L}/2 - \tilde{x})\mathcal{T}} \cdot \chi(k \mp 1)] \rangle}{\langle \chi(k - Q) | [e^{-(\tilde{L}/2 - \tilde{x})\mathcal{T}} \cdot \chi(k)] \rangle}, \tag{C.32}$$

in ions per length x_T. The function χ can be computed by finite difference integration of eq. (C.26): in practice, we start from the initial condition $\tilde{P}(k, 0) = f_0(k)$ and carry out the integration until convergence to the eigenfunction. Further numerical integration allows to compute $[e^{-(\tilde{L}/2 - \tilde{x})\mathcal{T}} \cdot \chi(k)]$. We define the neutralising charge $N(Q)$ as the average charge in the interval $[L/2 - 1.25\ \mathrm{nm}; L/2 + 1.25\ \mathrm{nm}]$, which can thus be computed by integration of the density obtained from eq. (C.32). The plots of $N(Q)$ versus Q obtained in such a way were used to obtain the data in figure 3.4. In an uncharged channel (or far away from the surface charge), eq. (C.32) is reduced to

$$\langle \rho_\pm^{\mathrm{bulk}} \rangle = z_T \frac{\langle \chi(k) | \chi(k \mp 1) \rangle}{\langle \chi(k) | \chi(k) \rangle}, \tag{C.33}$$

Insertion of $-i\phi(x)$ in direct space corresponds to differentiating with respect to $q(x)$ in Fourier space. Hence, in particular, the potential at $x = L/2$ can be computed as

$$\langle \Phi(L/2) \rangle = -\frac{\langle \chi(k) | \chi'(k-Q) \rangle}{\langle \chi(k) | \chi(k-Q) \rangle}. \tag{C.34}$$

In the Coulomb blockade regime, the $N(Q)$ ions are closely bound to the surface charge. Since an ion creates in its immediate vicinity a potential ξ/x_T, $[N(Q)+Q](\xi/x_T) = \langle \Phi(L/2) \rangle$, and therefore the neutralising charge is

$$N(Q) = -Q - \frac{x_T}{\xi} \frac{\langle \chi(k) | \chi'(k-Q) \rangle}{\langle \chi(k) | \chi(k-Q) \rangle}. \tag{C.35}$$

C.1.9 Strong coupling approximation

Strong interactions correspond to low values of x_T and, if ρ_0 is not too large, then the condition $z_T \ll 1$ holds. For instance, in our simulations, $x_T = 0.09$ nm, and for a channel of radius $R = 0.5$ nm, $z_T = 0.042 \times \rho_0$ (in M). Thus, for describing our system in the Coulomb blockade regime, it is reasonable to consider only the first terms in the expansion of observables in powers of z_T. To obtain such an expansion, we first need to compute the function χ. Equation (C.26) without the diffusion term,

$$\frac{\partial \tilde{P}}{\partial \tilde{x}} = -k^2 \tilde{P} + z_T \left[\tilde{P}(k+1, \tilde{x}) + \tilde{P}(k-1, \tilde{x}) \right], \tag{C.36}$$

is actually the Fourier-transformed Mathieu equation, and methods for computing the Fourier coefficients of its highest periodic eigenfunction χ_0 are known from the mathematical literature [246] (see section C.1.12):

$$\chi_0(k) = \frac{1}{2} \left[a_0 \delta(k) + \sum_{i>0} a_i (\delta(k-i) + \delta(k+i)) \right] \tag{C.37}$$

with

$$a_0 = 2 \tag{C.38}$$

$$a_1 = 2z_T - \frac{7}{2} z_T^3 + \frac{116}{9} z_T^5 + O(z_T^7) \tag{C.39}$$

$$a_2 = \frac{1}{2} z_T^2 - \frac{10}{9} z_T^4 + O(z_T^6) \tag{C.40}$$

$$a_3 = \frac{1}{18} z_T^3 - \frac{13}{96} z_T^5 + O(z_T^7) \tag{C.41}$$

$$a_4 = \frac{1}{288} z_T^4 + O(z_T^6) \tag{C.42}$$

$$a_{p>4} = O(z_T^p) \tag{C.43}$$

The function $\chi_0(k)$ is represented by an ensemble of discrete peaks at integer values of k. The effect of the diffusion term in eq. (C.26) will be to spread these discrete peaks over a non-zero width. In practice, keeping the diffusion term and taking $z_T = 0$, equation (C.26) becomes

$$\frac{\partial \tilde{P}}{\partial \tilde{x}} = -k^2 \tilde{P} + \frac{x_T^2}{4\xi^2} \frac{\partial^2 \tilde{P}}{\partial k^2}, \tag{C.44}$$

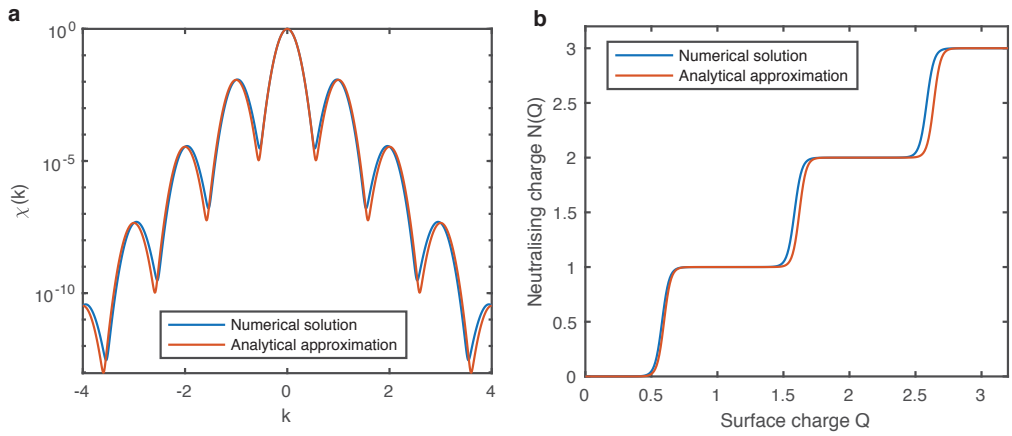

Figure C.1

a. Function $\chi(k)$, as computed by finite differences from equation (C.26), and analytically from equation (C.46), with $z_T = 0.012$ ($x_T = 0.9$Å and $\rho_0 = 0.28$ M). **b.** Neutralising charge $N(Q)$, as computed by finite differences from equation (C.32), and analytically from equation (C.47), with $z_T = 0.012$ ($x_T = 0.9$Å and $\rho_0 = 0.28$ M).

which is solved by

$$\tilde{P}(k,\tilde{x}) = e^{-\frac{x_T^2}{4\xi^2}\tilde{x}} e^{-\xi k^2/x_T}. \tag{C.45}$$

Thus one may heuristically assume that if the width $\sqrt{x_T/\xi}$ of solution (C.45) is much smaller than 1, an eigenfunction of the operator $\mathcal{T}$ will be well approximated by a set gaussian peaks centred on integer values of k. The highest eigenfunction χ will then be given by

$$\chi(k) = e^{-\xi k^2/x_T} + \frac{1}{2}\sum_{i\in\mathbb{Z}^*} a_{|i|} e^{-\xi(k-i)^2/x_T}. \tag{C.46}$$

This analytical approximation is actually in good agreement with the numerical result obtain from finite differences, as shown in figure C.1.

We can now use equation (C.35) to obtain an analytical expression for the neutralising charge. After computing the gaussian integrals,

$$\boxed{N(Q) = \frac{\sum_{ij} a_i a_j (j-i) e^{-\frac{\xi}{2x_T}(Q-(i-j))^2}}{\sum_{ij} a_i a_j e^{-\frac{\xi}{2x_T}(Q-(i-j))^2}} - Q}\,. \tag{C.47}$$

Figure C.1 shows the neutralising charge obtained by numerical integration from equation (C.32) and the analytical result from equation (C.47). They are in very good agreement, especially for $Q \lesssim 1$, since for larger values of Q higher orders in z_T are involved. The first step ($N(Q), Q \leq 1$) has the simple form

$$N_1(Q) = \frac{1}{1 + \frac{1}{2z_T} e^{-\frac{\xi}{x_T}\left(Q-\frac{1}{2}\right)}}. \tag{C.48}$$

The maximum slope is attained at

$$Q_{\max} = \frac{1}{2} - \frac{x_T}{\xi}\log(2z_T) \tag{C.49}$$

and the corresponding slope is

$$\left.\frac{\mathrm{d}N}{\mathrm{d}Q}\right|_{Q_{\max}} = \frac{\xi}{4x_T} + O(z_T^4), \tag{C.50}$$

so that steps are apparent when $x_T \geq \xi/4$ as stated in Chapter 3. Equation (C.49) shows that the steps are shifted to the right with respect to the half-integer values of Q by an amount that varies as the logarithm of the salt concentration. We thus recover on rigorous grounds the logarithmic dependence that was suggested in ref. [247].

C.1.10 Equation of state

The pressure of the Coulomb gas is defined as

$$P = -\frac{\partial F}{\partial L}, \tag{C.51}$$

with F the free energy. The total number N of ions can be obtained by deriving the free energy with respect to the chemical potential μ (which is the same for positive and negative ions). Given that $z = e^{\mu}$,

$$N = -z\frac{\partial F}{\partial z}. \tag{C.52}$$

Thus, the density is related to the pressure by

$$\rho = \frac{\partial N}{\partial L} = z\frac{\partial P}{\partial z}. \tag{C.53}$$

Now the total ion density can be computed from eq. (C.33), and using eq. (C.46) for the function $\chi(k)$ in the strong coupling approximation, we obtain

$$\rho = 2z_T\frac{\langle\chi(k)|\chi(k-1)\rangle}{\langle\chi(k)|\chi(k)\rangle} = 2z_T\frac{\sum_{ij} a_{|i-1|}a_{|j|}e^{-\frac{\xi}{2x_T}(i-j)^2}}{\sum_{ij} a_{|i|}a_{|j|}e^{-\frac{\xi}{2x_T}(i-j)^2}}, \tag{C.54}$$

the lengths being now expressed in units of x_T. The above sums can be considerably simplified if we may neglect the terms with $i \neq j$. The order p in z_T to which such an approximation is valid is given by

$$z_T^p \sim e^{-\frac{\xi}{2x_T}}, \text{ i.e. } p \sim \frac{\xi}{2x_T\log(1/z_T)}. \tag{C.55}$$

With the parameter values corresponding to our simulations, we obtain $p \sim 4.4$. We therefore neglect the terms with $i \neq j$ and expand the coefficients a_i up to order z_T^4. We obtain:

$$\rho = 4z_T^2 - 14z_T^4 + O(z_T^6) \tag{C.56}$$

and

$$\boxed{P = \frac{\rho}{2}\left(1 + \frac{7}{4}z_T^4 + O(z_T^6)\right)}. \tag{C.57}$$

Thus up to order z_T^4 we obtain the same equation of state as was derived for the ideal Coulomb gas ($\xi \to \infty$) in ref. [245]. It demonstrates that, in the strong coupling limit, the Coulomb gas of density ρ behaves as an ideal gas of density $\rho/2$: the positive and negative ions are associated in tightly bound pairs, that is the salt behaves as a weak electrolyte.

C.1.11 Paired fraction

Since the ions in the Coulomb gas associate in tightly bound pairs, we may be interested in estimating the fraction of paired ions for a given set of parameters. We may only give a qualitative estimate, since it depends on the way we define an ion pair. Consider a negative test charge placed at $x = x_0$ in a homogeneous Coulomb gas ($Q = 0$). If it is in a paired state, then there is a positive charge that we assume to be uniformly distributed in an interval $[x_0 - x_T; x_0 + x_T]$. (At this point, we may have chosen any interval $[x_0 - \lambda x_T, x_0 + \lambda x_T]$, with λ of order 1, which would give a quantitatively different result). The test charge therefore feels a potential

$$\Phi_{\text{paired}} = \frac{1}{x_T}\int_0^{x_T} \frac{\xi}{x_T} e^{-x/\xi} = \left(\frac{\xi}{x_T}\right)^2 (1 - e^{-x_T/\xi}) \equiv \frac{\xi}{x_T} f(x_T). \tag{C.58}$$

If the test charge is unpaired, then it feels a potential Φ_{unpaired} created by a negative charge uniformly distributed in an interval $[x_0 - \delta, x_0 + \delta]$, with $\delta = 1/(2\rho^-)$, ρ^- being the negative ion density:

$$\Phi_{\text{unpaired}} = \frac{\xi}{x_T} f(\delta) \tag{C.59}$$

Now the average potential at the location of the test charge can be computed from eq. (C.34):

$$\Phi(x_0) = -\frac{\langle \chi(k)|\chi'(k+1)\rangle}{\langle \chi(k)|\chi(k+1)\rangle}. \tag{C.60}$$

From the above considerations, if we denote n_p the fraction of paired ions, this potential may also be expressed as

$$\Phi(x_0) = \frac{\xi}{x_T}(n_p f(x_T) + (1 - n_p) f(\delta) - 1). \tag{C.61}$$

We thus obtain the paired fraction as

$$n_p = \frac{((x_T/\xi)\Phi(0) - 1) - f(\delta)}{f(x_T) - f(\delta)}. \tag{C.62}$$

Eq. (C.62) was used to compute the data in figure 3.5.

C.1.12 Solution of the Mathieu equation

In this section, we provide a method for deriving the series expansions of the coefficients a_i (eqs. (C.39)–(C.43)), following ref. [246]. We are looking for a solution of eq. (C.36),

$$\frac{\partial \tilde{P}}{\partial \tilde{x}} = -k^2 \tilde{P} + z_T \left[\tilde{P}(k+1,\tilde{x}) + \tilde{P}(k-1,\tilde{x}) \right], \tag{C.63}$$

in the form

$$\tilde{P}(k,\tilde{x}) = e^{\lambda \tilde{x}} \sum_{i \geq 0} \frac{1}{2} a_i (\delta(k-i) + \delta(k+i)). \tag{C.64}$$

Substituting this ansatz into eq. (C.36) we find the set of equations

$$\begin{cases} \lambda a_0/2 - z_T a_1 = 0 \\ -(\lambda+1)a_1 + z_T a_0 + z_T a_2 = 0 \\ -(\lambda + k^2)a_k + z_T(a_{k+1} + a_{k-1}) = 0, \forall k > 1 \end{cases} \tag{C.65}$$

We now define $\Lambda_k \equiv (\lambda + k^2)/z_T$. Successively rearranging the equations of system (C.65), we obtain

$$\Lambda_0 = \frac{2a_1}{a_0} = \frac{2}{\Lambda_1 - \dfrac{a_2}{a_1}} = \frac{2}{\Lambda_1 - \dfrac{1}{\Lambda_2 - \dfrac{a_3}{a_2}}} = ... \tag{C.66}$$

This yields a closed equation for the Λ_k's in the form of a continued fraction:

$$0 = \Lambda_0 - \cfrac{2}{\Lambda_1 - \cfrac{1}{\Lambda_2 - \cfrac{1}{\Lambda_3 - \cfrac{1}{\Lambda_4 - ...}}}}. \tag{C.67}$$

We can now perturbatively solve eq. (C.67) in the limit of small z_T. Starting at order 2, we have to solve $\Lambda_0 - 2/\Lambda_1 = 0$, which yields two solutions for λ: $\lambda_1 = 2z_T^2 + O(z_T^4)$ and $\lambda_2 = -1 - 2z_T^2 + O(z_T^4)$. Since we are looking for the largest eigenvalue λ we pick only the first solution. Having fixed the coefficient at order 2, we obtain only one solution for λ at the next orders. Iterating the procedure, we obtain the expansion

$$\lambda = 2z_T^2 - \frac{7}{2} z_T^4 + \frac{116}{9} z_T^6 - \frac{68687}{1152} z_T^8 + \frac{123707}{400} z_T^{10} + O(z_T^{12}), \tag{C.68}$$

in agreement with ref. [245]. Knowing the expansion of λ to arbitrary order, we can solve the system (C.65) truncated at the n^{th} equation to obtain the coefficients a_i to the n^{th} order in z_T, yielding eqs. (C.39)–(C.43).

C.2 Bjerrum pair dynamics and fractional Wien effect

The aim of this section is to provide a theory of non-equilibrium ion transport that accounts for the ionic Coulomb blockade phenomenology. From the equilibrium Coulomb gas theory and from the simulations we know that in the Coulomb blockade regime the salt behaves as a weak electrolyte, where the positive and negative ions are strongly

correlated as they from tightly bound pairs. However, it is reasonable to assume that the globally neutral ion pairs are largely uncorrelated. Hence we will study the dynamics of a single ion pair, and then incorporate the statistics of the Coulomb gas in order to describe the fractional Wien effect. *We recall that we use units such that* $k_BT = 1$ *and* $e = 1$.

C.2.1 Lifetime of an ion pair

We consider a mobile ion of charge $+1$, with diffusion coefficient D in one dimension, interacting with a fixed charge $-q$ placed at $x = 0$, under the effect of an electric field E. The two point charges interact with the pairwise potential $V(x) = \frac{\xi}{x_T} e^{-|x|/\xi}$. We wish to compute the average time $\tau(q, E)$ the mobile ion takes to escape from the confining potential $-qV(x) - Ex$, if placed initially at $x = 0$. We follow the well-known method described for example in [116]. The probability distribution $P(x, t)$ of the mobile ion is governed by the Fokker-Planck equation

$$\partial_t P = D\partial_x \left(P\partial_x \left[-qV(x) - Ex\right]\right) + D\partial_x^2 P, \tag{C.69}$$

with initial condition $P(x, 0) = \delta(x)$. We consider the ion has escaped once it has crossed the potential barrier on the right, the crossing point δ being defined by $\frac{\mathrm{d}}{\mathrm{d}x}\left(qV(x) - Ex\right)\big|_{x=\delta} = 0$, that is

$$\delta(q, E) = \xi \log\left(\frac{q}{Ex_T}\right). \tag{C.70}$$

Therefore we place an absorbing boundary condition at $x = \delta$ as schematically depicted in figure 3.4a.

The probability that the ion has already escaped at time t is $1 - \int P(x, t)\mathrm{d}x$. Thus, the probability density for escaping at time t is $-\int \partial_t P(x, t)\mathrm{d}x$, so the average time it takes to escape is

$$\tau(q, E) = \int_0^\infty t\left(-\int_{-\infty}^{+\infty} \partial_t P(x, t)\mathrm{d}x\right)\mathrm{d}t, \tag{C.71}$$

or, after integration by parts,

$$\tau(q, E) = \int_{-\infty}^{+\infty} \mathrm{d}x \int_0^\infty \mathrm{d}t P(x, t). \tag{C.72}$$

We now define the time-integrated probability density $G(x) = \int_0^\infty P(x, t)\mathrm{d}t$, which solves the time-integrated version of eq. (C.69):

$$-\delta(x) = D\partial_x \left(G\partial_x \left[-qV(x) - Ex\right]\right) + D\partial_x^2 G. \tag{C.73}$$

We solve eq. (C.73) enforcing:

- The absorbing boundary condition $G(\delta) = 0$.
- $G(x \to -\infty) = 0$.
- The continuity of G at $x = 0$, $G(0+) = G(0-)$.
- The discontinuity of $\partial_x G$ as imposed by the δ function: $\partial_x G|_{0^+} - \partial_x G|_{0^-} - qG(0)(\partial_x V|_{0^+} - \partial_x V|_{0^-}) = -1/D$.

We find a solution

$$G(x) = \frac{1}{D}\int_{\max(0,x)}^{\delta} e^{q(V(x)-V(y))+E(x-y)}\mathrm{d}y, \tag{C.74}$$

hence the mean escape time

$$\tau(q,E) = \int_{-\infty}^{+\infty} G(x)\mathrm{d}x = \frac{1}{D}\int_{-\infty}^{+\infty}\int_{\max(0,x)}^{\xi\log\frac{q}{Ex_T}} e^{q(V(x)-V(y))+E(x-y)}\mathrm{d}y\mathrm{d}x. \tag{C.75}$$

If we are considering a mobile ion coupled to an effective surface charge q, then the average lifetime of such a pair is indeed $\tau(q,E)$. But our computation also applies to a bulk ion pair: one should take $q=1$ and replace the diffusion coefficient D by $2D$ since both ions are mobile. Therefore the average lifetime of a bulk ion pair is $\tau(1,E)/2$.

C.2.2 From pair lifetime to ionic current

We shall separately consider the current resulting from ions dissociating from the fractional surface charge and from bulk ion pairs breaking apart.

The contribution from the surface charge dominates the ionic current at low electric fields, when bulk ion pairs do not dissociate. When all the bulk ions are paired, an ion that dissociates from the surface charge moves unhindered at a velocity DE, dragged by the electric field, through the periodic boundary condition, until it comes back to bind to the surface charge, after a time $t_f = L/(DE)$. We assume that the Grotthus-like exchange does not significantly affect t_f. Thus, an ion bound to an effective surface charge q is actually free for a fraction $t_f/(t_f+\tau(q,E))$ of the time, during which it contributes $I_0 = 1/t_f$ to the ionic current, so the resulting average current is

$$I_q(E) = \frac{t_f}{t_f+\tau(q,E)} I_0. \tag{C.76}$$

At larger electric fields, when the bulk ion pairs start to dissociate, the contribution of the single ion that may be released by the surface charge becomes negligible. Let N be the total number of positive ions and N_f the average number of free positive ions. When a bulk pair dissociates, the two free ions which are released travel in opposite directions, each producing a current I_0, until they encounter a free ion of the opposite sign, which occurs on average after a time $t_f/(2N_f)$. Thus N_f solves the self-consistent equation

$$\frac{N_f}{N} = \frac{t_f/N_f}{t_f/N_f+\tau(1,E)}, \tag{C.77}$$

from which we find N_f and the resulting positive ion current,

$$I^+_{\mathrm{bulk}}(E) = N_f I_0 = \frac{t_f}{2\tau(1,E)}\left(\sqrt{1+\frac{4N\tau(1,E)}{t_f}}-1\right) I_0. \tag{C.78}$$

C.2.3 Coulomb gas statistics and effective charge

We now discuss the value of the effective charge q. In the Coulomb blockade regime a surface charge Q can bind either $\lfloor Q\rfloor$ counterions with probability $1-p(Q)$ or $\lfloor Q\rfloor+1$

counterions with probability $p(Q)$. In the first case, all the counterions feel an effective charge which is larger than 1, so that the contribution to the current from their dissociation is negligible with respect to the contribution of bulk ion pairs. In the second case, however, there is a counterion which feels a charge $q = Q - \lfloor Q \rfloor < 1$ and may therefore have a non-negligible contribution to the current. The average number of counterions is $N(Q) = (1 - p(Q))\lfloor Q \rfloor + p(Q)(\lfloor Q \rfloor + 1)$, hence $p(Q) = N(Q) - \lfloor Q \rfloor$, with $N(Q)$ known from the equilibrium Coulomb gas theory (eq. (C.47)). If we admit that the current values can be averaged with the grand canonical probabilities of the corresponding numbers of counterions, we obtain an expression for the total positive ion current in the whole electric field range:

$$I^+(E) = (N(Q) - \lfloor Q \rfloor) I_{Q-\lfloor Q \rfloor}(E) + I^+_{\text{bulk}}(E). \tag{C.79}$$

The result given by this equation is plotted in figure 3.4.

C.2.4 Discussion

The first theory of the Wien effect was famously established by Onsager in 1934 [114]. However, it applies to the case of a three-dimensional electrolyte, interacting with a $1/r$ Coulomb potential. With our one-dimensional electrolyte and effective potential $V(x)$, we could not exactly follow Onsager's approach. Onsager computes the normalised two-point function $g(r) = \langle \rho_+(r)\rho_-(0)\rangle / (\langle \rho_+ \rangle \langle \rho_- \rangle)$, which solves the Fokker-Planck equation

$$\nabla \cdot (g \nabla [-V(\mathbf{r}) - Ex]) + \nabla^2 g = 0. \tag{C.80}$$

If $V(\mathbf{r})$ is a real Coulomb potential, it solves $\nabla^2 V = 0$, and thus a constant function is a solution of (C.80). Solutions of (C.80) can then be decomposed as a sum of a constant function, which corresponds to dissociated ion pairs, and a function which goes to 0 at infinity, which corresponds to tightly bound pairs. Onsager shows that the probability currents corresponding to these two solutions give access respectively to the association and dissociation rates of ion pairs. However, our one-dimensional effective potential $V(x)$ does not solve $\partial_x^2 V = 0$, hence no such decomposition is possible. The 1D solution of (C.80) satisfying $g(\pm\infty) = 1$ is

$$g^E(x) = E e^{V(x)+Ex} \int_x^{+\infty} e^{-V(y)-Ey} \mathrm{d}y, \tag{C.81}$$

but it does not give a straightforward access to the average number of ion pairs. One may resort to the drastic approximation used by Liu [248,249], which amounts to assimilating a ratio of integrals of g to a ratio of values at $x = 0$ at small electric fields. In this approximation the relative increase in the number N_f of free ions when applying an electric field E is given by

$$\frac{N_f(E)}{N_f(0)} = \sqrt{\frac{g^0(0)}{g^E(0)}} = \left(E \int_0^{+\infty} e^{-V(y)-Ey} \mathrm{d}y \right)^{-1/2}. \tag{C.82}$$

Unfortunately this result does not agree well with simulations, nor with our escape rate theory.

Even if the technical difficulties related to an Onsager-type approach could be overcome, it would not take into account correlations between ion pairs. While these correlations are negligible in three dimensions, they are important in one dimension: two

unpaired ions of opposite sign will necessarily encounter each other. The escape rate approach, on the contrary, does allow to take such correlations into account: for instance, they are introduced by eq. (C.77). In three dimensions, escape rate approaches have been attempted [250], but they could only proceed through strong approximations, and the end results thus poorly compared with Onsager's theory and with simulations [249].

Appendix D

Theory of two-dimensional electrolytes

Contents

D.1 Model definition

Our theoretical analysis of the equilibrium structure of 2D electrolytes is based on the 2D Coulomb gas model [106, 126], which we modify to take into account that nanofluidic slits are not exactly 2D systems. Therefore, we refer to our model as a '$2D^+$' Coulomb gas model. We assume ions to be rigid spheres of radius r_0 with a discrete charge ± 1 at their center that can freely move in a 2D plane located at the center of the slit. This approximation is justified as long as the potential created by an ion does not sensibly vary across the slit. For typical values of parameters, we find its relative variation is indeed less than a percent. Furthermore, ion pairs have a typical size of 4 Å in the case of NaCl, exceeding the vertical space available to the electrolyte between the confining sheets. This greatly constrains their rotational dregrees of freedom, and confirms the validity of our $2D^+$ approximation

Anions and cations are assumed to have same size, mass, valence and diffusion coefficient D. Results for ions with different valence (like $CaCl_2$) can be obtained in a similar way. Lastly, the pairwise interaction potential, derived in next section, is found to be for a $Z:Z$ electrolyte (Z the valence, charge $q_i = \pm Z$):

$$\beta V_{ij}(r) = -\frac{q_i q_j}{T^*} \log \frac{r}{r+\xi}, \tag{D.1}$$

which strongly resembles the interaction potential of the 2D Coulomb gas, and heavily deviates from Coulomb's law for bulk electrolytes, which is only recovered for $r \gg \xi$. The dielectric confinement length ξ can thus be interpreted as the distance over which electrostatic interactions are effectively 2D. Our computations will sometime consider the case where $\beta V_{ij}(r) = -\frac{q_i q_j}{T^*} \log r$, which we will refer to as the *exact* 2D Coulomb gas (2DCG) model. In many cases – where ξ happens to be much larger than any other relevant lengthscale – the 2DCG model provides reasonable predictions, matching the results of molecular dynamics simulations.

D.2 Equilibrium properties

D.2.1 Pairing transition

In this section, we detail under which conditions ionic pairing may occur in 2D electrolytes. The equilibrium properties of the system can be derived using the Debye–Hückel mean-field framework described in [106] and which we recall here for the sake of completeness. We consider an electrolyte with density ρ, with a single ion located at the origin, interacting with all surrounding ions. Assuming ions are rigid spheres of radius r_0 that cannot interpenetrate each other, the electrostatic potential created by the test ion is unchanged for $r < r_0$:

$$\Phi(r) \simeq \frac{-Ze\mathcal{K}}{2\pi\epsilon_0\epsilon_\parallel h} \log\left(\frac{r}{r+\xi}\right) + \psi(Z), \tag{D.2}$$

with ψ a constant to be determined. For $r > r_0$, the electrostatic potential is given by the Poisson–Boltzmann (PB) equation, modified to take the special geometry into account:

$$\left(\Delta - \frac{1}{r+\xi}\partial_r\right)\Phi = \frac{2Ze\mathcal{K}\rho}{\epsilon_0\epsilon_\parallel h} \sinh\frac{Ze\Phi}{k_B T}. \tag{D.3}$$

The operator on the left-hand side is chosen such that its Green function is given by equation (D.2). The PB equation must be linearised in order to make computations tractable; however, this underestimates the strength of ion-ion correlations and neglects the possibility of ion pairing. Bjerrum suggested to introduce pairs as a separate chemical species, decomposing:

$$2\rho = \rho_1 + 2\rho_2, \tag{D.4}$$

with ρ_1 the concentration in free ions of both signs and ρ_2 the concentration in pairs. We get:

$$\left(\Delta - \frac{1}{r+\xi}\partial_r\right)\Phi = \frac{Z^2e^2\mathcal{K}\rho_1}{\epsilon_0\epsilon_\parallel h k_B T}\Phi = \kappa_D^2\Phi, \tag{D.5}$$

where we introduced the inverse Debye length κ_D. This leads to:

$$\Phi(r > r_0) = \frac{Ze\mathcal{K}A}{2\pi\epsilon_0\epsilon_\parallel h}\left[K_0\left(\kappa_D r\right) - K_0\left(\kappa_D\left(r+\xi\right)\right)\right], \tag{D.6}$$

where K_0 is the modified Bessel function of the second kind. The constants A and ψ are determined using the boundary conditions at $r = r_0$, where Φ and its gradient must match the unscreened potential (D.2):

$$A = \frac{\xi}{\kappa_D r_0(r_0+\xi)}\left[K_1\left(\kappa_D r_0\right) - K_1\left(\kappa_D\left(r_0+\xi\right)\right)\right]^{-1}, \tag{D.7}$$

$$\psi(Z) = \frac{Ze\mathcal{K}}{2\pi\epsilon_0\epsilon_\parallel h}\left[\frac{\xi}{\kappa_D r_0(r_0+\xi)}\frac{K_0(\kappa_D r_0) - K_0(\kappa_D(r_0+\xi))}{K_1(\kappa_D r_0) - K_1(\kappa_D(r_0+\xi))} - \log\frac{r_0+\xi}{r_0}\right]. \tag{D.8}$$

Finally, for a system of size $L \times w$, the electrostatic free energy is obtained through a Debye charging process and reads:

$$F^{el} = Lwf^{el} = Lw\rho_1\int_0^Z \psi(\lambda)\,\mathrm{d}\lambda. \tag{D.9}$$

This allows us to compute the total free energy, which is the sum of this electrostatic term and of entropic terms:

$$\beta f = \beta f^{el} + \rho_1\log\frac{\rho_1\Lambda^2}{2} - \rho_1 + \rho_2\log\frac{\rho_2\Lambda^2}{\zeta_2} - \rho_2, \tag{D.10}$$

where ζ_2 is the internal partition function of a pair:

$$\zeta_2(R) = \int_{r_0}^R 2\pi r\exp\left[-\frac{1}{T^*}\log\frac{r}{r+\xi}\right]. \tag{D.11}$$

The large distance cut-off R plays little role in the physics of the system, and can be set to the inflection point of the integral [106]:

$$R = \frac{\xi}{T^*} = \frac{\beta Z^2e^2\mathcal{K}}{4\pi\epsilon_0\epsilon_m} = \ell_{Bj} = 130\,\mathrm{nm}. \tag{D.12}$$

This lengthscale is called the Bjerrum length. Note that in the limit $T^* \ll 1$, this matches the usual definition of the Bjerrum length $\beta V(\ell_B) = 1$. Its expression is identical to that of bulk water, with the dielectric permittivity of water $\epsilon_w = 80$ replaced by the permittivity of the confining medium $\epsilon_m = 2$. Then, chemical equilibrium between free ions and tightly bound pairs imposes:

$$\mu_2 = \mu_+ + \mu_-, \tag{D.13}$$

with $\mu_i = \frac{\partial F}{\partial N_i}$ is the chemical potential of species i. This yields:

$$\rho_2 = \frac{1}{4}\rho_1^2\zeta_2 e^{2\beta\mu^{ex}}, \tag{D.14}$$

where we introduced the excess chemical potential defined as:

$$\mu^{ex} = \frac{\partial f^{el}}{\partial\rho_1}. \tag{D.15}$$

We can then solve the system composed of equations (D.4), (D.10) and (D.14), by numerically computing the free energy f as a function of ionic concentration ρ. At temperature $T^* < T_C^* = 0.25$, f fails to be a convex function of ρ, and we define the low and high density branches ρ_{low} and ρ_{high} as the positions of the two inflection points. The curves of ρ_{low} and ρ_{high} as functions of temperature correspond to the spinodal curve. In the 2DCG model f is not convex at low concentration, which corresponds to $\rho_{\mathrm{low}}(T^*) = 0$: there is no low density branch. When T^* approaches T_C^*, $\rho_{\mathrm{high}}(T^*)$ approaches a finite

value: in the perfectly 2D case, there is no low density branch, and the high density branch ends at the critical line $T^* = 0.25$ (see figure 4.2, solid line).

In the 2D$^+$ model, the high density branch is only slightly shifted, but there is a low density branch. However, since we treated ion pairs as an ideal gas, we neglected their contribution to the free energy, and as a result the shape of the low density branch is unphysical. A solution would consist in including dipole-ion and dipole-dipole interaction terms, as suggested in [106]. Since we are only interested in the qualitative shape of the transition line, we simply assume that, at low concentration, the transition happens when there are roughly as many pairs as free ions, ie. $\rho \sim \rho_1$. Using this approximation, we plot the spinodal curve of the 2D$^+$ model in figure 4.2 (dashed red line). The low and high density branches again do not join, resulting in a critical line at $T^* \simeq 0.25$.

These results are remindful of the Kosterlitz–Thouless transition of the XY model [127]. The exact value of the critical temperature can be computed in the 2DCG model by considering the $\rho_1 \to 0$ limit:

$$\beta f^{el} = -\frac{\rho_1}{T^*} \frac{\log\left[\kappa_D r_0 K_1\left(\kappa_D r_0\right)\right]}{\left(\kappa_D r_0\right)^2}, \tag{D.16}$$

$$\beta \mu^{ex} = -\frac{\beta Z^2 e^2 \mathcal{K}}{4\pi\epsilon_0\epsilon_\parallel h} \frac{K_0(\kappa_D r_0)}{\kappa_D r_0 K_1(\kappa_D r_0)} \simeq -\frac{1}{T^*}\left[\frac{\gamma}{2} + \frac{\ln \kappa_D r_0/2}{2}\right]. \tag{D.17}$$

We obtain $\rho_2 \propto \rho_1^{2-1/2T^*}$. This cannot hold for $T^* < T_C^* = 0.25$: since $\rho_1 < 2\rho$, we would have $\rho_2 > \rho$ for low enough ρ.

D.2.2 Ion pairing in MD simulations

As discussed in next section, ionic pairing results in non-linear transport phenomena under an external field. However, a weak enough electric field should not be able to break Bjerrum pairs, and only free ions should contribute to conduction. Therefore, in MD simulations, the paired fraction can be computed from the ionic current at small voltage.

Assuming that pairing captures all relevant ion-ion correlations, free ions essentially behave as independent particles of electrical mobility $\mu_i = Zeq_iD/k_BT$. We obtain:

$$I = \left\langle \frac{Ze}{L} \sum_{\text{free ions}} q_i v_x^i \right\rangle = \frac{Z^2 e^2 D w \rho_1}{L k_B T} \Delta V = \frac{\rho_1}{2\rho} G_{\text{Ohm}} \Delta V, \tag{D.18}$$

where G_{Ohm} is the conductance of an ideal (non interacting) bulk electrolyte of concentration ρ. We use this result to define the free and paired fractions in MD simulations:

$$n_f = \frac{G_{\text{simulation}}}{G_{\text{Ohm}}} = \frac{\rho_1}{2\rho}, \tag{D.19}$$

$$n_p = 1 - n_f = \frac{\rho_2}{\rho}. \tag{D.20}$$

This definition of n_f is used in figure 4.2 to obtain the phase diagram of the system from brownian dynamics. At high temperature, $n_f \simeq 1$, and the system is in a purely ohmic regime: there are no pairs and its conductivity matches that of a bulk electrolyte. For $T^* < 0.25$, $n_f \simeq 0$ and the system is insulating as there no free ion left within the slit.

D.3 Onsager's Wien effect in 2D

D.3.1 Isolated pair model

In this section, we develop an extensive theory of conduction in confined 2D electrolytes far from equilibrium. We follow Onsager's original computation of Wien effect for bulk weak electrolytes [114], extending it to the 2D case, and then show how it must be modified to take Bjerrum polyelectrolytes into account.

Let us consider a 2D electrolyte (X^+, Y^-) in an external electric field $\mathbf{E} = E\,\hat{\mathbf{x}}$. We assume ions may pair up according to a chemical equilibrium of the form $XY \leftrightarrows X^+ + Y^-$. In what follows, we study the chemical kinetics associated with this equilibrium and we base our model on a generic reaction equation:

$$\dot{n}_f = \frac{1 - n_f}{\tau_d} - \frac{n_f^2}{\tau_a}, \tag{D.21}$$

The evolution of fraction n_f of free ions – that are not part of a pair and thus can conduct current – is governed by two timescales: the pair dissociation time τ_d and the free ions association time τ_a.

Onsager suggests to derive these two timescales from the shape of the out of equilibrium correlation function g. Assuming that a positive ion is fixed at the origin, $g(r, \theta)$ is (up to a normalization factor) the probability density of finding a negative ion at polar position (r, θ). It is solution of a Fokker–Planck equation:

$$\partial_t g = 2D\boldsymbol{\nabla} \cdot (\boldsymbol{\nabla} g + g\boldsymbol{\nabla}(\beta\Phi)), \tag{D.22}$$

where Φ is the total electrostatic potential felt by a hypothetical anion located at (r, θ). One has:

$$\beta\Phi = \frac{1}{T^*} \log \frac{r}{r + \xi} - \frac{r\cos\theta}{l_E}. \tag{D.23}$$

The first term of the potential corresponds to the unscreened interaction of two ions in confinement: we therefore neglect any influence of the ionic atmosphere or Debye screening. This means the current model only captures the effects of pairs dissociating and ions recombining independently from each others. We therefore call it an *isolated pair model*. The lengthscale l_E introduced in equation (D.23) measures the strength of the external field:

$$l_E = \frac{k_B T}{Ze|E|}. \tag{D.24}$$

Note that the potential Φ has its maximum for $r = l_E/T^*$ (plus a correction of order $l_E/\xi \sim 0.01$, which we neglect). This means an ion separated from the central ion by more than l_E/T^* will be carried away by the electric field, breaking the pair. Therefore, l_E is the spatial extension of electrostatic correlations in presence of an external field. The other relevant lengthscale is the Bjerrum length $\ell_{Bj} = \xi/T^*$, which governs the shape of g in the absence of an external field. However, the Wien effect is perceptible in brownian simulations starting for values of E such that $l_E/\ell_{Bj} \sim 10^{-2} \ll 1$, so we discard any effect caused by a finite dielectric confinement length, and set $\xi = \infty$ in what follows. This amounts to replacing the potential (D.23) by:

$$\beta\Phi = \frac{1}{T^*} \log \frac{r}{r_0} - \frac{r\cos\theta}{l_E} + \text{constant}, \tag{D.25}$$

where r_0 is the ion size. We then assume that the system has reached a steady state, so that $\partial_t = 0$:

$$\left[\Delta + \left(\frac{1}{T^* r} - \frac{\cos\theta}{l_E}\right)\partial_r + \frac{\sin\theta}{r l_E}\partial_\theta\right] g = 0. \tag{D.26}$$

Since the problem has a single lengthscale l_E, we perform the change of variable $\mathbf{r} \to \mathbf{u} = \mathbf{r}/l_E$. We obtain:

$$\left[\Delta + \left(\frac{1}{T^* u} - \cos\theta\right)\partial_u + \frac{\sin\theta}{u}\partial_\theta\right] g = 0. \tag{D.27}$$

It is remarkable that the system is now entirely determined by a single dimensionless parameter T^*, regardless of field strength. This is unique to the 2D case, because of the divergent Bjerrum length. Onsager then suggests to decompose g into two parts:

$$g = g_d + g_a, \tag{D.28}$$

where g_d and g_a are two solutions of (D.27) with the additional conditions:

$$\int_0^{2\pi} -2D\left[\boldsymbol{\nabla} g_a + g_a \boldsymbol{\nabla}(\beta\Phi)\right] \cdot \hat{\mathbf{r}}\, r \mathrm{d}\theta = -C, \tag{D.29}$$

$$\lim_{r\to\infty} g_a = \rho, \tag{D.30}$$

and

$$\int_0^{2\pi} -2D\left[\boldsymbol{\nabla} g_d + g_d \boldsymbol{\nabla}(\beta\Phi)\right] \cdot \hat{\mathbf{r}}\, r \mathrm{d}\theta = +C, \tag{D.31}$$

$$\lim_{r\to\infty} g_d = 0, \tag{D.32}$$

where C is a positive constant independant of r. It can be interpreted as a particle flux: g_a describes free ions far from the central ion, with which they can recombine and form a Bjerrum pair. This association process creates a net ionic flux from infinity to the origin; g_a is the solution of (D.27) associated with a sink at the origin. Similarly, g_d describes negative ions bound to the central cation and localized near the origin (hence the decay of g_d at infinity), forming a Bjerrum pair. This pair has a certain probability of breaking under the action of the external field, creating an ionic flux from the origin to infinity. These fluxes are of opposite signs and equal amplitude since the system is in steady state.

It is easy to see that in fact:

$$g_a = \rho, \tag{D.33}$$

and straigthfoward integration yields:

$$C = \frac{4\pi D\rho}{T^*}. \tag{D.34}$$

This is a recombination rate, defining the pair association time:

$$\tau_a = \frac{T^*}{4\pi D\rho}. \tag{D.35}$$

Under typical settings used in simulations, one has $\tau_a \sim 1\,\mu\mathrm{s}$. Computing g_d and the corresponding dissociation timescale τ_d is, however, a mathematical challenge. Onsager's

computation involved a series expansion in terms of families of special functions he invented specifically for this problem; and this solution is applicable if the Smoluchowski equation is spatially separable, which is not the case in 2D. Instead, we propose a solution based on the self-similarity of g, which allows us to derive all the relevant quantities (up to a geometrical factor of order 1) without resorting to in-depth mathematical analysis.

Another trivial solution of (D.27) is the Boltzmann distribution:

$$g_0(u,\theta) = \exp\left[-\frac{1}{T^*}\ln\frac{u l_E}{r_0} + u\cos\theta\right]. \tag{D.36}$$

This solution has, however, unphysical behaviour for $u \to \infty$, because the Boltzmann distribution is only relevant at thermal equilibrium. It should, however, bear some physical meaning for $u \ll 1$ because then the effect of the external field is negligible and the system is in quasi-equilibrium. Therefore, we admit that g_d is the unique solution of the following problem:

$$\left[\Delta + \left(\frac{1}{T^* u} - \cos\theta\right)\partial_u + \frac{\sin\theta}{u}\partial_\theta\right] g_d = 0, \tag{D.37}$$

$$g_d \sim K_a \left(\frac{l_E}{r_0}\right)^{-1/T^*} u^{-1/T^*} \text{ for } u \to 0, \tag{D.38}$$

$$\lim_{u\to\infty} g_d(u) = 0, \tag{D.39}$$

where K_a is chosen such that the particle flux associated with g_d compensates that of g_a. Because it is defined through the balance of fluxes, it can be interpreted as an association constant. The uniqueness of the solution is ensured because g_d is known on the whole boundary of the domain. Because l_E now only appears in the boundary condition at $u = 0$ as a multiplicative factor, it is easy to see that:

$$g_d(u) = K_a \left(\frac{l_E}{r_0}\right)^{-1/T^*} G(u), \tag{D.40}$$

where G is a universal function depending only on T^*. The resulting ionic flux reads:

$$2DK_a \left(\frac{l_E}{r_0}\right)^{-1/T^*} \mathcal{F} = \frac{4\pi D\rho}{T^*}, \tag{D.41}$$

where $\mathcal{F}$ is the flux associated to the universal function G:

$$\mathcal{F} = -\int_0^{2\pi} \left[\boldsymbol{\nabla} G + G\boldsymbol{\nabla}\left(\beta\Phi_{\mathbf{u}}\right)\right]\cdot\hat{\mathbf{u}}\, u \mathrm{d}\theta, \tag{D.42}$$

the dimensionless potential $\Phi_{\mathbf{u}}$ being defined as:

$$\beta\Phi_{\mathbf{u}} = \frac{1}{T^*}\log u - u\cos\theta. \tag{D.43}$$

The flux $\mathcal{F}$ has the dimension of an inverse length squared and is independent of l_E; it is also independent of ρ the total ionic concentration, since it is the property of a single isolated pair dissociating. Therefore, it must scale with r_0, the ionic radius, which is the

only relevant lengthscale remaining. We then obtain (up to a geometrical factor of order unity):

$$\mathcal{F} \simeq r_0^{-2}. \tag{D.44}$$

We finally get the expression of the association constant K_a:

$$K_a = 2\pi \left(\frac{l_E}{r_0}\right)^{1/T^*} \frac{\rho r_0^2}{T^*} = \frac{\tau_d}{\tau_a}, \tag{D.45}$$

as well as the dissociation time τ_d:

$$\tau_d = \frac{r_0^2}{2D} \left(\frac{l_E}{r_0}\right)^{1/T^*}. \tag{D.46}$$

At steady state, the free ion fraction n_f can be obtained from (D.21):

$$n_f = \frac{\tau_a}{2\tau_d} \left(\sqrt{1 + \frac{4\tau_d}{\tau_a}} - 1\right). \tag{D.47}$$

Notably, the above result predicts a power law dependency of n_f with applied field at low voltage:

$$n_f \propto E^{1/2T^*}. \tag{D.48}$$

Note that in particular n_f vanishes at zero voltage. This shows that our model is only valid in the low temperature phase, where all ions are paired up at thermal equilibrium (which is clearly the case in typical simulation settings). Otherwise, Debye screening cannot be neglected, as there remain some free ions even for vanishing electric field. This concludes our solution of the isolated pair model, and we plot its prediction using equations (D.18) and (D.47) in figure 4.3 (yellow line). The agreement with simulations is rather poor. Notably, the onset of conduction happens at much lower voltages than predicted by this model.

While it provides reasonable predictions for the bulk Wien effect, the isolated pair model must be modified for 2D confined electrolytes. One key element this model fails to account for is the formation of Bjerrum polyelectrolytes at non zero voltages. The existence of ionic strings, as shown in figure 4.3b, clearly indicates that the conduction in this system cannot be understood from the individual dynamics of ion pairs.

D.3.2 Role of the ionic atmosphere

In this section, we discuss the physical meaning of the expression of the dissociation timescale τ_d, so as to extend it to the case where Bjerrum polylectrolytes are relevant. Equation (D.46) can be recast as an Arrhenius law:

$$\tau_d = \tau_{\text{diffusion}} \exp\left[-2\beta\Delta F\right] = \frac{r_0^2}{2D} \left(\frac{l_E}{r_0}\right)^{1/T^*}, \tag{D.49}$$

where ΔF is the free energy barrier to overcome in order to break a pair. It reads:

$$\beta\Delta F \simeq -\frac{\log l_E/r_0}{2T^*}. \tag{D.50}$$

This expression is very similar to the free energy cost to create an ionic atmosphere of size l_E around an ion, see (D.16):

$$\beta F_{atm}(l_E) = -\frac{1}{T^*}\frac{\log\left[K_1\left(r_0/l_E\right) r_0/l_E\right]}{(r_0/l_E)^2} \simeq -\frac{\log l_E/r_0}{2T^*}. \tag{D.51}$$

In other words, the *kinetic* energy barrier to break a pair is equal to the *thermodynamic* energy gap between the paired and the unpaired states, if we admit that the typical size of the ionic atmosphere around a free ion is given by l_E instead of the Debye length λ_D.

Indeed, the Debye length reads:

$$\lambda_D = \sqrt{\frac{T^*}{2n_f\rho}}, \tag{D.52}$$

so that for low applied field, we obtain $\lambda_D \propto l_E^{1/4T^*}$. Therefore, $\lambda_D \gg l_E$ provided $T^* < 0.25$, ie. if the system is in the low temperature phase, and for large enough electric field. However, the electrostatic potential (D.23) has a maximum at $r = l_E/T^* \propto l_E$, and thus two ions separated by more than l_E will effectively cease to interact and be carried away by the electric field. This means the ionic atmosphere cannot be larger than l_E, and since $\lambda_D \gg l_E$, l_E is indeed its correct lengthscale in our simplified picture.

D.3.3 Anisotropic atmosphere and PEW effect

The above analysis only holds if the ionic atmosphere is destroyed by the external field. However, we should keep in mind the field only acts along the x axis, while the atmosphere extends in all directions. Hence, correlations along the y axis should remain strong, and the ionic atmosphere becomes anisotropic. It has an ovoid shape, with typical spatial extension $l = \sqrt{\lambda_D l_E}$. Therefore, we also need to compute fluxes along both axes separately. This introduces two quantities, n_x and n_y, which are the fractions of ions free to move along the x (resp. y) axis. Both follow a reaction equation:

$$\dot{n}_x = \frac{1-n_x}{\tau_{d,x}} - \frac{n_x^2}{\tau_{a,x}}, \tag{D.53}$$

$$\dot{n}_y = \frac{1-n_y}{\tau_{d,y}} - \frac{n_y^2}{\tau_{a,y}}, \tag{D.54}$$

where we also introduced distinct association times $\tau_{a,x} = \tau_{a,y} = \tau_a$ and dissociation times $\tau_{d,i}$. Assuming the Arrhenius law derived in last section still holds, the free energy cost to breaking a pair can be decomposed in the following way:

$$2\beta\Delta F(\sqrt{\lambda_{D,y} l_E}) \simeq -\frac{\log l_E/r_0}{2T^*} - \frac{\log \lambda_{D,y}/r_0}{2T^*} = 2\beta\Delta F_x + 2\beta\Delta F_y, \tag{D.55}$$

where $\lambda_{D,y} = \sqrt{T^*/2n_y\rho}$. This allows us to express both dissociation times using Arrhenius equations:

$$\tau_{d,x} = \frac{r_0^2}{2D}\left(\frac{l_E}{r_0}\right)^{1/2T^*}, \tag{D.56}$$

$$\tau_{d,y} = \frac{r_0^2}{2D}\left(\frac{\lambda_{D,y}}{r_0}\right)^{1/2T^*}. \tag{D.57}$$

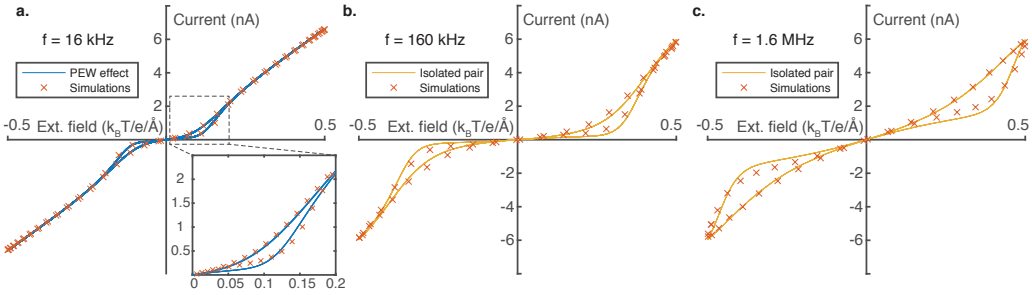

Figure D.1

Characterization of the ionic memristor. **a.-c.** Low frequency IV curves. The ionic memristor, with ionic concentration $\rho = 10^{-4}\text{atom/nm}^2$ is stimulated with an oscillating field of amplitude $E_0 = 0.5\,\text{k}_\text{B}\text{T/Å}$ and variable frequency. The IV curve exhibits a hysteresis loop for all frequencies in the range $10\,\text{kHz} - 10\,\text{MHz}$. **a.** At all frequencies below $f_c = 160\,\text{kHz}$, the shape of the curve can be predicted using a quasistatic version of equation (D.53). At higher frequencies (**b.**, **b.**) the description of the system in terms of Bjerrum polyelectrolytes fails and the isolated pair model must be used.

Chemical equilibrium along the y axis reads:

$$\rho(1-n_y) = (\rho n_y)^{2-1/4T^*} \frac{r_0^2}{T^*} \left(\frac{2}{T^*}\right)^{-1/4T^*}. \tag{D.58}$$

This equation is the equivalent of (D.14), with temperature divided by 2. Moreover, it can only hold if $T^* > 0.125$. At lower temperatures, the equilibrium is broken and no ion can move freely along the y axis – remindful of how, at thermal equilibrium, no ion can escape pairing if $T < 0.25$. In other words, at low temperature, the whole system collapses into a single (or several) ionic assemblies, which we call Bjerrum polyelectrolytes.

Chemical equilibrium along the direction of the applied field reads:

$$n_x = \frac{\tau_{a,x}}{2\tau_{d,x}} \left(\sqrt{1+\left(\frac{2\tau_{d,x}}{\tau_{a,x}}\right)^2} - 1\right) \underset{E\to 0}{\propto} E^{1/4T^*}. \tag{D.59}$$

This last result is similar to (D.47), however the corresponding low field exponent is modified by a factor 2. This shows that Bjerrum polyelectrolytes have a dramatic influence on conduction in confined electrolytes: their formation corresponds to a change of the power law exponent of the current-voltage characteristic, because tearing an ion out of a massive polyelectrolyte is easier than breaking a Bjerrum pair. Our Polyelectrolytic Wien (PEW) effect predicts a greatly increased conductance with respect to Onsager's isolated pair model, as shown on figure 4.3c (red solid line), in quantitative agreement with brownian simulations.

D.4 Memristor effect

We now consider the case of an alternating field $E = E_0 \cos 2\pi f t$ with frequency f ranging from 10 kHz to 10 MHz. An exact theoretical treatment would require to solve the

full time-dependent Smoluchowski equation (D.22). This introduces a new lengthscale $l_f = \sqrt{D/f}$ corresponding to a diffusion length over a period of the external field. However, for a typical frequency $f \sim 100\,\mathrm{kHz}$, one has $l_f \sim 100\,\mathrm{nm} \gg l_E \sim 1\,\mathrm{nm}$. This allows us to neglect terms proportional to $\partial_t g$, of order $(l_E/l_f)^2$, in (D.22) and consider quasistatic dynamics. The conclusions of previous sections are hence left unchanged upon replacing E by $E_0 \cos 2\pi f t$ in the expressions of τ_a and $\tau_{d,x}$. This quasistatic PEW effect model allows us to predict the shape of the AC IV curve with great accuracy up to a critical frequency $f_c = 160\,\mathrm{kHz}$, see figure D.1. At higher frequencies, however, simulations show that Bjerrum polyelectrolytes do not form, and the isolated pair model is in better accordance with simulations results compared to the PEW effect model. Moreover, the transition frequency f_c between the two regimes is surprisingly found to be independent of ionic concentration. This frequency must correspond to an intrinsic property of Bjerrum polyelectrolytes, whose formation dynamics are therefore independent of ionic concentration.

D.5 Hodgkin–Huxley neuron model

In this section, we detail the implementation of the molecular dynamics simulations of the Hodgkin–Huxley neuron model [119] using our ionic memristor. It consists in two graphene slits coupled by an external electronic circuit containing a current generator I and a capacitor C, see figure 4.5. We refer to these two slits as *discharging* and *charging* memristor due to their respective effect on the capacitor.

In the description of biological neurons by Hodgkin and Huxley, ion channels (typically sodium and potassium channels) play the role of memristors. Each channel is modelled by a history-dependent resistor in series with a Nernst potential which accounts for the concentration contrast of some ionic species in the reservoirs to which the memristor is connected (the extra- and intracellular media), see figure 4.5a. Hodgkin and Huxley then propose the following electronic model of the ion channels:

$$I_k = G_k(n_k)(U - V_k), \tag{D.60}$$

$$\dot{n}_k = f(n_k, U), \tag{D.61}$$

where I_k is the current flowing out of the k^{th} ion channel, G_k its conductance, V_k its Nernst potential, U the applied voltage and n_k an internal parameter (or array of parameters) describing the activity of the channel. The key point here is that the evolution of n_k only depends on the physical voltage U and not on the Nernst potential, which is of chemical origin. Lastly, since biological channels are ion-specific, their Nernst potential is directly linked to the concentrations of the corresponding ion inside and outside the neuron, c_k^{in} and c_k^{out}:

$$V_k = \frac{k_B T}{e} \log \frac{c_k^{\text{out}}}{c_k^{\text{in}}}. \tag{D.62}$$

Qualitatively, the spiking response observed in the Hodgkin–Huxley model stems from the sign difference in the Nernst potentials of sodium ions (which are more concentrated in the extracellular medium, flow inside the neuron and increase its charge) and potassium ions (which are more concentrated in the intracellular medium, flow outside the neuron and decrease its charge).

Because our description of 2D electrolytes is formally equivalent to Hodgkin and Huxley's model of ion channels, we can reproduce step by step their neuron model, using two nanofluidic memristors. Illustrating *e.g.* the mechanism with $CaSO_4$ as a salt, a "charging" memristor is connected on the left to a reservoir with more sulfate ions than calcium ions and on the right to a reservoir containing more calcium than sulfate ions. In both reservoirs, electroneutrality is imposed by some additional electrolyte that cannot enter the graphene slit (because, for example, it is too large). The situation is reversed for the discharging memristor: it is connected on the left to a reservoirs with many calcium ions, and on the right to a reservoir with many sulfate ions.

However in our simulations, we can simplify the setup by imposing *de facto* the additional Nernst potential. We cannot indeed afford to simulate the reservoirs explicitly, because we need to perform the simulation over very long timescales (up to a few milliseconds). Instead we implement them through additional Nernst electrochemical potentials $V_{\text{Discharge}} < 0$ and $V_{\text{Charge}} > 0$ being imposed on the slits.

Our simulation scheme is as follows. First, we impose the capacitor voltage $U(t)$ during a time $\Delta t = 50\,\text{ns}$ to both slits and compute the corresponding ionic current $I_{\text{Discharge}}(t+\Delta t)$ and $I_{\text{Charge}}(t+\Delta t)$ without taking Nernst potentials into account. We then deduce the conductance of each channel:

$$G_k(t+\Delta t) = \frac{I_k(t+\Delta t)}{U(t)}. \tag{D.63}$$

The actual ionic currents are then determined by:

$$I_{k,\text{Nernst}} = G_k(t+\Delta t)(U(t) - V_k), \tag{D.64}$$

as in the Hodgkin–Huxley model. This allows us to compute the new value of the voltage:

$$U(t+\Delta t) = U(t) + \frac{\Delta t}{C}\left[I - I_{\text{Discharge, Nernst}} - I_{\text{Charge, Nernst}}\right]. \tag{D.65}$$

Figure 4.5c shows the voltage U as function of time for $I = 0.1\,\text{nA}$, $C = 10^{-4}\,\text{pF}$ and $V_{\text{Charge}} = -V_{\text{Discharge}} = 0.2\,k_BT/\text{Å}$. The graphene slits have the same length $L = 2\,\mu\text{m}$ and different ionic concentrations $\rho_{\text{Discharge}} = 10^{-4}\,\text{atom/nm}^2$ and $\rho_{\text{Charge}} = 10^{-5}\,\text{atom/nm}^2$. A more realistic value of C can easily be used instead by reducing the slits length, as only the value of the product CL^2 matters, or by considering stacks of identical slits in parallel instead.

D.6 Orders of magnitude discussion

Our results, as discussed in previous sections, are based on molecular dynamics simulations of a graphene slit of length $2\,\mu\text{m}$ and height $h = 7\,\text{Å}$, where typical electric fields are of the order of $0.1\,\text{k}_\text{B}\text{T}/\text{Å}$. This corresponds to an applied voltage $U \sim 50\,\text{V}$. This is of course unrealistic due to water electrolysis starting at $U = 1.23\,\text{V}$. Similarly, to test the memristor effect we used frequencies in the range $10\,\text{kHz} - 10\text{MHz}$ which can hardly be accessed to in experiments due to capacitive effects observed in such nanofluidic systems.

This set of parameters was necessary for simulations, as testing a more reasonable frequencies around $f \sim 100\,\text{Hz}$ would require to simulate the system for $t \sim 0.1\,\text{s}$ which is not feasible due to numerical constraints. Likewise, only the value of the electric field

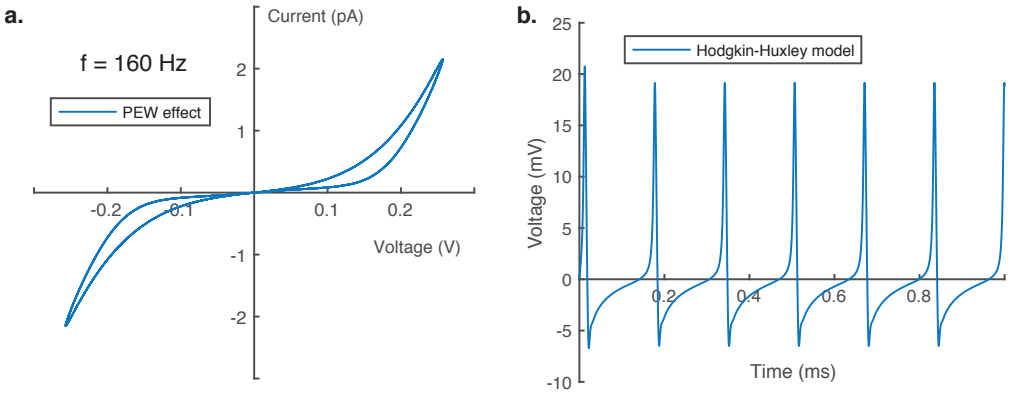

Figure D.2

Theoretical model of experimentally accessible devices. **a.** Memristor effect in a 100 nm long graphene slit excited by a voltage $U = U_0 \cos 2\pi f t$ such that $U_0 = 0.26\,\mathrm{V}$ and $f = 160\,\mathrm{Hz}$, obtained by solving equation (D.53) numerically. **b.** Voltage spiking in a Hodgkin–Huxley cell (see figure 4.5b) made of two 100 nm slits and a capacitance $C = 2\,\mathrm{pF}$, stimulated by an input current $I = 1\,\mathrm{pA}$. The two slits are connected to pairs of reservoirs with different cation and anion concentrations, corresponding to the Nernst potentials $V = \pm 50\,\mathrm{mV}$. The system is simulated using its equivalent electronic circuit (see figure 4.5b).

bears relevance to the ionic dynamics. Therefore, reducing the system size allows one to consider much more reasonable voltages. Another possibility would be to use lower ionic concentrations or slightly bigger channels ($h = 1\,\mathrm{nm}$), both of which lowers the electric field needed to observe conduction through Wien effect.

Our theoretical model, however, allows us to predict that the memristor effect should still be observed in experimental conditions. As a proof of concept, we show in figure D.2 the AC IV curve obtained for a sinusoidal voltage of amplitude $U = 0.26\,\mathrm{V}$ and frequency $f = 160\,\mathrm{Hz}$ for a slit of length $L = 100\,\mathrm{nm}$ and height $h = 0.7\,\mathrm{nm}$ containing an ionic concentration $\rho = 10^{-3}\,\mathrm{atom/nm^2}$. The resulting ionic current is less than 10 pA, which is harder to detect, but the experiment can be implemented using stacks of identical devices in parallel to increase the signal-to-noise ratio significantly.

Similarly, we can use our model to predict the spiking response of such experimentally available systems. We implement this by solving numerically the Hodgkin–Huxley equations corresponding to the device shown figure 4.5b, with $I = 1\,\mathrm{pA}$, $C = 2\,\mathrm{pF}$, $\rho_{\mathrm{Charge}} = 20\rho_{\mathrm{Discharge}} = 2 \times 10^{-3}\,\mathrm{atom/nm^2}$, and $T^* = 0.22$ (corresponding to slits of height $h = 1.4\,\mathrm{nm}$ and divalent ions). We also use $V_{\mathrm{Charge,\ Discharge}} = \pm 50\,\mathrm{mV}$, which corresponds to concentration ratios of 100 between the reservoirs. To compensate for the lower concentration (and hence lower conductivity), the discharging memristor is a stack of 5 identical slits. The result, showing voltage spike trains with frequency around 7 kHz, is presented on figure D.2b.

Appendix E

Theory of quantum friction

Contents

E.1 Many-body theory of solid-liquid friction

E.1.1 Model definition

We consider a semi-infinite solid extending into the half-space $z < 0$ in contact with a semi-infinite liquid (water) extending into the half-space $z > 0$, at temperature T. The whole system is described within a quantum field theory framework. For simplicity, we describe only the electronic degrees of freedom of the solid by the creation and anihilation fields $\Psi^\dagger(\mathbf{r}, t)$ and $\Psi(\mathbf{r}, t)$, respectively; we note that one could follow the steps described below with the addition of lattice degrees of freedom as a phonon field. The liquid is described by its charge density $n_\mathrm{w}(\mathbf{r}, t)$, assumed to have gaussian fluctuations fully determined by the two-point functions $\langle n_\mathrm{w}(\mathbf{r}, t) n_\mathrm{w}(\mathbf{r}', t')\rangle$, which are treated as inputs of the model. A flow parallel to the interface is induced in the liquid, and the system is assumed to have reached a non-equilibrium steady state. We assume that the liquid flow is slow enough so that it does not affect the form of microscopic correlations in the liquid.

In that case, the effect of the flow field $\mathbf{v}$ is to shift the coordinates within the liquid according to $n_{\mathrm{w}}(\mathbf{r},t) \mapsto n_{\mathrm{w}}(\mathbf{r}-\mathbf{v}t,t)$.

The liquid and the solid interact through long range Coulomb forces, and through short-range forces due to the coupling of electronic degrees of freedom of the solid with electronic degrees of freedom of the liquid, which we do not treat explicitly. If the frontier orbitals of the solid and the liquid are sufficiently far apart in energy, then these short-range forces amount simply to "Pauli repulsion", which prevents the solid and the liquid from interpenetrating each other [251, 252]. If not, there may be chemisorption of the liquid on the solid [253], which is a situation beyond the scope of this work. The former assumption is justified in particular for the water-carbon interface, where *ab initio* simulations show no water chemisorption [55]. In the following, we will treat explicitly only the long-range Coulomb forces, with the effect of Pauli repulsion taken into account in the bare correlation functions, computed for semi-infinite media.

The Coulomb interactions in the system are described by the Hamiltonian

$$\hat{H}_{\mathrm{int}} = \int \mathrm{d}\mathbf{r}\mathrm{d}\mathbf{r}' \hat{n}_{\mathrm{e}}(\mathbf{r}',t) V(\mathbf{r}-\mathbf{r}') \hat{n}_{\mathrm{w}}(\mathbf{r}-\mathbf{v}t,t) + \frac{1}{2}\int \mathrm{d}\mathbf{r}\mathrm{d}\mathbf{r}' \hat{n}_{\mathrm{e}}(\mathbf{r}',t) V(\mathbf{r}-\mathbf{r}') \hat{n}_{\mathrm{e}}(\mathbf{r},t), \quad \text{(E.1)}$$

where $n_{\mathrm{e}}(\mathbf{r},t) \equiv \Psi^{\dagger}(\mathbf{r},t)\Psi(\mathbf{r},t)$ is the electron density: the first term is the water-electron, and the second term is the electron-electron Coulomb interaction. Within the interacting system, we wish to compute the solid-liquid friction force

$$\langle \hat{\mathbf{F}}(t) \rangle = -\int \mathrm{d}\mathbf{r}\mathrm{d}\mathbf{r}' \, \nabla_{\mathbf{r}'} V(\mathbf{r}-\mathbf{r}') \langle \hat{n}_{\mathrm{w}}(\mathbf{r}'-\mathbf{v}t,t) \hat{n}_{\mathrm{e}}(\mathbf{r},t) \rangle, \quad \text{(E.2)}$$

where the average is taken over all quantum and thermal fluctuations in the system. Therefore, computing the friction force amounts to computing the equal-time water-electron density correlation function. We proceed by treating $\hat{H}_{\mathrm{int}}$ as a perturbation, and expanding the average in eq. (E.2) in powers of $\hat{H}_{\mathrm{int}}$ to arbitrary order. Because we are dealing with a non-equilibrium steady state, we do so in the Schwinger-Keldysh framework of perturbation theory.

E.1.2 Brief overview of the Keldysh framework

We make use of the out-of-equilibrium perturbation theory formalism originally proposed by L. V. Keldysh in 1965 [159], which has since then been extensively described in several books [254, 255] and reviews [160]. However, in order to keep the discussion as self-contained as possible, we give here a brief introduction, whose formulation is largely based on [255]. The reader who is familiar with the Keldysh formalism may directly skip to section E.1.3.

Our solid-liquid system is governed by the total Hamiltonian $\mathcal{H}(t) = \hat{H}_0 + \hat{H}_{\mathrm{int}}(t)$, where $\hat{H}_0$ is the quadratic Hamiltonian describing the system at equilibrium with Coulomb interactions switched off. Suppose we wish to compute the mean value of the Schrödinger picture operator $\mathcal{O}$ at time t. It is defined by

$$\langle \mathcal{O} \rangle(t) = \frac{\mathrm{Tr}[\hat{\rho}(t)\mathcal{O}]}{\mathrm{Tr}[\hat{\rho}(t)]}, \quad \text{(E.3)}$$

where $\hat{\rho}(t)$ is the density matrix of the out-of-equilibrium interacting system. In order to evaluate $\hat{\rho}(t)$, we assume that the Coulomb interactions and the fluid flow, which sets the

system out of equilibrium, are adiabatically switched on starting at $t = -\infty$. Then, we may express the interacting density matrix at time t as a function of the non-interacting density matrix $\hat{\rho}_0$ at $t = -\infty$, and the evolution operator $\mathcal{U}$: $\hat{\rho}(t) = \mathcal{U}_{t,-\infty}\hat{\rho}_0\mathcal{U}_{-\infty,t}$, with

$$\mathcal{U}_{t,t'} = \mathbb{T}\left[\exp\left(-\frac{i}{\hbar}\int_{t'}^{t}\mathcal{H}(t)\mathrm{d}t\right)\right], \tag{E.4}$$

$\mathbb{T}$ being the time-ordering operator. The average value in eq. (E.3) then becomes

$$\langle\mathcal{O}\rangle(t) = \frac{\mathrm{Tr}[\mathcal{U}_{-\infty,t}\mathcal{O}\mathcal{U}_{t,-\infty}\hat{\rho}_0]}{\mathrm{Tr}[\hat{\rho}_0]}, \tag{E.5}$$

where we have used circular permutation within the trace. The expression under the trace can be read (from left to right) in terms of time evolution: the system is evolved from $t = -\infty$ where the density matrix is known, to t where the observable is computed, and the back to $t = -\infty$. In equilibrium perturbation theory, one further assumes that the interactions are adiabatically switched off at $t = +\infty$, so that the state of the system at $t = +\infty$ differs from the state at $t = -\infty$ only by a phase factor. Then, instead of evolving the system from t to $-\infty$, one can evolve it from $t = +\infty$, thereby avoiding the complication of forward-backward time evolution. After a non-equilibrium evolution, however, the system has no reason to go back to its initial state, even if the interactions are switched off. Hence, one has to consider the evolution of the system on a contour that goes forwards then backwards in time. In practice, one defines the Schwinger-Keldysh closed time contour c, which travels from $t = -\infty$ to $t = +\infty$ and then back. It can then be shown that

$$\langle\mathcal{O}\rangle(t) = \frac{1}{\mathrm{Tr}[\hat{\rho}_0]}\mathrm{Tr}\left[\hat{\rho}_0\mathbb{T}_c\cdot\mathcal{O}^{H_0}(t)e^{-\frac{i}{\hbar}\int_c H_{\mathrm{int}}^{H_0}(t')\mathrm{d}t'}\right], \tag{E.6}$$

where the subscript H_0 indicates operators in the Heisenberg picture with respect to H_0, and $\mathbb{T}_c$ is the time-ordering operator along the contour c.

In practice, instead of average values of operators at one point in time, we will be interested in computing contour-ordered two-point functions of operators taken at different points in time, in particular

$$\chi_{ew}(e,w) \equiv -\frac{i}{\hbar}\left\langle\mathbb{T}_c\left\{n_e^{\mathcal{H}}(\mathbf{r}_e,t_e)n_w^{\mathcal{H}}(\mathbf{r}_w,t_w)\right\}\right\rangle. \tag{E.7}$$

It can be shown that, in analogy with eq. (E.6),

$$\chi_{ew}(e,w) = -\frac{i}{\hbar}\left\langle\mathbb{T}_c\left\{n_e^{H_0}(\mathbf{r}_e,t_e)n_w^{H_0}(\mathbf{r}_w,t_w)e^{-\frac{i}{\hbar}\int_c H_{\mathrm{int}}^{H_0}(t')\mathrm{d}t'}\right\}\right\rangle_0, \tag{E.8}$$

with $\langle\cdot\rangle_0 \equiv \mathrm{Tr}[\hat{\rho}_0\cdot]/\mathrm{Tr}[\hat{\rho}_0]$.

Under the form (E.8), the correlation function χ_{ew} can be evaluated as a perturbation series, by expanding the exponential to arbitrary order. Each term in the series consists in the average value of the contour-ordered product a certain number of field operators, taken with respect to the non-interacting density matrix $\hat{\rho}_0$. Since $\hat{\rho}_0$ is gaussian in the field operators, Wick's theorem applies, and those average values of many operators can be expressed as a convolution of two-operator correlation functions or Green's functions.

However, the contour-ordered correlation function is a complicated object, since it has a different form depending on the part, forward (c_1) or backward (c_2), of the contour

where its two time points are taken. It can actually be pictured as a 2×2 matrix, whose entries contain the four possible choices. For example,

$$\chi_{ew} = \begin{pmatrix} \chi_{ew}^{11} & \chi_{ew}^{12} \\ \chi_{ew}^{21} & \chi_{ew}^{22} \end{pmatrix}, \tag{E.9}$$

with χ_{ew}^{ij} corresponding to $t_e \in c_i$ and $t_w \in c_j$. It can be shown that the perturbation theory is consistent with this matrix structure: the convolution of two matrix correlation functions corresponds to matrix multiplication, followed by space-time convolution of the resulting component pairings. However, the components χ^{ij} are not convenient quantities in terms of physical meaning. Therefore, it is customary to redefine the correlation function through a certain matrix transformation, for which different conventions exist. We shall adopt the trigonal representation of Larkin and Ovchinnikov [256], which is obtained through the transformation

$$\chi \mapsto L\tau^3 \chi L^\dagger = \begin{pmatrix} \chi^R & \chi^K \\ 0 & \chi^A \end{pmatrix}, \tag{E.10}$$

with the matrices

$$L = \frac{1}{\sqrt{2}} \begin{pmatrix} 1 & -1 \\ 1 & 1 \end{pmatrix} \quad \text{and} \quad \tau^3 = \begin{pmatrix} 1 & 0 \\ 0 & -1 \end{pmatrix}. \tag{E.11}$$

This transformation reveals three physically meaningful components for χ: the *retarded*, *advanced* and *Keldysh* correlation functions. For the density cross-correlation function χ_{ew}, these components are defined as

$$\chi_{ew}^R(e,w) = -\frac{i}{\hbar}\theta(t_e - t_w)\langle[\hat{n}_e(e), \hat{n}_w(w)]\rangle \tag{E.12}$$

$$\chi_{ew}^A(e,w) = \frac{i}{\hbar}\theta(t_w - t_e)\langle[\hat{n}_e(e), \hat{n}_w(w)]\rangle \tag{E.13}$$

$$\chi_{ew}^K(e,w) = -\frac{i}{\hbar}\langle\{\hat{n}_e(e), \hat{n}_w(w)\}\rangle, \tag{E.14}$$

where $[,]$ is the commutator and $\{,\}$ the anticommutator; all the operators are in the Heisenberg picture with respect to $\hat{H}_0$, and we have used condensed notations of the type $e \equiv (\mathbf{r}_e, t_e)$. Similar definitions hold for the components of the electron-electron and water-water correlation functions χ_e and χ_w[1]. In terms of these definitions, the solid-liquid friction force (eq. (E.2)) can be recast as

$$\begin{aligned} \langle\hat{\mathbf{F}}\rangle &= -\int \mathrm{d}\mathbf{r}_e \mathrm{d}\mathbf{r}_w \, \nabla_{r_w} V(\mathbf{r}_w - \mathbf{r}_e) \cdot \frac{i\hbar}{2} \chi_{ew}^K(\mathbf{r}_e, t_e, \mathbf{r}_w, 0)|_{t_e=0} \\ &= -\frac{i\hbar}{4\pi} \int_{-\infty}^{+\infty} \mathrm{d}\omega \int \mathrm{d}\mathbf{r}_e \mathrm{d}\mathbf{r}_w \, \nabla_{r_w} V(\mathbf{r}_w - \mathbf{r}_e) \chi_{ew}^K(\mathbf{r}_e, \mathbf{r}_w, \omega). \end{aligned} \tag{E.15}$$

[1] Here we based our discussion on density-density correlation functions, because these are relevant for the solid-liquid problem. A more usual discussion in terms of Green's functions can be found, for example, in [160].

E.1.3 Diagrammatic perturbation theory

We have established in the previous section that evaluating the solid-liquid friction force amounts to computing the Keldysh component of the electron-water density correlation function, which supports a perturbative expansion in terms of the Coulomb interaction H_{int}. We discuss the structure of this expansion using a Feynman diagram representation. We adopt the following notations for the propagators:

(E.16)

Here $G_e(e', e) = -(i/\hbar)\langle \mathbb{T}_c \cdot \Psi(e')\Psi^\dagger(e)\rangle_0$ is the bare electron Green's function. Recalling that $\hat{n}_e(e) = \Psi^\dagger(e)\Psi(e)$, the Hamiltonian in eq. (E.1) allows for two types of vertices, corresponding to water-electron and electron-electron Coulomb interactions:

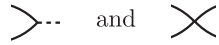

(E.17)

We start by considering only water-electron Coulomb interactions. Then, the series expansion of the exponential in eq. (E.8) has the following diagrammatic representation:

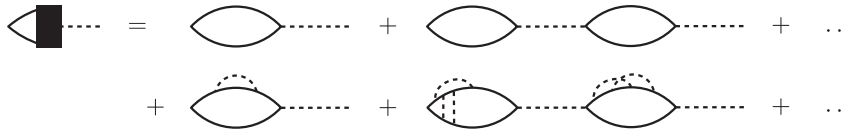

(E.18)

This expansion allows for partial resummation in the form of a Dyson equation:

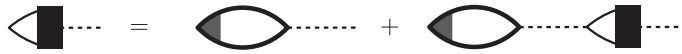

(E.19)

The thick line represents the electron Green's function renormalised by all self-energy corrections due to Coulomb interactions with water. For the water-graphene interface, we will compute the lowest order self-energy diagram (see section E.3.3). The grey triangle represents vertex corrections, which are analogous to electron-phonon vertex corrections, and we expect them in general to be negligible according to the Migdal theorem [257,258]. For simplicity, we drop these vertex corrections in the following, and leave their detailed investigation for future work.

We now include the electron-electron Coulomb interactions at the self-consistent Hartree (RPA) level. This amounts to renormalise the electron polarisation bubble (or density correlation function) according to

(E.20)

We note that in principle, electron-electron interactions beyond the RPA could be included, and would result in further self-energy and vertex corrections to the polarisation bubble. Ultimately, our Dyson equation for the electron-water density correlation function becomes

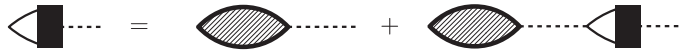

(E.21)

E.1.4 General result

We now explicit the analytical expressions corresponding to the Feynman diagrams. We denote χ_e the renormalised electron polarisation bubble, as defined in eq. (E.20). Then, the first term in eq. (E.21) reads

$$\begin{pmatrix} [\chi^{(1)}_{ew}]^R(e,w) & [\chi^{(1)}_{ew}]^K(e,w) \\ 0 & [\chi^{(1)}_{ew}]^A(e,w) \end{pmatrix} \equiv [\chi_e \otimes \chi_w](e,w)$$
$$= \int_{-\infty}^{+\infty} \mathrm{d}t \int \mathrm{d}\mathbf{r}'_e \mathrm{d}\mathbf{r}'_w V(\mathbf{r}'_e - \mathbf{r}'_w) \dots$$
$$\begin{pmatrix} \chi^R_e(\mathbf{r}_e, t_e, \mathbf{r}'_e, t) & \chi^K_e(\mathbf{r}_e, t_e, \mathbf{r}'_e, t) \\ 0 & \chi^A_e(\mathbf{r}_e, t_e, \mathbf{r}'_e, t) \end{pmatrix} \begin{pmatrix} \chi^R_w(\mathbf{r}'_w - \mathbf{v}t, t, \mathbf{r}_w, 0) & \chi^K_w(\mathbf{r}'_w - \mathbf{v}t, t, \mathbf{r}_w, 0) \\ 0 & \chi^A_w(\mathbf{r}'_w - \mathbf{v}t, t, \mathbf{r}_w, 0) \end{pmatrix}.$$

Having made explicit the definition of the convolution $\otimes$, we may rewrite the Dyson equation (E.21) in terms of the R, A, K components:

$$\begin{cases} \chi^K_{ew} = \chi^R_e \otimes \chi^K_w + \chi^K_e \otimes \chi^A_w + \chi^R_e \otimes \chi^R_w \otimes \chi^K_{ew} + (\chi^R_e \otimes \chi^K_w + \chi^K_e \otimes \chi^A_w) \otimes \chi^A_{ew} \\ \chi^{R,A}_{ew} = \chi^{R,A}_e \otimes \chi^{R,A}_w + \chi^{R,A}_e \otimes \chi^{R,A}_w \otimes \chi^{R,A}_{ew} \end{cases}. \tag{E.22}$$

Equation (E.22), together with eq. (E.15), is our most general result, that holds far from equilibrium, and for any shape of the solid-liquid interface.

E.1.5 Classical contribution

From now on, we will make several simplifying assumptions so as to obtain closed-form expressions for the solid-liquid friction coefficient. We start by splitting off the contribution to friction due to the solid's static roughness. The solid's charge density can always be split according to

$$\hat{n}_e(\mathbf{r}, t) = \langle n_e(\mathbf{r}) \rangle + \delta\hat{n}_e(\mathbf{r}, t) \equiv n^0_e(\mathbf{r}) + \delta\hat{n}_e(\mathbf{r}, t). \tag{E.23}$$

The static charge density $n^0_e(\mathbf{r})$ only contributes to the Keldysh component of the density correlation function χ_e. Precisely,

$$\begin{aligned} \chi^K_e(\mathbf{r}, t, \mathbf{r}', t') &= -\frac{i}{\hbar} \left[2n^0_e(\mathbf{r}) n^0_e(\mathbf{r}') + \langle \{ \delta\hat{n}_e(\mathbf{r}, t), \delta\hat{n}_e(\mathbf{r}', t') \} \rangle \right] \\ &\equiv -\frac{i}{\hbar} 2n^0_e(\mathbf{r}) n^0_e(\mathbf{r}') + \tilde{\chi}^K_e(\mathbf{r}, t, \mathbf{r}', t'). \end{aligned} \tag{E.24}$$

We consider the effect of static roughness only to first order in the solid-liquid Coulomb interaction. This would be exact in the case where the solid is completely static. If it is not, then we expect most electronic fluctuations to be at wavelengths that are large compared to the lattice spacing, so that the effect of these fluctuations on the surface roughness contribution is small. Nevertheless, the potential effect of these higher order contributions should be reassessed for any particular solid-liquid system under consideration. Using eqs. (E.15), (E.22) and (E.24), the first order surface roughness contribution to the friction force, which we call the *classical* contribution, reads

$$\mathbf{F}_{\mathrm{Cl}} = -\int_{-\infty}^{+\infty} \mathrm{d}t \int \mathrm{d}\mathbf{r}_e \mathrm{d}\mathbf{r}'_e \mathrm{d}\mathbf{r}_w \mathrm{d}\mathbf{r}'_w \, \nabla_{r_w} V(\mathbf{r}_w - \mathbf{r}_e) n^0_e(\mathbf{r}_e) n^0_e(\mathbf{r}'_e) V(\mathbf{r}'_e - \mathbf{r}'_w) \chi^A_w(\mathbf{r}'_w - \mathbf{v}t, t, \mathbf{r}_w, 0). \tag{E.25}$$

Since the liquid is translationally invariant parallel to the surface, we may carry out two-dimensional Fourier transforms. We obtain:

$$\mathbf{F}_{\mathrm{Cl}} = -\int_{-\infty}^{+\infty} \frac{\mathrm{d}\mathbf{q}}{(2\pi)^2}\,(i\mathbf{q}) \int \mathrm{d}z_e \mathrm{d}z'_e \mathrm{d}z_w \mathrm{d}z'_w\, e^{-q|z_e - z_w|} e^{-q|z'_e - z'_w|} \ldots \\ \ldots V_q^2 n_e^0(\mathbf{q}, z_e) n_e^0(-\mathbf{q}, z'_e) \int_{-\infty}^{+\infty} \mathrm{d}t e^{i\mathbf{q}\mathbf{v}(z'_w)t} \chi_w^A(q, z_w, z'_w, t), \tag{E.26}$$

with $V_q \equiv V_q(z=0)$ (see eq. (5.8)). We may now identify the Fourier transform of χ^A with respect to time. Then, we use that $\chi^A(q,z,z',-\omega) = \chi^A(q,z,z',\omega)^* = \chi^R(q,z,z',\omega)$ to obtain

$$\mathbf{F}_{\mathrm{Cl}} = \frac{e^2}{2\epsilon_0} \int \frac{\mathrm{d}\mathbf{q}}{(2\pi)^2} \frac{\mathbf{q}}{q} \int \mathrm{d}z_e \mathrm{d}z'_e \mathrm{d}z_w \mathrm{d}z'_w\, e^{-q|z_e - z_w|} e^{-q|z'_e - z'_w|} \ldots \\ \ldots \frac{e^2}{2\epsilon_0 q} n_e^0(\mathbf{q}, z_e) n_e^0(-\mathbf{q}, z'_e) \mathrm{Im}[\chi_w^R(q, z_w, z'_w, \mathbf{q}\mathbf{v}(z'_w))]. \tag{E.27}$$

This result may be further simplified under the assumption that there is a well-defined separation between the solid and the liquid, say at $z = 0$, so that the integration over the z_w's runs over $[0, +\infty[$, while the integration over the z_e's runs over $]-\infty, 0]$. As explained in Chapter 5, we will further assume that the flow velocity $\mathbf{v}$ is independent of z, which is true as long as the slip length (at least several nm on atomically smooth surfaces) is much larger than the range of the interactions contributing to the friction force (less than 1 nm). We then identify the (retarded) surface response function $g_w(q,\omega)$ of the liquid, so as to obtain

$$\mathbf{F}_{\mathrm{Cl}} = -\frac{e^2}{2\epsilon_0} \int \frac{\mathrm{d}\mathbf{q}}{(2\pi)^2} \frac{\mathbf{q}}{q} \int_{-\infty}^{0} \mathrm{d}z_e \mathrm{d}z'_e e^{q(z_e + z'_e)} n_e^0(\mathbf{q}, z_e) n_e^0(-\mathbf{q}, z'_e)\, \mathrm{Im}[g_w^R(q, \mathbf{q}\mathbf{v})]. \tag{E.28}$$

This result may be cast into a more physically transparent form. First, we define

$$|V_e(\mathbf{q})|^2 = \frac{1}{\mathcal{A}} \left| \frac{e^2}{2\epsilon_0 q} \int_{-\infty}^{0} \mathrm{d}z_e\, e^{qz_e} n_e^0(\mathbf{q}, z_e) \right|^2, \tag{E.29}$$

which is the squared Fourier component at wavevector $\mathbf{q}$ of the average potential acting on the liquid at $z = 0$, normalised by the area $\mathcal{A}$ of the interface. Then, eq. (E.28) becomes

$$\frac{\mathbf{F}_{\mathrm{Cl}}}{\mathcal{A}} = -\int \frac{\mathrm{d}\mathbf{q}}{(2\pi)^2}\, \mathbf{q}\, |V_e(\mathbf{q})|^2 \left[\frac{2\epsilon_0 q}{e^2} \mathrm{Im}[g_w^R(q, \mathbf{q}\mathbf{v})] \right]. \tag{E.30}$$

Second, the expression in brackets can recast in terms of the liquid dynamic structure factor. We make use of the equilibrium relation between the Keldysh and retarded components of the surface correlation functions, which plays the role of a fluctuation-dissipation theorem [259]:

$$g_w^K(q,\omega) = 2i \coth\left(\frac{\hbar\omega}{2k_{\mathrm{B}}T} \right) \mathrm{Im}[g_w^R(q,\omega)]. \tag{E.31}$$

Taking the limit $\omega \to 0$ of this relation, and using the definition (E.14), we obtain

$$\lim_{\omega\to 0} \left(\frac{2\epsilon_0 q}{e^2} \frac{\mathrm{Im}[g_w^R(q,\omega)]}{\omega} \right) = \frac{1}{2\mathcal{A}k_B T} \int_{-\infty}^{+\infty} \mathrm{d}t \langle n_w^s(\mathbf{q}, t) n_w^s(-\mathbf{q}, 0) \rangle, \tag{E.32}$$

where

$$n_w^s(\mathbf{q},t) = \int_0^{+\infty} \mathrm{d}z\, e^{-qz} n_w(\mathbf{q},z,t). \tag{E.33}$$

Defining the "surface" dynamic charge structure factor of the liquid as

$$S_w(q,t) = \frac{\langle n_w^s(\mathbf{q},t) n_w^s(-\mathbf{q},0)\rangle}{\mathcal{A}}, \tag{E.34}$$

and expanding eq. (E.30) to linear order in $\mathbf{v}$, we obtain

$$\frac{\mathbf{F}_{\mathrm{Cl}}}{\mathcal{A}} = -\frac{1}{8\pi^2 k_B T} \int \mathrm{d}\mathbf{q}\, \mathbf{q}(\mathbf{q}\cdot\mathbf{v}) \, |V_e(\mathbf{q})|^2 \int_{-\infty}^{+\infty} \mathrm{d}t\, S_w(q,t). \tag{E.35}$$

Finally, defining the classical friction coefficient λ_{cl} through $\mathbf{F}_{\mathrm{Cl}}\cdot\mathbf{v}/\mathcal{A} = -\lambda_{\mathrm{Cl}} v^2$, we obtain

$$\lambda_{\mathrm{Cl}} = \frac{1}{4\pi^2 k_B T} \int \mathrm{d}\mathbf{q}\, \frac{(\mathbf{q}\cdot\mathbf{v})^2}{v^2} \, |V_e(\mathbf{q})|^2 \int_0^{+\infty} \mathrm{d}t\, S_w(q,t), \tag{E.36}$$

which is equation (5.15) given in Chapter 5. This is formally identical to the result obtained in the classical treatment of solid-liquid friction where the solid has no internal degrees of freedom [163]; we recover it here in the corresponding limit of our quantum formalism. We note, however, that our formalism only deals with Coulomb interactions, and any roughness of the short-range Pauli repulsion forces is not taken into account. Nevertheless, this additional roughness could be dealt with in the exact same way as above, with the Coulomb potential replaced by a short-range repulsive potential, and the water charge density replaced by the water atom density.

E.1.6 Quantum contribution

Having dealt with the static roughness contribution, we assume that the solid's average charge density vanishes: this amounts to replacing $\chi_e^K \mapsto \tilde{\chi}_e^K$ in eq. (E.22). We then make the same simplifying assumptions as in the previous section: there is a separation between the solid and the liquid at $z = 0$, and the velocity field does not depend on z. We further assume that the various correlation functions are translationally invariant parallel to the interface. This assumption is not necessary to proceed, but it greatly simplifies notations and is relevant for most practical purposes: we will be considering fluctuations at wavelengths that are longer than the solid's lattice spacing.

With the above assumptions, we may define, for any correlation function χ, the surface correlation function g according to

$$\begin{aligned} g(\mathbf{q},\omega) = \frac{-e^2}{4\pi\epsilon_0}\frac{2\pi}{q} \int \mathrm{d}(\boldsymbol{\rho}-\boldsymbol{\rho}') e^{-i\mathbf{q}(\boldsymbol{\rho}-\boldsymbol{\rho}')} \int_{-\infty}^{+\infty} \mathrm{d}(t-t') e^{i\omega(t-t')} \dots \\ \dots \int_0^{+\infty} \mathrm{d}z \mathrm{d}z' e^{-q(|z|+|z'|)} \chi(\boldsymbol{\rho},\boldsymbol{\rho}',z,z',t,t'). \end{aligned} \tag{E.37}$$

These naturally satisfy the same Dyson equations (E.22) as the χ functions, and their convolution corresponds simply to multiplication in Fourier space. But, importantly, the effect of the flow velocty $\mathbf{v}$ is to shift the frequencies appearing in water correlation functions according to $\omega \mapsto \omega - \mathbf{q}\mathbf{v}$. With that, rearranging eq. (E.22) yields

$$g_{ew}^K(\mathbf{q},\omega) = -\frac{g_e^R(q,\omega)\, g_w^K(q,\omega-\mathbf{q}\mathbf{v}) + g_e^K(q,\omega)\, g_w^A(q,\omega-\mathbf{q}\mathbf{v})}{|1 - g_e^R(q,\omega)\, g_w^R(q,\omega-\mathbf{q}\mathbf{v})|^2}, \tag{E.38}$$

where we have used that $g^R(\mathbf{q},\omega) = [g^A(\mathbf{q},\omega)]^*$. We now notice that Fourier-transforming eq. (E.15) yields

$$\frac{\langle\hat{\mathbf{F}}\rangle}{\mathcal{A}} = \frac{1}{2}\frac{i\hbar}{(2\pi)^3}\int_{-\infty}^{+\infty}\mathrm{d}\omega\int\mathrm{d}\mathbf{q}\,(i\mathbf{q})g^K_{ew}(\mathbf{q},\omega). \tag{E.39}$$

In order to proceed, we make use of the fluctuation-dissipation theorem as in the previous section:

$$g^K_{e,w}(q,\omega) = 2i\coth\left(\frac{\hbar\omega}{2k_BT}\right)\mathrm{Im}[g^R_{e,w}(q,\omega)] \equiv 2if(\omega)\mathrm{Im}[g^R_{e,w}(q,\omega)]. \tag{E.40}$$

We may then expand eq. (E.38) as

$$\begin{aligned} g^K_{ew}(\mathbf{q},\omega) = {} & 2\frac{(f(\omega-\mathbf{qv})-f(\omega))\mathrm{Im}[g^R_e(q,\omega)]\,\mathrm{Im}[g^R_w(q,\omega-\mathbf{qv})]}{|1-g^R_e(q,\omega)\,g^R_w(q,\omega-\mathbf{qv})|^2} \\ & - 2i\frac{f(\omega-\mathbf{qv})\mathrm{Re}[g^R_e(q,\omega)]\,\mathrm{Im}[g^R_w(q,\omega-\mathbf{qv})] + f(\omega)\mathrm{Im}[g^R_e(q,\omega)]\,\mathrm{Re}[g^R_w(q,\omega-\mathbf{qv})]}{|1-g^R_e(q,\omega)\,g^R_w(q,\omega-\mathbf{qv})|^2}. \end{aligned} \tag{E.41}$$

The imaginary parts of the surface response functions g^R are odd functions of ω, while the real parts are even. Therefore, the second term in eq. (E.41) is even with respect to the transformation $\omega \mapsto -\omega, \mathbf{q} \mapsto -\mathbf{q}$ and vanishes upon integration in eq. (E.39). We hence obtain the quantum contribution to the friction force as:

$$\frac{\mathbf{F}_\mathrm{Q}}{\mathcal{A}} = \frac{\hbar}{(2\pi)^3}\int\mathrm{d}\mathbf{q}\,\mathbf{q}\int_{-\infty}^{+\infty}\mathrm{d}\omega\,\frac{(f(\omega)-f(\omega-\mathbf{qv}))\mathrm{Im}[g^R_e(q,\omega)]\,\mathrm{Im}[g^R_w(q,\omega-\mathbf{qv})]}{|1-g^R_e(q,\omega)\,g^R_w(q,\omega-\mathbf{qv})|^2}. \tag{E.42}$$

To linear order in $\mathbf{v}$, the friction force becomes

$$\frac{\mathbf{F}_\mathrm{Q}}{\mathcal{A}} = \frac{\hbar}{4\pi^3}\int\mathrm{d}\mathbf{q}\,\mathbf{q}\,(\mathbf{q}\cdot\mathbf{v})\int_0^{+\infty}\mathrm{d}\omega\left(\frac{\mathrm{d}f(\omega)}{\mathrm{d}\omega}\right)\frac{\mathrm{Im}[g^R_e(q,\omega)]\,\mathrm{Im}[g^R_w(q,\omega)]}{|1-g^R_e(q,\omega)\,g^R_w(q,\omega)|^2}, \tag{E.43}$$

with

$$\frac{\mathrm{d}f(\omega)}{\mathrm{d}\omega} = -\frac{\hbar}{2k_BT}\sinh^{-2}\left(\frac{\hbar\omega}{2k_BT}\right). \tag{E.44}$$

Defining the quantum friction coefficient λ_Q by $\mathbf{F}_\mathrm{Q}/\mathcal{A} = -\lambda_\mathrm{Q}\mathbf{v}$, we obtain after angular integration

$$\lambda_\mathrm{Q} = \frac{\hbar^2}{8\pi^2k_BT}\int_0^{+\infty}\mathrm{d}q\,q^3\int_0^{+\infty}\frac{\mathrm{d}\omega}{\sinh^2\left(\frac{\hbar\omega}{2k_BT}\right)}\frac{\mathrm{Im}[g^R_e(q,\omega)]\,\mathrm{Im}[g^R_w(q,\omega)]}{|1-g^R_e(q,\omega)\,g^R_w(q,\omega)|^2}, \tag{E.45}$$

which is equation (5.16) after minor rearrangement.

E.1.7 Discussion

Our result for the solid-liquid quantum friction coefficient (eq. (E.45)) is formally identical to the one obtained in the solid-solid case by Volokitin and Persson ([158] and references therein), and differs by a factor of 2 from the one obtained by Despoja, Echenique and Sunjic [260]. However, none of the literature derivations for non-contact solid-solid friction

may readily be extended to the solid-liquid case. Indeed, to our knowledge, the only derivation based on rigorous field theory arguments is restricted to the case of solids with local dielectric response [168]. At the solid-liquid interface, lengthscales as small as the solid's lattice spacing come into play, and an assumption of local dielectric response cannot hold. On the other hand, explicitly non-local derivations [166, 260] have treated the friction force rigorously to first order in the Coulomb interactions, and based the expression of higher order terms on an idea of multiple reflections of the electromagnetic field. This reasoning is difficult to justify fundamentally, especially when the two media are actually in contact, as in the solid-liquid case.

Our formalism deals rigorously with the Coulomb interactions up to arbitrary order in fully non-local media. This allows us to obtain contributions beyond the first order (the denominator in eq. (E.45)) without resorting to multiple reflection arguments, as the solution of a Dyson equation written in non-equilibrium perturbation theory. Beyond justifying the use of eq. (E.45) for the solid-liquid interface, our formalism unambiguously specifies in which way – if at all – the response functions appearing in eq. (E.45) should be renormalised by the solid-liquid interactions. Indeed, if interactions are taken into account at the RPA level, our computation shows that the response functions appearing in eq. (E.45) are bare response functions. Therefore, they do not need further RPA renormalisation, for instance according to [261]

$$\mathbf{g}^R_{e,w}(q,\omega) = \frac{g^R_{e,w}(q,\omega)}{1 - g^R_e(q,\omega) g^R_w(q,\omega)}. \tag{E.46}$$

The only interaction corrections that are not explicit in eq. (E.45) are self-energy corrections to the electronic response function.

E.2 Jellium model

E.2.1 Surface response

In order to qualitatively assess the role of electronic properties in the quantum friction of water, we consider a generic electronic system described within the infinite barrier jellium model, treated in the specular reflection (SR) approximation (for a detailed discussion of surface response functions and the SR approximation, see Appendix B). The non-interacting bulk density response function is computed according to eq. (B.21). For the bulk jellium, there is a single band with energy $E(k) = \frac{\hbar^2 k^2}{2m^*}$, with m^* the effective mass, and the eigenstates are Bloch waves, so that all the matrix elements are equal to 1. Setting the temperature to 0, the Fermi-Dirac distribution becomes $f(E) = \theta(E_\mathrm{F} - E)$, with E_F the Fermi energy. The integral in eq. (B.21) may then be evaluated analytically, yielding the Lindhard function [262, 263]:

$$v(q,q_z)\mathrm{Re}[\chi^0_\mathrm{B}(q,q_z,\omega)] = -\frac{\alpha r_s}{4x^2}\left(\frac{1}{2} + \frac{F(x,x_0) + F(x,-x_0)}{8x}\right), \tag{E.47}$$

$$v(q,q_z)\mathrm{Im}[\chi^0_\mathrm{B}(q,q_z,\omega)] = -\frac{\alpha r_s}{4x^2}\left[\frac{\pi(1-(x_0/x-x)^2)}{8x}\theta(x_0 - |x-x^2|)\theta(x+x^2-x_0)\dots \right.$$
$$\left. + \frac{\pi x_0}{2x}\theta(x_0)\theta(x-x^2-x_0)\right]. \tag{E.48}$$

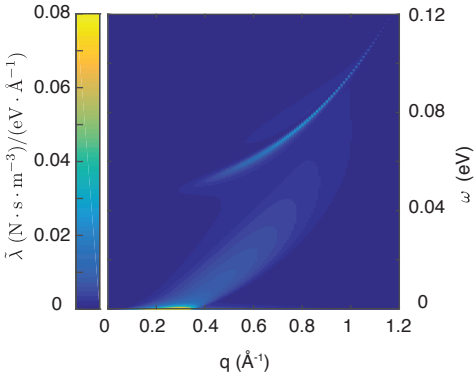

Figure E.1

The friction integrand $\tilde{\lambda}$ (defined in the text), in the jellium model with $E_\mathrm{F} = 2$ meV and $m^* = 50\,m_e$, as a function of q and ω.

We used the following notations:

$$F(x, x_0) = \left(1 - \left(\frac{x_0}{x} - x\right)^2\right) \log\left|\frac{x + x^2 - x_0}{x - x^2 + x_0}\right|; \tag{E.49}$$

$x = \sqrt{q^2 + q_z^2}/(2k_\mathrm{F})$, $x_0 = \omega/(4\omega_\mathrm{F})$. $\omega_\mathrm{F} = E_\mathrm{F}/\hbar$ is the Fermi frequency, $k_\mathrm{F} = \sqrt{2m^* E_\mathrm{F}/\hbar^2}$ is the Fermi wavevector. $v(q, q_z) = e^2/(\epsilon_0(q^2+q_z^2))$ is the 3D Coulomb potential. Once the frequencies and wavevectors have been normalised by the Fermi frequency and wavevector, the Lindhard function depends only on the electron density parameter r_s, defined by

$$r_s = \left(\frac{9\pi}{4}\right)^{1/3} \frac{(m^*/m_e)}{k_\mathrm{F} a_0}, \tag{E.50}$$

with $a_0 = 4\pi\epsilon_0\hbar^2/(m_e e^2)$ the Bohr radius and m_e the electron mass. The prefactor α is $\alpha = (4/\pi)(9\pi/4)^{-1/3} \approx 0.66$. Given the Lindhard function, the surface response function of the semi-infinite jellium can be evaluated by carrying out numerically the integration in eq. (B.20).

E.2.2 Friction coefficient

In order to evaluate the quantum friction coefficient of water on a semi-infinite jellium according to eq. (5.16), we fit the numerically determined jellium surface response function with analytical expressions. Such a procedure is necessary because the integral in eq. (5.16) has contributions at very low frequencies (typically, the water Debye mode frequency), and much higher frequencies corresponding to the electronic surface plasmon mode, which makes numerical sampling difficult. Figure E.1 shows the integrand of eq. (5.16), that is

$$\tilde{\lambda}(q, \omega) = \frac{\hbar^2}{8\pi^2 k_B T} \frac{q^3}{\sinh^2\left(\frac{\hbar\omega}{2k_B T}\right)} \frac{\mathrm{Im}[g_e(q,\omega)]\,\mathrm{Im}[g_w(q,\omega)]}{|1 - g_e(q,\omega)\,g_w(q,\omega)|^2}, \tag{E.51}$$

in (q, ω) space, with parameter values such that the surface plasmon frequency is low enough to make a non-negligible contribution ($E_\mathrm{F} = 2$ meV and $m^* = 50\,m_e$). We observe observe that the integrand $\tilde{\lambda}(q, \omega)$ has contributions from two disjoint regions of the (q, ω) space: at very low frequencies ($\omega \to 0$), and at frequencies around the surface

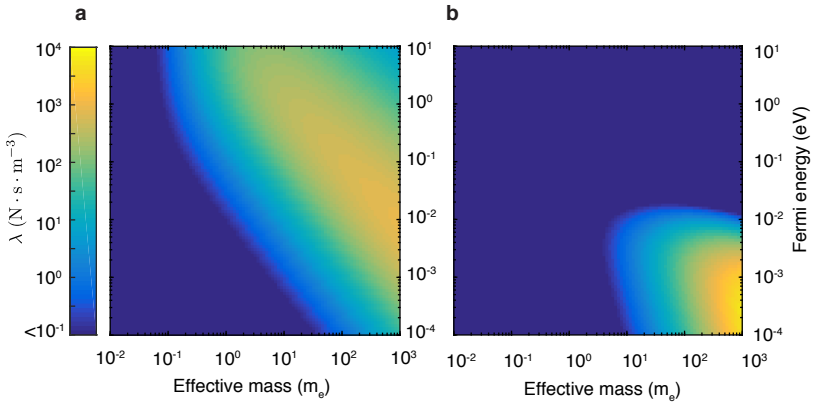

Figure E.2

a. Low frequency particle-hole excitation contribution to the quantum friction coefficient. **b**. Surface plasmon contribution to the quantum friction coefficient.

plasmon frequency. Hence, we may fit the jellium surface response separately in these two regions.

Our choice of fit functions is guided by [174]. In the low frequency region, we use

$$g_e(q,\omega) = e^{-q/(k_\mathrm{F} C[r_s])} + iA[r_s]\frac{\omega}{E_\mathrm{F}}\frac{q}{k_F}e^{-q/(k_\mathrm{F} B[r_s])}\theta(q-2k_\mathrm{F}). \tag{E.52}$$

For the surface plasmon region, we fitted the imaginary part of the surface response function by a Lorentzian:

$$\mathrm{Im}\, g_e(q,\omega) = \frac{D[q/k_\mathrm{F}, r_s]}{2}\frac{1}{(\omega-\omega_P[q/k_\mathrm{F}, r_s])^2+\gamma[q/k_\mathrm{F}, r_s]^2}. \tag{E.53}$$

The real part was then consistently determined through the Kramers-Krönig relation:

$$\begin{aligned}\mathrm{Re}\, g_e(q,\omega) &= \frac{2}{\pi}\mathcal{P}\int_0^{+\infty}\mathrm{d}\omega'\frac{\omega'\mathrm{Im}\, g_e(q,\omega')}{\omega'^2-\omega^2}\\ &= \frac{D[q/k_\mathrm{F}, r_s]}{2}\frac{\omega_P[q/k_\mathrm{F}, r_s](\omega_P[q/k_\mathrm{F}, r_s]-\omega)}{(\omega-\omega_P[q/k_\mathrm{F}, r_s])^2+\gamma[q/k_\mathrm{F}, r_s]^2},\end{aligned} \tag{E.54}$$

where $\mathcal{P}$ indicates that the Cauchy principal value of the integral is taken. We carry out the fit up to $q_\mathrm{max}/k_\mathrm{F} = -1+\sqrt{1+2\omega_P^0[r_s]/\omega_\mathrm{F}}$, where

$$\omega_P^0[r_s] = \sqrt{\frac{8}{3\pi}\left(\frac{4}{9\pi}\right)^{1/3}} r_s^{1/2}\omega_\mathrm{F} \approx 0.67\times r_s^{1/2}\omega_\mathrm{F} \tag{E.55}$$

is the surface plasmon frequency at zero wavevector. For wavevectors beyond q_max the surface plasmon is Landau-damped, effectively disappearing from the spectrum. We found that the fit results were well-reproduced by the following analytical expressions:

$$\omega_P[q,r_s] = \omega_P^0[r_s]\left(1+\frac{q^2}{q_\mathrm{max}[r_s]^2}\right) \quad \text{and} \quad A[q,r_s] = e^{-q/(0.45\times q_\mathrm{max}[r_s])}, \tag{E.56}$$

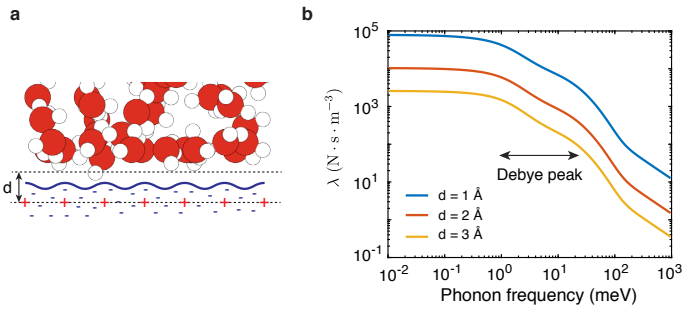

Figure E.3

Phonon contribution to quantum friction. **a**. Definition of the distance d appearing in eq. (E.59). **b**. Phonon contribution to the quantum friction coefficient as a function of phonon frequency ω_s, for different values of d. The phonon width is set at $\gamma = \omega_s/20$.

and $\gamma = 0.01 \times \omega_P^0[r_s]$. Figure E.2 shows separately the low frequency and the plasmon contribution to the quantum friction coefficient as a function of the jellium parameters m^* and ω_F. It clearly appears that the friction is dominated by the plasmon contribution in the region of low Fermi energy and high effective mass, where the plasmon is at low energy and is weakly damped up to high momenta.

E.2.3 Phonon contribution

In addition to electronic excitations, phonon modes can make a contribution to the surface response function of a solid, precisely in the low frequency and high momentum region relevant for water quantum friction. We expect that the phonon contribution will be most significant for polar materials such as hBN or SiO_2, which have nearly dispersionless optical phonon modes, so that their dielectric response may be considered local up to momenta comparable with the Brillouin zone size. We consider for simplicity a material with a single optical phonon mode with frequency ω_ph and width γ. Assuming $\epsilon_\infty \approx 1$, its dielectric function may be written as

$$\epsilon(\omega) = \epsilon_\infty + (\epsilon_s - 1)\frac{\omega_\mathrm{ph}^2}{\omega_\mathrm{ph}^2 - \omega^2 - i\gamma\omega}, \tag{E.57}$$

where ϵ_∞ is the high frequency background dielectric constant and ϵ_s is the static dielectric constant. The corresponding surface response function is

$$g(\omega) = \frac{\epsilon(\omega) - 1}{\epsilon(\omega) + 1} = \frac{\epsilon_s - 1}{\epsilon_s + 1}\frac{\omega_s^2}{\omega_s^2 - \omega^2 - i\gamma\omega}, \tag{E.58}$$

with $\omega_s = \omega_\mathrm{ph}\sqrt{(1+\epsilon_s)/2}$ the surface phonon frequency. The ratio $(\epsilon_s - 1)/(\epsilon_s + 1)$ defines a surface phonon "oscillator strength", which is close to 1 since $\epsilon_s \sim 3 - 10$.

Now, in the case of phonons, eq. (E.58) cannot be directly used to evaluate a quantum friction coefficient according to eq. (E.45). Indeed, one should take into account a microscopic distance d between the interfacial water layer and the first atomic layer of

the solid, which supports the phonon mode (see figure E.3). Eq. (E.45) is then modified according to

$$\lambda^{\mathrm{q}} = \frac{\hbar^2}{8\pi^2 k_B T}\int_0^{+\infty} \mathrm{d}q\, q^3 e^{-2qd}\int_0^{+\infty} \frac{\mathrm{d}\omega}{\sinh^2\left(\frac{\hbar\omega}{2k_BT}\right)} \frac{\mathrm{Im}[g_e^R(q,\omega)]\,\mathrm{Im}[g_w^R(q,\omega)]}{|1-e^{-2qd}g_e^R(q,\omega)\,g_w^R(q,\omega)|^2}, \tag{E.59}$$

We note that in the case of electronic excitations, there is no need to add explicitly a distance d, as the water molecules are in direct contact with the solid's electronic density. The position of the image plane within the solid is then taken into account in the momentum dependence of the electronic surface response function. Figure E.3 shows the friction coefficient computed according eq. (E.59) for different values of d in the angström range as a function of phonon frequency (the "oscillator strength" is taken equal to 1). We assume a small phonon width $\gamma = \omega_s/20$. We find that, for reasonable surface phonon frequencies ($\omega_s \sim 100$ meV), the phonon contribution to water quantum friction is rather small ($\lambda \sim 10^2$ N · s · m^{-3}), even at $d = 1$ Å.

In figure E.3, we plotted the quantum friction coefficient for a wide range of phonon frequencies (beyond physically reasonable ones), in order to study in a simple case the dependence of the friction coefficient on mode frequencies. In eqs. (E.45) and (E.59), the product of surface response functions suggests that there should be a resonance for the friction coefficient when a solid (phonon) mode has the same frequency as the water Debye mode. This is however not the case, and the friction coefficient is found to be a monotonically decreasing function of the phonon frequency. This is due to the thermal factor $\sinh(\hbar\omega/2k_{\mathrm{B}}T)$, which gives more weight to lower frequency modes, and to the very broad shape of the Debye peak. If the Debye peak was replaced by a weakly damped harmonic oscillator peak centred at ω_{D}, the friction coefficient would show a maximum at $\omega_s = \omega_{\mathrm{D}}$, but would still converge to a non-zero value as $\omega_s \to 0$.

E.3 Water-carbon interface

E.3.1 Graphene surface response function

We compute the surface response function of monolayer graphene according to the definition in eq. (B.3). In order to explicit the density response function $\chi(q, z, z', \omega)$, we make use of the tight binding model of graphene [264, 265]. In the tight binding description, the Hilbert space of the graphene π electrons is restricted to linear combinations of localised states $|i\rangle$. We denote $c_i^\dagger, c_i$ the corresponding creation and anihilation operators and $\varphi(\mathbf{r} - \mathbf{r}_i)$ the corresponding wavefunctions. We use for φ the generalised hydrogenic wavefunction representing the carbon $2p_z$ orbital [265]:

$$\varphi(\rho, z) = Aze^{-Z\sqrt{\rho^2+z^2}/2a_0}, \tag{E.60}$$

with A a normalisation factor, a_0 the Bohr radius and $Z = 3.18$. All overlaps between neighbouring orbitals are neglected, so that the electron density reads

$$n(\mathbf{r}, t) = \sum_i |\varphi(\mathbf{r} - \mathbf{r}_i)|^2 c_i^\dagger(t) c_i(t) \tag{E.61}$$

We introduce the Bloch state operators, defined separately for the sublattices A and B:

$$c_A^\dagger(\mathbf{k}) = \sum_{i\in A} e^{i\mathbf{k}\boldsymbol{\rho}_i} c_i^\dagger \quad \text{and} \quad c_B^\dagger(\mathbf{k}) = \sum_{i\in B} e^{i\mathbf{k}\boldsymbol{\rho}_i} c_i^\dagger. \tag{E.62}$$

The inverse transformation is

$$c^\dagger_{i\in A} = \int_{\mathrm{BZ}} \frac{\mathrm{d}\mathbf{k}}{\mathcal{A}_{\mathrm{BZ}}} e^{-i\mathbf{k}\boldsymbol{\rho}_i} c^\dagger_A(\mathbf{k}) \quad \text{and} \quad c^\dagger_{i\in B} = \int_{\mathrm{BZ}} \frac{\mathrm{d}\mathbf{k}}{\mathcal{A}_{\mathrm{BZ}}} e^{-i\mathbf{k}\boldsymbol{\rho}_i} c^\dagger_B(\mathbf{k}), \tag{E.63}$$

with $\mathcal{A}_{\mathrm{BZ}}$ the area of the Brillouin zone. We further note the property

$$\sum_{i\in A,B} e^{i\mathbf{k}\boldsymbol{\rho}_i} = \mathcal{A}_{\mathrm{BZ}} \sum_{\mathbf{G}} \delta(\mathbf{k}+\mathbf{G}), \tag{E.64}$$

where the $\mathbf{G}$ are vectors of the reciprocal lattice. Inserting (E.63) into (E.61), and using (E.64), we obtain

$$n(\boldsymbol{\rho}, z, t) = \int_{\mathrm{BZ}} \frac{\mathrm{d}\mathbf{q}}{(2\pi)^2} \sum_{\mathbf{G}} \xi(\mathbf{q}+\mathbf{G}, z) e^{i(\mathbf{q}+\mathbf{G})\boldsymbol{\rho}} n_{\mathbf{q}}(t), \tag{E.65}$$

with

$$\xi(\mathbf{q}, z) = \int \mathrm{d}\boldsymbol{\rho} |\varphi(\rho, z)|^2 e^{-i\mathbf{q}\boldsymbol{\rho}} \tag{E.66}$$

and

$$n_{\mathbf{q}}(t) = \int_{\mathrm{BZ}} \frac{\mathrm{d}\mathbf{k}}{\mathcal{A}_{\mathrm{BZ}}} \sum_{a\in\{A,B\}} c^\dagger_a(\mathbf{k}+\mathbf{q}, t) c_a(\mathbf{k}, t). \tag{E.67}$$

We now focus on the non-interacting density response function χ^0. Inserting (E.67) into the definition (E.13), we obtain

$$\begin{aligned}\chi^0(\mathbf{r}, t, \mathbf{r}', t') = \int_{\mathrm{BZ}} \frac{\mathrm{d}\mathbf{q}\mathrm{d}\mathbf{q}'}{(2\pi)^4} \sum_{\mathbf{G},\mathbf{G}'} \xi(\mathbf{q}+\mathbf{G}, z)\xi(\mathbf{q}'+\mathbf{G}', z') e^{i(\mathbf{q}+\mathbf{G})\boldsymbol{\rho}} e^{i(\mathbf{q}'+\mathbf{G}')\boldsymbol{\rho}'} \dots \\ \dots \left[-\frac{i}{\hbar}\theta(t-t')\langle[n_{\mathbf{q}}(t), n_{\mathbf{q}'}(t')]\rangle_0\right].\end{aligned} \tag{E.68}$$

Now, momentum conservation imposes

$$\langle[n_{\mathbf{q}}(t), n_{\mathbf{q}'}(t')]\rangle_0 = \mathcal{A}_{\mathrm{BZ}}\delta(\mathbf{q}+\mathbf{q}')\langle[n_{\mathbf{q}}(t), n_{-\mathbf{q}}(t')]\rangle_0. \tag{E.69}$$

Hence, eq. (E.68) becomes

$$\begin{aligned}\chi^0(\mathbf{r}, t, \mathbf{r}', t') = \int_{\mathrm{BZ}} \frac{\mathrm{d}\mathbf{q}}{(2\pi)^2} \sum_{\mathbf{G},\mathbf{G}'} \xi(\mathbf{q}+\mathbf{G}, z)\xi(\mathbf{q}+\mathbf{G}', z')^* e^{i(\mathbf{q}+\mathbf{G})\boldsymbol{\rho}} e^{-i(\mathbf{q}+\mathbf{G}')\boldsymbol{\rho}'} \dots \\ \dots \left[-\frac{i}{\hbar}\theta(t-t')\frac{\mathcal{A}_{\mathrm{BZ}}}{(2\pi)^2}\langle[n_{\mathbf{q}}(t), n_{-\mathbf{q}}(t')]\rangle_0\right].\end{aligned} \tag{E.70}$$

The quantity in brackets is the non-interacting density response function χ^0_{2D} of graphene that has been evaluated in the literature [176, 266]. It has the usual expression as a function of the graphene eigenenergies $E_\nu(\mathbf{k})$ and eigenstates $|\mathbf{k}, \nu\rangle$, which is the 2D analogue of eq. (B.21):

$$\chi^0_{\mathrm{2D}}(\mathbf{q}, \omega) = \sum_{\nu,\nu'=\pm1} \int_{\mathrm{BZ}} \frac{\mathrm{d}^2k}{2\pi^2} |\langle\mathbf{k}+\mathbf{q}, \nu|e^{i\mathbf{q}\cdot\mathbf{r}}|\mathbf{k}, \nu'\rangle|^2 \frac{n_{\mathrm{F}}[E_\nu(\mathbf{k}+\mathbf{q})] - n_{\mathrm{F}}[E_{\nu'}(\mathbf{k})]}{E_\nu(\mathbf{k}+\mathbf{q}) - E_{\nu'}(\mathbf{k}) - \hbar(\omega+i\delta)}. \tag{E.71}$$

For momenta $\mathbf{q}$ that are small compared to the intervalley distance (1.7 Å^{-1}), the integration over the Brillouin zone may be carried out separately for the two valleys, and the matrix elements have the expression

$$|\langle \mathbf{k}+\mathbf{q}, \nu | e^{i\mathbf{q}\cdot\mathbf{r}} | \mathbf{k}, \nu' \rangle| = \frac{1}{2}\left(1 + \nu\nu' \frac{k + q\cos\theta}{\|\mathbf{k}+\mathbf{q}\|}\right), \tag{E.72}$$

where θ is the angle between $\mathbf{k}$ and $\mathbf{q}$. If one further assumes zero temperature, the integral in eq. (E.71) can be carried out analytically, yielding the expression reported in [176], which we reproduce here for completeness:

$$\begin{aligned}\chi^0_{\text{2D}}(q,\omega) = &-i\pi\frac{F(q,\omega)}{v_F^2} - \frac{2E_F}{\pi v_F^2} + \dots \\ &+ \frac{F(q,\omega)}{v_F^2}\left[G\left(\frac{\omega+2E_F}{v_F q}\right) - \theta\left(\frac{2E_F-\omega}{v_F q} - 1\right)\left\{G\left(\frac{2E_F-\omega}{v_F q}\right) - i\pi\right\} + \dots \right. \\ &\left. + \theta\left(\frac{\omega-2E_F}{v_F q} + 1\right) G\left(\frac{\omega-2E_F}{v_F q}\right)\right].\end{aligned} \tag{E.73}$$

Here, E_F is the graphene Fermi energy (doping level), $v_F = 6.73\ \text{eV}\cdot\text{Å}$ is the graphene Fermi velocity, and the functions F and G are given by

$$F(q,\omega) = \frac{1}{4\pi}\frac{v_F^2 q^2}{\sqrt{\omega^2 - v_F^2 q^2}}, \tag{E.74}$$

and

$$G(x) = x\sqrt{x^2-1} - \log\left(x + \sqrt{x^2-1}\right). \tag{E.75}$$

Having written out the non-interacting density response function for graphene, we may examine the corresponding surface response function. We found (eq. (E.70)), that the non-interacting density response function χ^0 has a Fourier expansion of the form

$$\chi^0(\mathbf{r},\mathbf{r}',\omega) = \int_{\text{BZ}} \frac{\mathrm{d}\mathbf{q}}{(2\pi)^2} \sum_{\mathbf{G},\mathbf{G}'} \chi^0_{\mathbf{G}\mathbf{G}'}(\mathbf{q},z,z',\omega). \tag{E.76}$$

Therefore, in principle, one should define a non-interacting surface response function for every $(\mathbf{G},\mathbf{G}')$:

$$g^0_{\mathbf{G}\mathbf{G}'}(\mathbf{q},\omega) = -\frac{e^2}{2\epsilon_0\|\mathbf{q}+\mathbf{G}'\|}\int \mathrm{d}z\mathrm{d}z' e^{\|\mathbf{q}+\mathbf{G}\|z} e^{\|\mathbf{q}+\mathbf{G}'\|z'} \chi^0_{\mathbf{G}\mathbf{G}'}(\mathbf{q},z,z',\omega). \tag{E.77}$$

Physically, $g_{\mathbf{G}\mathbf{G}'}$ determines the induced potential at wavevector $\mathbf{q}+\mathbf{G}'$ in response to an applied potential at wavevector $\mathbf{q}+\mathbf{G}$. Now, since we are considering applied potentials at wavevectors much smaller than the reciprocal lattice spacing $G_1 = 2.9\ \text{Å}^{-1}$, we will only be interested in $g^0_{00}(q,\omega) \equiv g^0(q,\omega)$. Expanding eq. (E.77),

$$g^0(q,\omega) = -\frac{e^2}{2\epsilon_0 q}\int \mathrm{d}z\mathrm{d}z' e^{qz} e^{qz'} \xi(q,z)\xi(q,z')^* \chi^0_{\text{2D}}(q,\omega). \tag{E.78}$$

In the water-graphene configuration, the z integration should in principle run from $z = -\infty$ up to some fixed $z_0 > 0$, which sets the limit between solid and liquid. However, the

atomic orbitals φ extend formally up to $z = +\infty$, and they should be somehow cutoff at $z = z_0$. We expect z_0 to be in the angström range, comparable to the typical extension of the $2p_z$ orbital. Hence, for wavevectors $q \lesssim 1/z_0$, the exact choice of z_0 plays no significant role. We may then set $e^{qz} \approx 1$ in eq. (E.78), which reduces to

$$g^0(q,\omega) = -\frac{e^2}{2\epsilon_0 q}|\xi(q)|^2 \chi^0_{2\mathrm{D}}(q,\omega), \tag{E.79}$$

with $\xi(q) \equiv \int \mathrm{d}z \xi(q,z)$. From the expression (E.60) of the $2p_z$ orbital, one obtains [265]

$$|\xi(q)|^2 = \left(1 + (qa_0/Z)^2\right)^{-6}. \tag{E.80}$$

In order to obtain the interacting surface response function, in general one has to solve the RPA Dyson equation (B.10) for the density response function. However, for wavevectors smaller than the reciprocal lattice spacing, it reduces to a Dyson equation involving directly the surface response function:

$$g(q,\omega) = g^0(q,\omega) - g^0(q,\omega) g(q,\omega). \tag{E.81}$$

Hence, we finally obtain the graphene surface response function as

$$g(q,\omega) = \frac{-\frac{e^2}{2\epsilon_0 q}|\xi(q)|^2 \chi^0_{2\mathrm{D}}(q,\omega)}{1 - \frac{e^2}{2\epsilon_0 q}|\xi(q)|^2 \chi^0_{2\mathrm{D}}(q,\omega)}. \tag{E.82}$$

This expression was used to obtain figure 5.6a and figure 5.8a. The charge carrier (electron or hole) density in graphene (n) is related to the Fermi level E_F according to $|E_F| = v_F\sqrt{\pi n}$.

E.3.2 1D chain model

In this section, we present a qualitative model for the surface response of graphite, which accounts for the presence of a dispersionless low energy mode in the surface excitation spectrum. It is based on the physical interpretation of this low energy mode as originating from interlayer excitations of electrons located mainly on the B sublattices (figure 5.6b). The lack of dispersion indicates that, from the point of view of low energy excitations, the 1D chains formed by the B sublattice atoms behave as if they were independent, with no in-plane tunnelling between the chains. This behaviour can be tied, to some extent, to the flattening of the π bands in graphite with respect to graphene, though the very flat dispersion observed in experiment does not seem to fully grasped by the band structure of graphite at the tight-binding level. Hence, as a phenomenological model for the experimentally observed graphite surface response, we consider an array of semi-infinite tight-binding chains, with coupling parameter $\gamma_2 = 10$ meV [184].

E.3.2.1 Local Green's function

As a first step, we evaluate the local non-interacting (retarded) Green's function at the topmost atom of a 1D chain, denoted $G_{11}(\omega)$. We introduce the creation and anihilation

operators $c_i^\dagger, c_i$ at the chain atoms, and the tight-binding Hamiltonian

$$\hat{H} = \sum_{i=1}^{\infty} \gamma_2 (c_i^\dagger c_{i+1} + c_i c_{i+1}^\dagger). \tag{E.83}$$

The Green's function G_{11} is given by the first coefficient of the matrix $(\hbar\omega\hat{I} - \hat{H})^{-1}$, with $\hat{I}$ the identity matrix:

$$G_{11}(\omega) = (\hbar\omega\hat{I} - \hat{H})^{-1}_{11}. \tag{E.84}$$

G_{11} may thus be computed with the help of cofactor expansions. We denote $\hat{H}_N$ the Hamiltonian of a tight-binding chain with finite length N, and $\tilde{H}_N = \hbar\omega\hat{I}_N - \hat{H}_N$, so that the local Green's function at the finite chain's topmost atom is $\tilde{G}_{11}^N = (\tilde{H}_N^{-1})_{11}$. In matrix form,

$$\tilde{H}_N = \begin{pmatrix} \hbar\omega & -\gamma_2 & 0 & \ddots & \ddots \\ -\gamma_2 & \hbar\omega & -\gamma_2 & 0 & \ddots \\ 0 & -\gamma_2 & \hbar\omega & -\gamma_2 & \ddots \\ \ddots & 0 & -\gamma_2 & \hbar\omega & \ddots \\ \ddots & \ddots & \ddots & \ddots & \ddots \end{pmatrix}. \tag{E.85}$$

Using the cofactor expansion formula for the matrix inverse, we obtain

$$G_{11}^N(\omega) = \frac{\det \tilde{H}_{N-1}}{\det \tilde{H}_N}. \tag{E.86}$$

We then expand the determinant of $\tilde{H}_N$ along the first row:

$$\det \tilde{H}_N = \hbar\omega \det \tilde{H}_{N-1} + \gamma_2 \det M_{N-1}, \tag{E.87}$$

with

$$M_{N-1} = \begin{pmatrix} -\gamma_2 & -\gamma_2 & 0 & \ddots & \ddots \\ 0 & \hbar\omega & -\gamma_2 & 0 & \ddots \\ 0 & -\gamma_2 & \hbar\omega & -\gamma_2 & \ddots \\ \ddots & 0 & -\gamma_2 & \hbar\omega & \ddots \\ \ddots & \ddots & \ddots & \ddots & \ddots \end{pmatrix}. \tag{E.88}$$

Then, expanding the determinant of M_{N-1} along the first column, we find $\det M_{N-1} = -\gamma_2 \det \tilde{H}_{N-2}$. Replacing into eq. (E.86), we obtain

$$G_{11}^N(\omega) = \frac{\det \tilde{H}_{N-1}}{\hbar\omega \det \tilde{H}_{N-1} - \gamma_2^2 \det \tilde{H}_{N-2}} \tag{E.89}$$

$$= \frac{1}{\hbar\omega - \gamma_2^2 G_{11}^{N-1}(\omega)}. \tag{E.90}$$

Taking the limit $N \to \infty$, this yields a self-consistent equation for G_{11}, which is solved by

$$G_{11}(\omega) = \frac{1}{2\gamma_2^2}\left(\omega - \sqrt{\omega^2 - 4\gamma_2^2}\right). \tag{E.91}$$

Here we chose the $-$ sign in the solution of the second order equation so that G_{11} has a negative imaginary part as required by causality.

E.3.2.2 Local density response

We may now compute the non-interacting local density response function at the topmost atom, defined as

$$\chi_1(\omega) = \int_{-\infty}^{+\infty} \mathrm{d}(t-t') e^{i\omega t}\left[-\frac{i}{\hbar}\theta(t-t')\langle[n_1(t), n_1(t')]\rangle_0\right], \tag{E.92}$$

with $n_1 \equiv c_1^\dagger c_1$. For that, we require the spectral function

$$A_1(\omega) = -2\,\mathrm{Im}\,G_{11}(\omega) = \frac{2}{\gamma_2}\sqrt{1-\left(\frac{\omega}{2\gamma_2}\right)^2}\,\theta(2\gamma_2 - |\omega|). \tag{E.93}$$

Then, density response function is obtained as [242]

$$\chi_1(\omega) = \frac{1}{2\pi^2}\int_{-\infty}^{+\infty} \mathrm{d}E\mathrm{d}E'\,\frac{n_F(E') - n_F(E)}{E' - E + \hbar\omega + i\delta} A_1(E)A_1(E'). \tag{E.94}$$

Using eq. (E.93),

$$\chi_1(\omega) = \frac{2}{\gamma\pi^2}\int_{-1}^{+1} \mathrm{d}E\mathrm{d}E'\,\frac{n_F(E') - n_F(E)}{E' - E + \hbar\omega/(2\gamma_2) + i\delta}\sqrt{(1-E^2)(1-E'^2)} \equiv \frac{2}{\gamma\pi^2}\tilde{\chi}_1\left(\frac{\omega}{2\gamma_2}\right). \tag{E.95}$$

The function $\tilde{\chi}_1(x)$ is evaluated numerically, assuming one electron per atom so that the Fermi level is at 0. In order to facilitate subsequent computations, we introduce an analytical representation for $\mathrm{Im}\,\tilde{\chi}_1(x)$ at $T = 300$ K and $x > 0$:

$$\mathrm{Im}\,\tilde{\chi}_1(x) = -0.38 \times x(2-x)\theta(2-x). \tag{E.96}$$

We then determine the corresponding real part through the Kramers-Krönig relation (see eq. (E.54)):

$$\mathrm{Re}\,\tilde{\chi}_1(x) = 0.38 \times \frac{2}{\pi}\left(2x\,\mathrm{Arctanh}\left[\tilde{f}_1(x/2)\right] - 2 + \frac{1}{2}x^2\log\left|\frac{4-x^2}{x^2}\right|\right), \tag{E.97}$$

with $\tilde{f}_1(x) = x\theta(1-x) + (1/x)\theta(x-1)$. The numerical result for $\chi_1(\omega)$ is plotted alongside the analytical representation in figure E.4a.

E.3.2.3 Graphite surface response

We now use our results for a single atomic chain to obtain an expression for the surface response function of graphite, within our independent chain model. For not too small

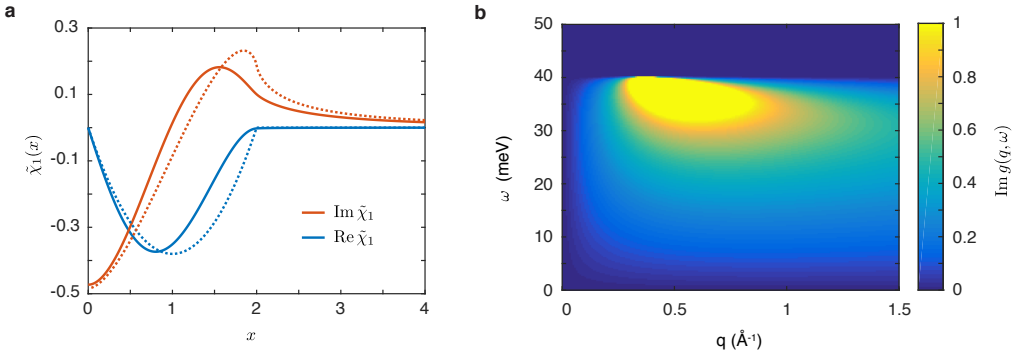

Figure E.4

Independent chain model for the graphite surface response. **a.** Normalised local density response function as defined in eq. (E.95). Full lines are obtained by numerical integration, and the dashed lines correspond to the analytical representation in eqs. (E.96) and (E.97). **b.** Graphite surface response function as obtained in the independent chain model (eq. (E.101)). We set $n_s = 2.3 \times 10^{12}$ cm^{-2} (free carrier density in graphite at 300 K).

wavevectors ($q \gtrsim 1/(2c) = 0.14$ Å^{-1}), we may consider that the external field acts only on the first graphene layer. Then, the non-interacting density response function reads

$$\chi^0(\mathbf{r}, t, \mathbf{r}', t') = \sum_{i,j \in B} |\varphi(\mathbf{r} - \mathbf{r}_i)|^2 |\varphi(\mathbf{r}' - \mathbf{r}_j)|^2 \left[-\frac{i}{\hbar} \theta(t - t') \langle [n_i(t), n_j(t')] \rangle_0 \right]. \tag{E.98}$$

But since the 1D chains below atoms i and j are assumed to be decoupled (there is no electron tunnelling between them), $[n_i(t), n_j(t')] = \delta_{ij}[n_i(t), n_i(t')]$. Hence,

$$\chi^0(\mathbf{r}, t, \mathbf{r}', t') = \sum_{i \in B} |\varphi(\mathbf{r} - \mathbf{r}_i)|^2 |\varphi(\mathbf{r}' - \mathbf{r}_i)|^2 \chi_1(\omega). \tag{E.99}$$

Carrying out Fourier transforms as in section E.3.1, we obtain the Fourier components

$$\chi^0_{\mathbf{G}\mathbf{G}'}(\mathbf{q}, z, z', \omega) = \frac{\mathcal{A}_{\mathrm{BZ}}}{(2\pi)^2} \chi_1(\omega) \xi(\mathbf{q} + \mathbf{G}, z) \xi(\mathbf{q} + \mathbf{G}', z')^*. \tag{E.100}$$

The factor $\mathcal{A}_{\mathrm{BZ}}/(2\pi)^2$ represents the electron density n_s in the first graphene layer, which is one electron per unit cell in our computation so far. However, we do not expect that all the π electrons of the B sublattice contribute to the low energy excitations we are describing, but rather only the free (electron and hole) charge carriers. Hence, from now on, we treat n_s as a parameter of our model, which represents the charge carrier density that contributes to the low energy interlayer excitations.

Since we are making the approximation that the external field affects only atoms in the first graphene layer, we need only consider Coulomb interactions between atoms in that first layer. At wavevectors q that are small enough to set $e^{qz} \approx 1$ for z on the scale of a p_z orbital, the interacting surface response function satisfies the same Dyson equation (E.81) as for graphene. We then obtain

$$g(q, \omega) = \frac{n_s v_q |\xi(q)|^2 \chi_1(\omega)}{n_s v_q |\xi(q)|^2 \chi_1(\omega) - 1}, \tag{E.101}$$

with $v_q = e^2/(2\epsilon_0 q)$. This is equivalent to eq. (5.27) (where we have set $\chi_a(q,\omega) \equiv |\xi(q)|^2\chi_1(\omega)$), which was used to obtain figure 5.8. We plot in figure E.4b the imaginary of the surface response function in eq. (E.101) as a function of q and ω. We find that it accounts for a continuum of low energy excitations (below 40 meV), whose intensity decays slowly with increasing momentum, reproducing qualitatively the features observed in graphite electron energy loss spectroscopy [178,179]. We note, however, that our model is bound to be incorrect at small values of q. Because of the 2D nature of our computation for the surface response function, its imaginary part decays to 0 at small q, while it would be expected to have a finite limit in a 3D setting. We therefore underestimate the friction coefficient by resorting to a 2D approximation, though we do not expect the underestimation to be significant, as the friction is most sensitive to the surface response function at large values of q.

E.3.3 Electron self-energy in the presence of water

E.3.3.1 General derivation

Our main result for the quantum friction coefficient (eq. (E.45)) completely takes into account Coulomb interactions at the RPA level. Beyond RPA, self-energy corrections due to the presence of water have to be taken into account in the electron Green's functions. Diagramatically, the electron Green's function is renormalised according to

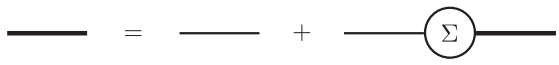

(E.102)

We will consider a single diagram for the self-energy Σ:

(E.103)

with the thick dashed line representing the full water propagator, defined by

(E.104)

In order to give explicit expressions for these diagrams, we rewrite the water-electron interaction Hamiltonian (E.1) in the basis of eigenstates $|\mathbf{k},\nu\rangle$ of the electronic system, where $\mathbf{k}$ is a two-dimensional wavevector. Considering wavevectors $\mathbf{q}$ that are small compared to the size of the surface Brillouin zone, we find

$$H_{\text{int}} = \int \frac{\mathrm{d}\mathbf{q}}{(2\pi)^2}\frac{e^2}{2\epsilon_0 q} n_s(q,t) \sum_{\mathbf{k},\nu,\nu'} \langle \mathbf{k}+\mathbf{q},\nu|e^{i\mathbf{q}\boldsymbol{\rho}}e^{qz}|\mathbf{k},\nu'\rangle c^\dagger_{\mathbf{k}+\mathbf{q},\nu}(t)c_{\mathbf{k},\nu'}(t), \tag{E.105}$$

with

$$n_s(q) = \int \mathrm{d}\boldsymbol{\rho}\int_0^{+\infty} \mathrm{d}z\, e^{-i\mathbf{q}\boldsymbol{\rho}}e^{-qz} n_w(\boldsymbol{\rho},z,t), \tag{E.106}$$

and $\sum_{\mathbf{k}} \equiv (1/\mathcal{A}_{\text{SBZ}})\int_{\text{SBZ}}\mathrm{d}\mathbf{k}$, SBZ standing for surface Brillouin zone. We note that the sum over spin degrees of freedom is implied, and the relevant factor of 2 will be added when needed. We will consider the self-energy correction at equilibrium, hence we may

interpret the diagrammatic equations (E.102) – (E.104) in the Matsubara formalism [267]. The bare Matsubara Green's function in the band ν is defined as

$$\mathcal{G}^0_\nu(\mathbf{k}, ik_n) = -\int_0^\beta \mathrm{d}\tau e^{ik_n\tau}\langle \mathbb{T} c^\dagger_{\mathbf{k},\nu}(\tau) c_{\mathbf{k},\nu}(0)\rangle = \frac{1}{ik_n - E_\nu(\mathbf{k})}, \tag{E.107}$$

with $k_n = (2n+1)\pi k_\mathrm{B}T$ the fermionic Matsubara frequencies, and τ the imaginary time that runs between 0 and $\beta = 1/k_\mathrm{B}T$. Then, the Dyson equation (E.102) reduces to

$$\mathcal{G}_\nu(\mathbf{k}, ik_n) = \frac{1}{\dfrac{1}{\mathcal{G}^0_\nu(\mathbf{k}, ik_n)} - \Sigma_\nu(\mathbf{k}, ik_n)}. \tag{E.108}$$

The self-energy in the band ν reads

$$\Sigma_\nu(\mathbf{k}, ik_n) = \frac{e^2}{2\epsilon_0\beta}\int \frac{\mathrm{d}\mathbf{q}}{(2\pi)^2}\frac{1}{q}\sum_{\nu'} |\langle \mathbf{k}+\mathbf{q}, \nu | e^{i\mathbf{q}\boldsymbol{\rho}} e^{qz} | \mathbf{k}, \nu'\rangle|^2 \sum_m g_w(q, i\omega_m)\mathcal{G}^0_{\nu'}(\mathbf{k}+\mathbf{q}, ik_n + i\omega_m), \tag{E.109}$$

where $\omega_m = 2m\pi k_\mathrm{B}T$ are the bosonic Matsubara frequencies. This expression for the self-energy involves directly the water surface response function. Indeed, the bare surface response function in Matsubara representation is

$$g^0_w(q, i\omega_m) = \int_0^\beta \mathrm{d}\tau e^{i\omega_m\tau}\langle \mathbb{T} n_s(\mathbf{q}, \tau) n_s(-\mathbf{q}, 0)\rangle. \tag{E.110}$$

The full surface response function is obtained according to the Dyson equation (E.104):

$$g_w(q, i\omega_m) = \frac{g^0_w(q, i\omega_m)}{1 - g^0_w(q, i\omega_m) g_e(q, i\omega_m)}. \tag{E.111}$$

The sum over Matsubara frequencies may be carried out once the Lehmann representation is used for the water surface response function:

$$g_w(q, i\omega_m) = -\int_{-\infty}^{+\infty} \frac{\mathrm{d}\omega}{\pi}\frac{\mathrm{Im}\, g_w(q, \omega)}{i\omega_m - \omega}. \tag{E.112}$$

Upon using the definition (E.107), we are left with a standard Matsubara sum [267]:

$$-\frac{1}{\beta}\sum_m \frac{1}{i\omega_m - \omega}\frac{1}{ik_n + i\omega_m - E_{\nu'}(\mathbf{k}+\mathbf{q})} = \frac{n_\mathrm{B}(\omega) + n_\mathrm{F}(E_{\nu'}(\mathbf{k}+\mathbf{q}))}{ik_n + \omega - E_{\nu'}(\mathbf{k}+\mathbf{q})}. \tag{E.113}$$

Finally, we obtain for the self-energy

$$\begin{aligned}\Sigma_\nu(\mathbf{k}, ik_n) = \frac{e^2}{2\epsilon_0}\int \frac{\mathrm{d}\mathbf{q}}{(2\pi)^2}\frac{1}{q}\sum_{\nu'} |\langle \mathbf{k}+\mathbf{q}, \nu | e^{i\mathbf{q}\boldsymbol{\rho}} e^{qz} | \mathbf{k}, \nu'\rangle|^2 \ldots \\ \ldots \int_{-\infty}^{+\infty} \frac{\mathrm{d}\omega}{\pi}\mathrm{Im}\, g_w(q, \omega)\frac{n_\mathrm{B}(\omega) + n_\mathrm{F}(E_{\nu'}(\mathbf{k}+\mathbf{q}))}{ik_n + \omega - E_{\nu'}(\mathbf{k}+\mathbf{q})}.\end{aligned} \tag{E.114}$$

The retarded self-energy is obtained by analytical continuation $ik_n \mapsto E + i\delta$. Then, using the identity $\mathrm{Im}[1/(E - \omega + i\delta)] = -\pi\delta(E - \omega)$, we obtain for the imaginary part of the self-energy

$$\begin{aligned}\mathrm{Im}\,\Sigma_\nu(\mathbf{k}, E) = \frac{-e^2}{2\epsilon_0}\int \frac{\mathrm{d}\mathbf{q}}{(2\pi)^2}\frac{1}{q}\sum_{\nu'} |\langle \mathbf{k}+\mathbf{q}, \nu | e^{i\mathbf{q}\boldsymbol{\rho}} e^{qz} | \mathbf{k}, \nu'\rangle|^2 \ldots \\ \ldots \mathrm{Im}[\, g_w(q, E_{\nu'}(\mathbf{k}+\mathbf{q}) - E)] \cdot [n_\mathrm{B}(E_{\nu'}(\mathbf{k}+\mathbf{q}) - E) + n_\mathrm{F}(E_{\nu'}(\mathbf{k}+\mathbf{q}))].\end{aligned} \tag{E.115}$$

E.3.3.2 Graphene

We numerically evaluate (at $T = 300$ K) the self-energy in eq. (E.115) in the case where the electronic system is a single graphene sheet, treated in the Dirac cone approximation for its bare band structure. We give the label $\nu = \pm 1$ to the two π bands. Then, the band energies are $E_\nu(k) = \mathrm{sign}(\nu) v_F k$, and the matrix elements reduce to [176]:

$$|\langle \mathbf{k}+\mathbf{q}, \nu | e^{i\mathbf{q}\boldsymbol{\rho}} e^{qz} | \mathbf{k}, \nu' \rangle|^2 = \frac{1}{2}\left(1 + \nu\nu' \frac{k + q\cos\theta}{\|\mathbf{k}+\mathbf{q}\|}\right), \tag{E.116}$$

where θ is the angle between $\mathbf{k}$ and $\mathbf{q}$. Note that eq. (E.115) is then multiplied by 2 to account for the valley degeneracy. We further take into account the renormalisation of the water surface response function according to eq. (E.112). The water Debye peak at $\omega_\mathrm{D} = 1.5$ meV is sensitive only to the static response function of graphene $g_e(q, 0)$. For undoped graphene, it is essentially independent of q: $g_e(q, 0) = 0.78$ according to our computation in section E.3.1. We determine the real part of the self-energy through a Kramers-Krönig relation:

$$\mathrm{Re}\,\Sigma_\nu(k, E) = \mathrm{Re}\,\Sigma_\nu(k, E) - \mathrm{Re}\,\Sigma_\nu(k, 0) = \frac{1}{\pi}\int_{-\infty}^{+\infty} \mathrm{d}E'\, \frac{E\,\mathrm{Im}\,\Sigma_\nu(k, E')}{E'(E' - E)}. \tag{E.117}$$

Then, the renormalised electron Green's function is determined according to eq. (E.108):

$$G_\nu(k, \omega) = \frac{1}{\omega - E_\nu(\mathbf{k}) - \Sigma_\nu(k, \omega)}. \tag{E.118}$$

The renormalised spectral density, $A(k, \omega) = -2\sum_\nu \mathrm{Im}G_\nu(k, \omega)$, is plotted as a function of energy and momentum in figure 5.7.

E.3.4 Multiwall nanotubes

For the radius-dependence of the average interlayer spacing in multiwall carbon nanotubes, we rely on the transmission electron microscopy data of ref. [186]. For tube radii between 7.5 nm and 50 nm, we used a linear approximation to the data:

$$d(R) = 3.35 + 0.002 \times (R\,(\mathrm{nm}) - 50) \quad (\text{Å}). \tag{E.119}$$

In figure 5.8, the curve labeled "Decoupling + gap" is obtained by considering a scaling $n_s(R) = (1 - p(R)) n_s^0 e^{-E_\mathrm{g}(R)/k_\mathrm{B}T}$.

Appendix F

Simulation methods

Contents

F.1 Brownian dynamics simulations of ionic Coulomb blockade

F.1.1 Numerical details

Our 1D brownian dynamics simulations are carried out using the LAMMPS software [268]. The simulation system consists of N_+ positive ions and N_- negative ions, in a one-dimensional box of length L with periodic boundary conditions. An immobile point charge Q is placed at $x = L/2$ to model the surface charge. We typically use $N_- = 100$, $N_+ = 100+n$ with $0 \leq n \leq 3$, and $L = 12.5$ μm, unless stated otherwise. We only simulate the motion of ions (the solvent is implicit), and the ion positions at timestep $i+1$ are determined from the positions at timestep i by solving a Euler-discretised overdamped Langevin equation:

$$x_{i+1} = x_i - \Delta t \frac{eD}{k_B T} \partial_x \Phi|_{x=x_i} + \eta_i \sqrt{2D\Delta t}, \tag{F.1}$$

where Φ is the electrostatic potential and η_i a gaussian random variable of 0 mean and unit variance. We use a timestep $\Delta t = 5$ ps, diffusion coefficient $D = 10^{-9}$ m$^2 \cdot$ s^{-1} and temperature $T = 298$ K. The potential Φ acting on the ion i takes into account the interaction with the ions $j \neq i$ with the pairwise potential $V(x) = \frac{\xi}{x_T} e^{-|x|/\xi}$, the interaction with the surface charge Q with the same pairwise potential, and the contribution $-Ex$ from the applied electric field E. Unless stated otherwise, we used the

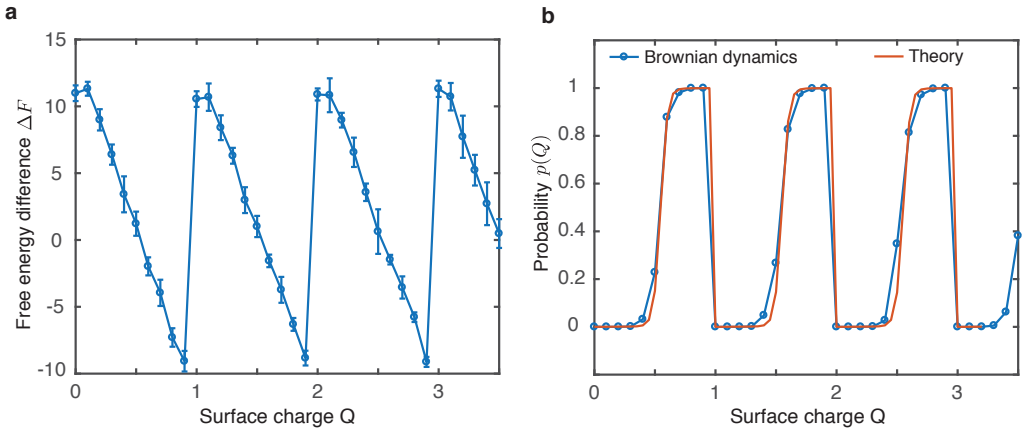

Figure F.1

a. Free energy difference $\Delta F = F(\lfloor Q \rfloor + 1) - F(\lfloor Q \rfloor)$, as a function of surface charge Q, as obtained from the brownian dynamics simulations by the thermodynamic integration method. **b.** Probability $p(Q)$ of the channel containing $N_+ = N_- + \lfloor Q \rfloor + 1$ positive ions as a function of Q, as obtained from the simulation results for ΔF (using eq. (F.3)), and from the Coulomb gas theory.

values $x_T = 0.9$ Å and $\xi = 3.5$ nm, which physically correspond to divalent ions confined in a channel of diameter 1 nm. With these values of the parameters, the ion density we imposed in the channel (200 ions per 12.5 μm) corresponds to a salt concentration $c = 0.44$ M in the reservoirs, as determined from eq. (C.33). In each simulation run, we measured the neutralising charge $N(Q)$ as the average number of positive ions in the interval $[L/2 - 1.25\text{ nm}, L/2 + 1.25\text{ nm}]$, and the positive and negative ion currents:

$$I_\pm = \left\langle \frac{\pm e}{L} \sum_{\pm \text{ ions}} \frac{x_{i+1} - x_i}{\Delta t} \right\rangle_{\text{dynamics}} \tag{F.2}$$

The ions were initially randomly distributed in the simulation box. The simulations lasted for 5×10^8 timesteps, with the first 10^7 timesteps left for equilibration. Error bars represent the standard deviation of the sampled observable, corrected by its correlation time.

F.1.2 Grand canonical averaging

Our simulations aim to account for a channel connecting two reservoirs, therefore the number of ions in the system should be able to fluctuate, the chemical potential μ of the reservoirs being fixed. At equilibrium, we can account for these fluctuations by carrying out simulations at a fixed number of ions (N_+, N_-) and then averaging the observables obtained for different (N_+, N_-) with the grand canonical probabilities of having (N_+, N_-) ions in the channel. We assume that we may extend this approach out of equilibrium and carry out the same type of averaging for the observables $N(Q)$ and $I_\pm$ even when the system is driven by an electric field.

We must now determine how many different values of (N_+, N_-) should be taken into account. In the absence of surface charge, the system tries to maintain electroneutrality, $N_+ = N_-$. Departing from electroneutrality by a unit charge has an energy cost which is approximately the dielectric self-energy of the unit charge: $E_s = \xi/(2x_T) = 19.6\ k_BT$ with our simulation settings (see section 1.6). Thus, the probability of observing a non-neutral state is negligible and the only allowed fluctuations are those that keep the system neutral, that is fluctuations in the number of ion pairs. In the CB regime, the ion pairs behave essentially as ideal gas particles, thus the fluctuations in their number become gaussian in the thermodynamic limit, with variance $\Delta N^2 \sim N$. Hence, when there is no surface charge, the grand canonical averaging takes care of itself thanks to the equivalence of ensembles, and we may carry out simulations with a fixed number $N = 100$ of ion pairs. At $N = 100$ we are not well into the thermodynamic limit, but we do not expect small fluctuations in the number of ion pairs to significantly affect the observables of interest.

Now in the presence of a surface charge Q, the system tries to get as close to electroneutrality as possible, meaning that $N_+ = N_- + \lfloor Q \rfloor$ or $N_+ = N_- + \lfloor Q \rfloor + 1$. If Q is close to a half-integer, these two values of N_+ may have very similar probabilities, while other values of N_+ are essentially forbidden, since breaking the quasi-electroneutrality has an energy cost which is again at least $E_s = 19.6\ k_BT$. This means that the fluctuations in N_+ and N_- are not gaussian, whatever the system size, so that there is no equivalence of ensembles in the thermodynamic limit. One should therefore carry out separate simulations for the two allowed values of N_+.

Let us denote $p(Q)$ the probability of the channel containing $N_+ = N_- + \lfloor Q \rfloor + 1$ positive ions, as in section C.2.3. It is given by

$$p(Q) = \frac{e^{-F(\lfloor Q \rfloor + 1)}}{e^{-F(\lfloor Q \rfloor + 1)} + e^{-F(\lfloor Q \rfloor)}} \equiv \frac{1}{1 + e^{\Delta F(Q)}}, \tag{F.3}$$

where $F(q)$ is a shorthand for $F(N_- + q, N_-)$, the free energy at fixed particle numbers $(N_- + q, N_-)$. We determined the free energy difference ΔF from brownian dynamics simulations by a thermodynamic integration method [269]. Consider a system containing N_+ positive ions, N_- negative ions and an extra particle of charge λe. Let $F(\lambda)$ be the free energy of such a system. The derivative of the free energy with respect to λ can be computed as

$$\frac{\partial F(\lambda)}{\partial \lambda} = \frac{\int \mathrm{d}\{x_i\} (\partial E(\{x_i\}, \lambda)/\partial \lambda) e^{-E(\{x_i\}, \lambda)}}{\int \mathrm{d}\{x_i\} e^{-E(\{x_i\}, \lambda)}} = \left\langle \frac{\partial E(\{x_i\}, \lambda)}{\partial \lambda} \right\rangle_\lambda, \tag{F.4}$$

where $\langle \cdot \rangle_\lambda$ denotes averaging over the dynamics with a given value of λ. The energy $E(\{x_i\}, \lambda)$ can be decomposed as

$$E(\{x_i\}, \lambda) = E(\{x_i\}, 0) + \lambda \cdot [E(\{x_i\}, 1) - E(\{x_i\}, 0)]. \tag{F.5}$$

Here we did not take into account the dielectric self-energy of the extra particle, which is proportional to λ^2, but it can be added *a posteriori* in the free energy difference. Precisely, $\Delta F = E_s + F(\lambda = 1) - F(\lambda = 0)$, hence

$$\Delta F = E_s + \int_0^1 \mathrm{d}\lambda \frac{\partial F(\lambda)}{\partial \lambda} = E_s + \int_0^1 \mathrm{d}\lambda \left\langle E(\{x_i\}, 1) - E(\{x_i\}, 0) \right\rangle_\lambda \tag{F.6}$$

This expression suggests a numerical scheme for computing ΔF. Simulations are carried out at a range of values of λ between 0 and 1. For each simulation one computes

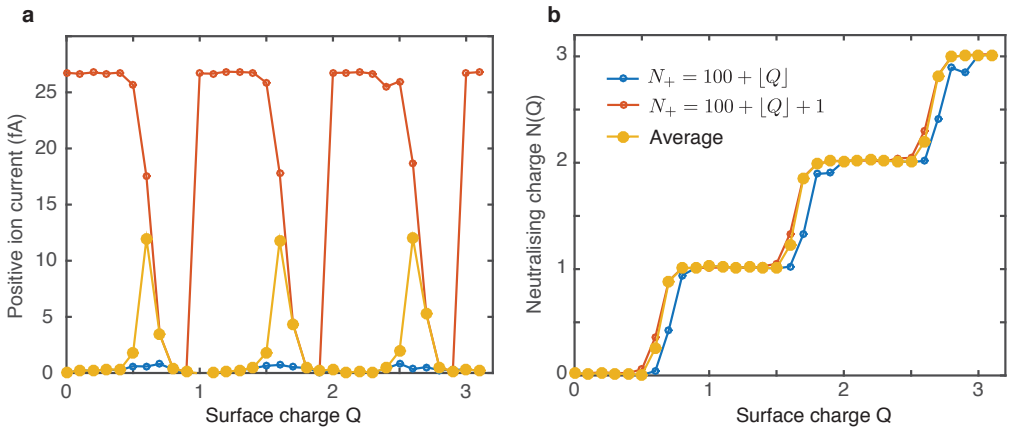

Figure F.2

a. Positive ion current as a function of surface charge, as obtained from brownian dynamics simulations, for each of the two allowed values of N_+, and the resulting grand-canonical average. **b.** Neutralising charge $N(Q)$ as a function of surface charge, as obtained from brownian dynamics simulations, for each of the two allowed values of N_+, and the resulting grand-canonical average.

the average of the quantity $E(\{x_i\}, 1) - E(\{x_i\}, 0)$. Concretely, this means that every few timesteps, we set λ to 1, compute the energy, then set λ to 0, compute the energy, take the difference between the two, then return λ to its original value and continue the dynamics. We then numerically compute the integral in eq. (F.6) to obtain ΔF. We implemented this numerical scheme for a range of values of Q. For each value of Q we sampled 20 values of λ, and each 5×10^8-timestep-long simulation was repeated 5 times, since the exploration of the configuration space is slower in the absence of driving by an electric field.

Figure F.1 shows the results we obtained for ΔF as a function of Q, and the resulting probability $p(Q)$, with parameters $x_T = 0.9$ Å, $\xi = 3.5$ nm, and $L = 1.25$ μm (a line density of 80 ions/μm). The simulation results for $p(Q)$ can be compared with the Coulomb gas theory. In the CB regime, any unpaired positive ions are most likely to be closely bound to the surface charge, hence it does not matter whether to consider the number of positive ions in the whole system or in the vicinity of the surface charge. Thus, $p(Q) = N(Q) - \lfloor Q \rfloor$, with $N(Q)$ given for example by eq. (C.35). Panel b shows that this analytical result is in excellent agreement with simulations. Thus, to carry out the grand canonical averaging in non-equilibrium simulations, we used the $p(Q)$ given by the Coulomb gas theory.

In order to give an idea of the effect of grand-canonical averaging, figure F.2 shows the neutralising charge $N(Q)$ and the positive ion current I^+ obtained with each of the two allowed values of N_+, and the resulting average.

F.1.3 Ion pump

We carried out a proof-of-concept simulation of a device that functions as an ion pump. The device consists of a nanochannel connected to not one, but several gating electrodes,

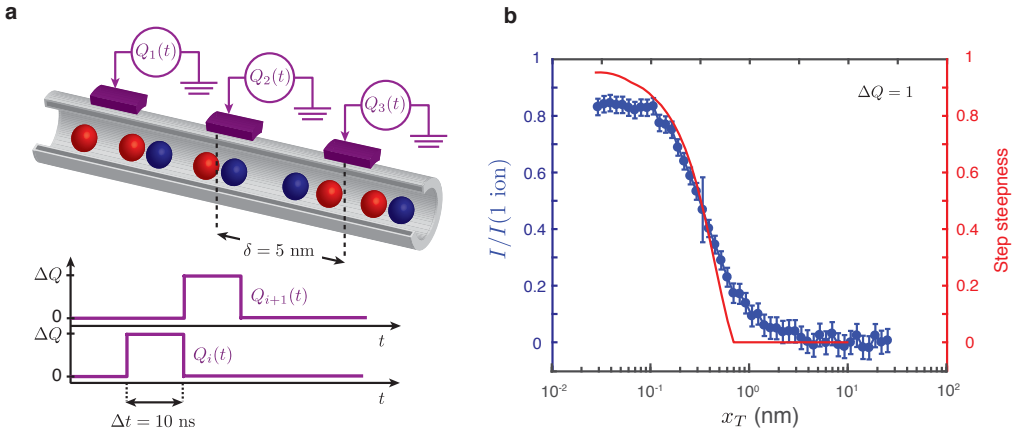

Figure F.3

a. Schematic of the ion pump and time dependence of the variable surface charges $Q_i(t)$. **b.** Positive ion current in the ion pump (blue circles), at fixed pumping amplitude $\Delta Q = 1$, as a function the thermal length x_T. The pumping current drops down to 0 for large values of x_T (weak interactions), and correlates well with the CB step steepness obtained from the Coulomb gas theory (red line).

which may induce time dependent surface charges on the channel walls. Its operating principle is shown in figure 3.6, and recalled in figure F.3. The variable charges are placed every 5 nm along the channel. At a given point in time, all the charges are set to 0, except one which takes the value $-\Delta Q$. Every 10 ns, the charge $-\Delta Q$ is moved to the next site, 5 nm further along the channel. We used a channel of length $L = 625$ nm with periodic boundary conditions. Intuitively, this displacement of a negative surface charge should result in the dragging of a positive ion along the channel. In figure 3.6, we show the ionic current normalised by $I(1\text{ ion})$, the current that would result from the perfect pumping of a single ion, that is an ion moving at a velocity of 5 nm per 10 ns. It appears that the interactions need to be strong enough (that is x_T low enough) for the pumping current to be close to the theoretical maximum. We carried out further simulations at fixed amplitude $\Delta Q = 1$, and a range of values of x_T, whose results are shown in figureF.3b. We observe that the pumping current drops down to 0 at large values of x_T, and this decrease correlates well with step steepness obtained from the Coulomb gas theory at a given value of x_T. This highlights that the operation of the ion pump relies on the system being in the CB regime.

For the simulation in figure F.3b, with pumping amplitude $\Delta Q = 1$, we used a fixed number of particles: $N_- = 100$ and $N_+ = 101$. For the simulation in figure 3.6b, with $x_T = 0.1$ nm, we used the same type of grand-canonical averaging as described in section F.1.2. With $x_T = 2$ nm, setting either $N_+ = N_- + \lfloor Q \rfloor$ or $N_+ = N_- + \lfloor Q \rfloor + 1$ does not alter the result.

F.2 Molecular simulations of two-dimensional electrolytes

F.2.1 Methods – Molecular dynamics

We use both all-atom molecular dynamics simulations (where water molecules and graphene are simulated explicitly) and brownian dynamics simulations (where water molecules and graphene are treated implicitly as continuous media). Both are carried out using the LAMMPS software [268].

All-atom simulations consist in two graphene sheets separated by a single or a few layers of water, with periodic boundary conditions. This forms a slit of dimensions $L \times w \times h$, with typical values being $L = w = 20\,\text{nm}$. Channels of three different heights are tested: $h = 0.7$, 1 or 1.4 nm, corresponding to one, two and three water layers between the graphene sheets, respectively. The number N_w of water molecules is approximately 4500 for each water layer. This value was obtained from previous studies [270]. The number N of ions of each sign is varied between $N = 10$ and $N = 500$. Simulations involve various binary salts, such as sodium chloride (NaCl), calcium chloride ($CaCl_2$) and calcium sulfate ($CaSO_4$). Generic salts of formula X_pY_n of various valence and stoechiometries were also considered. All initial configurations were obtained using the Packmol software [271].

Water molecules are described using either the TIP4P model or the SPC/E model, and maintained rigid with the SHAKE algorithm [272]. Lennard-Jones (LJ) parameters of all considered species are summarized in Table F.1, with cross-parameters determined with the Lorentz-Berthelot mixing rules [273]. Interactions are computed using a spherical 1 nm cut-off for LJ potentials, and long-range Coulomb interactions are treated with the particle-particle particle-mesh (PPPM) method and a slab correction to deal with the non-periodicity in the z direction [274]. Finally, the integration time step is 1 fs and temperature is fixed to 298 K using the Nosé–Hoover thermostat [275] with a time constant of 0.1 ps. Simulations last $1.5 \cdot 10^7$ time steps, corresponding to approximately 15 ns of physical time.

In brownian dynamics simulations, systems consist in N positive and N negative ions, with typically $N = 4000$ in a two-dimensional box of dimensions $L \times w$ and periodic boundary conditions, with $L = 2\,\mu\text{m}$. The width w of the simulation box was fixed depending on the desired electrolyte concentration, with typical values ranging from $w = 0.2\,\mu\text{m}$ to $w = 200\,\mu\text{m}$. The solvent as well as graphene walls are treated implicitly, and the ion positions at timestep $n+1$ are determined from the positions at time step n by solving a Euler-discretised overdamped Langevin equation:

$$\mathbf{r}_{n+1} = \mathbf{r}_n - \Delta t \frac{eD}{k_B T} \boldsymbol{\nabla} \Phi + \boldsymbol{\eta}_n \sqrt{2D\Delta t}, \tag{F.7}$$

where $\mathbf{r}_n$ is the position of a given ion at time step n, Φ is the electrostatic potential felt by the ion and $\boldsymbol{\eta}_n$ is a Gaussian random variable of zero mean and unit variance. We use the value $D = 10^{-9}\,\text{m}^2\,\text{s}^{-1}$ for the diffusion coefficient of ions in water at 298 K, in line with experimental measurements of the diffusion coefficient of various ions under monolayer confinement [16].

The typical value of the time step is $\Delta t = 5\,\text{ps}$, and is lowered down to 5 fs when fast dynamics are considered. The electrostatic potential is determined by taking into account the contribution $-Ex$ from the external electric field $\mathbf{E} = E\,\hat{\mathbf{x}}$, as well as pairwise interactions. We assume that ions interact with a pairwise '$2D^+$' quasi-logarithmic

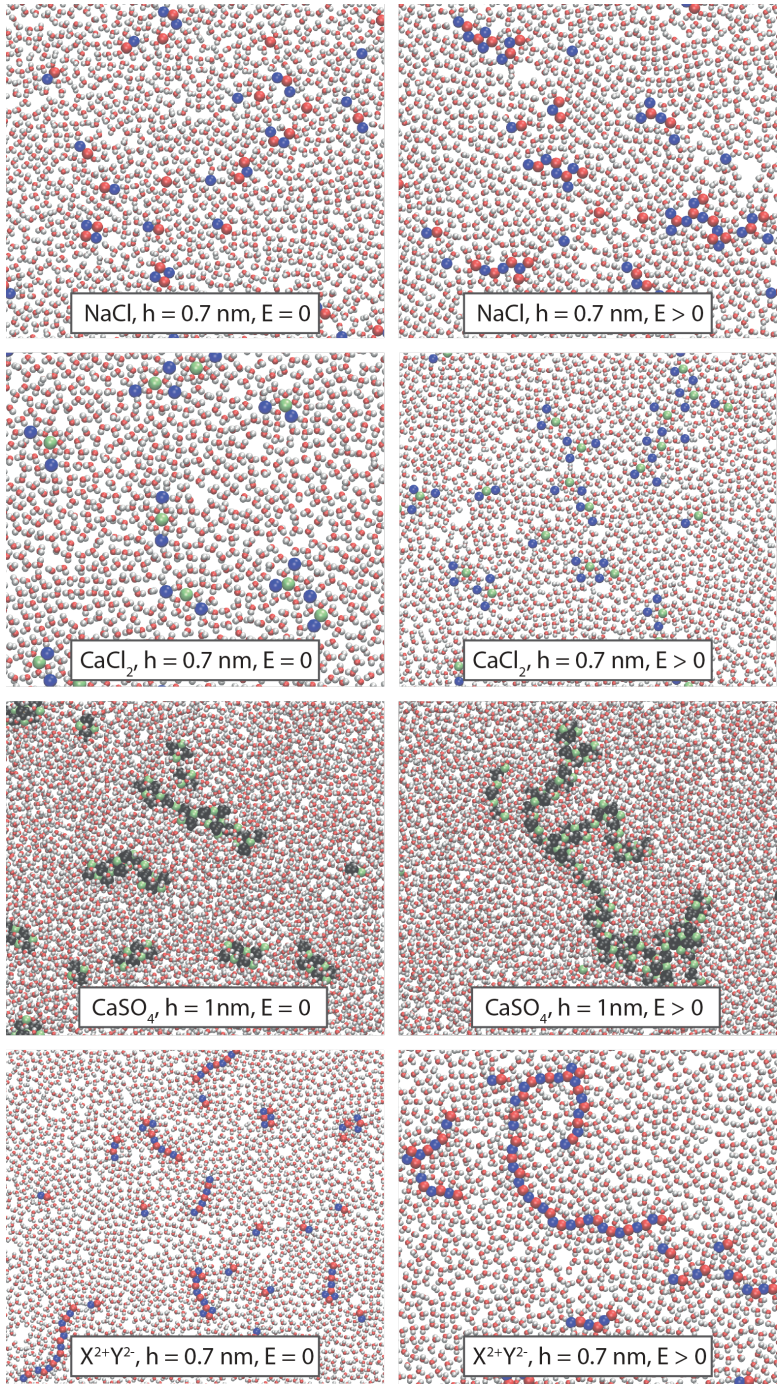

Figure F.4

MD simulation snapshots of various 2D electrolytes in and out of equilibrium. For out of equilibrium snapshots, a constant electric field E of the order of $1\,k_BT/\text{Å}$ is applied.

Atom	Charge (e)	σ (Å)	ϵ kcal/mol	Reference
O (H_2O)	-0.8476	3.165	0.155	[277]
H (H_2O)	$+0.4238$	–	–	[277]
C (graphene, SPC/E)	0	3.214	0.0566	[278]
C (graphene, TIP4P)	0	3.214	0.0566	[278]
Na^+	$+1$	2.35	0.123	[279]
Cl^-	-1	4.401	0.100	[279]
Ca^{2+}	$+2$	2.895	0.100	[280]
S (SO_4^{2-})	$+2$	3.55	0.250	[281]
O (SO_4^{2-})	-1	3.15	0.200	[281]
B (hBN)	$+0.3$	3.402	0.0951	[282]
N (hBN)	-0.3	3.490	0.0622	[282]
X^{p+}	$p = 1, 2, 3$	2.35	0.123	–
Y^{n-}	$n = 1, 2, 3$	4.401	0.100	–

Table F.1

Lennard–Jones parameters used in all-atom MD simulations.

potential given by eq. (A.30). In typical simulations, we use $T^* = 0.11$ and $\xi = 14\,\text{nm}$, which corresponds to divalent ions in a slit of height $h = 7\,\text{Å}$. Quasi-coulombic, long-range interactions are regularized using both a short- and a long-distance cut-off of 1 Å and 20 nm, respectively. Simulations last typically $2 \cdot 10^8$ time steps, corresponding to 1 ms of physical time.

For both types of simulations, ionic current is computed by averaging the velocities of ions across the slit:

$$I = \left\langle \frac{e}{L} \sum_i Z_i q_i \frac{x_{n+1}^i - x_n^i}{\Delta t} \right\rangle_{\text{dynamics}}, \tag{F.8}$$

where $q_i = \pm 1$ is the charge of ion i, Z_i its valence and the sum is over all ions of both signs. Simulation results were visualized using VMD [276].

F.2.2 Effect of the nature of the salt

All-atom MD simulations allow us to study the system's configuration qualitatively. Figure F.4 shows simulation snapshots for all studied chemical species, both at thermal equilibrium (no external field) and out of equilibrium (in presence of an electric field $E \sim 1\,k_BT/\text{Å}$). These snapshots correspond to monolayer confinement ($h = 0.7\,\text{nm}$), except for simulations with sulphate ions, which are too big to enter these slits, and are instead studied in bilayer confinement ($h = 1\,\text{nm}$). Sodium chloride forms pairs, or very short clusters (3 to 4 ions) at thermal equilibrium, and assembles into short but tightly bound chains (typically 10 ions or less) under a non-zero electric field. Calcium sulphate mainly forms round clusters (typically 4 to 8 ions) instead of pairs at equilibrium, and very large, branched assemblies for $E \neq 0$. The same is true for a generic divalent salt X^{2+},Y^{2-}, except the clusters are linear even at equilibrium, and they almost never branch.

Calcium chloride, however, behaves slightly differently. It can form either pairs or triplets at equilibrium, or sometimes some short linear assemblies. All these structures are usually not tightly bound, as they include water molecules, solvating calcium ions in a circular arrangement. In the case of triplets, there seem to be different possible values of the dihedral angle formed by the three ions, depending on the number of water molecules surrounding the central cation, or whether that circle is complete or not. Similarly, the Bjerrum polyelectrolytes formed by these triplets have a more complex structure than simple linear chains. We expect that the thermodynamic properties of these triplets and chains to bear some signature of the molecular nature of water; however, the study of these properties is beyond the scope of this thesis.

F.3 Water surface response function from molecular dynamics

We carried out classical molecular dynamics (MD) simulations of water in contact with a hydrophobic surface in order to determine the water surface response function. As a consistency check, we also carried out bulk water simulations, from which we extracted the frequency-dependent dielectric constant.

F.3.1 Details of the simulations

All simulations were carried out using the LAMMPS software [268]. We used the SPC/E water model [283] with the SHAKE algorithm [284]. The simulations were carried out in the canonical (NVT) ensemble, with a stochastic CSVR thermostat [285] with time constant 1 ps maintaining a temperature $T = 298.15$ K. We used a timestep of 2 fs, and atomic positions were written out every 4 fs. Electrostatic interactions were calculated with a particle-mesh Ewald summation with a Coulomb cutoff of 1.4 nm.

F.3.1.1 Bulk simulation

The bulk simulation used $N = 8000$ water molecules. The volume of the simulation box was first adjusted in the NPT ensemble to yield a mass density $\rho = 0.99715\ \mathrm{g \cdot cm^{-3}}$. The resulting volume was $V = (64.145)^3\ \mathrm{Å}^3$. The simulation was then equilibrated in the NVT ensemble for 200 ps, and the subsequent 20 ns were used for analysis.

F.3.1.2 Interface simulation

The interface simulation was carried out with $N = 20200$ water molecules. The solid surface consisted of three graphene layers (with ABA stacking), with surface area $128.316 \times 123.490\ \mathrm{Å}^2$, and the simulation box height was 6.5 nm. The positions of the carbon atoms were frozen during the simulation. The direction normal to the surface was aperiodic, and spurious slab-slab interactions were removed. A reflective wall was placed close to the top edge of the box to prevent gaseous water molecules from crossing the top boundary. We used two sets of Lennard-Jones parameters for the water-carbon interaction, to which we refer to as "Werder" and "Aluru", listed in the following table.

Ref.	Name	ϵ_{CO} (kcal/mol)	σ_{CO} (Å)	ϵ_{CH} (kcal/mol)	σ_{CH} (Å)
[143]	Werder	0.0937	3.19	-	-
[169]	Aluru	0.0850	3.436	0.0383	2.69

The simulation was equilibrated in the NVT ensemble for 200 ps and the subsequent 6 ns were used for analysis.

F.3.2 Analysis of the simulations

The computation of response functions from equilibrium MD simulations is based on the fluctuation-dissipation theorem.

F.3.2.1 Bulk simulation

The simulation was split into $N_s = 20$ pieces of length $\Delta t = 1$ ns, and the results obtained from each of the pieces were averaged to obtain the final result. The accessible frequencies were thus from 1 GHz to 62.5 THz. At every sampled time t, we computed the Fourier-transformed water charge density $n_w(\mathbf{k}, t) = \sum_i Z_i e^{i\mathbf{k}\mathbf{r}_i(t)}$, with the index i running over all the charged sites of the SPC/E water molecules, and Z_i the corresponding charge. We define the dynamic charge structure factor according to

$$S(\mathbf{k}, \omega) = \frac{1}{\mathcal{V}} \int_{-\infty}^{+\infty} \mathrm{d}t \langle n_w(\mathbf{k}, t) n_w(-\mathbf{k}, 0) \rangle e^{i\omega t}, \tag{F.9}$$

where $\mathcal{V}$ is the volume of the simulation box. Then, the fluctuation-dissipation theorem yields the susceptibility $\bar{\chi}$ according to:

$$\mathrm{Im}\, \bar{\chi}(\mathbf{k}, \omega) = \frac{e^2}{2\epsilon_0 k^2} \frac{\omega}{k_\mathrm{B} T} S(\mathbf{k}, \omega). \tag{F.10}$$

The susceptibility is related to the dielectric permittivity according to $\bar{\chi}(\mathbf{k}, \omega) = 1 - 1/\epsilon(\mathbf{k}, \omega)$. We therefore require also the real part of the susceptibility, which can be determined through a Kramers-Krönig relation:

$$\mathrm{Re}\, \bar{\chi}(\mathbf{k}, \omega) = \frac{2}{\pi} \mathcal{P} \int_0^{+\infty} \mathrm{d}\omega' \frac{\omega' \mathrm{Im}\, \bar{\chi}(\mathbf{k}, \omega')}{\omega'^2 - \omega^2}, \tag{F.11}$$

where $\mathcal{P}$ indicates that the principal part of the integral is taken. In practice, the structure factor in eq. (F.9) was computed from the simulation data by making use of the Wiener-Khinchin theorem. The resulting spectra were convoluted with a gaussian filter of half-width 50 GHz. This allowed for some smoothing of the spectra, while not affecting their low-energy region, since the spectra are constant below 200 GHz. Then, spherical averaging was performed over the quantity $S(\mathbf{k}, \omega)/k^2$.

F.3.2.2 Interface simulation

The simulation was split into $N_s = 60$ pieces of length $\Delta t = 0.1$ ns, and the results obtained from each of the pieces were averaged to obtain the final result. The accessible frequencies were thus from 0.1 GHz to 62.5 THz. At every sampled time t, we computed the Fourier-Laplace transform of the water charge density $n_w^s(\mathbf{q}, t) = \sum_i Z_i e^{i\mathbf{q}\mathbf{r}_i(t)} e^{-qz_i}$, with the index i running over all the charged sites of the SPC/E water molecules, and Z_i the corresponding charge. We define the dynamic surface structure factor according to

$$S_s(\mathbf{q}, \omega) = \frac{1}{\mathcal{A}} \int_{-\infty}^{+\infty} \mathrm{d}t \langle \delta n_w^s(\mathbf{q}, t) \delta n_w^s(-\mathbf{q}, 0) \rangle e^{i\omega t}, \tag{F.12}$$

with $\mathcal{A}$ the surface area, and $\delta n_w^s = n_w^s - \langle n_w^s \rangle$. We then obtain the imaginary part of the surface response function through the fluctuation-dissipation theorem:

$$\operatorname{Im} g_w(\mathbf{q},\omega) = \frac{e^2}{4\epsilon_0 q}\frac{\omega}{k_\mathrm{B}T} S_s(\mathbf{q},\omega), \tag{F.13}$$

In practice, the structure factor in eq. (F.12) was computed from the simulation data by making use of the Wiener-Khinchin theorem. The resulting spectra were convoluted with a gaussian filter of half-width 50 GHz. Then, radial averaging was performed over the quantity $S(\mathbf{q},\omega)/q$.

The surface response function evaluated in this way depends on the choice of origin for the vertical coordinate z. By default, the origin is placed at the first graphene plane, but this introduces a spurious vacuum gap (we call its thickness d) in the computation of the surface response. In fact, the procedure described above yields $e^{-2qd} g_w(q,\omega)$ instead of $g_w(q,\omega)$. However, there is no clear way of determining d from microscopic considerations. Instead, we fixed d by enforcing the compressibility sum rule for the surface response function in the long wavelength limit. The procedure is derived in detail in section F.3.2.3. In brief, we first compute the static surface structure factor: $\bar{S}_s(q) = (1/\mathcal{A})\langle \delta n_w^s(\mathbf{q}) \delta n_w^s(-\mathbf{q})\rangle$, with the average performed over the whole length of the simulation. Then, the compressibility sum rule reads

$$\frac{e^2}{8\epsilon_0 k_\mathrm{B} T}\frac{\bar{S}_s(q)}{q} = \int_0^\infty \mathrm{d}\omega \, \frac{\operatorname{Im} g_w(q,\omega)}{\omega} = \frac{\pi}{2} g_w(q,0). \tag{F.14}$$

In the same way as the bulk structure factor has only even powers of q in its low q expansion, the surface structure factor is expanded only in odd powers of q (see Appendix). Therefore $\bar{S}_s(q)/q$ has a horizontal asymptote as $q \to 0$, while $e^{-2qd}\bar{S}_s(q)/q$ has a linear scaling. Hence, in order to cancel the gap d, we adjust the origin of the coordinate z so that $\bar{S}_s(q)/q$ has indeed a horizontal asymptote. Then, to ensure consistency, the sum rule (F.14) is enforced when fitting $\operatorname{Im} g_w(q,\omega)$.

This procedure yielded $d = 1.3$ Å with the Werder parameters and $d = 1.76$ Å with the Aluru parameters. This last value agrees well with the position of the electronic density minimum at the water-graphene interface, as determined from DFT (figure 5.1b). This is consistent with the fact that the Aluru parameters are based on DFT calculations for water on a graphene surface [169]. Therefore, our sum-rule-based approach does place the origin of the z axis where it would be expected from microscopic considerations.

F.3.2.3 Compressibility sum rule

The Kramers-Krönig relation for the surface response function is

$$\operatorname{Re} g_w(q,\omega) = \frac{1}{\pi}\mathcal{P}\int_{-\infty}^{+\infty} \mathrm{d}\omega' \frac{\operatorname{Im} g_w(q,\omega')}{\omega' - \omega}. \tag{F.15}$$

Taking $\omega = 0$, this yields

$$g_w(q,0) = \frac{2}{\pi}\int_0^{+\infty} \mathrm{d}\omega \, \frac{\operatorname{Im} g_w(q,\omega)}{\omega}, \tag{F.16}$$

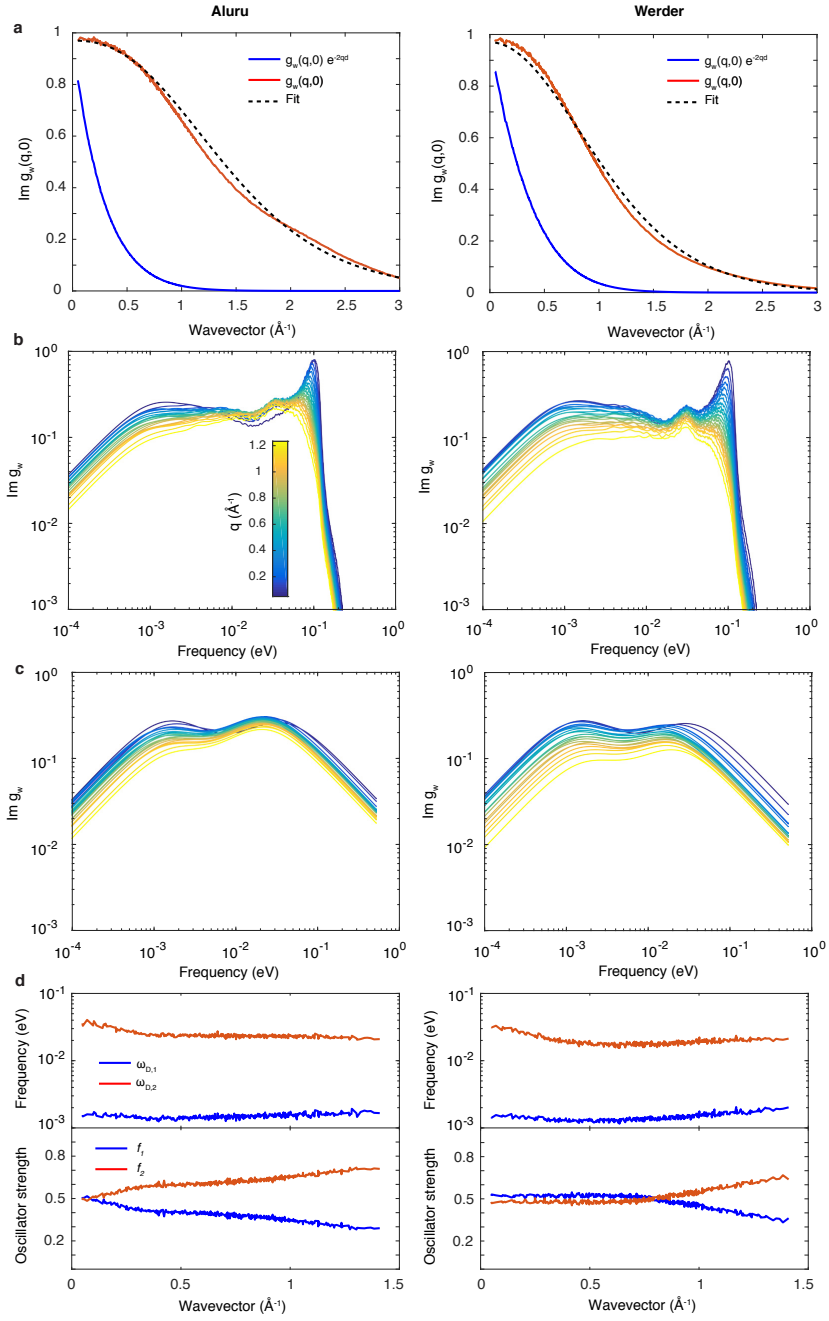

Figure F.5

Surface respose of water: simulation results. The left (right) column corresponds to Aluru (Werder) parameters. **a**. Static surface response function, as obtained from the static structure factor, before and after cancellation of the gap d. The dashed line shows a fit to the data (eq. (F.21)). **b**. Surface response as a function of frequency, for different values of the wavevector q. **c**. Result of fitting the surface excitation spectra with two Debye peaks, for different wavevectors. **d**. Fitting parameter values. Frequencies of the Debye peaks (top), and relative oscillator strengths (bottom).

since $\mathrm{Im}\, g_w(q,\omega)$ is an odd function of frequency. Using the fluctuation-dissipation theorem (F.13), we obtain

$$\int_0^{+\infty} \mathrm{d}\omega \, \frac{\mathrm{Im}\, g_w(q,\omega)}{\omega} = \frac{e^2}{8\epsilon_0 k_\mathrm{B} T} \int_{-\infty}^{+\infty} \mathrm{d}\omega \, \frac{S_s(q)}{q}. \tag{F.17}$$

Then, using the definition (F.12) of the static structure factor, we recover the sum rule (F.14). The surface structure factor is related to the full three-dimensional structure factor according to

$$\bar{S}_s(q) = \int_0^{+\infty} \mathrm{d}z \mathrm{d}z' e^{-q(z+z')} \bar{S}(q,z,z'), \tag{F.18}$$

with $\bar{S}(q,z,z') = (1/\mathcal{A})\langle n_w(\mathbf{q},z) n_w(-\mathbf{q},z')\rangle$. We may assume that the main contribution to the integral in eq. (F.18) comes from the terms $z \approx z'$, due to the layering of the liquid near the surface [163]. Then $S(q,z,z') \approx S(q|z)\delta(z-z')$, and we further assume that the structure factor is similar in all layers: $S(q|z) \approx S(q|0)$. Then, we have simply

$$\bar{S}_s(q) = \int_0^{+\infty} \mathrm{d}z e^{-2qz} \bar{S}(q|0) = \frac{S(q|0)}{2q}, \tag{F.19}$$

$S(q|0)$ is defined by the Fourier transform

$$S(q|0) = \int \mathrm{d}\boldsymbol{\rho} \, e^{-i\mathbf{q}\boldsymbol{\rho}} S(\rho|0). \tag{F.20}$$

Since the structure factor is isotropic, the coefficients of odd powers of q in a Taylor expansion around $q = 0$ vanish upon angular integration in eq. (F.20). Hence the small q expansion of $S_s(q|0)$ contains only even powers of q, and the one of $S_s(q)$ only odd powers, justifying the procedure described in section F.3.2.2.

F.3.3 Fitting

The evaluation of quantum friction coefficients with eq. (E.45) required to fit the MD simulation data, so as to avoid issues with numerical integration. The MD simulation results are reported in figure 5.3 and figure F.5. Figures F.5 a and b show the static surface response function $g_w(q,0)$, as obtained from the static structure factor (eq. (F.14)), before and after cancellation of the gap d, for both sets of LJ parameters. The simulation data was fitted with the following expression:

$$g_w(q,0) = \exp\left[a + a'(1 + (q/b)^\alpha)^{1/\alpha}\right], \tag{F.21}$$

with the constraint $a + a' = \log(g_w(0,0)) = \log(0.97)$, since the long wavelength limit of $g_w(q,0)$ is imposed by the static permittivity $\epsilon(0) = 71$ of SPC/E water: $g_w(0,0) = (\epsilon(0)-1)/(\epsilon(0)+1)$. The following results were obtained for the fit parameters:

	a	a'	b $(^{-1})$	α
Werder	5.16	−5.19	1.95	2
Aluru	3.38	−3.41	1.79	2.4

The imaginary part of the surface response function was then fitted by a sum of two Debye peaks:

$$\operatorname{Im} g_w(q,\omega) = \operatorname{Im}\left[\frac{f_1(q)}{1 - i\omega/\omega_{D,1}(q)} + \frac{f_2(q)}{1 - i\omega/\omega_{D,2}(q)}\right], \tag{F.22}$$

with the constraint $f_1(q) + f_2(q) = g_w(q,0)$ so as to satisfy the sum rule (F.14). As can be seen in figure F.5c, this fitting function reproduces quite well the general shape of the surface response function below 100 meV. The values we obtain for quantum friction coefficients are insensitive to the water response at higher frequencies, since these are cut off by the thermal factor in eq. (E.45). Furthermore, our classical simulations become inaccurate at frequencies above 100 meV, since at these frequencies the quantum nature of the dynamics can no longer be neglected (see, for instance, the comparison with an experimental result in the long wavelength limit, figure 5.3b). For both sets of LJ parameters, the frequencies of the two Debye peaks remain roughly constant (figure F.5d), at $\omega_{D,1} = 1.5$ meV and $\omega_{D,2} = 20$ meV. In the long wavelength limit, the two Debye peaks have the same oscillator strength, but the wavevector dependence is different for the two sets of parameters. The general trend is that the oscillator strength is transferred from the lower to the upper Debye peak as the wavevector increases.

For evaluating quantum friction coefficients, we used the results obtained with Aluru parameters. Precisely, we represented the surface response function by the following analytical expression:

$$g_w(q,\omega) = \frac{g_w(q,0)}{2}\left[\frac{e^{-q/q_0}}{1 - i\omega/\omega_{D,1}} + \frac{2 - e^{-q/q_0}}{1 - i\omega/\omega_{D,2}}\right], \tag{F.23}$$

with $\omega_{D,1} = 1.5$ meV, $\omega_{D,2} = 20$ meV, $q_0 = 3.12$ $^{-1}$ and $g_w(q,0)$ given by eq. (F.21). The result in eq. (F.23) is plotted in figure 5.3c as a function of frequency and wavevector.

F.3.4 DFT calculation

We carried out an ab-initio molecular dynamics (AIMD) simulation of a graphene-water interface of area 12.83 $\times$ 12.35 using the CP2K software. The simulation is identical to the one described in [55] with the difference that the hydroxide ion is replaced by a water molecule. A VASP calculation was performed on a single configuration extracted from the dynamics, again following [55]. We used the Perdew, Burke and Ernzerhof functional [286] with the D3 dispersion correction scheme [287, 288], which has been shown to provide a good description of the water/graphene interface [289]. Plane waves with kinetic energy larger than 600 eV were cut off and convergence was reached when the difference between total energy and eigenvalue energies was smaller than 10^{-6} eV. The resulting electronic density, once averaged in the direction parallel to the interface, is shown in figure 5.1b.

Bibliography

[1] Murata, K. *et al.* Structural determinants of water permeation through aquaporin 1. *Nature* **407**, 599–605 (2000).

[2] MacKinnon, R. Potassium Channels and the Atomic Basis of Selective Ion Conduction. *Biosci. Rep.* **24**, 75–100 (2004).

[3] Wu, J., Lewis, A. H. & Grandl, J. Touch, Tension, and Transduction - The Function and Regulation of Piezo Ion Channels. *Trends Biochem. Sci.* **42**, 57–71 (2017).

[4] Bocquet, L. & Tabeling, P. Physics and technological aspects of nanofluidics. *Lab Chip* **14**, 3143–3158 (2014).

[5] Siria, A., Bocquet, M. L. & Bocquet, L. New avenues for the large-scale harvesting of blue energy. *Nat. Rev. Chem.* **1** (2017).

[6] McKay, D. J. C. *Sustainable Energy Without the Hot Air* (Cambridge UIT, 2009).

[7] Sholl, D. S. & Lively, R. P. Seven chemical separations to change the world. *Nature* **532**, 435–437 (2016).

[8] Bocquet, L. Nanofluidics coming of age. *Nat. Mater.* **19**, 254–256 (2020).

[9] Kavokine, N., Netz, R. R. & Bocquet, L. Fluids at the Nanoscale: From Continuum to Subcontinuum Transport. *Annu. Rev. Fluid Mech.* **53** (2021).

[10] Siria, A. *et al.* Giant osmotic energy conversion measured in a single transmembrane boron nitride nanotube. *Nature* **494**, 455–458 (2013).

[11] Chun, H. & Chung, T. D. Iontronics. *Annu. Rev. Anal. Chem.* **8**, 441–462 (2015).

[12] Bocquet, L. & Charlaix, E. Nanofluidics, from bulk to interfaces. *Chem. Soc. Rev.* **39**, 1073–1095 (2010).

[13] Lee, C. Y., Choi, W., Han, J.-H. & Strano, M. S. Coherence Resonance in a Single-Walled Carbon Nanotube Ion Channel. *Science* **329**, 1320–1324 (2010).

[14] Choi, W. *et al.* Diameter-dependent ion transport through the interior of isolated single-walled carbon nanotubes. *Nat. Commun.* **4**, 1–8 (2013).

[15] Radha, B. *et al.* Molecular transport through capillaries made with atomic-scale precision. *Nature* **538**, 222–225 (2016).

[16] Esfandiar, A. *et al.* Size effect in ion transport through angstrom-scale slits. *Science* **358**, 511–513 (2017).

[17] Gopinadhan, K. *et al.* Complete steric exclusion of ions and proton transport through confined monolayer water. *Science* **363**, 145–148 (2019).

[18] Keerthi, A. *et al.* Ballistic molecular transport through two-dimensional channels. *Nature* **558**, 420–423 (2018).

[19] Majumder, M., Smalley, R. E. & Hinds, B. J. Mass transport through carbon nanotube membranes in three different regimes: Ionic, liquid and gas. *AIChE Annu. Meet. Conf. Proc.* 3867–3877 (2008).

[20] Holt, J. K. *et al.* Fast Mass Transport Through Sub-2-Nanometer Carbon Nanotubes. *Science* **312**, 1034–1037 (2006).

[21] Whitby, M., Cagnon, L., Thanou, M. & Quirke, N. Enhanced fluid flow through nanoscale carbon pipes. *Nano letters* **8**, 2632–2637 (2008).

[22] Nair, R., Wu, H., Jayaram, P., Grigorieva, I. & Geim, A. Unimpeded permeation of water through helium-leak–tight graphene-based membranes. *Science* **335**, 442–444 (2012).

[23] Secchi, E. *et al.* Massive radius-dependent flow slippage in carbon nanotubes. *Nature* **537**, 210–213 (2016).

[24] Tunuguntla, R. H. *et al.* Enhanced water permeability and tunable ion selectivity in subnanometer carbon nanotube porins. *Science* **357**, 792–796 (2017).

[25] Xie, Q. *et al.* Fast water transport in graphene nanofluidic channels. *Nat. Nanotech.* **13**, 238–245 (2018).

[26] Faucher, S. *et al.* Critical Knowledge Gaps in Mass Transport through Single-Digit Nanopores: A Review and Perspective. *J. Phys. Chem. C* **123**, 21309–21326 (2019).

[27] Eijkel, J. C. & van den Berg, A. Nanofluidics: What is it and what can we expect from it? *Microfluid. Nanofluidics* **1**, 249–267 (2005).

[28] Sparreboom, W., Van Den Berg, A. & Eijkel, J. C. Transport in nanofluidic systems: A review of theory and applications. *New J. Phys.* **12** (2010).

[29] Schoch, R. B., Han, J. & Renaud, P. Transport phenomena in nanofluidics. *Rev. Mod. Phys.* **80**, 839–883 (2008).

[30] Vlassiouk, I. & Siwy, Z. S. Nanofluidic diode. *Nano Lett.* **7**, 552–556 (2007).

[31] Feng, J. *et al.* Single-layer MoS2 nanopores as nanopower generators. *Nature* **536**, 197–200 (2016).

[32] Keyser, U. F. *et al.* Direct force measurements on DNA in a solid-state nanopore. *Nat. Phys.* **2**, 473–477 (2006).

[33] Dekker, C. Solid-state nanopores. *Nat. Nanotechnol.* **2**, 209–215 (2007).

[34] Garaj, S. *et al.* Graphene as a subnanometre trans-electrode membrane. *Nature* **467**, 190–193 (2010).

[35] Sahu, S. & Zwolak, M. Ionic phenomena in nanoscale pores through 2D materials. *Rev. Mod. Phys.* **91**, 021004 (2019).

[36] Celebi, K. *et al.* Ultimate permeation across atomically thin porous graphene. *Science* **344**, 289–292 (2014).

[37] Feng, J. *et al.* Electrochemical reaction in single layer MoS2: Nanopores opened atom by atom. *Nano Lett.* **15**, 3431–3438 (2015).

[38] Feng, J. *et al.* Observation of ionic Coulomb blockade in nanopores. *Nat. Mater.* **15**, 850–855 (2016).

[39] Walker, M. I. *et al.* Extrinsic Cation Selectivity of 2D Membranes. *ACS Nano* **11**, 1340–1346 (2017).

[40] O'Hern, S. C. *et al.* Selective molecular transport through intrinsic defects in a single layer of CVD graphene. *ACS Nano* **6**, 10130–10138 (2012).

[41] Koenig, S. P., Wang, L., Pellegrino, J. & Bunch, J. S. Selective molecular sieving through porous graphene. *Nat. Nanotechnol.* **7**, 728–732 (2012).

[42] Jain, T. *et al.* Heterogeneous sub-continuum ionic transport in statistically isolated graphene nanopores. *Nat. Nanotechnol.* **10**, 1053–1057 (2015).

[43] Lee, C. Y., Choi, W., Han, J. H. & Strano, M. S. Coherence resonance in a single-walled carbon nanotube ion channel. *Science* **329**, 1320–1324 (2010).

[44] Yazda, K. *et al.* Voltage-activated transport of ions through single-walled carbon nanotubes. *Nanoscale* **9**, 11976–11986 (2017).

[45] Pang, P., He, J., Park, J. H., Krstić, P. S. & Lindsay, S. Origin of giant ionic currents in carbon nanotube channels. *ACS Nano* **5**, 7277–7283 (2011).

[46] Marcotte, A., Mouterde, T., Niguès, A., Siria, A. & Bocquet, L. Mechanically activated ionic transport across single-digit carbon nanotubes. *Nat. Mater.* **19**, 1057–1061 (2020).

[47] Liu, L., Yang, C., Zhao, K., Li, J. & Wu, H. C. Ultrashort single-walled carbon nanotubes in a lipid bilayer as a new nanopore sensor. *Nat. Commun.* **4**, 1–8 (2013).

[48] Maali, A., Cohen-Bouhacina, T. & Kellay, H. Measurement of the slip length of water flow on graphite surface. *Appl. Phys. Lett.* **92**, 2007–2009 (2008).

[49] Sampson, R. On Stokes's current function. *Philos. Trans. R. Soc. London.* **182**, 449–518 (1891).

[50] Dagan, Z., Weinbaum, S. & Pfeffer, R. An infinite-series solution for the creeping motion through an orifice of finite length. *J. Fluid Mech.* **115**, 505–523 (1982).

[51] Gravelle, S. *et al.* Optimizing water permeability through the hourglass shape of aquaporins. *Proc. Natl. Acad. Sci. U. S. A.* **110**, 16367–16372 (2013).

[52] Chmiola, J. *et al.* Anomalous increase in carbon at pore sizes less than 1 nanometer. *Science* **313**, 1760–1763 (2006).

[53] Merlet, C. *et al.* On the molecular origin of supercapacitance in nanoporous carbon electrodes. *Nat. Mater.* **11**, 306–310 (2012).

[54] Perram, J. W., Hunter, R. J. & Wright, H. J. Charge and potential at the oxide/solution interface. *Chem. Phys. Lett.* **23**, 265–269 (1973).

[55] Grosjean, B., Bocquet, M. L. & Vuilleumier, R. Versatile electrification of two-dimensional nanomaterials in water. *Nat. Commun.* **10**, 1–8 (2019).

[56] Mouhat, F., Coudert, F.-X. & Bocquet, M.-L. Structure and chemistry of graphene oxide in liquid water from first principles. *Nat. Commun.* **11**, 1566 (2020).

[57] Levine, S., Marriott, J. R. & Robinson, K. Theory of electrokinetic flow in a narrow parallel-plate channel. *J. Chem. Soc. Faraday Trans. 2 Mol. Chem. Phys.* **71**, 1–11 (1975).

[58] Andelman, D. Electrostatic properties of membranes: The poisson-boltzmann theory. *Handb. Biol. Phys.* **1**, 603–642 (1995).

[59] Israelachvili, J. *Intermolecular and Surface Forces*, chap. 14, 291–292 (Academic Press, 2011).

[60] Stein, D., Kruithof, M. & Dekker, C. Surface-charge-governed ion transport in nanofluidic channels. *Phys. Rev. Lett.* **93**, 035901–1 (2004).

[61] Secchi, E., Niguès, A., Jubin, L., Siria, A. & Bocquet, L. Scaling behavior for ionic transport and its fluctuations in individual carbon nanotubes. *Phys. Rev. Lett.* **116**, 1–5 (2016).

[62] Hille, B. Pharmacological modifications of the sodium channels of frog nerve. *J. Gen. Physiol.* **51**, 199–219 (1968).

[63] Hall, J. E. Access resistance of a small circular pore. *J. Gen. Physiol.* **66**, 531–532 (1975).

[64] Lee, C. *et al.* Large apparent electric size of solid-state nanopores due to spatially extended surface conduction. *Nano Lett.* **12**, 4037–4044 (2012).

[65] Khair, A. S. & Squires, T. M. Surprising consequences of ion conservation in electro-osmosis over a surface charge discontinuity. *J. Fluid Mech.* **615**, 323–334 (2008).

[66] Xie, Y., Fu, L. & Joly, L. Liquid-solid slip on charged walls: dramatic impact of charge distribution. *arXiv:2002.02444* (2020).

[67] Mouterde, T. & Bocquet, L. Interfacial transport with mobile surface charges and consequences for ionic transport in carbon nanotubes. *Eur. Phys. J. E* **41** (2018).

[68] Mouterde, T. *et al.* Molecular streaming and its voltage control in ångström-scale channels. *Nature* **567**, 87–90 (2019).

[69] Parsegian, A. Energy of an Ion crossing a Low Dielectric Membrane: Solutions to Four Relevant Electrostatic Problems. *Nature* **221**, 844–846 (1969).

[70] Teber, S. Translocation energy of ions in nano-channels of cell membranes. *J. Stat. Mech. Theory Exp.* 1–17 (2005).

[71] Levin, Y. Electrostatics of ions inside the nanopores and trans-membrane channels. *Europhys. Lett.* **76**, 163–169 (2006).

[72] Loche, P., Ayaz, C., Schlaich, A., Uematsu, Y. & Netz, R. R. Giant Axial Dielectric Response in Water-Fille Nanotubes an Effective Electrostatic Ion-Ion Interactions from a Tensorial Dielectric Model. *J. Phys. Chem. B* **123**, 10850–10857 (2019).

[73] Fumagalli, L. *et al.* Anomalously low dielectric constant of confined water. *Science* **360**, 1339–1342 (2018).

[74] Bonthuis, D. J., Gekle, S. & Netz, R. R. Profile of the static permittivity tensor of water at interfaces: Consequences for capacitance, hydration interaction and ion adsorption. *Langmuir* **28**, 7679–7694 (2012).

[75] Bonthuis, D. J., Gekle, S. & Netz, R. R. Dielectric profile of interfacial water and its effect on double-layer capacitance. *Phys. Rev. Lett.* **107**, 1–5 (2011).

[76] Schlaich, A., Knapp, E. W. & Netz, R. R. Water Dielectric Effects in Planar Confinement. *Phys. Rev. Lett.* **117**, 1–5 (2016).

[77] Zhang, C., Gygi, F. & Galli, G. Strongly anisotropic dielectric relaxation of water at the nanoscale. *J. Phys. Chem. Lett.* **4**, 2477–2481 (2013).

[78] Weber, E. The electrostatic field produced by a point charge in the axis of a cylinder. *J. Appl. Phys.* **10**, 663–666 (1939).

[79] Kondrat, S. & Kornyshev, A. Superionic state in double-layer capacitors with nanoporous electrodes. *J. Phys. Condens. Matter* **23**, 022201 (2011).

[80] Lee, J., Laoui, T. & Karnik, R. Nanofluidic transport governed by the liquid/vapour interface. *Nat. Nanotechnol.* **9**, 317–323 (2014).

[81] Ritchie, R. H. & Marusak, A. L. The surface plasmon dispersion relation for an electron gas. *Surf. Sci.* **4**, 234–240 (1966).

[82] Mahan, G. *Many-Particle Physics*, chap. 5, 442–443 (Dover, 1990).

[83] Miyazaki, H. *et al.* Inter-layer screening length to electric field in thin graphite film. *Appl. Phys. Express* **1**, 0340071–0340073 (2008).

[84] Richards, L. A., Schäfer, A. I., Richards, B. S. & Corry, B. The importance of dehydration in determining ion transport in narrow pores. *Small* **8**, 1701–1709 (2012).

[85] Epsztein, R., Shaulsky, E., Qin, M. & Elimelech, M. Activation behavior for ion permeation in ion-exchange membranes: Role of ion dehydration in selective transport. *J. Memb. Sci.* **580**, 316–326 (2019).

[86] Apell, H. J. & Karlish, S. J. Functional properties of Na,K-ATpase, and their structural implications, as detected with biophysical techniques. *J. Membr. Biol.* **180**, 1–9 (2001).

[87] Heginbotham, L., Kolmakova-Partensky, L. & Miller, C. Functional reconstitution of a prokaryotic k+ channel. *The Journal of General Physiology* **111**, 741–749 (1998).

[88] Dayan, P. *Theoretical Neuroscience* (MIT-Press, 2000).

[89] Kaufman, Igor Kh. *et al.* Ionic coulomb blockade and anomalous mole fraction effect in the nachbac bacterial ion channel and its charge-varied mutants. *EPJ Nonlinear Biomed. Phys.* **5**, 4 (2017).

[90] Fedorenko, Olena A. *et al.* Quantized dehydration and the determinants of selectivity in the nachbac bacterial sodium channel. *arXiv:1803.07063* .

[91] Stopa, M. Rectifying Behavior in Coulomb Blockades: Charging Rectifiers. *Phys. Rev. Lett.* **88**, 4 (2002).

[92] Krems, M. & Di Ventra, M. Ionic Coulomb blockade in nanopores. *J. Phys. Condens. Matter* **25** (2013).

[93] Tanaka, H., Iizuka, H., Pershin, Y. V. & Di Ventra, M. Surface effects on ionic Coulomb blockade in nanometer-size pores. *Nanotechnology* **29** (2018).

[94] Li, W. *et al.* Gated water transport through graphene nanochannels: From ionic coulomb blockade to electroosmotic pump. *The Journal of Physical Chemistry C* **121**, 17523–17529 (2017).

[95] Beenakker, C. W. Theory of Coulomb-blockade oscillations in the conductance of a quantum dot. *Phys. Rev. B* **44**, 1646–1656 (1991).

[96] Nazarov, Y. V. & Blanter, Y. M. *Quantum Transport: Introduction to Nanoscience* (Cambridge University Press, 2009).

[97] Feng, J. *et al.* Single-layer MoS2 nanopores as nanopower generators. *Nature* **536**, 197–200 (2016).

[98] Kaufman, I. K., McClintock, P. V. & Eisenberg, R. S. Coulomb blockade model of permeation and selectivity in biological ion channels. *New J. Phys.* **17** (2015).

[99] von Kitzing, E. A novel model for saturation of ion conductivity in transmembrane channels. In Pullman, A., Jortner, J. & Pullman, B. (eds.) *Membrane Proteins: Structures, Interactions and Models*, 297–314 (Springer Netherlands, Dordrecht, 1992).

[100] Luchinsky, D. G., Gibby, W. A. T., Kaufman, I., Timucin, D. A. & McClintock, P. V. E. Statistical theory of selectivity and conductivity in biological channels. *arXiv:1604.05758v3* (2016).

[101] Netz, H. H. & Orland, H. Variational charge renormalization in charged systems. *Eur. Phys. J. E* **11**, 301–311 (2003).

[102] Buyukdagli, S., Manghi, M. & Palmeri, J. Variational approach for electrolyte solutions: From dielectric interfaces to charged nanopores. *Phys. Rev. E - Stat. Nonlinear, Soft Matter Phys.* **81**, 1–20 (2010).

[103] Buyukdagli, S., Manghi, M. & Palmeri, J. Ionic capillary evaporation in weakly charged nanopores. *Phys. Rev. Lett.* **105**, 1–4 (2010).

[104] Bazant, M. Z., Storey, B. D. & Kornyshev, A. A. Double layer in ionic liquids: Overscreening versus crowding. *Phys. Rev. Lett.* **106**, 6–9 (2011).

[105] De Souza, J. P. & Bazant, M. Z. Continuum Theory of Electrostatic Correlations at Charged Surfaces. *J. Phys. Chem. C* **124**, 11414–11421 (2020).

[106] Levin, Y. Electrostatic correlations: From plasma to biology. *Reports Prog. Phys.* **65**, 1577–1632 (2002).

[107] Kamenev, A., Zhang, J., Larkin, A. I. & Shklovskii, B. I. Transport in one-dimensional Coulomb gases: From ion channels to nanopores. *Phys. A Stat. Mech. its Appl.* **359**, 129–161 (2006).

[108] Zhang, J., Kamenev, A. & Shklovskii, B. I. Conductance of ion channels and nanopores with charged walls: A toy model. *Phys. Rev. Lett.* **95**, 1–4 (2005).

[109] Zhang, J., Kamenev, A. & Shklovskii, B. I. Ion exchange phase transitions in water-filled channels with charged walls. *Phys. Rev. E - Stat. Nonlinear, Soft Matter Phys.* **73**, 1–16 (2006).

[110] Gulden, T. & Kamenev, A. Dynamics of Ion Channels via Non-Hermitian Quantum Mechanics. *Entropy* **23**, 125 (2021).

[111] Cooper, K. & Jakobsson, E. The theory of ion transport through membrane channels. *Prog. Biophys. Mol. Biol.* **46**, 51–96 (1985).

[112] Edwards, S. F. & Lenard, A. Exact statistical mechanics of a one-dimensional system with coulomb forces. II. The method of functional integration. *J. Math. Phys.* **3**, 778–792 (1962).

[113] Démery, V., Dean, D. S., Hammant, T. C., Horgan, R. R. & Podgornik, R. The one-dimensional Coulomb lattice fluid capacitor. *J. Chem. Phys.* **137** (2012).

[114] Onsager, L. Deviations from Ohm's law in weak electrolytes. *J. Chem. Phys.* **2**, 599–615 (1934).

[115] Kaiser, V., Bramwell, S. T., Holdsworth, P. C. & Moessner, R. Onsager's Wien effect on a lattice. *Nat. Mater.* **12**, 1033–1037 (2013).

[116] Redner, S. *A Guide to First Passage Problems* (Cambridge University Press, 2001).

[117] Pothier, H., Lafarge, P., Urbina, C., Esteve, D. & Devoret, M. H. Single-electron pump based on charging effects. *Epl* **17**, 249–252 (1992).

[118] Sebastian, A., Le Gallo, M., Khaddam-Aljameh, R. & Eleftheriou, E. Memory devices and applications for in-memory computing. *Nat. Nanotechnol.* **15**, 529–544 (2020).

[119] Hodgkin, A. L. & Huxley, A. F. The components of membrane conductance in the giant axon of *Loligo*. *The Journal of Physiology* **116**, 473–496 (1952).

[120] Hille, B. Ionic channels in excitable membranes. Current problems and biophysical approaches. *Biophysical Journal* **22**, 283–294 (1978).

[121] Gerstner, W. & Kistler, W. M. *Spiking Neuron Models: Single Neurons, Populations, Plasticity* (Cambridge University Press, 2002).

[122] Chandrakasan, A. P., Sheng, S. & Brodersen, R. W. Low-Power CMOS Digital Design. *Low-Power C. Des.* **27**, 36–46 (1998).

[123] Kavokine, N., Marbach, S., Siria, A. & Bocquet, L. Ionic Coulomb blockade as a fractional Wien effect. *Nat. Nanotechnol.* **14**, 573–578 (2019).

[124] Chua, L. Memristor-The missing circuit element. *IEEE Transactions on Circuit Theory* **18**, 507–519 (1971).

[125] Strukov, D. B., Snider, G. S., Stewart, D. R. & Williams, R. S. The missing memristor found. *Nature* **453**, 80–83 (2008).

[126] Minnhagen, P. The two-dimensional Coulomb gas, vortex unbinding, and superfluid-superconducting films. *Reviews of Modern Physics* **59**, 1001–1066 (1987).

[127] Kosterlitz, J. M. & Thouless, D. J. Ordering, metastability and phase transitions in two-dimensional systems. *J. Phys. C: Solid State Phys.* **6**, 1181–1203 (1973).

[128] Fuoss, R. M. Conductance of Dilute Solutions of 1-1 Electrolytes. *J. Am. Chem. Soc.* **81**, 2659–2662 (1959).

[129] Park, H. G. & Jung, Y. Carbon nanofluidics of rapid water transport for energy applications. *Chem. Soc. Rev.* **43**, 565–576 (2014).

[130] Joshi, R. *et al.* Precise and ultrafast molecular sieving through graphene oxide membranes. *Science* **343**, 752–754 (2014).

[131] Abraham, J. *et al.* Tunable sieving of ions using graphene oxide membranes. *Nat. Nanotech.* **12**, 546 (2017).

[132] Bocquet, L. & Barrat, J. L. Flow boundary conditions from nano- to micro-scales. *Soft Matter* **3**, 685–693 (2007).

[133] Joseph, S. & Aluru, N. Why are carbon nanotubes fast transporters of water? *Nano letters* **8**, 452–458 (2008).

[134] Thomas, J. A. & McGaughey, A. J. Reassessing fast water transport through carbon nanotubes. *Nano Lett.* **8**, 2788–2793 (2008).

[135] Falk, K., Sedlmeier, F., Joly, L., Netz, R. R. & Bocquet, L. Molecular origin of fast water transport in carbon nanotube membranes: Superlubricity versus curvature dependent friction. *Nano Lett.* **10**, 4067–4073 (2010).

[136] Neek-Amal, M. *et al.* Fast water flow through graphene nanocapillaries: A continuum model approach involving the microscopic structure of confined water. *Appl. Phys. Lett.* **113**, 083101 (2018).

[137] Tocci, G., Joly, L. & Michaelides, A. Friction of water on graphene and hexagonal boron nitride from Ab initio methods: Very different slippage despite very similar interface structures. *Nano Lett.* **14**, 6872–6877 (2014).

[138] Lauga, E., Brenner, M. & Stone, H. Microfluidics: The No-Slip Boundary Condition. *Springer Handb. Exp. Fluid Mech.* 1219–1240 (2007).

[139] Barrat, J.-L. & Bocquet, L. Influence of wetting properties on hydrodynamic boundary conditions at a fluid/solid interface. *Faraday Discuss.* **112**, 119–128 (1999).

[140] Bocquet, L. & Barrat, J. L. On the Green-Kubo relationship for the liquid-solid friction coefficient. *J. Chem. Phys.* **139** (2013).

[141] Bocquet, L. & Barrat, J. L. Hydrodynamic boundary conditions, correlation functions, and Kubo relations for confined fluids. *Phys. Rev. E* **49**, 3079–3092 (1994).

[142] Huang, D. M., Sendner, C., Horinek, D., Netz, R. R. & Bocquet, L. Water slippage versus contact angle: A quasiuniversal relationship. *Phys. Rev. Lett.* **101**, 1–4 (2008).

[143] Werder, T., Walther, J. H., Jaffe, R., Halicioglu, T. & Koumoutsakos, P. On the water- carbon interaction for use in molecular dynamics simulations of graphite and carbon nanotubes. *J. Phys. Chem. B* **107**, 1345–1352 (2003).

[144] Kannam, S. K., Todd, B. D., Hansen, J. S. & Daivis, P. J. How fast does water flow in carbon nanotubes? *J. Chem. Phys.* **138** (2013).

[145] Misra, R. P. & Blankschtein, D. Insights on the Role of Many-Body Polarization Effects in the Wetting of Graphitic Surfaces by Water. *J. Phys. Chem. C* **121**, 28166–28179 (2017).

[146] Tocci, G., Bilichenko, M., Joly, L. & Iannuzzi, M. Ab initio Nanofluidics: Disentangling the role of the energy land-scape and of density correlations on liquid/solid friction. *Nanoscale* (2020).

[147] Persson, B. N. & Volokitin, A. I. Electronic friction of physisorbed molecules. *J. Chem. Phys.* **103**, 8679–8683 (1995).

[148] Zwanzig, R. Dielectric friction on a moving ion. ii. revised theory. *J. Chem. Phys.* **52**, 3625–3628 (1970).

[149] Sedlmeier, F., Shadkhoo, S., Bruinsma, R. & Netz, R. R. Charge/mass dynamic structure factors of water and applications to dielectric friction and electroacoustic conversion. *J. Chem. Phys.* **140** (2014).

[150] Boyer, T. H. Penetration of the electric and magnetic velocity fields of a nonrelativistic point charge into a conducting plane. *Phys. Rev. A* **9**, 68–82 (1974).

[151] Nunez, R., Echenique, P. M. & Ritchie, R. H. The energy loss of energetic ions moving near a solid surface. *J. Phys. C Solid State Phys.* **13**, 4229–4246 (1980).

[152] Head-Gordon, M. & Tully, J. C. Molecular dynamics with electronic frictions. *J. Chem. Phys.* **103**, 10137–10145 (1995).

[153] Tomassone, M. & Widom, A. Electronic friction forces on molecules moving near metals. *Phys. Rev. B* **56**, 4938–4943 (1997).

[154] Dou, W. & Subotnik, J. E. Perspective: How to understand electronic friction. *J. Chem. Phys.* **148** (2018).

[155] Sokoloff, J. B. Enhancement of the water flow velocity through carbon nanotubes resulting from the radius dependence of the friction due to electron excitations. *Phys. Rev. E* **97**, 33107 (2018).

[156] Sokoloff, J. B. Effects of electronic friction from the walls on water flow in carbon nanotubes and on water desalination. *Phys. Rev. E* **100**, 023112 (2019).

[157] Dzyaloshinksii, I., Lifshitz, E., Pitaevskii, L. & Priestley, M. The general theory of van der Waals forces. *Adv. Phys.* 165–209 (1961).

[158] Volokitin, A. I. & Persson, B. N. Near-field radiative heat transfer and noncontact friction. *Rev. Mod. Phys.* **79**, 1291–1329 (2007).

[159] Keldysh, L. V. Diagram Technique for Nonequilibrium Processes. *Sov. Phys. JETP* **20**, 1018 (1965).

[160] Rammer, J. & Smith, H. Quantum field-theoretical methods in transport theory of metals. *Rev. Mod. Phys.* **58**, 323–359 (1986).

[161] Chandler, D. Gaussian field model of fluids with an application to polymeric fluids. *Phys. Rev. E* **48**, 2898–2905 (1993).

[162] Song, X., Chandler, D. & Marcus, R. A. Gaussian field model of dielectric solvation dynamics. *J. Phys. Chem.* **100**, 11954–11959 (1996).

[163] Barrat, J. L. & Bocquet, L. Infuence of wetting properties on hydrodynamic boundary conditions at a fluid/solid interface. *Faraday Discuss.* **112**, 119–127 (1999).

[164] Levitov, L. S. Van Der Waals' Friction. *Europhys. Lett.* **8**, 499–504 (1989).

[165] Pendry, J. B. Shearing the vacuum - Quantum friction. *J. Phys. Condens. Matter* **9**, 10301–10320 (1997).

[166] Persson, B. & Zhang, Z. Theory of friction: Coulomb drag between two closely spaced solids. *Phys. Rev. B.* **57**, 7327–7334 (1998).

[167] Volokitin, A. I. & Persson, B. N. Van der Waals frictional drag induced by liquid flow in low-dimensional systems. *Phys. Rev. B* **77**, 2–5 (2008).

[168] Volokitin, A. I. & Persson, B. N. Quantum field theory of van der Waals friction. *Phys. Rev. B - Condens. Matter Mater. Phys.* **74**, 1–11 (2006).

[169] Wu, Y. & Aluru, N. R. Graphitic carbon-water nonbonded interaction parameters. *J. Phys. Chem. B* **117**, 8802–8813 (2013).

[170] Elton, D. C. *Understanding the dielectric properties of water*. Ph.D. thesis, Stony Brook University (2016).

[171] Carlson, S., Brünig, F. N., Loche, P., Bonthuis, D. J. & Netz, R. R. Exploring the Absorption Spectrum of Simulated Water from MHz to Infrared. *J. Phys. Chem. A* **124**, 5599–5605 (2020).

[172] Popov, I., Ishai, P. B., Khamzin, A. & Feldman, Y. The mechanism of the dielectric relaxation in water. *Phys. Chem. Chem. Phys.* **18**, 13941–13953 (2016).

[173] Lang, N. D. & Kohn, W. Theory of metal surfaces: Charge density and surface energy. *Phys. Rev. B* **1**, 4555–4568 (1970).

[174] Penzar, Z. & Sunjić, M. Surface electronic response in the random phase approximation and infinite barrier model: Surface plasmons, electron-hole pairs and the interaction with external particles. *Phys. Scr.* **30**, 431–443 (1984).

[175] Griffin, A. & Harris, J. Sum rules for a bounded electron gas. *Can. J. Phys.* **54**, 1396–1408 (1976).

[176] Wunsch, B., Stauber, T., Sols, F. & Guinea, F. Dynamical polarization of graphene at finite doping. *New J. Phys.* **8** (2006).

[177] Jensen, E. T., Palmer, R. E., Allison, W. & Annett, J. F. Temperature-dependent plasmon frequency and linewidth in a semimetal. *Phys. Rev. Lett.* **66**, 492–495 (1991).

[178] Laitenberger, P. & Palmer, R. E. Plasmon dispersion and damping at the surface of a semimetal. *Phys. Rev. Lett.* **76**, 1952–1955 (1996).

[179] Portail, M., Carrere, M. & Layet, J. M. Dynamical properties of graphite and peculiar behaviour of the low-energy plasmon. *Surf. Sci.* **433**, 863–867 (1999).

[180] Vitali, L., Schneider, M. A., Kern, K., Wirtz, L. & Rubio, A. Phonon and plasmon excitation in inelastic electron tunneling spectroscopy of graphite. *Phys. Rev. B - Condens. Matter Mater. Phys.* **69**, 1–4 (2004).

[181] Dresselhaus, M. S. & Dresselhaus, G. Intercalation compounds of graphite. *Adv. Phys.* **51**, 1–186 (1981).

[182] Lavor, I. R., Cavalcante, L. S. R., Chaves, A., Peeters, F. M. & Van Duppen, B. Probing the structure and composition of van der Waals heterostructures using the nonlocality of Dirac plasmons in the terahertz regime. *2D Mater.* **8**, 015014 (2020).

[183] Tománek, D. *et al.* Theory and observation of highly asymmetric atomic structure in scanning-tunneling-microscopy images of graphite. *Phys. Rev. B* **35**, 7790–7793 (1987).

[184] Partoens, B. & Peeters, F. M. From graphene to graphite: Electronic structure around the K point. *Phys. Rev. B - Condens. Matter Mater. Phys.* **74**, 1–11 (2006).

[185] Grüneis, A. *et al.* Tight-binding description of the quasiparticle dispersion of graphite and few-layer graphene. *Phys. Rev. B - Condens. Matter Mater. Phys.* **78**, 1–16 (2008).

[186] Endo, M. *et al.* Stacking nature of graphene layers in carbon nanotubes and nanofibres. *J. Phys. Chem. Solids* **58**, 1707–1712 (1997).

[187] Franklin, R. E. The structure of graphitic carbons. *Acta Crystallogr.* **4**, 253–261 (1951).

[188] Speck, J. S., Endo, M. & Dresselhaus, M. S. Structure and intercalation of thin benzene derived carbon fibers. *J. Cryst. Growth* **94**, 834–848 (1989).

[189] Charlier, J. C., Blase, X. & Roche, S. Electronic and transport properties of nanotubes. *Rev. Mod. Phys.* **79**, 677–732 (2007).

[190] Park, J. Y. & Salmeron, M. Fundamental aspects of energy dissipation in friction. *Chem. Rev.* **114**, 677–711 (2014).

[191] Venables, D. S. & Schmuttenmaer, C. A. Spectroscopy and dynamics of mixtures of water with acetone, acetonitrile, and methanol. *J. Chem. Phys.* **113**, 11222–11236 (2000).

[192] Sato, T. & Buchner, R. Dielectric relaxation processes in ethanol/water mixtures. *J. Phys. Chem. A* **108**, 5007–5015 (2004).

[193] Koeberg, M., Wu, C. C., Kim, D. & Bonn, M. THz dielectric relaxation of ionic liquid:water mixtures. *Chem. Phys. Lett.* **439**, 60–64 (2007).

[194] Pisana, S. *et al.* Breakdown of the adiabatic Born-Oppenheimer approximation in graphene. *Nat. Mater.* **6**, 198–201 (2007).

[195] Stauber, T. & Kohler, H. Quasi-Flat Plasmonic Bands in Twisted Bilayer Graphene. *Nano Lett.* **16**, 6844–6849 (2016).

[196] Secchi, E., Marbach, S., Niguès, A., Siria, A. & Bocquet, L. The Landau-Squire plume. *J. Fluid Mech.* **826**, R3 (2017).

[197] Walz, T., Smith, B. L., Zeidel, M. L., Engel, A. & Agre, P. Biologically active two-dimensional crystals of aquaporin CHIP. *J. Biol. Chem.* **269**, 1583–1586 (1994).

[198] Pohl, P., Saparov, S. M. & Antonenko, Y. N. The effect of a transmembrane osmotic flux on the ion concentration distribution in the immediate membrane vicinity measured by microelectrodes. *Biophys. J.* **72**, 1711–1718 (1997).

[199] Saparov, S. M. *et al.* Mobility of a one-dimensional confined file of water molecules as a function of file length. *Phys. Rev. Lett.* **96**, 1–4 (2006).

[200] Laohakunakorn, N. *et al.* A Landau-Squire nanojet. *Nano Lett.* **13**, 5141–5146 (2013).

[201] Cuenca, A. & Bodiguel, H. Submicron flow of polymer solutions: Slippage reduction due to confinement. *Phys. Rev. Lett.* **110**, 1–5 (2013).

[202] Lee, C. *et al.* Osmotic flow through fully permeable nanochannels. *Phys. Rev. Lett.* **112**, 1–5 (2014).

[203] Jeffery, G. The two-dimensional steady motion of a viscous fluid. *London, Edinburgh, Dublin Philos. Mag. J. Sci.* **29**, 455–465 (1915).

[204] Hamel, G. Spiralformige bewegungen zaher flussigkeiten. *Jahresbericht der Deutschen Mathematiker-Vereinigung* **25**, 34–60 (1917).

[205] Millsaps, K. & Pohlhausen, K. Thermal Distributions in Jeffery-Hamel Flows Between Nonparallel Plane Walls. *J. Aeronaut. Sci.* **20**, 187–196 (1953).

[206] Crookes, W. On attraction and repulsion resulting from radiation. *Philosophical transactions of the Royal Society* **164**, 501–527 (1874).

[207] Clerk Maxwell, J. VII. On stresses in rarified gases arising from inequalities of temperature. *Philosophical transactions of the Royal Society* **170**, 231–256 (1878).

[208] White, T. J. (ed.) *Photomechanical Materials, Composites, and Systems.* Wireless Transduction of Light into Work (John Wiley & Sons, Ltd, Chichester, UK, 2017).

[209] Tsuda, Y. *et al.* Flight status of IKAROS deep space solar sail demonstrator. *Acta Astronautica* **69**, 833–840 (2011).

[210] Tsu, T. C. Interplanetary Travel by Solar Sail. *ARS Journal* **29**, 422–427 (1959).

[211] Phipps, C. *et al.* Review: Laser-Ablation Propulsion. *Journal of Propulsion and Power* **26**, 609–637 (2010).

[212] Dogariu, A., Sukhov, S. & Sáenz, J. Optically induced 'negative forces'. *Nature Photonics* **7**, 24–27 (2013).

[213] Zhang, T. *et al.* Macroscopic and direct light propulsion of bulk graphene material. *Nature Photonics* **9**, 471–476 (2015).

[214] Schermer, R. T., Olson, C. C., Coleman, J. P. & Bucholtz, F. Laser-induced thermophoresis of individual particles in a viscous liquid. *Optics Express* **19**, 10571–10586 (2011).

[215] Jiang, H.-R., Yoshinaga, N. & Sano, M. Active Motion of a Janus Particle by Self-Thermophoresis in a Defocused Laser Beam. *Physical Review Letters* **105**, 268302 (2010).

[216] Irimajiri, A., Hanai, T. & Inouye, A. A dielectric theory of "multi-stratified shell" model with its application to a lymphoma cell. *Journal of Theoretical Biology* **78**, 251–269 (1979).

[217] Würger, A. Thermal non-equilibrium transport in colloids. *Reports on Progress in Physics* **73**, 126601 (2010).

[218] Piazza, R. & Parola, A. Thermophoresis in colloidal suspensions. *Journal of Physics: Condensed Matter* **20**, 153102 (2008).

[219] Duhr, S. & Braun, D. Why molecules move along a temperature gradient. *Proceedings of the National Academy of Sciences* **103**, 19678–19682 (2006).

[220] Putnam, S. A. & Cahill, D. G. Transport of nanoscale latex spheres in a temperature gradient. *Langmuir* **21**, 5317–5323 (2005).

[221] Braibanti, M., Vigolo, D. & Piazza, R. Does thermophoretic mobility depend on particle size? *Physical Review Letters* **100**, 1–4 (2008).

[222] Lauterborn, W. & Kurz, T. Physics of bubble oscillations. *Reports on Progress in Physics* **73**, 106501 (2010).

[223] Borkent, B. M. *et al.* The acceleration of solid particles subjected to cavitation nucleation. *Journal of Fluid Mechanics* **610**, 157–182 (2008).

[224] Hou, L., Yorulmaz, M., Verhart, N. R. & Orrit, M. Explosive formation and dynamics of vapor nanobubbles around a continuously heated gold nanosphere. *New Journal of Physics* **17**, 013050 (2015).

[225] Jollans, T. & Orrit, M. Explosive, oscillatory, and leidenfrost boiling at the nanoscale. *Phys. Rev. E* **99**, 063110 (2019).

[226] Wang, Y. *et al.* Giant and explosive plasmonic bubbles by delayed nucleation. *Proceedings of the National Academy of Sciences of the United States of America* **115**, 7676–7681 (2018).

[227] Golestanian, R. Collective Behavior of Thermally Active Colloids. *Physical Review Letters* **108**, 539 (2012).

[228] Saha, S., Golestanian, R. & Ramaswamy, S. Clusters, asters, and collective oscillations in chemotactic colloids. *Physical Review E* **89**, 062316 (2014).

[229] Jeans, J. H. The stability of a spherical nebula. *Philos. Trans. Royal Soc. A* **199**, 312–320 (1902).

[230] Battaner, E. *Astrophysical Fluid Dynamics*, 166–167 (Cambridge University Press, 1996).

[231] Keller, E. F. & Segel, L. A. Initiation of slime mold aggregation viewed as an instability. *Journal of Theoretical Biology* **26**, 399–415 (1970).

[232] Brenner, M. P., Levitov, L. S. & Budrene, E. O. Physical Mechanisms for Chemotactic Pattern Formation by Bacteria. *Biophysical Journal* **74**, 1677–1693 (1998).

[233] Theurkauff, I., Cottin-Bizonne, C., Palacci, J., Ybert, C. & Bocquet, L. Dynamic Clustering in Active Colloidal Suspensions with Chemical Signaling. *Physical Review Letters* **108**, 268303 (2012).

[234] Marbach, S. & Bocquet, L. Osmosis, from molecular insights to large-scale applications. *Chem. Soc. Rev.* **48**, 3102–3144 (2019).

[235] Bleibel, J., Dietrich, S., Domínguez, A. & Oettel, M. Shock Waves in Capillary Collapse of Colloids: A Model System for Two-Dimensional Screened Newtonian Gravity. *Physical Review Letters* **107**, 128302 (2011).

[236] Leveugle, E., Sellinger, A., Fitz-Gerald, J. M. & Zhigilei, L. V. Making Molecular Balloons in Laser-Induced Explosive Boiling of Polymer Solutions. *Physical Review Letters* **98**, 216101 (2007).

[237] West, D. M., Lal, I. K., Leamy, M. J. & Hu, D. L. Locomotion of mexican jumping beans. *Bioinspiration & Biomimetics* **7**, 036014 (2012).

[238] Noblin, X. *et al.* The Fern Sporangium: A Unique Catapult. *Science* **335**, 1322–1322 (2012).

[239] Chen, F. *et al.* Ionic conductance oscillations in sub-nanometer pores probed by optoelectronic control (2020). 2012.14093.

[240] Rabinowitz, J., Cohen, C. & Shepard, K. L. An Electrically Actuated, Carbon-Nanotube-Based Biomimetic Ion Pump. *Nano Lett.* (2020).

[241] Ghosh, S., Sood, A. K. & Kumar, N. Carbon Nanotube Flow Sensors. *Science* **299**, 1042–1044 (2003).

[242] Rammer, J. *Quantum Field Theory of Non-Equilibrium States*, chap. 6 (Cambridge University Press, Cambridge, 2007).

[243] Démery, V., Monsarrat, R., Dean, D. S. & Podgornik, R. Phase diagram of a bulk 1d lattice Coulomb gas. *Epl* **113**, 1–6 (2016).

[244] Démery, V., Dean, D. S., Hammant, T. C., Horgan, R. R. & Podgornik, R. Over-screening in a 1D lattice Coulomb gas model of ionic liquids. *Epl* **97** (2012).

[245] Dean, D. S., Horgan, R. R. & Sentenac, D. Boundary Effects in the One-Dimensional Coulomb Gas. *J. Stat. Phys.* **90**, 899–926 (1998).

[246] Abramowitz, M. & Stegun, I. *Handbook of Mathematical Functions* (Dover Publications, 1964).

[247] Kaufman, I. K. *et al.* Ionic Coulomb blockade and anomalous mole fraction effect in the NaChBac bacterial ion channel and its charge-varied mutants. *EPJ Nonlinear Biomed. Phys.* **5**, 4 (2017).

[248] Liu, C.-T. *The effect of screening of the ionic atmosphere on the theory of the Wien effect in weak electrolytes.* Ph.D. thesis, Yale (1965).

[249] Kaiser, V. *The Wien Effect in Electric and Magnetic Coulomb systems - from Electrolytes to Spin Ice.* Ph.D. thesis, ENS Lyon (2014).

[250] McIlroy, D. K. & Mason, D. P. Wien dissociation in very low intensity electric fields. *J. Chem. Soc., Faraday Trans. 2* **72**, 590–596 (1976).

[251] Salem, L. The forces between polyatomic molecules. II. Short-range repulsive forces. *Proc. R. Soc. London. Ser. A. Math. Phys. Sci.* **264**, 379–391 (1961).

[252] Rackers, J. A. & Ponder, J. W. Classical Pauli repulsion: An anisotropic, atomic multipole model. *J. Chem. Phys.* **150** (2019).

[253] Muscat, J. & Newns, D. Chemisorption on metals. *Prog. Surf. Sci.* **9**, 1–43 (1978).

[254] Rammer, J. *Quantum Field Theory of Non-Equilibrium States* (Cambridge University Press, Cambridge, 2007).

[255] Kamenev, A. *Field Theory of Non-Equilibrium Systems* (Cambridge University Press, 2011).

[256] Larkin, A. & Ovchinnikov, Y. Nonlinear conductivity of superconductors in the mixed state. *Sov. Phys. JETP* **41**, 960 (1975).

[257] Migdal, A. Interaction Between Electrons and the Lattice Vibrations in a Normal Metal. *Sov. Phys. JETP* **34**, 996–1001 (1958).

[258] Roy, B., Sau, J. D. & Das Sarma, S. Migdal's theorem and electron-phonon vertex corrections in Dirac materials. *Phys. Rev. B* **89**, 1–8 (2014).

[259] Rammer, J. *Quantum Field Theory of Non-Equilibrium States*, chap. 3 (Cambridge University Press, Cambridge, 2007).

[260] Despoja, V., Echenique, P. M. & Sunjic, M. Quantum friction between oscillating crystal slabs: Graphene monolayers on dielectric substrates. *Phys. Rev. B* **98** (2018).

[261] Despoja, V., Maruić, L. & Unjić, M. Quantum mechanical response of coupled metallicslabs. *J. Phys. Condens. Matter* **18**, 8217–8228 (2006).

[262] Lindhard, J. On the properites of a gas of charged particles. *Dan. Mat. Phys. Medd.* **28**, 8 (1954).

[263] Bruus, H. & Flensberg, K. *Many-Body Quantum Theory in Condensed Matter Physics*, chap. 13 (Oxford University Press, 2004).

[264] Blinowski, J. *et al.* Band structure model and dynamical dielectric function in lowest stages of graphite acceptor compounds. *J. Phys.* **41**, 47–58 (1980).

[265] Shung, K. W. Dielectric function and plasmon structure of stage-1 intercalated graphite. *Phys. Rev. B* **34**, 979–993 (1986).

[266] Hwang, E. H. & Das Sarma, S. Dielectric function, screening, and plasmons in two-dimensional graphene. *Phys. Rev. B - Condens. Matter Mater. Phys.* **75**, 1–6 (2007).

[267] Mahan, G. D. *Many-Particle Physics*, chap. 3 (Springer, 2000).

[268] Plimpton, S. Fast parallel algorithms for short-range molecular dynamics. *J. Comput. Phys.* **117**, 1–19 (1995).

[269] Frenkel, D. & Smit, B. *Understanding Molecular Simulation* (Academic Press, 1996).

[270] Yoshida, H., Kaiser, V., Rotenberg, B. & Bocquet, L. Dripplons as localized and superfast ripples of water confined between graphene sheets. *Nature Communications* **9**, 1496 (2018).

[271] Martinez, L., Andrade, R., Birgin, E. G. & Martinez, J. M. PACKMOL: A package for building initial configurations for molecular dynamics simulations. *Journal of Computational Chemistry* **30**, 2157–2164 (2009).

[272] Ryckaert, J.-P., Ciccotti, G. & Berendsen, H. J. Numerical integration of the cartesian equations of motion of a system with constraints: molecular dynamics of n-alkanes. *Journal of Computational Physics* **23**, 327–341 (1977).

[273] Allen, M. P. & Tildesley, D. J. *Computer Simulation of Liquids* (Oxford University Press, 2017).

[274] Yeh, I.-C. & Berkowitz, M. L. Ewald summation for systems with slab geometry. *J. Chem. Phys.* **111**, 3155–3162 (1999).

[275] Frenkel, D. & Smit, B. *Understanding Molecular Simulation: From Algorithms to Applications* (Elsevier, 2001).

[276] Humphrey, W., Dalke, A. & Schulten, K. VMD - Visual Molecular Dynamics. *Journal of Molecular Graphics* **14.1**, 33–38 (1996).

[277] Berendsen, H. J. C., Postma, J. P. M., van Gunsteren, W. F. & Hermans, J. Interaction Models for Water in Relation to Protein Hydration. In Pullman, B. (ed.) *Intermolecular Forces: Proceedings of the Fourteenth Jerusalem Symposium on Quantum Chemistry and Biochemistry Held in Jerusalem, Israel, April 13, 1981*, The Jerusalem Symposia on Quantum Chemistry and Biochemistry, 331–342 (Springer Netherlands, Dordrecht, 1981).

[278] Werber, J. R., Osuji, C. O. & Elimelech, M. Materials for next-generation desalination and water purification membranes. *Nature Reviews Materials* **1**, 1–15 (2016).

[279] Smith, D. E. & Dang, L. X. Computer simulations of NaCl association in polarizable water. *J. Chem. Phys.* **100**, 3757–3766 (1994).

[280] Dang, L. X. & Smith, D. E. Comment on mean force potential for the calcium chloride ion pair in water. *The Journal of Chemical Physics* **102**, 3483–3484 (1995).

[281] Cannon, W. R., Pettitt, B. M. & McCammon, J. A. Sulfate Anion in Water: Model Structural, Thermodynamic, and Dynamic Properties. *The Journal of Physical Chemistry* **98**, 6225–6230 (1994).

[282] Wu, Y., Wagner, L. K. & Aluru, N. R. Hexagonal boron nitride and water interaction parameters. *J. Chem. Phys.* **144** (2016).

[283] Berendsen, H. J., Grigera, J. R. & Straatsma, T. P. The missing term in effective pair potentials. *J. Phys. Chem.* **91**, 6269–6271 (1987).

[284] Ryckaert, J. P., Ciccotti, G. & Berendsen, H. J. Numerical integration of the cartesian equations of motion of a system with constraints: molecular dynamics of n-alkanes. *J. Comput. Phys.* **23**, 327–341 (1977).

[285] Bussi, G., Donadio, D. & Parrinello, M. Canonical sampling through velocity rescaling. *J. Chem. Phys.* **126** (2007).

[286] Perdew, J. P., Burke, K. & Ernzerhof, M. Generalized gradient approximation made simple. *Phys. Rev. Lett.* **77**, 3865–3868 (1996).

[287] Grimme, S., Antony, J., Ehrlich, S. & Krieg, H. A consistent and accurate ab initio parametrization of density functional dispersion correction (DFT-D) for the 94 elements H-Pu. *J. Chem. Phys.* **132** (2010).

[288] Grimme, S., Ehrlich, S. & Goerigk, L. Effect of the damping function in dispersion corrected density functional theory. *J. Comput. Chem.* **32**, 1456–1465 (2011).

[289] Brandenburg, J. G. *et al.* Physisorption of Water on Graphene: Subchemical Accuracy from Many-Body Electronic Structure Methods. *J. Phys. Chem. Lett.* **10**, 358–368 (2019).

RÉSUMÉ

Cette thèse explore plusieurs phénomènes de transport de fluides aux nanoéchelles qui résultent de corrélations entre les particules. Nous montrons que dans un canal nanométrique, les parois affectent non seulement le mouvement du fluide, mais aussi ses interactions. Ainsi, nous prédisons des corrélations ioniques renforcées dans les électrolytes confinés, avec des conséquences allant du blocage de Coulomb ionique aux effets de mémoire. Nous explorons ensuite les corrélations entre la dynamique de l'eau interfaciale et des électrons de la paroi solide, qui induisent une contribution quantique à la friction hydrodynamique. Enfin, nous présentons le développement d'un dispositif expérimental pour la mesure de flux d'eau dans des canaux bidimensionnels.

MOTS CLÉS

Nanofluidique, Électrolytes, Physique statistique, Théorie des champs

ABSTRACT

This thesis explores several phenomena that arise in nanoscale fluid transport due to inter-particle correlations. We show that in nanoscale channels, the walls affect not only the fluid motion, but also its interactions. As a result, we predict enhanced ionic correlations in confined electrolytes, with consequences ranging from ionic Coulomb blockade to memory effects. We further explore how correlations between interfacial water and electron dynamics in the channel wall result in a quantum contribution to hydrodynamic friction. Finally, we present the development of an experimental setup for measuring water flow through two-dimensional channels.

KEYWORDS

Nanofluidics, Electrolytes, Statistical mechanics, Field theory